# Structural Effects, Solvent Interactions, and Machine Learning Potentials in Photochemistry of Cyclohexadiene and Hexatriene Derivatives: A Computational Investigation

*A dissertation submitted in partial fulfillment for the degree of*

*Doctor of Philosophy*


*Submitted By*

**Biman Medhi**

**Roll No. 196122009**




Under the Supervision of

**Prof. Manabendra Sarma**

DEPARTMENT OF CHEMISTRY

INDIAN INSTITUTE OF TECHNOLOGY GUWAHATI

GUWAHATI-781039, ASSAM, INDIA


**August 2025**

*Dedicated to my Parents and Sisters (Jumi baa and Chumi baa)*

**INDIAN INSTITUTE OF TECHNOLOGY GUWAHATI**
**Department of Chemistry**

# Statement

I do hereby declare that the matter embodied in this thesis is the result of investigations carried out by me in the Department of Chemistry, Indian Institute of Technology Guwahati, India, under the guidance of Prof. Manabendra Sarma. I have submitted this thesis to the Department of Chemistry, Indian Institute of Technology Guwahati for the award of the degree of Doctor of Philosophy.

In keeping with the general practice of reporting scientific observations, due acknowledgments have been made wherever the work described is based on the findings of other investigators. I further declare that this work has not been submitted anywhere else for any degree, diploma, associateship or membership, etc. of any Institute or University to the best of my knowledge.

August, 2025

IIT Guwahati **Biman Medhi**

**INDIAN INSTITUTE OF TECHNOLOGY GUWAHATI**
**Department of Chemistry**

# Certificate

This is to certify that Biman Medhi has been working under my supervision since July 2019 as a registered Ph.D. student. His thesis entitled "**Structural Effects, Solvent Interactions, and Machine Learning Potentials in Photochemistry of Cyclohexadiene and Hexatriene Derivatives: A Computational Investigation**" is an authentic record of the results obtained from the research work in the Department of Chemistry, Indian Institute of Technology Guwahati, Assam, India. I am forwarding his thesis to submit for the Ph.D. (Science) degree from this institute. I certify that he has fulfilled all the requirements according to the rules of this institute regarding the investigations embodied in his thesis, and this work has not been submitted elsewhere for a degree.

August, 2025

**Prof. Manabendra Sarma**
(Thesis Supervisor)
Department of Chemistry
IIT Guwahati

# *Acknowledgement*

*Completing this Ph.D. journey has been a long, enriching, and exciting experience, and it would not have been possible without the support, encouragement, and contributions of many individuals directly or indirectly. I would like to take this opportunity to express my deepest gratitude to everyone who stood by me throughout this endeavor.*

*First and foremost, I owe my sincerest thanks to my Ph.D. supervisor, Prof. Manabendra Sarma, whose mentorship has been the cornerstone of my academic journey. His insightful guidance, constant encouragement, and constructive criticism helped me grow not only as a researcher but also as a person. I am deeply grateful for his patience, his trust in my abilities, and the freedom he gave me to explore, question, and learn. His unwavering support during difficult times, both academically and personally, kept me motivated and focused. I will always cherish the opportunity to have worked under his supervision and carry forward the values, discipline, and curiosity I have imbibed during this journey.*

*I would like to extend my heartfelt gratitude to my doctoral committee members, Prof. Ashish Kumar Gupta (Chairperson), Prof. Ranjan Tamuli (Member), Dr. Sunanda Chatterjee (Member), and Dr. Debdas Dhabal (Member), for their invaluable guidance, encouragement, and thoughtful feedback throughout the course of my PhD journey. Their diverse perspectives, critical insights, and unwavering support have significantly enriched the quality of my research. Each discussion and suggestion, whether during formal reviews or casual conversations, helped me refine my work and pushed me to think more deeply and critically. Beyond the technical guidance, their mentorship has also shaped my approach to scientific inquiry and academic integrity. I am truly grateful for their time, patience, and commitment to my growth as a researcher.*

*Although not a formal member of my doctoral committee, I am deeply grateful to Prof. Aditya Narayan Panda, for his generous support, valuable advice, and consistent encouragement throughout my research journey. His willingness to share his insights had a meaningful*

*impact on both my academic progress and personal development. I truly appreciate the time and attention he devoted to my work, despite not being officially obligated to do so.*

*I extend my heartfelt thanks to my labmates who made the lab feel like a second home. I especially wish to acknowledge my seniors Dr. Juhi Dutta, Dr. Haobam Kisan Singh, Dr. Himangshu Pratim Bhattacharyya, and Bittu Lama for their role models during my initial years. Their willingness to help, their knowledge, and their camaraderie left a lasting impression on me. My juniors Shubham, Manash, Samsung (Syam), Anand, Rimi, Yugant, Madhab, and Ruckshana brought energy, curiosity, and fresh perspectives into our workspace, and I thoroughly enjoyed working with and learning from them. I am equally thankful to my batchmates Niharika, Upasana, Monalisha, and Rabu da who walked alongside me through every step of this journey. From helping each other during research work to jamming near the Serpentine Lake the company was amazing and I will cherish forever.*

*To my dear friends Surjya, Hirak, Debika, Sukesh, Raktim, Rajdikshit da, Abhay, Jagnyesh, Shantanu, and Rahul da thank you for being my anchor. Your presence, both near and far, was a source of comfort and strength. Whether it was a call during tough times, a laugh during coffee breaks, or words of reassurance when things seemed uncertain, your unwavering support made all the difference.*

*I am fortunate to have found friends like family beyond the walls of my lab. To Anandita, Mira, Kima, Dino, Palak, Deepak, Debashmita, Nishanta, Hrishikesh (Prof. U. Manna Sir's Lab), Priyanka, Derek, Hrishikesh (Prof. Gupta Sir's Lab), Hrishikesh (Prof. Tamal Sir's Lab), Partha, Ruchi, and Adyasha my "brothers and sisters" from other research labs, you were always there to exchange ideas, share resources, offer advice, or simply be a friendly face. Your companionship and support enriched my academic and personal life.*

*To the MSc/BSc/Intern students I had the privilege to work with Papu, Simran, Mohit, and Kabyashree thank you for trusting me, for asking questions that made me think deeper, and for reminding me of the excitement of starting out in research. Watching your growth was one of the most fulfilling parts of my own journey.*

*I would also like to thank my cricket companions cum brothers, Pran Da, Biraj Da, NMD da, Shekhar da, Samar da, Kalpa, Ketan Bhiaya, Sheshraj, Akshya, Ranjit, BDN Deo, Anit, Rakesh, and many others, who shared the field with me during our time at IIT. From the PhD Premier League to the Interstate Premier League and the IIT Premier League, every match we played together was not just a game, but a celebration of friendship, teamwork, and much-*

*needed relief from the stress of not getting a successful trajectory in surface hopping simulations or not getting a conical intersection. Those moments of joy, competition, and camaraderie will always remain special to me.*

*I would like to extend heartfelt thanks to my dear friend Bubul, with whom I shared countless hours of discussion, not just about science, but about life. From playing cricket and watching movies to pulling each other's legs and standing by one another in tough times, his presence made this journey not only bearable but joyful. Thank you for being a constant source of strength and laughter.*

*I am equally grateful to Himani, whose unwavering support, encouragement, and friendship have meant a great deal to me throughout this PhD journey. Her calming presence and thoughtful words helped me stay grounded and focused, and for that, I am truly thankful.*

*I would also like to express my gratitude to special friend, Mrinal, Pinku, Dimpi, and Palash, whose constant support and encouragement have meant a great deal to me. Mrinal, who has been a friend since our school days in class 8/9, has been a steady presence in my life. Pinku and Dimpi, my close companions from MSc, brought comfort and familiarity that carried through to my PhD years. Palash, whom I've known for more than three years, has also been a strong pillar of motivation. Thank you all for being there through the highs and lows of this journey.*

*I would also like to acknowledge the invaluable computational support provided by the PARAM-ISHAN supercomputing facility and the resources of PARAM-KAMRUPA under the National Supercomputing Mission (NSM) at IIT Guwahati. This initiative, implemented by C-DAC and supported by the Ministry of Electronics and Information Technology (MeitY) and the Department of Science and Technology (DST), Government of India, greatly facilitated the computational aspects of my research. I am also thankful to the Department of Chemistry, IIT Guwahati, for providing the necessary laboratory and infrastructure support. Additionally, I gratefully acknowledge the financial assistance received from the Ministry of Human Resource Development (MHRD), Government of India.*

*I would also like to express my deepest respect and gratitude to all the teachers, who laid the foundation for my academic journey. Each of you has, in some way, contributed to my growth and shaped the way I think and work. Thank you for your dedication, passion, and belief in your students.*

*Lastly, my deepest gratitude goes to my family, my parents and my two sisters (Jumi baa and Chumi baa). No words can ever fully capture the love and sacrifices you have made for me. Your constant encouragement, understanding, and faith in me have been the backbone of this journey. Thank you for everything, for letting me dream and for giving me the strength to pursue those dreams.*

**Biman Medhi**

# Contents

**Synopsis** **1**

**List of Publications** **11**

**Conferences/Workshops Attended** **13**

**List of Abbreviations** **15**

**List of Figures** **17**

**List of Tables** **25**

**1 Introduction** **27**

1.1 A Brief Historical Overview of Photochemistry . . . . . 27

1.2 Understanding the Basics of Photochemistry . . . . . 28

1.3 Photochemistry of Cyclohexadiene to Hexatriene Conversion . . . . . 30

1.4 Substituents' Impact on Photochemistry . . . . . 32

1.5 Solvation Effects on Photochemistry . . . . . 33

1.6 Photochemistry as a Tool for Functional Materials . . . . . 34

1.7 Machine Learning for Photochemistry Exploration . . . . . 35

1.8 Overview of Thesis . . . . . 36

**2 Theoretical and Computational Methodology** **39**

2.1 Breakdown of Born-Oppenheimer Approximation . . . . . 39

2.2 Configuration Interaction . . . . . 41

2.3 Complete Active Space Self-Consistent Field (CASSCF) . . . . . 42

2.4 Complete Active Space Second-Order Perturbation Theory (CASPT2) . . . . . 42

2.5 Classical Molecular Dynamics Simulations . . . . . 43

2.6 Trajectory Surface Hopping (TSH) Approach . . . . . 45
2.6.1 Fewest-Switches Surface Hopping (FSSH) . . . . . 45
2.6.2 Landau–Zener Surface Hopping (LZSH) . . . . . 46
2.6.3 Landau-Zener-Belyaev-Lebedev (LZBL) Surface Hopping . . . . . 47
2.7 Neural Networks for PESs . . . . . 47

**3 Impact of Structural Modifications on Internal Conversion Processes in Cyclohexadiene Photochemistry 49**
3.1 Introduction . . . . . 49
3.2 Computational Details . . . . . 53
3.3 Results and Discussion . . . . . 55
3.3.1 Structural Analysis and Energetics . . . . . 55
3.3.2 From Geodesic Interpolation to On-the-fly Molecular Dynamics . . . . 60
3.4 Conclusions . . . . . 69

**4 Effect of Polar and Non-Polar Media on Photoinduced Ring-Opening of Cyclohexadiene: A QM/MM-based Surface Hopping Approach 71**
4.1 Introduction . . . . . 71
4.2 Computational Details . . . . . 72
4.2.1 Initial Molecular Geometry Optimizations . . . . . 72
4.2.2 Classical Molecular Dynamics Simulations . . . . . 73
4.2.3 Non-adiabatic Surface Hopping Molecular Dynamics Simulations using QM/MM approach . . . . . 74
4.3 Results and Discussion . . . . . 75
4.3.1 Excitation Energy of Classically Sampled Initial CHD Geometries . . . 75
4.3.2 QM/MM Non-adiabatic Surface Hopping Simulations . . . . . 77
4.4 Conclusions . . . . . 84

**5 Photochemistry and Functionality in a Fulgide Molecule with Hexatriene Core 85**
5.1 Introduction . . . . . 85
5.2 Computational Details . . . . . 88
5.3 Results and Discussion . . . . . 91
5.3.1 Optimization of the Molecular Structures: Ground State, Excited State, MECI, and TSC . . . . . 91

5.3.2 Vertical Excitation to the First Excited State . . . . . 92
5.3.3 Conical Intersection Topography and Reaction Energy Profile Diagram 94
5.3.4 Geodesic Interpolation . . . . . 95
5.3.5 Surface Hopping Molecular Dynamics Simulation . . . . . 97
5.3.6 Electron Transport Calculations . . . . . 100
5.4 Conclusions . . . . . 102

**6 Application and Comparison of Machine Learning Potentials in Studying Photochemistry of Cyclohexadiene 105**
6.1 Introduction . . . . . 105
6.2 Preparation of Dataset for Training the MLP Models . . . . . 107
6.3 Results and Discussion . . . . . 109
6.3.1 Training and Testing of PES Models . . . . . 109
6.3.2 Energy Gap Analysis . . . . . 113
6.3.3 Geodesic Interpolations of Electronic States Energies . . . . . 115
6.3.4 Surface Hopping Simulations . . . . . 116
6.4 Conclusions . . . . . 119

**7 Summary and Conclusions 121**

**Appendix 123**

**Bibliography 143**

# *Synopsis*

# Synopsis

Photochemistry is a branch of chemistry that explores how a molecular system absorbs and interacts with light to initiate chemical reactions. One key photochemical process studied widely is the ring-opening/closure reaction associated with the cyclohexadiene (CHD) system. This process is vital in the photochemical synthesis of Vitamin $D_3$ in the skin and is also found in various photoswitches and photoactive materials. Depending on the system, photochemical reactions may follow adiabatic or non-adiabatic pathways, and understanding these mechanisms is important for unraveling the complex dynamics within molecular systems. The role of internal conversion in governing photochemical ring-opening/closure processes in CHD and its related derivatives are explored using computational approach based on quantum mechanical and machine learning approaches. The thesis is structured as follows-

Chapter I begins with an introduction to photochemistry, emphasizing various adiabatic and non-adiabatic processes occurring within a molecular system.

Chapter II explains the details of the theoretical and computational methodology used throughout our research works.

Chapter III explores the photochemical ring-opening dynamics of substituted CHD derivatives to investigate the effects of substitutions in internal conversion processes.

Chapter IV understands the effect of polar and non-polar environments in photochemical ring-opening dynamics of CHD molecule.

Chapter V explores an experimentally synthesized fulgide molecule made up of a hexatriene (HT) core, photochemistry, and electron transport properties.

Chapter VI employs machine learning potentials trained on three datasets to run extended MD simulations, comparing ring-opening dynamics using SS-ANI and MS-ANI models.

Chapter VII summarizes and concludes the outcomes of our work during the research journey.

# Chapter I

## Introduction

This chapter gives a general overview of different aspects, from important fundamental photochemistry to machine learning in quantum chemical methods. When a molecule absorbs light, it gets excited to a higher electronic state. After that, it can relax to lower potential energy surfaces through adiabatic and non-adiabatic pathways. We discuss how the usual Born-Oppenheimer approach fails to explain such processes and why we need to go beyond it. Then, we look at the photochemistry of the CHD molecule and some important related biological and synthetic compounds, that have had a strong impact on the scientific community. We also explain how machine learning in quantum chemistry has helped researchers run complex simulations for longer times and uncover interesting photochemical behaviors. Finally, we end this chapter by outlining the goals and boundaries of our research.

# Chapter II

## Theoretical and Computational Methodology

This chapter gives brief descriptions of all the theoretical and computational approaches utilized throughout the research work. During our study, we have employed electronic structure theory calculations, classical molecular dynamics simulations, and mixed quantum-classical molecular dynamics simulations based on quantum mechanical and machine learning potentials. The investigation employed electronic structure theory methods, including density functional theory (DFT) and wavefunction-based approaches like CASSCF and XMS-CASPT2. Classical molecular dynamics simulations were performed using OPLS-AA force fields and the TIP3P water model. Further, mixed quantum-classical dynamics was performed at the quantum mechanical level using the QM/MM approach to study the effect of the nature of the solvent in the considered photochemical reaction. Moreover, photochemistry was also explored using machine learning potentials based on single-state ANI (SS-ANI) and multi-state ANI (MS-ANI) models. This mixed quantum-classical dynamics was carried out using Tully's surface hopping with the Decoherence-Corrected Fewest Switches Surface Hopping (DC-FSSH) and the Landau–Zener–Belyaev–Lebedev (LZBL) based surface hopping, where the former requires explicit calculation of non-adiabatic couplings, and the latter does not. A detailed description of the theoretical background and working principles of all these methods is provided in this chapter.

# Chapter III

## Impact of Structural Modifications on Internal Conversion Processes in Cyclohexadiene Photochemistry

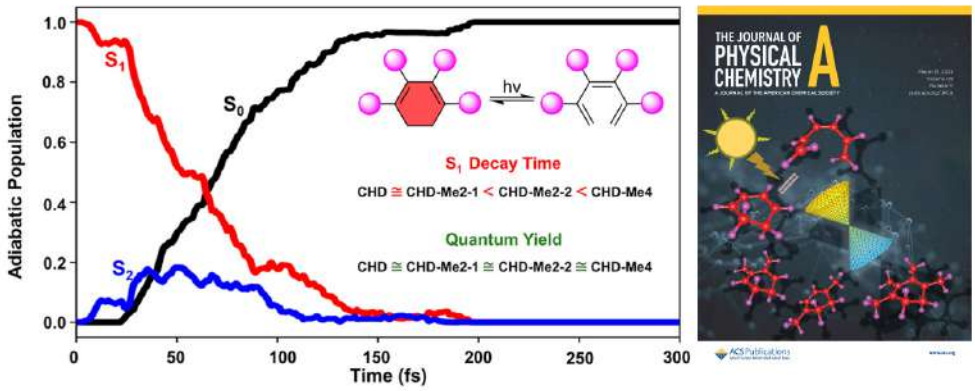


Chemical substituents can significantly modulate the photochemical behavior of molecular systems and are key to understanding nonadiabatic processes. In this study, we present a comparative analysis of how different substituents influence the photochemical ring-opening of 1,3-cyclohexadiene (CHD). Four systems were examined: CHD, 2,3-dimethylcyclohexadiene (CHD-Me2-1), 1,4-dimethylcyclohexadiene (CHD-Me2-2), and 1,2,3,4-tetramethylcyclohexadiene (CHD-Me4), using electronic structure calculations and nonadiabatic molecular dynamics simulations. Reactants, first excited states ($S_1$), conical intersections (CIs), and products were optimized using XMS-CASPT2 approach, revealing structural and energetic trends in agreement with previous findings. To explore the excited-state dynamics, we employed surface hopping simulations at the SA-CASSCF level of theory. Notably, CHD-Me4 showed lower rate of carbon–carbon single bond cleavage due to steric hindrance from proximal substituents, resulting in reduced ring-opening efficiency. Additionally, CHD-Me2-2 and CHD-Me4 exhibited longer excited-state lifetimes, indicating the pronounced effects of substitution on nonadiabatic relaxation dynamics. Analysis of kinetic energy profiles of specific carbon atoms also revealed restrained atomic displacements, particularly in CHD-Me2-2 and CHD-Me4. These findings advance our understanding of how substituents modulate photochemical reactions in CHD derivatives, guiding new molecular design and future research.

# Chapter IV

## Effect of Polar and Non-Polar Media on Photoinduced Ring-Opening of Cyclohexadiene: A QM/MM-based Surface Hopping Approach

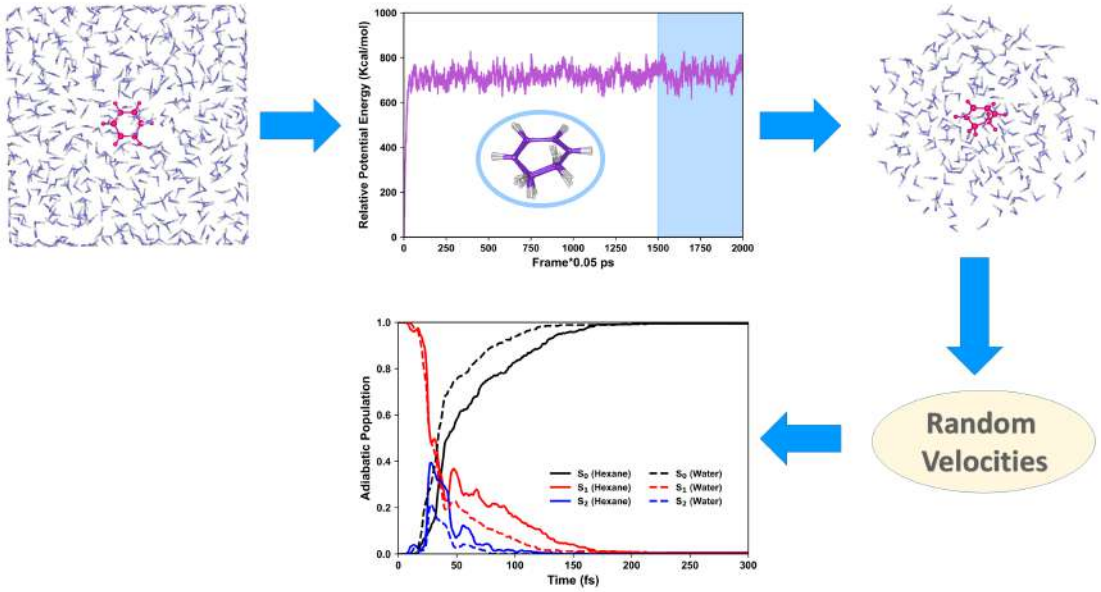


In this study, we investigate the influence of polar (water) and non-polar (n-hexane) solvents on the photochemical ring-opening dynamics of CHD to HT. The effect of solvent polarity on the excited state dynamics is explored using a combination of electronic structure theory, classical molecular dynamics, and QM/MM-based non-adiabatic surface hopping simulations. This exploration reveals that water can facilitate faster and more efficient ring-opening, with a higher quantum yield (61%) compared to n-hexane (53%), due to enhanced solute-solvent interactions and stabilization of excited states. The excited state decay process was also found to be faster in polar solvent environments. Further, solvation shell analysis confirms the dynamic role of water in influencing the reaction pathway. These findings underscore the critical role of solvent environments in modulating photochemical processes and offer insights applicable to molecular electronics, photopharmacology, and solar energy conversion.

# Chapter V

## Photochemistry and Functionality in a Fulgide Molecule with Hexatriene Core

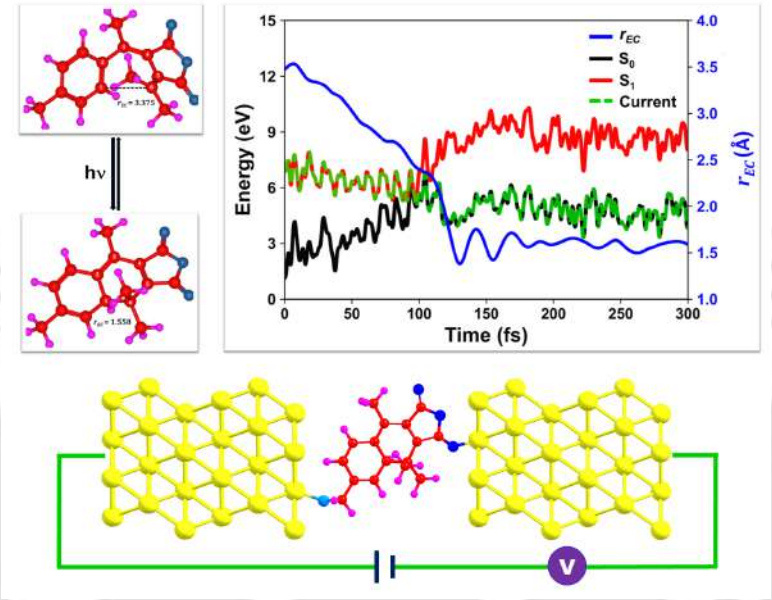


The photochemistry of fulgide molecules hinges on the mechanisms of ring-closure and ring-opening through conical intersections during excited state alterations between isomers. Employing electronic structure theory with density functional theory and wavefunction methods, as well as surface hopping simulations, we have analyzed the photochemical behavior of the experimentally synthesized fulgide molecule, specifically (E)-*p*-methylacetophenylisopropylidene-succinic anhydride. Our findings reveal a conical intersection between the first excited state ($S_1$) and the ground electronic state ($S_0$), located beyond the $S_1$ minimum towards ring closure, with a distinct sloped topography. This configuration suggests a reduced quantum yield for closed isomer formation, indicating a higher likelihood of open isomer(s) reformation. Surface hopping simulations validate this observation, showing an approximately $\sim$8% quantum yield for closed isomer formation. Additionally, our investigation into electron transport properties underscores the enhanced conductivity of the closed isomer, highlighting potential applications in molecular electronics. This study contributes to a deeper understanding of the intricate photochemical dynamics of fulgide molecules and their relevance in molecular electronics.

# Chapter VI

## Application and Comparison of Machine Learning Potentials in Studying Photochemistry of Cyclohexadiene

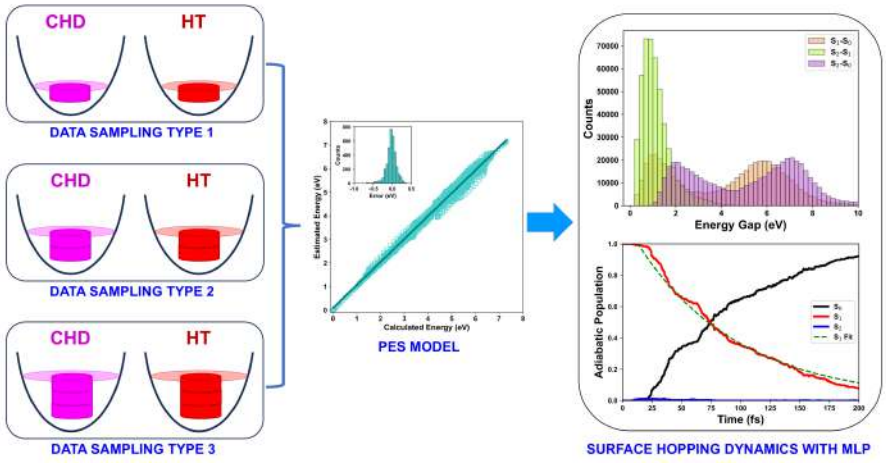


This chapter focuses on the CHD ring-opening reaction and explores the use of two different types of machine learning potential (MLP) models, SS-ANI and MS-ANI, for performing excited-state dynamics using surface hopping simulations. Sampling of the initial dataset for training and testing the PES models was done by performing LZBL-based surface hopping simulations, generating three different types of datasets. The reference method is based on the wavefunction-based multireference SA-3-CASSCF(6,4)/cc-pVDZ level of theory, which is a widely used approach for TSH simulations for CHD-related systems. Using all three datasets, training and testing were performed using both the energies and gradients calculated from the reference QM method for SS-ANI and MS-ANI models. Using the MLP models for electronic states, we conducted surface hopping simulations for CHD ring-opening systems and carried out a comparative analysis. Our results suggest that although the SS-ANI models accurately predict electronic state energies, they fail to predict energy gap values reliably. In contrast, MS-ANI models demonstrate improved accuracy in predicting energy gaps. Furthermore, a detailed analysis of our surface hopping simulation results indicates that while MS-ANI models can reasonably predict energetic parameters, sufficient data sampling from an accurately described PES region is essential for faithful excited-state dynamics.

# Chapter VII

## Summary and Conclusions

The final chapter summarizes key findings and contributions of the thesis and outlines future research directions to further explore and expand upon the present work. In the first working chapter, we explored the effect of symmetric methyl substitutions on the photochemical ring-opening reaction of the CHD molecule. Our investigations reveal that the position of substituents plays a crucial role in the excited-state behavior, influencing the ring-opening rate and excited-state decay times. In the second working chapter, we studied the ring-opening reaction of CHD in polar (water) and non-polar (n-hexane) media to understand how the surrounding environment affects the photochemistry of CHD molecule. We observed a significant impact of the solvent environment, with electronic states found to be stabilized in the polar medium, resulting in faster excited-state decay. The polar solvent notably influenced the overall photochemical process. In the third working chapter, we evaluated an experimentally synthesized fulgide molecule having a HT core to investigate its ring-closure dynamics. Our study further examined its potential as a molecular switch and found that the molecule can be a promising candidate for switch-on/off applications. The fourth working chapter focused on the application of machine learning potentials in surface hopping simulations of the CHD ring-opening reaction. We assessed the quality of the data and compared the performance of two machine learning models, SS-ANI and MS-ANI. We found that a sufficient amount of data obtained from sampling of proper potential energy surface region in combination with the MS-ANI model can be a good candidate for excited state dynamics simulations. Together, these results highlight how structural modifications, environmental effects, and modern computational techniques like machine learning collectively contribute to a deeper understanding and control of photochemical reaction dynamics.

# List of Publications

## Thesis Work

1. **B. Medhi**, U. Nath, and M. Sarma*, "Revisiting fulgide photochromism: Mechanistic decoding and electron transport from computational exploration", J. Chem. Phys. **160**, 154308 (2024).

2. **B. Medhi** and M. Sarma*, "Deciphering the Internal Conversion Processes Involved in the Photochemical Ring-Opening of 1,3-Cyclohexadiene by Symmetric $sp^2$-Carbon Substitutions", J. Phys. Chem. A **128**, 2025 (2024). **(This article has appeared as a Cover Feature of the Journal)**.

3. **B. Medhi**, M. Sarmah, M. Morang, and M. Sarma*, "Effect of Polar and Non-Polar Media on Photoinduced Ring-Opening of Cyclohexadiene: A QM/MM-based Surface Hopping Approach", **(Manuscript under Consideration)**.

4. **B. Medhi**, M. Morang, and M. Sarma*, "Evaluating SS-ANI and MS-ANI Machine Learning Potentials for Non-Adiabatic Photodynamics of Cyclohexadiene", **(Manuscript to be Submitted)**.

## Outside of Thesis Work

1. P. Kalita$^{+}$, **B. Medhi**$^{+}$, H. K. Singh, H. P. Bhattacharyya, N. Gupt, and M. Sarma*, "Perturbing $\pi$-clouds with Substituents to Study the Effects on Reaction Dynamics of gauche-1,3-Butadiene to Bicyclobutane Electrocyclization", ChemPhysChem **24**, e202200727 (2023). ($^{+}$Equal Contribution)

2. S. K. Bora, **B. Medhi**, M. Sarma, and A. K. Saikia*, "$BF_3{\cdot}OEt_2$-Mediated Cascade Synthesis of 4H-3,1-Benzoxazines from 2-Azidobenzaldehydes and Homoallylic Alcohols", J. Org. Chem. **90**, 6443 (2025).

# Conferences/Workshops Attended

1. **B. Medhi**, and M. Sarma*, “Exploring Fulgide Photochromism: Mechanistic Pathways and Electron Transport via Computational Approach", **CZS Summer School “Machine Learning for Chemistry”**, September 09 - 13, 2024, Karlsruhe Institute of Technology, Karlsruhe, Germany (Poster).

2. Workshop on **“Foundation of Python in Data Science”**, March 16 - 17, 2024, Organized by Students’ Academic Board, Indian Institute of Technology (IIT) Guwahati, Assam, India.

3. **B. Medhi**, and M. Sarma*, “Unraveling Fulgide Photochromism: A Computational Approach to Mechanistic Understanding”, **Spectroscopy and Dynamics of Molecules and Clusters**, February 22 - 25, 2024, Kaziranga, Assam, India (Poster).

4. **B. Medhi**, and M. Sarma*, “Decoding Fulgide Photochromism: Computational Perspectives on Mechanistic Understanding”, **Theoretical Chemistry Symposium**, December 07 - 10, 2023, Indian Institute of Technology (IIT) Madras, Tamil Nadu, India (Poster).

5. P. Kalita, **B. Medhi**, H. K. Singh, H. P. Bhattacharyya, N. Gupt, and M. Sarma*, “Probing the Effects of Electron Withdrawing and Donating Substituents in gauche-1,3-Butadiene to Bicyclobutane Electrocyclization”, **Recent Advances in Chemistry: Theoretical and Computational Aspects (RAC: TCA) 2022**, November 18 – 20, 2022, National Institute of Technology (NIT) Meghalaya, Shillong, India (Poster).

6. **Mumbai Workshop on Quantum Chemistry**, July 6-11, 2022, Indian Institute of Technology (IIT) Bombay, Maharashtra, India.

7. **B. Medhi**, and M. Sarma*, “Effects of Substitution on Reaction Dynamics at the Conical Intersections of Cyclohexadiene Molecule”, **North-East Research Conclave**, May 20-22, 2022, Indian Institute of Technology (IIT) Guwahati, Assam, India (Poster).

8. **B. Medhi**, and M. Sarma*, “Effects of Substitution on Reaction Dynamics at the Conical Intersections of Cyclohexadiene Molecule”, **International Conference on Theoretical Chemistry Symposium 2021 (Online)**. December 11 - 14, 2021, organized by IISER Kolkata, IACS Kolkata, Kalyani University and S.N. Bose National Centre for Basic Sciences Kolkata, India (Poster).

9. Five Days Online Workshop on **MD Simulation with GROMACS**, December 07-12, 2020.

# List of Abbreviations

| | |
|---|---|
| CHD | 1,3-Cyclohexadiene |
| HT | Hexatriene |
| QM | Quantum Mechanics |
| IC | Internal Conversion |
| ISC | Intersystem Crossing |
| UVB | Ultraviolet B |
| 7-DHC | 7-dehydrocholesterol |
| MD | Molecular Dynamics |
| DFT | Density Functional Theory |
| UV-Vis | Ultraviolet-Visible |
| CI | Conical Intersection |
| MECI | Minimum Energy Conical Intersection |
| QY | Quantum Yield |
| LUMO | Lowest Unoccupied Molecular Orbital |
| HOMO | Highest Occupied Molecular Orbital |
| TSH | Trajectory Surface Hopping |
| CFS | Configuration State Function |
| FCI | Full Configuration Interaction |
| CIS | Configuration Interaction Singles |
| CISD | Configuration Interaction Singles Doubles |
| B3LYP | Becke, 3-parameter, Lee–Yang–Parr functional |
| TD-DFT | Time-Dependent Density Functional Theory |
| FSSH | Fewest-Switches Surface Hopping |
| IRC | Intrinsic Reaction Coordinate |
| NTO | Natural Transition Orbital |

| | |
|---|---|
| VEE | Vertical Excitation Energy |
| NEGF | Nonequilibrium Green's Function |
| ZPE | Zero-Point Energy |
| SZP | Single-$\zeta$ Polarized |
| GGA | General Gradient Approximation |
| PBE | Perdew-Burke-Ernzerhof |
| MPSH | Molecular Projected Self-consistent Hamiltonian |
| ICT | Intramolecular Charge Transfer |
| IR | Infrared |
| ML | Machine Learning |
| TSC | Transition State Conrotatory |
| MECI | Minimum Energy Conical Intersection |
| TS | Transition State |
| PES | Potential Energy Surface |
| NN | Neural Network |
| NNPs | Neural Network Potentials |
| ANNs | Artificial Neural Networks |
| DNNs | Deep Neural Networks |
| ANI | Accurate NeurAl networK engINe for Molecular Energies |
| ReLU | Rectified Linear Unit |
| RBF | Radial Basis Function |
| SS-ANI | Single-state ANI |
| MS-ANI | Multi-state ANI |
| MLP | Machine Learning Potential |
| LZSH | Landau–Zener Surface Hopping |
| LZBL | Landau-Zener-Belyaev-Lebedev |
| MAE | Mean Absolute Error |
| RMSE | Root Mean Square Error |
| RMSD | Root Mean Square Deviation |

# List of Figures


1.1 Photochemical processes occurring within a molecular system. . . . . 29

1.2 Formation of previtamin $D_3$, tachysterol, lumisterol, and, vitamin $D_3$ from 7-DHC initiated by UVB irradiation. . . . . 30

1.3 The conventional photoinduced interconversion between CHD and HT. . . . . 31

1.4 The conrotatory and disrotatory ring closure pathway for bicyclobutane formation. 32

1.5 A schematic representation of potential energy surfaces (black: $S_0$, blue: $S_1$) of a molecule in gas (dotted line) and solvent (solid line) phase. The solute and solvent molecules are denoted as larger and smaller-sized ellipses, respectively, and dipoles are shown using crossed arrows. . . . . 33

1.6 Photochemical reactions involved in (a) fulgide, (b) azobenzenes, and (c) diarylethene molecular system. . . . . 35

2.1 MD simulations workflow. . . . . 44

2.2 A schematic neural network framework. . . . . 48

3.1 (a) Provitamin $D_3$, (b) an unsymmetrical dithienylethene, (c) a symmetrical diarylethene, and (d) a fulgide molecule. . . . . 50

3.2 Schematic representation of CHD to cZc-HT photochromism along with the carbon atom numbering used throughout the work. . . . . 51

3.3 Systems under investigation: 1,3-cyclohexadiene (CHD), 2,3-dimethylcyclohexadiene (CHD-Me2-1), 1,4-dimethylcyclohexadiene (CHD-Me2-2), and 1,2,3,4-tetramethylcyclohexadiene (CHD-Me4). . . . . 52

3.4 Active molecular orbitals of CHD (left) and HT (right) taken within the active space of SA-3-CASSCF(6,6)/6-31G(d) calculations. . . . . 54

3.5 Optimized equilibrium geometries, (a) $S_0$-CHD, (b) $S_2/S_1$-CHD, (c) $S_1/S_0$-CHD, (d) $S_0$-HT, (e) $S_0$-CHD-Me2-1, (f) $S_2/S_1$-CHD-Me2-1, (g) $S_1/S_0$-CHD-Me2-1, (h) $S_0$-HT-Me2-1, (i) $S_0$-CHD-Me2-2, (j) $S_2/S_1$-CHDMe2-2, (k) $S_1/S_0$-CHD-Me2-2, (l) $S_0$-HT-Me2-2, (m) $S_0$-CHD-Me4, (n) $S_2/S_1$-CHD-Me4, (o) $S_1/S_0$-CHD-Me4, and (p) $S_0$-HT-Me4 at SA-3-XMS-CASPT2(6,6)/6-31G(d) level of theory. Distances are in Å. . . . . 56

3.6 CASSCF(6,6)/6-31G(d) optimized $S_0$ first-order saddle points involved in (a) CHD, (b) CHD-Me2-1, (c) CHD-Me2-2, and (d) CHD-Me4 photochemical ring-opening reactions. Distances are in Å. . . . . 58

3.7 Geodesic interpolation calculated from reactant to (a) $S_2/S_1$ MECI at the SA-3-XMS-CASPT2(6,6)/6-31G(d), (b) $S_1/S_0$ MECI at the SA-3-XMS-CASPT2(6,6)/6-31G(d), (c) $S_2/S_1$ MECI at the SA-3-CASSCF(6,4)/6-31G(d), and (d) $S_1/S_0$ MECI at the SA-3-CASSCF(6,4)/6-31G(d) level of theory. . . . . 61

3.8 $C_1$-$C_6$ bond length variations for all the trajectories of (a) CHD, (b) CHD-Me2-1, (c) CHD-Me2-2, and (d) CHD-Me4 along with the hopping types (★:$S_1 \leftrightarrow S_2$, ★:$S_0 \leftrightarrow S_1$) at corresponding time and bond length; $C_1$-$C_6$ bond length distributions throughout the dynamics for (e) CHD, (f) CHD-Me2-1, (g) CHD-Me2-2, and (h) CHD-Me4. . . . . 62

3.9 Dihedral angle variation for CHD: (a) $\angle C_3C_4C_5C_6$, (b) $\angle C_2C_3C_4C_5$, and (c) $\angle C_1C_2C_3C_4$; CHD-Me2-1: (d) $\angle C_3C_4C_5C_6$, (e) $\angle C_2C_3C_4C_5$, and (f) $\angle C_1C_2C_3C_4$; CHD-Me2-2: (g) $\angle C_3C_4C_5C_6$, (h) $\angle C_2C_3C_4C_5$, and (i) $\angle C_1C_2C_3C_4$; and CHD-Me4: (j) $\angle C_3C_4C_5C_6$, (k) $\angle C_2C_3C_4C_5$, and (l) $\angle C_1C_2C_3C_4$ along with the hopping types (★:$S_1 \leftrightarrow S_2$, ★:$S_0 \leftrightarrow S_1$) at corresponding time and angle. . . . . 63

3.10 Ensemble-averaged adiabatic population of the system (a) CHD, (b) CHD-Me2-1, (c) CHD-Me2-2, and (d) CHD-Me4, along with fitted curve for $S_1$ population decay. . . . . 64

3.11 Ensemble-averaged adiabatic potential energy evolution of (a) CHD, (b) CHD-Me2-1, (c) CHD-Me2-2, and (d) CHD-Me4 systems. . . . . 66

3.12 $S_1/S_0$ $CI^n$ topography calculated at the SA-3-CASSCF(6,4)/6-31G(d) level of theory for (a) CHD, (b) CHD-Me2-1, (c) CHD-Me2-2, and (d) CHD-Me4 systems. . . . . 67

3.13 Ensemble-averaged kinetic energy variations for $C_1$ and $C_6$ atoms of (a) CHD, (b) CHD-Me2-1, (c) CHD-Me2-2, and (d) CHD-Me4 systmes. . . . . 68

4.1 Cropping of cubic box to spherical shape for water solvated system around CHD (magenta). For n-hexane medium, the figure is shown in the **Figure B.2** of the Appendix B. . . . . 74

4.2 Relative potential energy of the thermalized trajectory of (a) n-hexane and (b) water-solvated medium along with the shaded region for collection of random PDB geometries are shown. . . . . 75

4.3 Ensemble averaged adiabatic population of electronic states during the surface hopping simulations. . . . . 77

4.4 In the n-hexane-solvated medium: (a) time evolution of the $C_1$–$C_6$ bond length, (b) hopping distribution over time of simulation, and (c) hopping distribution over $C_1$–$C_6$ bond length. In the water-solvated medium: (d) time evolution of the $C_1$–$C_6$ bond length, (e) hopping distribution time of simulation, and (f) hopping distribution over $C_1$–$C_6$ bond length. The blue colored dotted line represents the ensemble averaged $C_1$–$C_6$ bond length. . . . . 78

4.5 Ensemble averaged electronic state energy behavior in (a) n-hexane and (b) water-solvated medium. Energies are relative to the ensemble averaged value at time, t = 0 fs. . . . . 79

4.6 Radial pair distribution function, g(r), curve for (a) n-hexane, and (b) water-solvated medium; and the first solvation sphere (FSS) in (c) n-hexane, and (d) water medium. The green colored dotted lines represent the intermolecular hydrogen bonding in the FSS of water. . . . . 81

4.7 RMSD curves of CHD and first solvation sphere (FSS) for ring opening and ring-closed typical trajectories for (a) n-hexane and (b) water-solvated media. (c) Ring-opening (upper row: n-hexane, lower row: water) and (d) ring-closed (upper row: n-hexane, lower row: water) typical trajectory snapshots at 0 fs, 50 fs, 100 fs, and 300 fs. The green colored dotted lines represent the intermolecular hydrogen bonding in the FSS of water. . . . . 82

5.1 Photochromism of (E)-*p*-methylacetophenylisopropylidenesuccinic anhydride (1E) studied in this work. . . . . 86

5.2 Active molecular orbitals of 1E molecule taken within the active space of SA-2-CASSCF(8,7)/cc-pVDZ calculations along with the electron occupation number. . . . . 87
5.3 (a) Bond length and dihedral angle notation used throughout the work, (b) optimized 1E-$S_0$ at the $\omega$B97xD, (c) optimized 1C-$S_0$ at the $\omega$B97xD, (d) superimposed structures of DFT optimized (Green) and crystal structure (Blue) (e) optimized $S_1$-min at the SA-2-CASSCF(8,7), (f) optimized $S_1/S_0$ MECI at SA-2-CASSCF(8,7), (g) optimized TSC at the CASSCF(8,7) along with the IRC pathway. Calculations are performed with the cc-pVDZ basis set. . . . . 91
5.4 (a) NTOs calculated at the SA-2- CASSCF(8,7)/cc-pVDZ level of theory and (b) fragmentation representation of our considered molecular system for charge transfer analysis. . . . . 93
5.5 (a) $S_1/S_0$ MECI topography calculated at the SA-2-CASSCF(8,7)/cc-pVDZ level of theory and (b) energy profile diagram calculated at the SA-2-XMS-CAS(8,7)PT2/cc-pVDZ level of theory. . . . . 95
5.6 Geodesic interpolation calculated between (a) 1E-$S_0$ and $S_1/S_0$ MECI [at SA-2-CASSCF(4,3), SA-2-CASSCF(8,7), and XMS-CAS(8,7)PT2 approach] and (b) 1E-$S_0$ and 1C-$S_0$ [at SA-2-CASSCF(4,3) and SA-2-CASSCF(8,7) approach]. Calculations are performed using the cc-pVDZ basis set. . . . . 96
5.7 (a) Time evolution of $r_{EC}$ bond length of all trajectories (★:$S_1 \rightarrow S_0$,★:$S_0 \rightarrow S_1$, Golden line represents the average $r_{EC}$ value) and (b) $r_{EC}$ bond length distribution during the dynamics. . . . . 97
5.8 One trajectory showing the formation of 1C with (a) potential energy and $r_{EC}$ bond length evolution and (b) initial (0 fs), hopping (97.2 fs), and last (300 fs) snapshots of the molecule. . . . . 98
5.9 One trajectory showing the formation of 1Z with (a) potential energy and $\beta$ dihedral angle evolution and (b) initial (0 fs), hopping (148.8 fs), and last (300 fs) snapshots of the molecule. . . . . 99
5.10 Ensemble-averaged, (a) potential energy evolution (upward triangle: maximum value, downward triangle: minimum value) and (b) adiabatic population during the dynamics. . . . . 100

5.11 Schematic representation of the molecular device, where the 1C-isomer of the fulgide derivative is sandwich between Au (111) electrode. Yellow, blue, red, pink, and light blue balls denote gold, oxygen, carbon, hydrogen, and sulfur, atoms respectively. . . . . 100
5.12 (a) The I–V characteristic of the molecular switch with two isomers (1E and 1C) along with the current on-off ratio. (b) Zero bias transmission spectra T(E) plot of 1E and 1C isomers. . . . . 101

6.1 (a) Photochemical conversion of CHD to HT with the atom numbering used throughout the work, (b) active molecular orbitals used for the CASSCF approach along with the occupation number. . . . . 107
6.2 Testing results of SS-ANI MLP models using TYPE-1 dataset for the state (a) $S_0$, (b) $S_1$, and (c) $S_2$; using TYPE-2 dataset for the state (d) $S_0$, (e) $S_1$, and (f) $S_2$; using TYPE-3 dataset for the state (g) $S_0$, (h) $S_1$, and (i) $S_2$. . . . . 108
6.3 Testing results of MS-ANI MLP models using TYPE-1 dataset for the state (a) $S_0$, (b) $S_1$, and (c) $S_2$; using TYPE-2 dataset for the state (d) $S_0$, (e) $S_1$, and (f) $S_2$; using TYPE-3 dataset for the state (g) $S_0$, (h) $S_1$, and (i) $S_2$. . . . . 110
6.4 Root Mean Square Error (RMSE) related to energy predictions of the models (a) SS-ANI and (b) MS-ANI. . . . . 111
6.5 The energy gap predictions between $S_1$ and $S_2$, by the SS-ANI (a) TYPE-1, (b) TYPE-2, and (c) TYPE-3 models; and by the MS-ANI (d) TYPE-1, (e) TYPE-2, and (f) TYPE-3 models. . . . . 112
6.6 The energy gap predictions between $S_1$ and $S_0$, by the SS-ANI (a) TYPE-1, (b) TYPE-2, and (c) TYPE-3 models; and by the MS-ANI (d) TYPE-1, (e) TYPE-2, and (f) TYPE-3 models. . . . . 112
6.7 The energy gap predictions between $S_2$ and $S_0$, by the SS-ANI (a) TYPE-1, (b) TYPE-2, and (c) TYPE-3 models; and by the MS-ANI (d) TYPE-1, (e) TYPE-2, and (f) TYPE-3 models. . . . . 113
6.8 Optimized (a) $S_0$-CHD at B3LYP/cc-pVDZ, (b) CI-$S_1$/$S_2$ at SA-3-CASSCF(6,4)/cc-pVDZ, (c) CI-$S_0$/$S_1$ at SA-3-CASSCF(6,4)/cc-pVDZ, and (d) $S_0$-HT at B3LYP/cc-pVDZ level of theory, along with the $C_1$-$C_6$ bond length (Å) parameter. . . . . 114

6.9 Geodesic interpoaltion pathways, calculated from $S_0$-CHD to CI-$S_1/S_2$ by SS-ANI (a) TYPE-1, (b) TYPE-2, and (c) TYPE-3 model; from $S_0$-CHD to CI-$S_1/S_0$ by SS-ANI (d) TYPE-1, (e) TYPE-2, and (f) TYPE-3 model; from $S_0$-CHD to CI-$S_1/S_2$ by MS-ANI (g) TYPE-1, (h) TYPE-2, and (i) TYPE-3 model; and from $S_0$-CHD to CI-$S_1/S_0$ by MS-ANI (j) TYPE-1, (k) TYPE-2, and (l) TYPE-3 model (—○— QM, —⋆— MLP). . . . . 115

6.10 $C_1$-$C_6$ bond length evolutions along with hopping types (★:$S_1 \leftrightarrow S_2$, ★:$S_0 \leftrightarrow S_1$, ★:$S_0 \leftrightarrow S_2$) during surface hopping simulations performed using, SS-ANI (a) TYPE-1, (b) TYPE-2, and (c) TYPE-3 PES models; MS-ANI (d) TYPE-1, (e) TYPE-2, and (f) TYPE-3 PES models. The golden solid line represents the ensemble-averaged $C_1$-$C_6$ bond length. . . . . 116

6.11 Ensemble-averaged electronic state energy evolutions during surface hopping simulations performed using SS-ANI (a) TYPE-1, (b) TYPE-2, and (c) TYPE-3 PES models; MS-ANI (d) TYPE-1, (e) TYPE-2, and (f) TYPE-3 PES models. 117

6.12 Ensemble-averaged adiabatic population evolutions during surface hopping simulations performed using, SS-ANI (a) TYPE-1, (b) TYPE-2, and (c) TYPE-3 PES models; MS-ANI (d) TYPE-1, (e) TYPE-2, and (f) TYPE-3 PES models. . 118

A.1 Active molecular orbitals of (a) CHD-Me2-1, (b) CHD-Me2-2, and (c) CHD-Me4 obtained within the active space of SA-3-CASSCF(6,6) calculations. . . . 123

A.2 Active orbitals of the CHD molecule used in molecular dynamics simulations at the SA-3-CASSCF(6,4)/6-31G(d) level of theory. . . . . 124

A.3 Active orbitals of the CHD molecule used in molecular dynamics simulations at the SA-3-CASSCF(6,4)/6-31G(d) level of theory. . . . . 124

A.4 CASSCF(6,6)/6-31G(d) calculated intrinsic reaction coordinate (IRC) pathways for (a) CHD, (b) CHD-Me2-1, (c) CHD-Me2-2, and (d) CHD-Me4. Energies are relative to the corresponding CHD derivatives. . . . . 126

A.5 SA-3-XMS-CASPT2 level generated energy profile diagram of (a) CHD, (b) CHD-Me2-1, (c) CHD-Me2-2, and (d) CHD-Me4. Energies are relative to the corresponding CHD derivatives. . . . . 127

A.6 The root-mean-square deviation (RMSD) plots for (a) CHD, (b) CHD-Me2-1, (c) CHD-Me2-2, and (d) CHD-Me4. . . . . 128

A.7 Bond dissociation in CHD molecule. . . . . 129

A.8 Energy gap distributions throughout the dynamics for (a) CHD, (b) CHD-Me2-1, (c) CHD-Me2-2, and (d) CHD-Me4. . . . . 130
A.9 SA-3-XMS-CASPT2 level generated energy profile diagram of (a) CHD, (b) CHD-Me2-1, (c) CHD-Me2-2, and (d) CHD-Me4. Energies are relative to the corresponding CHD derivatives. . . . . 131
A.10 SA-3-XMS-CASPT2 level generated energy profile diagram of (a) CHD, (b) CHD-Me2-1, (c) CHD-Me2-2, and (d) CHD-Me4. Energies are relative to the corresponding CHD derivatives. . . . . 132
B.1 Molecular orbitals considered within the active space of (a) six electrons in four orbitals, (6,4), (b) six electrons in six orbitals, (6,6). . . . . 133
B.2 Cropping the cubic box to a spherical shape for n-hexane-solvated system. . . . 133
B.3 RMSD plots for the collected CHD geometries of p1, p2, ..., p10 PDB frames in both (n-hexane and water) medium. The first geometry corresponds to the optimized CHD geometry. . . . . 134
B.4 Ensemble averaged (a) $C_1$-$C_6$ bond length and (b) bond alteration coordinate (BAC) evolution during the surface hopping simulations. . . . . 134
B.5 (a) Optimized CHD at B3LYP/cc-pVTZ, (b) optimized conrotatory transition state geometry at CASSCF(6,4)/cc-pVDZ, (c) intrinsic reaction coordinate (IRC) pathway at CASSCF(6,4)/cc-pVDZ, and (d) optimized HT geometry at B3LYP/cc-pVTZ level of theory. . . . . 135
B.6 (a) RMSD distribution, (b) $C_1$-$C_6$ bond length, (c) dihedral angle evolution, (d) electronic state energies, and (e) population evolution during surface hopping simulations of 30 trajectories for the initial geometry ‘p1’ in n-hexane medium. 136
B.7 (a) RMSD distribution, (b) $C_1$-$C_6$ bond length, (c) dihedral angle evolution, (d) electronic state energies, and (e) population evolution during surface hopping simulations of 30 trajectories for the initial geometry ‘p1’ in water medium. . . 137
C.1 NTOs calculated at B3LYP/cc-pVDZ level of theory. . . . . 140
C.2 Root-mean-square deviation (RMSD) plots during the surface hopping simulations. . . . . 141
C.3 Time evolution of dihedral angles, (a) $\angle C_1C_2C_3C_4$, (b) $\angle C_2C_3C_4C_5$, and (c) $\angle C_3C_4C_5C_6$ during surface hopping simulations of all trajectories. . . . . 141

C.4 Time evolution of (a) $\angle C_2C_3C_4C_5$ dihedral angle in the trajectory resulting in 1C, and (b) $C_1 - C_6$ bond length in the trajectory resulting in 1Z, during surface hopping simulations. . . . . 142
C.5 At zero bias, molecular projected self-consistent Hamiltonian (MPSH) orbitals of Fulgide molecule [1C (a) and 1E (b) isomer] and electrode interactions along with the HOMO-LUMO of the isolated molecules. . . . . 142

# List of Tables


3.1 Bond length parameters of the optimized geometries. Reactants, $S_1$-min, MECI, and Products are optimized at the SA-3-XMS-CASPT2(6,6)/6-31G(d) level of theory, while the TSC are optimized with the CASSCF(6,6)/6-31G(d) level of theory. Distances are in Å. . . . . 57

3.2 Dihedral angle parameters of optimized $S_0$ geometries at the SA-3-XMS-CASPT2(6,6)/6-31G(d) level of theory. . . . . 58

3.3 SA-3-XMS-CASPT2(6,6)/6-31G(d) calculated energies (in eV) of the lowest three singlet states. For TSC, corrected energies were used with the SA-3-XMS-CASPT2(6,6)/6-31G(d) approach. Energies are relative to the corresponding CHD derivatives. . . . . 59

3.4 Analysis of time to reach bond dissociation limit. . . . . 65

4.1 Excitation energies (in eV) calculated for the collected CHD geometries at the SA-3-CASSCF(6,4)/cc-pVDZ level of theory. Values in parentheses correspond to those calculated at the SA-3-XMS-CAS(6,6)PT2/cc-pVDZ level of theory. . . . . 76

5.1 Dihedral angle parameters of optimized geometries. . . . . 92

5.2 Vertical excitation energy (VEE) to the $S_1$ state of 1E with oscillator strength. . 92

5.3 Wavefunction analysis and Mulliken charge investigation during the excitation to $S_1$ at the SA-2-XMS-CAS(8,7)PT2/cc-pVDZ level of theory. u and d represent up spin and down spin, respectively. . . . . 94

6.1 Number of epochs and the time taken for training the models. . . . . 111

6.2 Time measurements for different types of MLP models. . . . . 119

A.1 Statistical comparison of three sets of trajectories (100, 150, 200 Traj). . . . . 125

A.2 Topographical parameters for $S_1/S_0$ conical intersection at SA-3-CASSCF(6,4)/6-31G(d) level of theory. . . . . 126
C.1 Topographical parameters for $S_1/S_0$ conical intersection calculated at the SA-2 CASSCF(8,7)/6-31G(d) level of theory. . . . . 139
C.2 Single point corrected molecular energies at the SA-2-XMS-CAS(8,7)PT2/cc-pVDZ level of theory. . . . . 140

# Chapter 1

# Introduction

## 1.1 A Brief Historical Overview of Photochemistry

Ancient civilizations realized the importance of light in the perpetuation and subsistence of life and utilized it in traditional medicine, even without knowing the scientific foundation of light. Systematic scientific investigation started in the late 19th and early 20th centuries, revealing that exposure to light could induce specific chemical reactions.[1] In the 1930s and 1940s, researchers revealed that exposure to light could induce specific chemical reactions in the gas-phase, confirming the existence of excited states like the triplet state, which played a crucial role in photosensitized reactions.[2–5] The innovation of spectroscopic techniques during this period allowed scientists to explore the intriguing mechanism related to how molecules absorb light and reach excited states. In the 1950s, advances like laser flash photolysis and emission spectroscopy made it possible to observe short-lived intermediates in real time, further clarifying reaction pathways.[6–8] The 1960s brought about the integration of quantum mechanics and potential energy surface (PES) concepts, shifting focus to detailed mechanistic models of reactions. The establishment of photophysical rules, such as the Woodward-Hoffmann rules, facilitated the prediction and explanation of photochemical reactions based on molecular orbital configurations.[9–14] Subsequently, the field expanded into multidisciplinary realms, examining how external factors like solvents, interfaces, and electromagnetic fields influence reactions, leading to studies on multiphoton effects and reaction control.[15–19] By the late 20th century, photochemistry matured into a sophisticated science that connects organic, inorganic, biological, and material chemistry, addressing global issues such as energy conversion and environmental protection.[16,20–23] Today, the field continues to evolve through technological innovation

and interdisciplinary research, maintaining its origins in curiosity, experimentation, and discovery.[24–28]

## 1.2 Understanding the Basics of Photochemistry

The detailed picture of a molecular system, starting from photon absorption leading to its transformation from the ground to the excited electronic state and continuing until it relaxes back to the ground state or forms a stable byproduct in the ground state, essentially signifies the realm of photochemistry. A photochemical reaction is a chemical reaction that is initiated when a molecule absorbs light, typically in the visible or ultraviolet range. For such a reaction to occur, the molecule must have an absorption band that matches the wavelength of the incoming light. This absorption provides the energy needed to drive the reaction.

When a molecule absorbs a photon of light, several dynamic processes can unfold, determining whether the energy leads to chemical transformation, emission, or non-radiative relaxation. To understand these processes, it is crucial to recognize the central role of the molecule's PESs, which map the energy variations as a function of nuclear configurations for each electronic state. After the absorption of a photon, the molecule gets excited and jumps from its stable ground state to an excited state. This excited state, to which the molecule is transformed, is called a "bright state". After this jump, the atoms in the molecule suddenly feel an unstable force of the respective potential energy landscape, which is different from the one where the molecule was before. As a result, to minimize this force, the atoms start to move, leading to stretching, bending, or even twisting bonds. Because of this, the molecule can acquire a different geometry in that excited state. After the excitation, the molecule can follow various possible pathways. It might stay in the initially excited state for a while, and then it can return to the ground electronic state by emitting radiation. If the spin of the electrons does not change, i.e., the multiplicity remains the same during the process; this is called fluorescence. If the molecule enters a triplet state and emits light to come to the ground state, it is called phosphorescence, a slower process. However, a molecule can relax to a low-lying electronic state with the same multiplicity without giving off light through internal conversion (IC). This usually occurs when the energy of two electronic states comes closer to each other, along with that, the process happens very fast. Sometimes, the molecule may reach a triplet state, where the electrons have a different spin, through intersystem crossing (ISC). This usually happens in molecules with heavy atoms

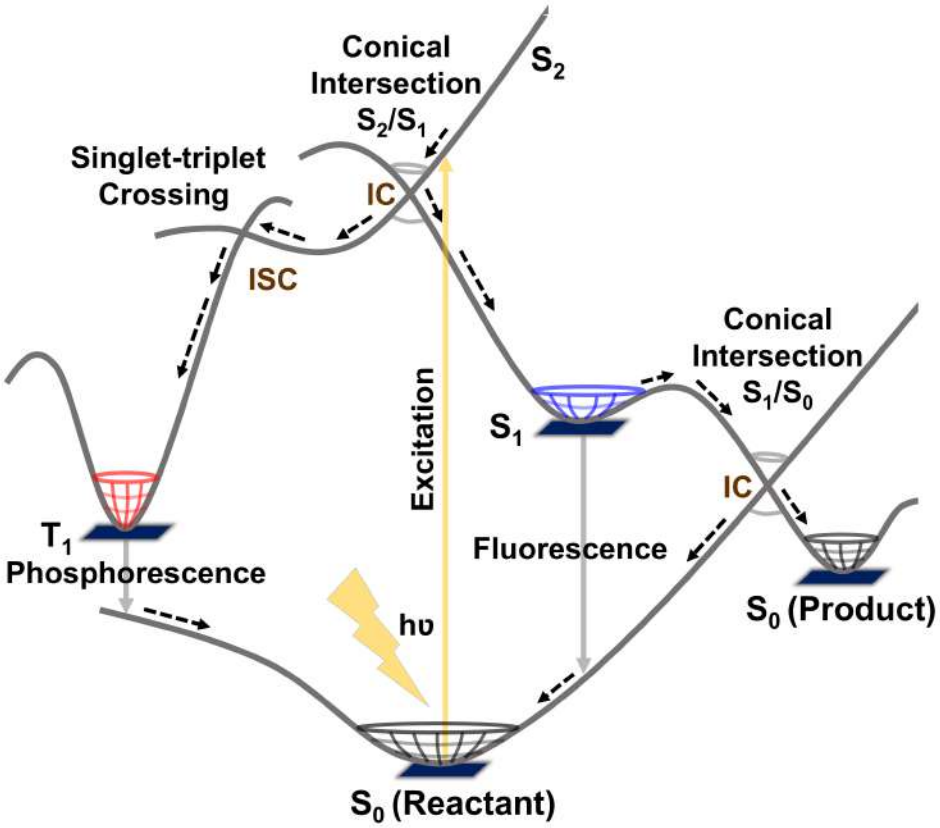


**Figure 1.1.** Photochemical processes occurring within a molecular system.

or special arrangements leading to slower processes like phosphorescence or further reactions. In some cases, the molecule may have enough energy to undergo bond breaking or formation, resulting in a photochemical reaction. These types of key processes are crucial for processes like vision[29,30] and photosynthesis.[31] After all this key photochemical processes, the molecule returns to the relaxed state and ready to absorb another photon or take part in more reactions. A pictorial representation of various processes that can occur within a molecule is presented in **Figure 1.1**. Therefore, understanding these processes is crucial for controlling photochemical reactions, designing light-sensitive materials, or developing new phototherapeutic agents. The entire cascade is governed by the intricate landscape of the PESs, the accessibility of crossing points like conical intersections, and the specific electronic and nuclear properties of the molecule involved.[32] The influence of a conical intersection on a general molecular system was first highlighted through the investigation of an unusual feature, referred to as the "mystery band", in the photoelectron spectrum of butatriene.[33]

## 1.3 Photochemistry of Cyclohexadiene to Hexatriene Conversion

Among various photochemical reactions, one of the most important and widely studied photoinduced transformations is the conversion of 1,3-cyclohexadiene (CHD) to hexatriene (HT) moiety. As shown in **Figure 1.2**, this reaction plays a key role in the cutaneous synthesis of vitamin $D_3$. Vitamin $D_3$ forms in the skin when it is exposed to UVB light, which has wavelengths between 280 and 315 nm.[31] When UVB radiation strikes the skin, it initiates a photochemical isomerization of 7-dehydrocholesterol (7-DHC), a compound naturally present in the skin, converting it to previtamin $D_3$. This is followed by a slower, thermally driven isomerization process over several hours, resulting in the formation of vitamin $D_3$.[31,34,35]

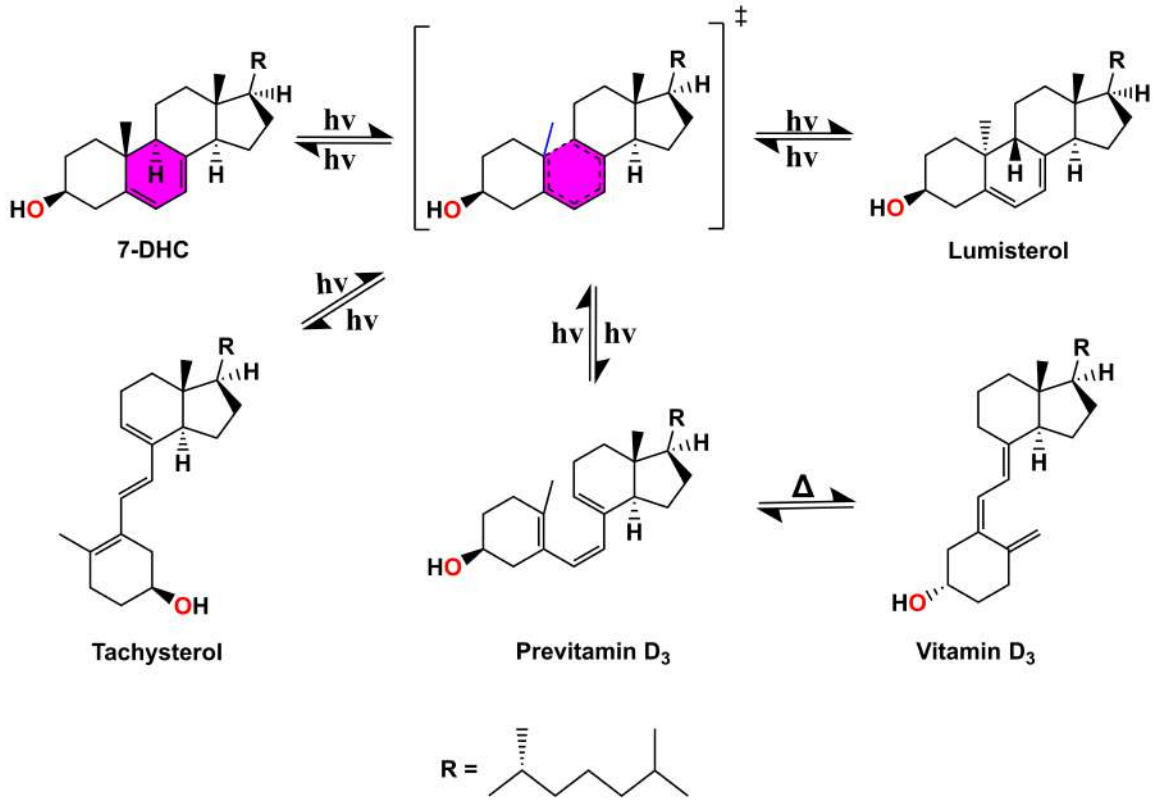


**Figure 1.2.** Formation of previtamin $D_3$, tachysterol, lumisterol, and vitamin $D_3$ from 7-DHC is initiated by UVB irradiation.

The popular photochemical ring-opening dynamics of CHD to HT photochemical conversion are schematically represented in **Figure 1.3**. Mainly, two low-lying excited electronic states are crucial for governing the photochemical ring-opening in the CHD molecular system. Under $C_2$ point group, these electronic states are $1^1B$ and $2^1A$. The CHD molecule gets excited to the lowest-lying bright excited state, $1^1B$, in the Franck–Condon region upon absorption of

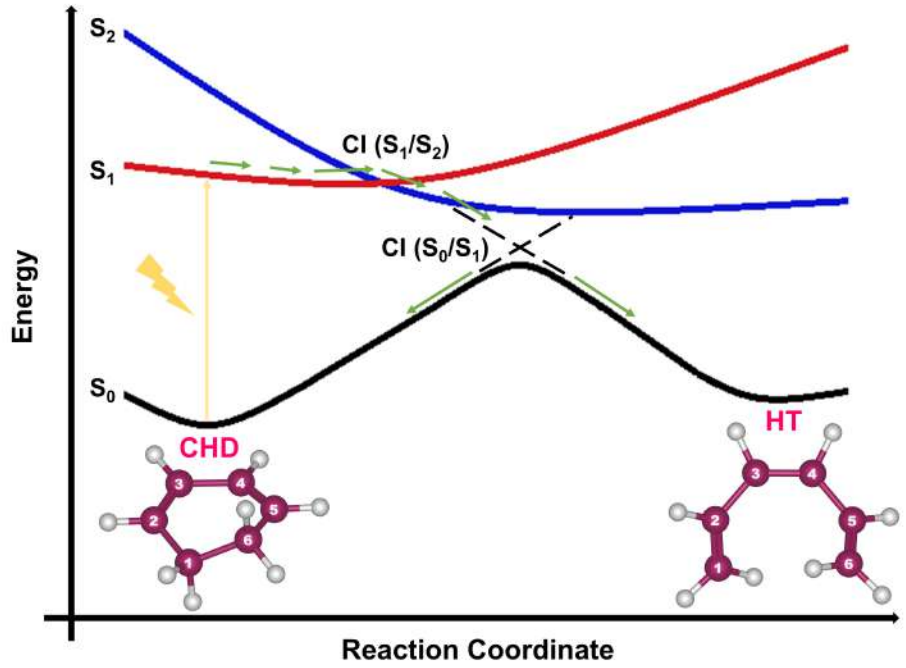


**Figure 1.3.** The conventional photoinduced interconversion between CHD and HT.

light at a suitable wavelength. Subsequently, the wave packet travels toward the ring-opening pathway and reaches the $S_1/S_2$ conical intersection, which arises between the first and second excited states. Finally, the wave packet proceeds to meet the second conical intersection, $S_0/S_1$, and in due course various ring-opened structures of HT are formed or the closed ring CHD system, which may result from the revert back of the wave packet towards the reactant side.[36–41]

Photochemical ring-opening of CHD is one of the most fundamental non-adiabatic reactive processes, which has served as a prototype for understanding photoinduced reactions in relatively larger systems, including biologically relevant molecules. The insight into the reaction mechanism is illustrated experimentally using multielectron dissociative ionization and time-resolved photoelectron spectroscopy, revealing details about excited-state lifetimes, conical intersection regions, and product yields.[42–48] Many theoretical efforts support these experimental results by exploring the PESs involved in the photochemical reaction.[37,38,44,49–54] Earlier, the theoretical calculations mainly focused on identifying critical points on these surfaces, such as conical intersections, which govern nonradiative deactivation pathways. More recent advanced simulations, including quantum dynamical[55–57] and mixed quantum-classical trajectory[39,58–63] methods, have provided detailed atomistic pictures of the reaction pathways, highlighting the importance of nuclear wavepacket motion and PES topology. However, despite these advances,

recent developments in ultrafast X-ray sources and electron diffraction techniques have enabled real-time visualization of the subpicosecond dynamics of CHD photodissociation.[64–66] Such direct imaging complements prior spectroscopic studies, offering unprecedented insights into the ultrafast structural changes and the influence of PES on the reaction outcome.

## 1.4 Substituents' Impact on Photochemistry

The excited state dynamics of a molecular system can be greatly affected by substitutions.[67–76] These substitution effects can be divided mainly into electronic and inertial, as reported by Schuurman and Stolow.[77] The changes in the UV absorption spectra, the alteration in the topography of the PESs around the conical intersection leading to the changes in the position of crossing points, etc., can be considered as key electronic effects. In contrast, the inertial effects include the changes in the mass distribution in the molecule, which influence the motion of nuclear wavepackets on the PES by altering the vibrational modes and ultimately affecting the reaction mechanism. For example, the addition of methyl groups in unsaturated hydrocarbons like allenes[69] and cyclopentadienes[68] has been shown to affect specific nuclear motions and, as a result, alter the excited-state relaxation pathways.[78] Recently, we investigated how -$CH_3$ and -F substituents influence the photochemical conversion of gauche-1,3-butadiene to bicyclobutane.[79] Minimum energy conical intersections were optimized using

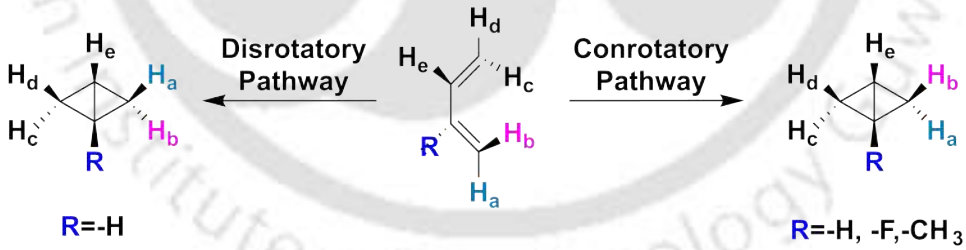


**Figure 1.4.** The conrotatory and disrotatory ring closure pathway for bicyclobutane formation.

CASSCF,[80,81] while ground-state pathways were explored using density functional theory with B3LYP-D3[82,83] functional. The results from XMS-CASPT2[84] energy corrections, topography analysis, and nonadiabatic dynamics indicate that -$CH_3$-substituted derivatives exhibit faster ground-state thermal conversion to the product, with a lower activation energy barrier than their F-substituted derivatives. Additionally, our study shows that the gauche-1,3-butadiene to bicyclobutane transformation occurs via both conrotatory and disrotatory pathways in the unsubstituted case, while substitution with either -F or -$CH_3$ restricts the reaction to proceed exclusively

through the conrotatory pathway (**Figure 1.4**).[79]

## 1.5 Solvation Effects on Photochemistry

The outcome of a photochemical process is greatly affected by a solvent,[85,86] as it can influence the reaction pathways and electronic states of a molecule.[87] A schematic diagram showing the effects of solvation on the PESs involved in the photochemical processes of a molecular system is shown in **Figure 1.5**. Upon absorption of a photon, a molecular system undergoes transitions to an excited electronic state; following this, its relaxation or transformation to another electronic state is strongly reliant on the surrounding solvent environment.[85,86] From viscosity,

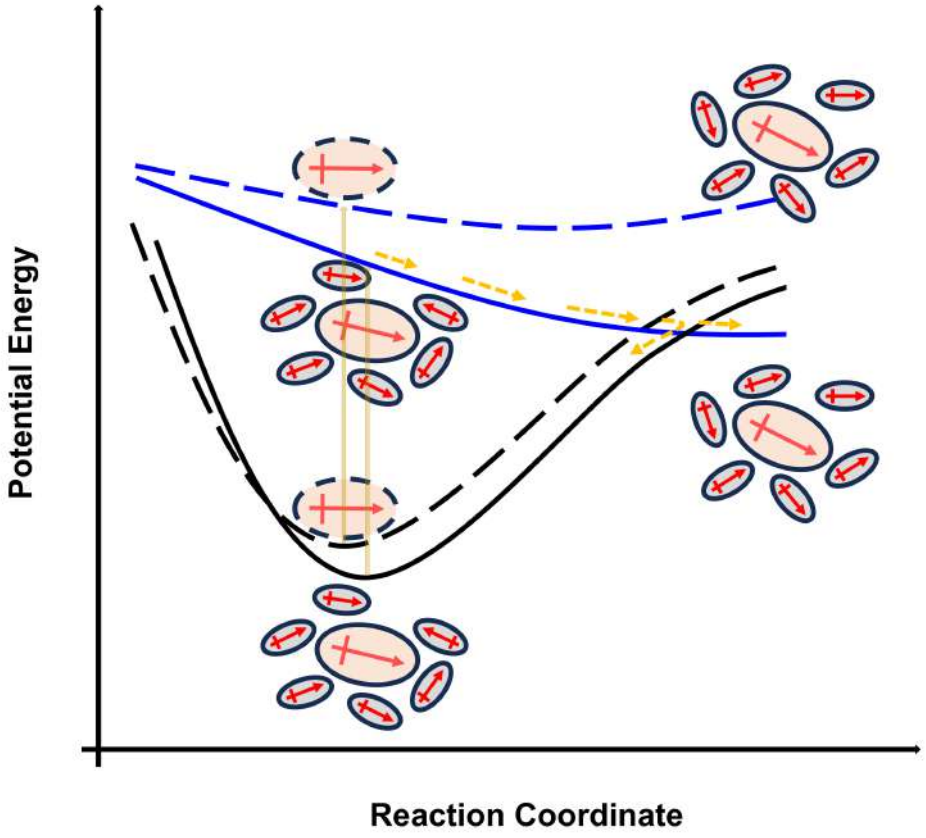


**Figure 1.5.** A schematic representation of potential energy surfaces (black: $S_0$, blue: $S_1$) of a molecule in gas (dotted line) and solvent (solid line) phase. The solute and solvent molecules are denoted as larger and smaller-sized ellipses, respectively, and dipoles are shown using crossed arrows.

polarity, and dielectric constants to specific interactions, such as van-der-Waals forces, hydrogen bonding, and coordination with ions or solutes, are crucial in determining the results of a

photochemical event in a solvent.[88–90] These interactions can alter the excited states' relative energies, resulting in shifting the positions of crossing points and affecting the rates of radiative and non-radiative transitions.[77,91,92]

The non-adiabatic transitions in a molecular system are also affected significantly by the dynamic nature of solvent molecules.[93,94] Immediately after absorption of light, a solute molecule changes its electronic as well as vibrational configurations, while the solvent molecules around the solute stay in their initial position. However, the new charge distribution can be stabilized gradually over time by the reorganization of solvent molecules around the solute.[95] Therefore, understanding these processes in complex environments is important for exploring photochemical reactions in various contexts, including photoredox catalysis,[96] biological imaging,[97,98] and the development of photoactive materials.[99,100]

## 1.6 Photochemistry as a Tool for Functional Materials

Photochemistry plays a significant role in material science, specifically in the development of advanced functional materials such as molecular switches, data storage materials, biomedical imaging agents, etc. The ultrafast photochemical processes, which take place within the femtosecond (fs) to picosecond (ps) scale, can control the efficiency and effectiveness of the molecule as a photoresponsive material. Investigating such excited-state photochemical processes, including the PES topography and reaction pathways through conical intersections (CIs), allows researchers to rationally design molecular structures that can exhibit efficient photoinduced reactions like isomerization, ring closure, ring opening, etc., thereby innovating materials with enhanced photostability, quantum yields, and switching speeds. **Figure 1.6** shows some of the crucial photoisomerisation reactions occurring within several important classes of photochromic switches, namely fulgides/fulgimides,[101,102] azobenzenes/diazocines,[103–108] diarylethenes,[109,110] etc.

Photochromism in fulgide-related molecules, which have an HT core, is of great significance due to their remarkable ability to reversibly change their absorption and optical properties upon irradiation with specific wavelengths of light. This behavior arises from its unique molecular structure, which facilitates efficient and controllable isomerization between different forms, such as open and closed forms, as that of the photochemical ring-opening/closure reaction in CHD to HT conversion. Fulgides are useful photoactive compounds, which are used in data

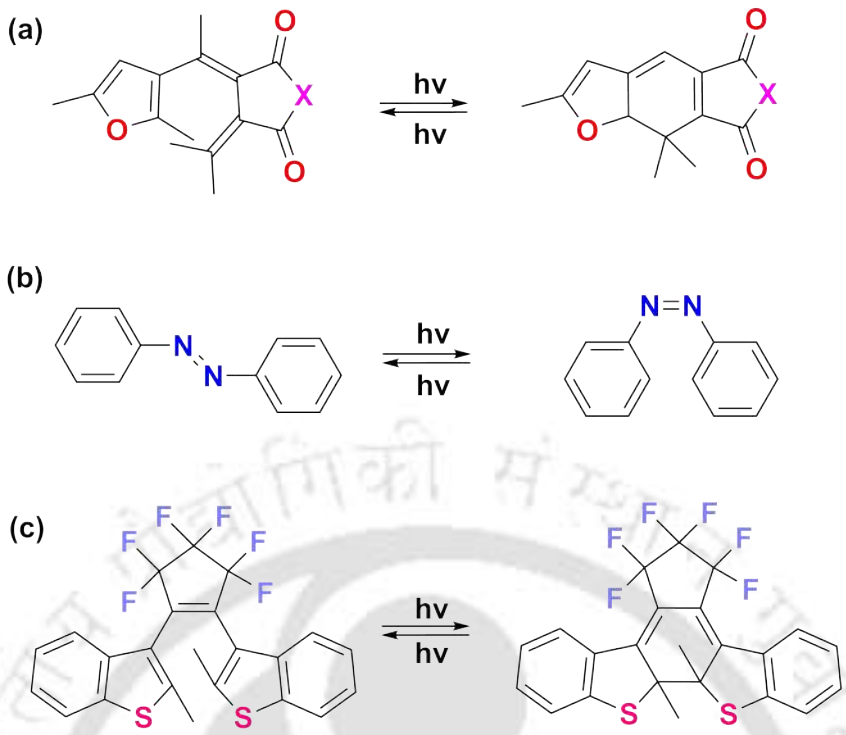


**Figure 1.6.** Photochemical reactions involved in (a) fulgide,[101,102] (b) azobenzenes,[103–108] and (c) diarylethene[109,110] molecular system.

storage, sensors, and smart materials. Their capacity for high-density optical data storage is exemplified by their use in optical memory devices, where information can be written, read, and erased via controlled light exposure. These molecules are also helpful in imaging and sensing, especially due to their ability to operate under visible light and exhibit minimal fatigue over repeated cycles. Researchers are continuously carrying out their investigations to improve their speed, efficiency, and safety for future uses in advanced imaging and light-based computing.[111]

## 1.7 Machine Learning for Photochemistry Exploration

Traditionally, QM methods have provided detailed insights into excited-state properties, such as excitation energies and PESs.[112] However, considering the investigations of relatively larger systems (similar to those shown in **Figure 1.6**) the computational cost becomes very high, and limited information on the photochemistry of the molecular systems is explored. In that case, machine learning (ML) approach has emerged as an alternative implementation in photochemistry, which can offer unprecedented speed and efficiency in exploring excited state phenomena.[27,113–120] ML models can learn from existing QM databases and help in carrying out the molecular simulations by accurately predicting the properties like excitation energies, non-

adiabatic couplings, and transition probabilities of complex molecules and condensed-phase systems that are computationally expensive to find out in traditional QM-based approaches.[121–124] Without needing expensive or time-consuming experiments or calculations, ML can facilitate the discovery and design of new photoreactive materials, such as organic semiconductors and dyes, by providing quick predictions of structure-property relationships.[125] Hence, it has become vital contribution in accelerating the development of materials for photovoltaics, light-emitting devices, and photocatalysis. According to the requirement, specific ML approaches can be considered to study the photochemistry of a molecule. These techniques can come under supervised and unsupervised approaches. Supervised ML techniques can be used to learn the properties of a PES by training a model on a sufficiently large amount of data based on QM methods calculated energies, gradients, and non-adiabatic couplings. This includes mainly the neural network-based potentials (NNPs)[126–132] and kernel method potentials (KMPs)[133–138] based potential models. These models leverage labeled data, which helps to achieve near-quantum chemical methods level accuracy in energy, gradients, and non-adiabatic coupling predictions for new configurations. On the other hand, unsupervised ML methods focus on exploring the inherent patterns or clustering the data without depending on any explicit labels, which can be useful for inspecting conformational space or analyzing distinct molecular motifs. Therefore, such advanced ML methods are making it possible to simulate complex molecules, materials, and light-related processes with higher accuracy and on a larger scale. As a result, this is speeding up the discovery and design in chemistry and materials science.[27]

## 1.8 Overview of Thesis

Therefore, this thesis extensively explores the factors influencing photochemical reactions, particularly focusing on the CHD to HT conversion process (**Figure 1.3**).

In Chapter 3, we incorporated symmetric substitutions in the CHD molecule, analyzed how the substituents can modulate the excited-state dynamics and reaction pathways, and explored the electronic and inertial impacts on the photoinduced ring-opening of the CHD molecule.

Chapter 4 was dedicated to understand the effects of solvent polarity, examining how the surrounding environment, including viscosity, polarity, and specific interactions, alters electronic states and reaction mechanisms associated with the CHD photochemistry.

In Chapter 5, we considered an experimentally synthesized fulgide molecule to evaluate its

potential as a molecular photoswitch, assessing its photochemical behavior, efficiency in light-induced structural transformations, and dissecting the electron transport phenomena through the molecule. We believe this research can contribute to the development of photoresponsive materials with targeted functionalities.

Lastly, Chapter 6 involved the application and comparison of machine learning potential (MLPs) models through non-adiabatic surface hopping molecular dynamics simulations of the CHD to HT photoconversion. It reflects recent progress in applying ML to photochemistry, which makes it easier to study the photochemical behavior of complex molecules.

These integrated studies broaden our understanding of light-driven reactions and motivate experimental scientists to design efficient photoactive compounds.

# Chapter 2

# Theoretical and Computational Methodology

## 2.1 Breakdown of Born-Oppenheimer Approximation

The Born–Oppenheimer approximation,[139,140] which forms the foundation of most studies of chemical processes, assumes that the electronic and nuclear motions in a molecule can be separated due to the large mass difference between them. This allows us to treat the nuclei as moving on a potential energy surface (PES) determined by the electronic energy. However, this approximation is not adequate to study every chemical process. While many thermal processes can be studied using this approximation, breakdown of the same is common in polyatomic molecules' photochemistry.[112,141] This is because electronic states can come close to each other, resulting in non-adiabatic coupling.[33] This coupling results in conical intersections, a crossing point of electronic states.

The common total non-relativistic molecular Hamiltonian is,

$$H_{to} = T_{nu} + T_{el} + V(\mathbf{r};\mathbf{R}) \tag{2.1}$$

Here, **R** is the nuclear coordinate, and **r** is the electronic coordinate, with $T_{nu}$ and $T_{el}$ representing their corresponding kinetic energy operators, and the potential energy is described by $V(\mathbf{r};\mathbf{R})$. We can obtain the electronic Hamiltonian, $H_{el}(\mathbf{r};\mathbf{R})$, by removing the kinetic energy contribution from the nuclei.

$$H_{el}(\mathbf{r};\mathbf{R}) = T_{el} + V(\mathbf{r};\mathbf{R}) \tag{2.2}$$

If $U_i(\mathbf{R})$ and $\Phi_i(\mathbf{r};\mathbf{R})$ represents the eigenvalues and eigenfunction, respectively, we get

$$H_{el}(\mathbf{r};\mathbf{R})\Phi_i(\mathbf{r};\mathbf{R}) = U_i(\mathbf{R})\Phi_i(\mathbf{r};\mathbf{R}) \tag{2.3}$$

By solving **Equation 2.3**, one can gain insights into molecular structures, reaction pathways, and transition states in chemical reactions, as well as electronic energies to carry out spectral analysis and investigate a range of static properties.

The total wavefunction is represented as follows, in accordance with the Born-Oppenheimer expansion,[33]

$$\Psi_{to}(\mathbf{r},\mathbf{R}) = \sum_i \chi_i(\mathbf{R})\Phi_i(\mathbf{r};\mathbf{R}) \tag{2.4}$$

$\chi_i(\mathbf{R})$ are the expansion coefficients. $\Psi_{to}(\mathbf{r},\mathbf{R})$ is exact if truncation is not performed. We have the time-independent Schrödinger equation,

$$H_{to}\Psi_{to}(\mathbf{r},\mathbf{R}) = E_{to}\Psi_{to}(\mathbf{r},\mathbf{R}) \tag{2.5}$$

Using **Equation 2.4** in **Equation 2.5** and multiplying by $\Phi_j^*(\mathbf{r};\mathbf{R})$ and integrating,

$$[T_{nu} + U_i(\mathbf{R})]\chi_i(\mathbf{R}) - \sum_j \sum_\beta \frac{1}{2M_\beta}\left(2d_{ij}^\beta \cdot \nabla_\beta \chi_j(\mathbf{R}) + \kappa_{ij}^\beta \chi_j(\mathbf{R})\right) = E_{to}\chi_i(\mathbf{R}) \tag{2.6}$$

$\nabla_\beta$ denotes the nuclear coordinate gradient, with $\beta$ denoting nuclear degrees of freedom. Terms $\kappa_{ij}$ and $d_{ij}$ denote couplings between states i and j, typically ignored under Born–Oppenheimer approximation. These terms stem from the nuclear kinetic energy operator acting on the electronic wavefunctions and govern non-adiabatic transitions. They have the form,

$$d_{ij}(\mathbf{R}) = \langle \Phi_i(\mathbf{r};\mathbf{R}) | \nabla \Phi_j(\mathbf{r};\mathbf{R}) \rangle \tag{2.7}$$

$$\kappa_{ij}(\mathbf{R}) = \langle \Phi_i(\mathbf{r};\mathbf{R}) | \nabla^2 \Phi_j(\mathbf{r};\mathbf{R}) \rangle \tag{2.8}$$

The $d_{ij}$ is the vector quantity and known as non-adiabatic derivative coupling. This factor is the most dominant one and is used to investigate the non-adiabatic transitions in non-adiabatic

dynamics. This term also depends on the energy difference between the electronic states (i, j). Furthermore, even though the Born-Oppenheimer approximation breaks down in non-adiabatic processes, the analysis of the same typically still follows a two-step procedure. First, the electronic Schrödinger equation is solved to obtain the PES of various electronic states and the coupling terms. This electronic structure information is then used to determine the nuclear dynamics through the integration of nuclear equations of motion.[112]

## 2.2 Configuration Interaction

In quantum chemistry, configuration interaction[139,142] extends the Hartree–Fock[143–145] method by incorporating electron correlation in systems with multiple electrons. It expresses the wavefunction as a linear combination of electronic configurations, each represented by a Slater determinant, which enables a more precise representation of electron interactions. This method facilitates the combination of various electronic states, capturing the correlation effects that occur when electrons interact instantaneously.

Mathematical Framework:

$$\Psi = \sum_i c_i \Phi_i \tag{2.9}$$

Where, $\Psi$ is the total wave function, $c_i$ are coefficients, and $\Phi_i$ are configuration state functions (CSFs).

Configuration Interaction (CI) can be categorized into different types based on the extent of configurations considered. Full Configuration Interaction (Full CI) accounts for every possible electronic configuration by including all the Slater determinants constructed from the occupied and virtual orbitals, offering an exact solution to the electronic Schrödinger equation within the chosen basis. However, its factorial computational scaling with respect to the number of electrons and orbitals renders it feasible only for very small systems. To make the method more practical, Truncated Configuration Interaction techniques are employed, where only a subset of configurations is considered. Common examples include Configuration Interaction Singles (CIS), which includes only single excitations, and Configuration Interaction Singles and Doubles (CISD), which incorporates both single and double excitations. These truncated approaches offer a balance between computational efficiency and accuracy, although they may introduce limitations such as size inconsistency.[112,139,146]

## 2.3 Complete Active Space Self-Consistent Field (CASSCF)

This method is one of the important computational techniques in quantum chemistry. CASSCF is also a variational approach, which is based on the similar expression as in the **Equation 2.9**. In addition to the optimization of the coefficients, it also optimizes the orbitals. More so for systems that exhibit substantial electron correlation. Instead of depending solely on a single reference state, these methods, by considering various configurations,[147] provide a broader characterization of electronic states. The CASSCF[80,148] approach is a key method within this framework. CASSCF defines a wave function as a linear combination of CFSs, which is generated using a specified subset of molecular orbitals referred to as the 'active'.

CAS method involves choosing the electrons and orbitals that are important for examining any chemical reactions occurring within a molecule. In this specified active region, every conceivable configuration is produced using a Full CI method, considering all possible electron distributions within the active orbitals. This approach captures static, or nondynamical correlation, which arises from near-degeneracies among electronic states, and involves re-optimizing the active orbitals to achieve an optimal representation of the molecular system.

## 2.4 Complete Active Space Second-Order Perturbation Theory (CASPT2)

It is a multireference perturbation approach,[146] which is introduced for the improvement of electronic excited state description. This is a post-CASSCF approach designed to incorporate the dynamic correlation effects beyond the static electron correlation effects captured by CASSCF. The main idea is to treat the correlation energy perturbatively starting from a multiconfigurational reference wave function. In CASPT2[81,149] formulation, the zeroth-order wavefunction, $|\Psi_0\rangle$, is obtained from a CASSCF calculation that optimizes both the configuration coefficients and the orbitals within a selected active space. The total Hamiltonian, H,

$$H = H_0 + V \tag{2.10}$$

Here, $H_0$ is the zeroth-order Hamiltonian and V is the perturbation. The zeroth-order Hamiltonian has the form,

$$H_0 = PFP + QFQ \tag{2.11}$$

$P$ and $Q$ are the projector on reference space and the first-order interacting space, respectively, and $F$ denotes the Fock operator.[81,149] This method is extensively used and implemented in programs like MOLCAS,[150] MOLPRO,[151] BAGEL,[152,153] etc. It is favored for its ability to model dynamical and nondynamical correlation, especially for states with multiconfigurational character. However, it has some limitations, such as problems because of the presence of intruder states and the regions with state crossings, which require the use of shifts (e.g., IPEA shift, imaginary shift) to stabilize calculations.

There are many variants of the CASPT2 approach. Among which, MS-CASPT2 (Multistate CASPT2)[149] extends the CASPT2 framework to deal with the coupling between multiple electronic states. It takes into account the interaction of states, making it more suitable for regions where states are close in energy. It uses a multistate formalism to produce coupled energies, which is crucial for studying conical intersections and non-adiabatic processes. XMS-CASPT2 (Extended Multistate CASPT2)[84] is designed to improve invariance under the rotation of reference states. It uses a Fock operator, which is state-averaged, and during calculations, it helps to maintain the multiple states' descriptions in a consistent manner. It employs a dynamic weighting approach to smoothly transition between state-specific and state-averaged regimes, yielding improved accuracy in cases involving near-degenerate states and mitigating problems related to state mixing.

## 2.5 Classical Molecular Dynamics Simulations

Classical Molecular Dynamics (MD)[154] is a simulation technique that computes the trajectories of particles, such as atoms and ions, by applying numerical methods to integrate Newton's equations of motion over time.[155–157] Particles are modeled as explicit entities interacting via analytical potential functions, known as force fields,[158–163] allowing detailed investigation of structural and dynamic properties at the molecular level. Newton's equation of motion is expressed as,

$$F_z = m_z a_z \tag{2.12}$$

$$\frac{d^2 r_z}{dt^2} = \frac{F_z}{m_z} \tag{2.13}$$

Where $F_z$ is the force applied to the particle of mass $m_z$, and $a_z$ is the acceleration. MD simulations generate trajectories in phase space, and these trajectories allow computation of time averages of physical properties, positions, velocities, etc. **Figure 2.1** shows an overall workflow of principles for MD simulations.

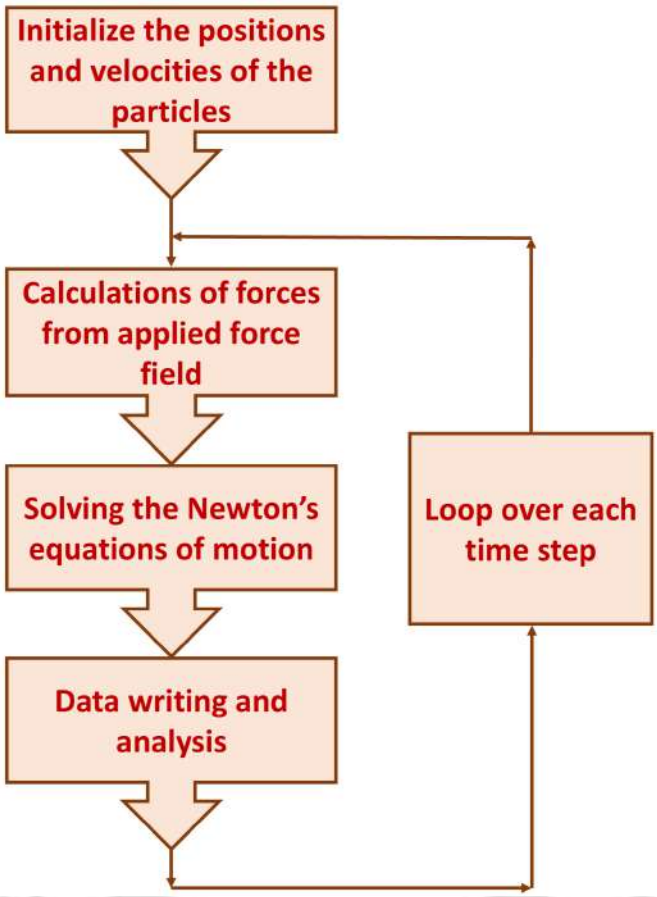


**Figure 2.1.** MD simulations workflow.

Compared to methods like quantum mechanics[139] or Monte Carlo simulations,[164] classical MD[154] can simulate larger systems over longer time scales. This enables detailed molecular-level insights into processes such as diffusion, phase transitions, and structural organization, often complementing experimental observations or providing interpretations in cases where experiments are difficult to perform.

## 2.6 Trajectory Surface Hopping (TSH) Approach

Currently, the trajectory surface hopping (TSH)[165,166] approaches have become the main tool for investigating the photoinduced chemical processes. Within the TSH framework, multiple classical trajectories evolve on adiabatic PESs derived from the electronic Hamiltonian's eigenfunctions. The hopping probability between the electronic states is calculated using various approaches.[166] Among all, the widely used approaches are the FSSH[167–170] and LZSH[171–174] approaches. The TSH approach considers the nucleus motion classically as described in **Section 2.5**. To update the trajectories, the velocity Verlet algorithm[155] is employed, where calculations of position and velocities are done at the same time step.

The dynamics of nuclei is influenced by more than one electronic state and changes in the active PES occur via, so called "hops". In this way, the non-adiabatic effects are introduced in the TSH approach. Further, once a hopping occurs, instant changes in the potential energy take place, therefore, the total energy to be conserved, adjustments in the velocities, i.e., velocity rescaling, have to be performed. This is done via one of the following ways,

$$v_z^j = v_z^i + \gamma_{ij}\frac{a_z}{M_z} \tag{2.14}$$

$$v_z^j = \left(1 + \frac{H_{ii} - H_{jj}}{T}\right)^{\frac{1}{4}} v_z^i \tag{2.15}$$

$\gamma_{ij}$ is the scaling factor which adjusts the vector, $a_z$, and $H$ and $T$ represent the potential and kinetic energy, and $i$ represents the initial state and $j$ is the final state. The choice of $a_z$ can be along the momentum or the non-adiabatic coupling vector.[175,176]

### 2.6.1 Fewest-Switches Surface Hopping (FSSH)

In addition to the propagation of nuclei under Newton's mechanics, in FSSH,[169,170,177] the electronic dynamics are also integrated. The electronic wavefunction, evolving in time, is expanded as-

$$\psi(\mathbf{r},\mathbf{R},\mathbf{t}) = \sum_{\mathrm{j}} \mathrm{c_j}(\mathbf{t})\Phi_{\mathrm{j}}(\mathbf{r};\mathbf{R}) \tag{2.16}$$

Here, $\mathbf{r}$ and $\mathrm{c_j}(\mathbf{t})$ are the electronic coordinates and expansion coefficients that depend on time, respectively, and $\Phi_{\mathrm{j}}(\mathbf{r};\mathbf{R})$ are the electronic basis functions.

Time-dependent Schrödinger equation,

$$i\hbar\frac{\partial}{\partial t}\psi(\mathbf{r},\mathbf{R},\mathbf{t}) = H_{el}\psi(\mathbf{r},\mathbf{R},\mathbf{t}) \tag{2.17}$$

For $c_k$:

$$i\hbar\frac{\partial c_k}{\partial t} + \sum_j(-H_{kj} + i\hbar F_{kj}\cdot v)c_j = 0 \tag{2.18}$$

Where $H_{kj}$ are the matrix elements associated with electronic states k and j, and is given by $\langle\Phi_k|H_e|\Phi_j\rangle$. Further, v and $F_{kj}$ define nuclear velocity and the coupling between the two electronic states, respectively.[177]

Using time-dependent coefficients and coupling, the hopping probability, $P_{j\to k}$, between two electronic states, j and k, is calculated as follows,

$$P_{j\to k} = \max\left\{0, \frac{-2\Delta t}{|c_k|^2}\mathrm{Re}\left(c_j c_k^*\right)\sigma_{jk}\right\} \tag{2.19}$$

Here, $\sigma_{jk}$ is the dynamic coupling and it is equal to $F_{jk}.v$.[177]

For QM/MM-based surface hopping simulations,[178,179] the whole system is separated into two different regions: the inner (In) and the outer (Ou). The inner region will be treated using quantum mechanics (QM), while the outer region is described using molecular mechanics (MM). The total energy of the whole system is-

$$E_{QM/MM} = E_{QM}(In) + E^{el}(In,Ou) + E^{vdW}_{MM}(In,Ou) + E^{b+vdW}_{MM}(Ou) + E^{el}_{MM}(Ou) \tag{2.20}$$

Here, 'b' represents bonding, 'vdW' represents van der Waals, and electrostatic interactions are represented by 'el'.

### 2.6.2 Landau–Zener Surface Hopping (LZSH)

The Landau–Zener surface-hopping method is widely used to avoid explicit calculations of non-adiabatic couplings when determining hopping probabilities. In the original Landau-Zener[171] algorithm, the transition probability between adjacent electronic states is calculated using a formula based on the diabatic representation. In the Landau-Zener algorithm,[171] the non-adiabatic transition probability, $P^{LZSH}_{j\to k}$, between the adjacent adiabatic states j and k is given as,

$$P_{j\to k}^{LZSH} = \exp\left(-\frac{2\pi H_{mn}^2}{\hbar\dot{R}|H'_{nn} - H'_{mm}|}\right) \tag{2.21}$$

Here, for two diabatic states m and n, $H_{mm}$ and $H_{nn}$ are matrix elements that are diagonal, and $H_{mn}$ is the matrix element which is off-diagonal. The terms $H'_{mm}$ and $H'_{nn}$ are the nuclear gradients of $H_{mm}$ and $H_{nn}$, respectively. $\dot{R}$ is the rate of change of $R$ with time. The formula involves matrix elements and their nuclear derivatives, without requiring non-adiabatic coupling vectors.[171,180]

### 2.6.3 Landau-Zener-Belyaev-Lebedev (LZBL) Surface Hopping

In 2011, Belyaev and Lebedev[172] used the adiabatic representation to rewrite the Landau-Zener[171] algorithm. In their formula, the hopping probability, $P_{j\to k}^{LZBL}$, is calculated using the gap in energy along with the second derivative with respect to time.

$$p_{j\to k}^{LZBL} = \exp\left(-\frac{\pi}{2\hbar}\sqrt{\left(\frac{Z_{jk}^3}{\ddot{Z}_{jk}}\right)}\right) \tag{2.22}$$

$Z_{jk}$ denotes the absolute difference in energy, and its second-order time derivative is $\ddot{Z}_{jk}$, between two adiabatic states.

This approach simplifies implementation and has been widely utilized for surface-hopping dynamics.[180,181] In practice, the second-order derivative is often estimated using a three-point finite difference approach,[182] which requires data from previous and future time steps.

## 2.7 Neural Networks for PESs

Potentials based on neural network (NNPs)[126–132] are very popular for simulating chemical processes, like, hydration of ions,[183] zinc proteins,[184] and combustion reactions.[185,186] Artificial Neural Networks (ANNs), which are commonly known as perceptrons,[187,188] creates these potentials. It transforms the input into a new feature space, and then the output correlates with the feature space. When input features are transformed through many layers, the model is referred to as a Deep Neural Network (DNNs), which enables it to learn complex relationships. The **Figure 2.2** shows a representation of a simple neural network architecture.

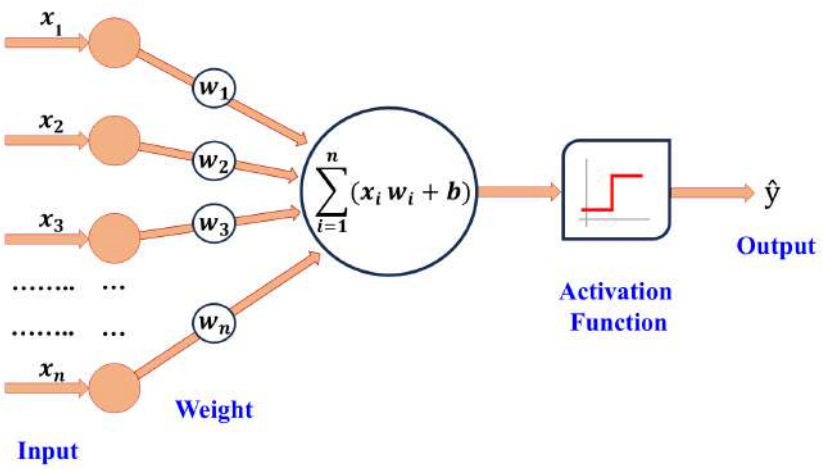


**Figure 2.2.** A schematic neural network framework.

Where, $x_i$'s are the input, $w_i$'s represents the weight, $b$ is the bias, and $\hat{y}$ is the predicted output. Activation functions, such as rectified linear unit (ReLU)[189], radial basis function (RBF),[189,190] etc., are used to determine whether a neuron should be activated during training process. If a neuron contributes effectively to accurate prediction, the associated weights are updated to reflect its importance. In a feed-forward training process, the output of each neuron is computed. After that, the difference between the predicted output and the real output is calculated. To minimize this error, the weights are updated using the backpropagation algorithm, which propagates the error backward through the network to the input layer. Numerical optimization techniques, such as the gradient descent algorithm, are used for this minimization.[191,192]

For training a PES using NN models, the system's potential energy is calculated by summing the contributions from each atom.[185,191] This individual energy of an atom is associated with its surrounding environment within a given cut-off distance. This surrounding chemical environment gives rise to the concept of "Descriptor".[193] The "Descriptor" is nothing but the transformations of the Cartesian coordinates into symmetry-invariant features, which is crucial for the generation of an ML based PES model.[191,193]

# Chapter 3

# Impact of Structural Modifications on Internal Conversion Processes in Cyclohexadiene Photochemistry

This work was published as a cover page article in

THE JOURNAL OF PHYSICAL CHEMISTRY A
A JOURNAL OF THE AMERICAN CHEMICAL SOCIETY

J. Phys. Chem. A **128**, 2025 (2024)

pubs.acs.org/JPCA

## 3.1 Introduction

Since the discovery of orbital symmetry conservation rules in pericyclic reactions by Woodward and Hoffmann,[11,12] numerous studies have been carried out for a better understanding of the photochemical and photophysical behaviour in molecular systems.[194–197] One of the most famous examples of photochemical reactions involved in the cutaneous synthesis of vitamin $D_3$[31,198] is the photodissociation of 1,3-cyclohexadiene (CHD) molecule to yield an all-cis-hexatriene molecule (cZc-HT).[199,200] This photo-induced ring-opening/closure reaction is among the reactions that obey the Woodward-Hoffmann rules and is thus studied widely experimentally and theoretically.[36,61,201–203]

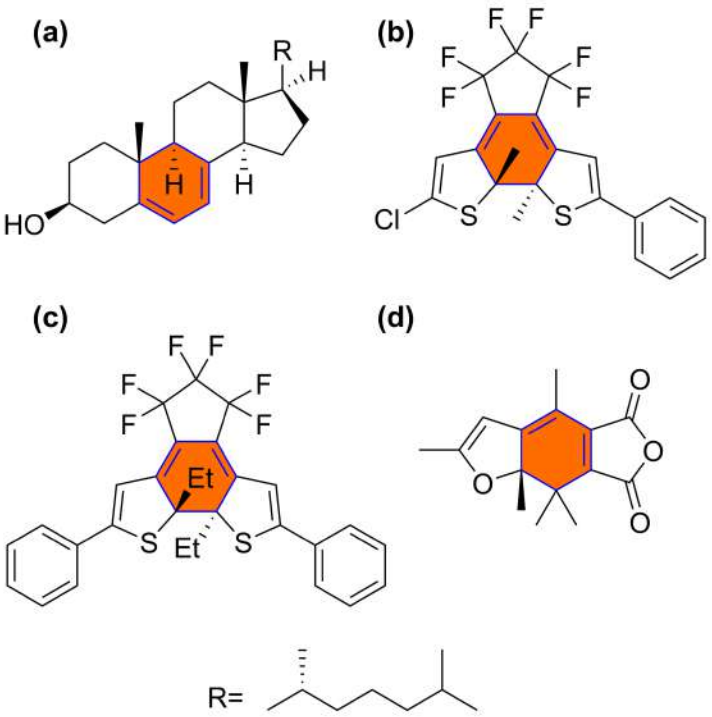


**Figure 3.1.** (a) Provitamin $D_3$, (b) an unsymmetrical dithienylethene,[204] (c) a symmetrical diarylethene,[205] and (d) a fulgide molecule.[101]

Woodward-Hoffmann's rules can explain electronic state transformations along reactive coordinates and the theoretical perspective of a particular system.[12] These rules can also predict the formation of products from the reactants based on symmetry elements present in the system.[206] Further, even though a system does not contain symmetry elements like a mirror plane or a $C_2$ axis, these rules are very efficient in predicting the electronic state transformations along with product formation.[206–208]

On the contrary, photochemical reactions deviate from the Born-Oppenheimer approximation.[141,209] This deviation led to non-adiabatic phenomena, precisely conical intersections ($CI^n$), and avoided crossings.[141] These crossings facilitate electronic state transformation by opening funnel-type radiationless decay channels, which ultimately help form the photoproducts.[208,210,211] Molecules showing these phenomena are relevant to modern technologies, especially because they can be used as photomedicines,[212,213] nanomachines,[214,215] molecular photoswitches,[99,100] and molecular electronic devices.[216,217] **Figure 3.1** shows some cyclohexadiene derivatives that exhibit important photochromism behaviour.[101,204,205]

As illustrated in the **Section 1.3** of **Chapter 1**, one-photon bright excitation from the ground state of the CHD takes place to the lowest-lying excited state, generally labeled as $1^1B$, restricting the symmetry of the molecule to the $C_2$ point group in the Frank-Condon region. Then,

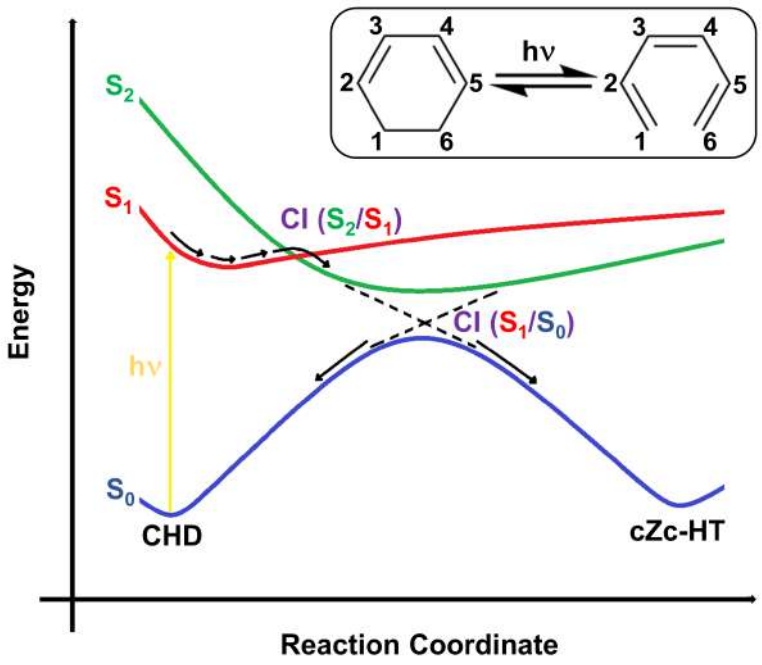


**Figure 3.2.** Schematic representation of CHD to cZc-HT photochromism along with the carbon atom numbering used throughout the work.

the wavepacket proceeds via a narrow path along the ring opening in the CHD moiety. The reaction path next meets its first $CI^n$ ($S_2/S_1$) formed with the second excited state $2^1A$, which is the dark state to one-photon absorption. The wavepacket is then expected to meet its second $CI^n(S_1/S_0)$, which eventually results in the formation of various hexatriene products: cZc-HT, cZt-HT, and tZt-HT or return to the reactant side, producing the closed ring CHD molecule (**Figure 3.2**).[36–39,41,218]

The photodissociation process of the CHD molecule is well-established to be involved in three diabatic states ($1^1B$, $2^1A$, and $1^1A$). A study using linear-response time-dependent density functional theory (TD-DFT) has raised doubts about this notion, proposing that instead of three diabatic states, only one excited state might play a role in the reaction pathway.[39] However, TD-DFT, a single-reference method, appears to conflict with findings from multireference approaches like complete active space second-order perturbation theory (CASPT2)[38,219,220] or multireference configuration interaction (MRCI)[37] calculations.[53,221] Therefore, using a single-reference method, e.g., TD-DFT, sometimes may not provide accurate results about a system that has a multi-configurational character. In addition to the one-photon excitation study, several experimental and theoretical studies are reported where the initial two-photon excitation's lowest Rydberg states are included and explore the alternative pathways of the photochemical reaction.[222,223] Various efforts have also been made to study the pho-

todissociation dynamics and reaction pathways using the most widely used multiconfigurational methods: complete active space self-consistent field (CASSCF)[80,224] and state-averaged CASSCF (SA-CASSCF)[225,226] methods using different active spaces, such as SA-CAS(6,4),[60] SA-CAS(6,6),[38] SA-CAS(14,8),[39] etc. Among all, SA-CAS(6,4) and SA-CAS(14,8) provide qualitatively correct order of the first two excited states, i.e., $1^1$B and $2^1$A, whereas SA-CAS(6,6) gives an opposite order in the Frank-Condon region, however, the order gets improved while going further towards the ring-opening side.

Ohta *et al.*[61] employed a surface-hopping approach using multi-state multireference complete active space second-order perturbation theory (MS-MR-CASPT2)[149] in CHD to investigate potential energy surfaces and gradients of the three lowest electronic states, where the Zhu-Nakamura theory[227–232] was used to carry out the investigation. They observed fast internal conversion processes occurring primarily within 100 fs, considering the initial excitation to $S_1$ and $S_2$ separately. Polyak *et al.*[36] performed on-the-fly non-adiabatic surface hopping molecular dynamics to study the photochemical electrocyclic reaction. Transition probability among the three lowest electronic states was calculated using extended multi-state complete active space second-order perturbation (XMS-CASPT2)[84] theory. They observed an initial transformation between $S_1 \leftrightarrow S_2$, a large number of $S_1 \leftrightarrow S_0$ hoppings in the 35 - 75 fs range, and a late hopping cluster between 70 - 100 fs.

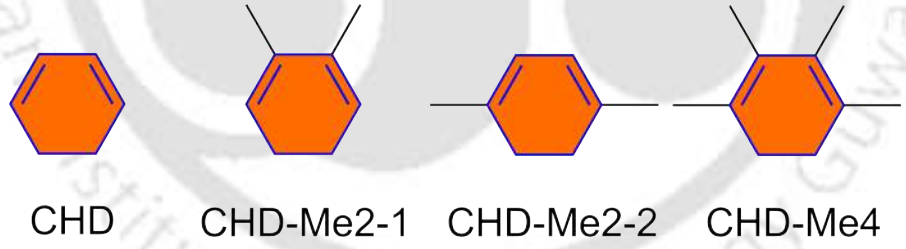


**Figure 3.3.** Systems under investigation: 1,3-cyclohexadiene (CHD), 2,3-dimethylcyclohexadiene (CHD-Me2-1), 1,4-dimethylcyclohexadiene (CHD-Me2-2), and 1,2,3,4-tetramethylcyclohexadiene (CHD-Me4).

A systematic idea about the topography and dynamic behavior of a molecular system near $CI^n$ can be accessed by a phenomenological study of substitution(s) effects. Additionally, a substituent can significantly alter the electronic structure, density of the state, and impact the non-adiabatic dynamics mediated via conical intersection species.[70,76,79] Therefore, in this study, our primary focus is the introduction of symmetric methyl (-$CH_3$) substitutions into the 1,3-cyclohexadiene (CHD) molecule, with the goal of understanding their influence on the reac-

tion dynamics near $CI^n$(s). Our investigation includes two dimethyl derivatives, specifically 2,3-dimethylcyclohexadiene (CHD-Me2-1) and 1,4-dimethylcyclohexadiene (CHD-Me2-2), as well as one tetramethyl derivative, 1,2,3,4-tetramethylcyclohexadiene (CHD-Me4). These compounds are studied alongside the prototype CHD system as integral components of our investigation approach (**Figure 3.3**). Throughout the work, we have optimized all the $S_0$ minimum of reactants and products, $S_1$-minimum and minimum energy conical intersection (MECI) structures involved in the photochemical electrocyclic ring-opening of the considered systems (**Figure 3.3**). We have also located the conrotatory transition state (TSC) structure, using the multiconfigurational CASSCF approach, that connects the ground state minimum energy pathway with the second $CI^n$ ($S_1/S_0$) and helps the wavepacket to flow through it to form the products. Further, the MECI structures are optimized using the XMS-CASPT2 level of theory. Afterwards, a qualitative energy profile diagram at the XMS-CASPT2 approach is presented for each system. To observe the electronic state transformations through the $CI^n$s and to analyze the overall effect in photochemical ring-opening dynamics, we performed on-the-fly surface hopping non-adiabatic molecular dynamics simulations[165] at the SA-CASSCF level of theory.

## 3.2 Computational Details

The static electronic structure theory calculations are carried out in the current work with BAGEL[152,153] and GAUSSIAN 16[233] software packages. In the beginning, the active molecular orbitals for each of the four systems (**Figure 3.3**) are determined using the SA-CASSCF(6,6) level of theory. The three lowest electronic states are weights averaged during the SA-CASSCF calculation, i.e., SA-3-CASSCF. The active space formed by one $\sigma$ -bonding (HOMO-2, localized over $C_1$-$C_6$ bond), two $\pi$-bonding (HOMO-1, HOMO), and their corresponding antibonding counterparts (LUMO, LUMO+1, LUMO+2) are shown for the system CHD in **Figure 3.4** (active orbitals for the other three systems are shown in **Figure A.1** of the Appendix A. We utilized the 6-31G(d) basis set for investigating the reaction path as well as performing the surface hopping dynamics. In spite of the fact that the CHD systems fall in the $C_2$ point group, it was not enforced during any of our calculations.

For each system, we determined the $S_0$ minimum energy stationary points of the reactant and product at the XMS-CASPT2 level of theory based on the SA-CASSCF(6,6) reference wavefunction, i.e., SA-3-XMS-CASPT2(6,6), which was further confirmed by normal mode

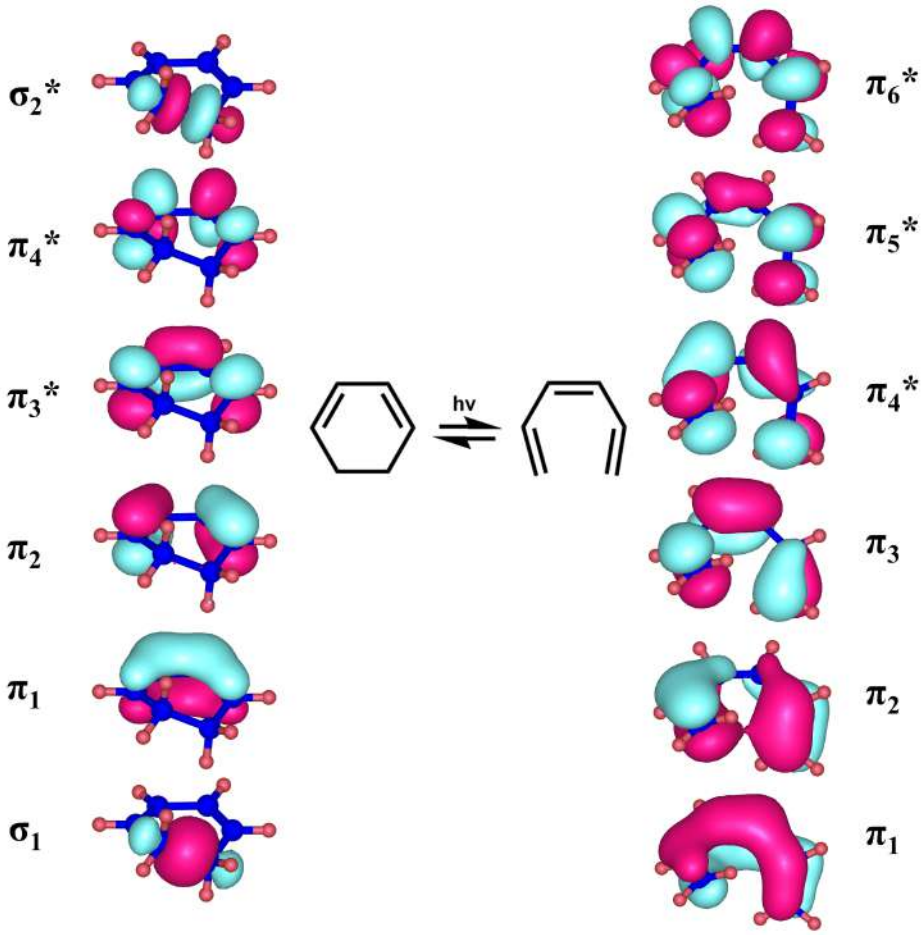


**Figure 3.4.** Active molecular orbitals of CHD (left) and HT (right) taken within the active space of SA-3-CASSCF(6,6)/6-31G(d) calculations.

analysis. We also conducted geometry optimizations and frequency calculation of the reactant and product geometries for all systems at the MN15/May-cc-pVTZ level of theory. The minimum of the first excited state and the minimum energy conical intersection (MECI) optimization is carried out at the SA-3-XMS-CASPT2(6,6) level of theory. For finding MECI structures, we have used the gradient projection algorithm implemented in the BAGEL software.[152,153] Further, the TSC geometries are also optimized at the CASSCF(6,6) level of theory. The presence of a single imaginary frequency confirms the first-order saddle point along the ring-opening and closure pathway, which was further validated by calculating the intrinsic reaction coordinate (IRC) pathways at the same level of theory. Furthermore, the TSC energies are corrected by performing single point energy calculation using the second-order perturbative approach, SA-3-XMS-CASPT2(6,6), to get an idea about the energetics of chemical species involved in the photoconversion process for each system. The SA-3-XMS-CASPT2 calculations are carried out by adding a level shift parameter of 0.5 $E_h$ to the zeroth-order Hamiltonian. The reaction coor-

dinate pathway from the ground state minimum energy geometry of CHD to the MECI ($S_2/S_1$) and MECI ($S_1/S_0$) was calculated employing a geodesic interpolation algorithm.[234] This reactive pathway search was carried out using SA-3-CASSCF and SA-3-XMS-CASPT2 methods with two different active spaces (6,4) and (6,6).

Mixed quantum-classical "fewest switches" surface hopping molecular dynamics simulation, based on Tully's approach,[165] is employed to study the electronic state transformations involved in the considered photochemical electrocyclic reactions. For that purpose, we utilised the NEWTON-X[177] software interfaced with COLUMBUS.[235] We considered the simulation of CHD molecule using three different sets of initial coordinates: 100, 150, and 200. All sets of initial coordinates were sampled with the Wigner distribution model for harmonic oscillator[236] using the normal mode of the CHD molecule calculated at the MN15/may-cc-pVTZ level of theory. All the trajectories were considered for non-adiabatic simulations of the lowest three electronic states without applying any energy restrictions to the excitation energies. A default value of $\alpha = 0.1\ E_h$ was used for decoherence correction.[167,237] We initialized the trajectories at the $S_1$ surface and were run for 100 fs with a classical time step of 0.5 fs and quantum time step of 0.025 fs to observe the effect of substitution on excited state relaxation. All the energies, gradients, and coupling vectors are calculated on-the-fly at the SA-3-CASSCF(6,4)/6-31G(d) approach. The active orbitals used in SA-3-CASSCF(6,4)/6-31G(d) level of theory are shown for the CHD molecule in **Figure A.2** of the Appendix A. After completing three sets of dynamics simulations (100 Traj, 150 Traj, and 200 Traj; Traj refers to the Trajectory) for CHD molecule, we noted consistent results (Appendix A. **Table A.1**) in terms of hoppings and product formation within the initial 100 fs of simulations. Consequently, we concluded that employing 100 trajectories with same protocol would be sufficient for comprehensively studying the photochemical processes in all considered systems. Nevertheless, to observe and analyze non-adiabatic effects within the molecular systems under consideration, we extended the simulation runtime to 300 fs.

## 3.3 Results and Discussion

### 3.3.1 Structural Analysis and Energetics

In **Figure 3.5**, we have shown the optimized reactant, MECI, and product geometries for all the reactions, along with $C_1$-$C_6$ bond length parameters ($S_1$ optimized structures are shown in

**Figure A.3** of the Appendix A). Other significant bond length parameters relevant to ring-

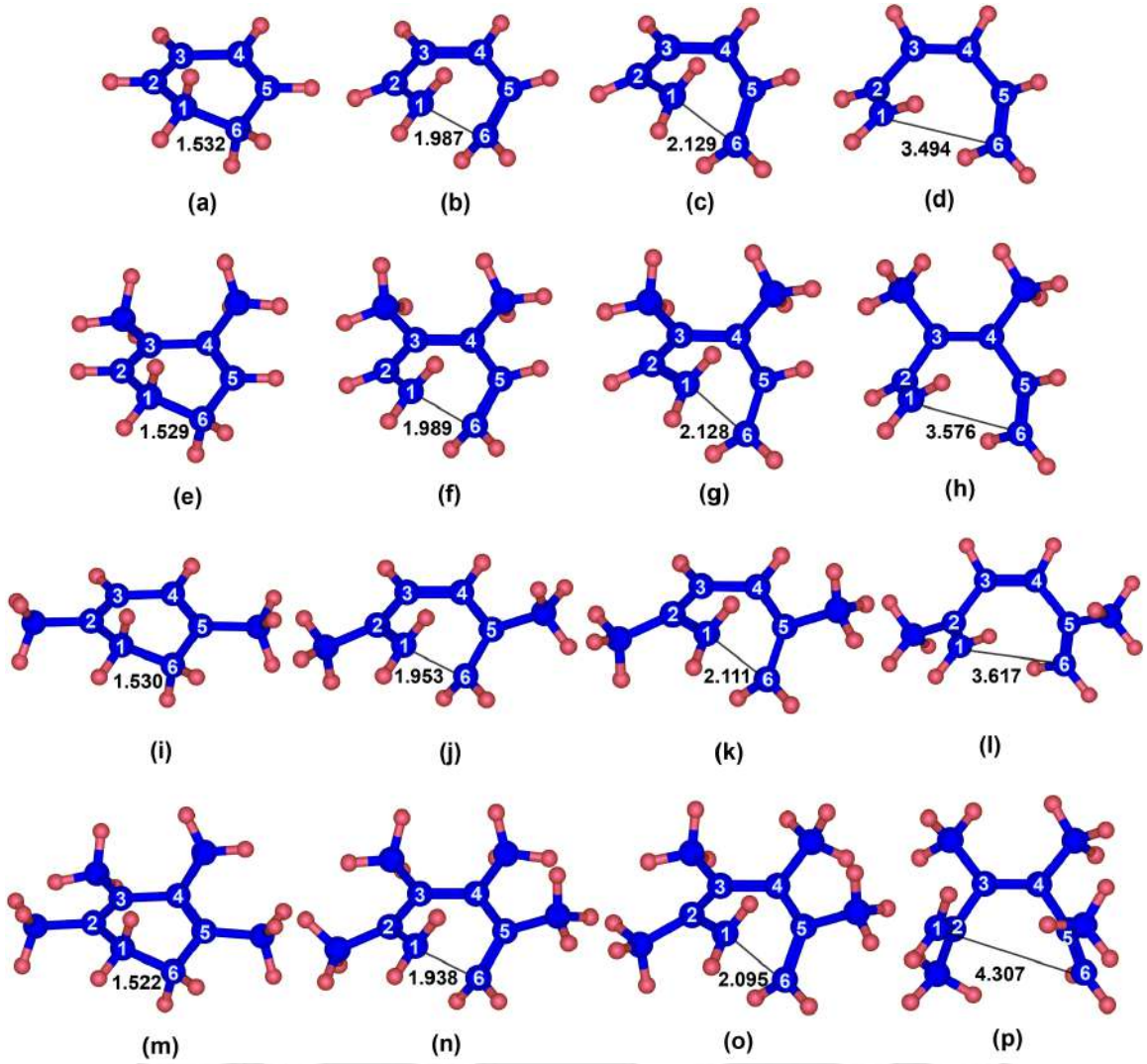


**Figure 3.5.** Optimized equilibrium geometries, (a) $S_0$-CHD, (b) $S_2/S_1$-CHD, (c) $S_1/S_0$-CHD, (d) $S_0$-HT, (e) $S_0$-CHD-Me2-1, (f) $S_2/S_1$-CHD-Me2-1, (g) $S_1/S_0$-CHD-Me2-1, (h) $S_0$-HT-Me2-1, (i) $S_0$-CHD-Me2-2, (j) $S_2/S_1$-CHDMe2-2, (k) $S_1/S_0$-CHD-Me2-2, (l) $S_0$-HT-Me2-2, (m) $S_0$-CHD-Me4, (n) $S_2/S_1$-CHD-Me4, (o) $S_1/S_0$-CHD-Me4, and (p) $S_0$-HT-Me4 at SA-3-XMS-CASPT2(6,6)/6-31G(d) level of theory. Distances are in Å.

opening dynamics are reported in **Table 3.1**. Among all the structures, the $S_1/S_0$ MECI structures of the four systems have the most unsymmetrical shape since all other species are symmetric with a $C_2$-point group. While the $C_1$-$C_2$/$C_5$-$C_6$ and $C_2$-$C_3$/$C_4$-$C_5$ bond pairs show the same bond length values across the optimized reactant, product, and $S_1$ geometries, these values vary in the $S_1/S_0$ MECI structures. The $C_1$-$C_6$ bond has an almost similar length of around 1.530 Å in the case of CHD, CHD-Me2-1, and CHD-Me2-2 molecules, whereas, for CHD-Me4 molecule, it has a comparatively small value of 1.522 Å. Further, for the product geometries, the $C_1$-$C_6$ distance is found to have significantly different values, with the most considerably

**Table 3.1.** Bond length parameters of the optimized geometries. Reactants, $S_1$-min, MECI, and Products are optimized at the SA-3-XMS-CASPT2(6,6)/6-31G(d) level of theory, while the TSC are optimized with the CASSCF(6,6)/6-31G(d) level of theory. Distances are in Å.

| Optimized geometry | $C_5$-$C_6$ | $C_4$-$C_5$ | $C_3$-$C_4$ | $C_2$-$C_3$ | $C_1$-$C_2$ |
|---|---|---|---|---|---|
| CHD $S_0$-min | 1.506 | 1.348 | 1.466 | 1.348 | 1.506 |
| $S_1$-min | 1.442 | 1.418 | 1.406 | 1.418 | 1.442 |
| $S_2/S_1$ MECI | 1.416 | 1.422 | 1.402 | 1.422 | 1.416 |
| $S_1/S_0$ MECI | 1.409 | 1.432 | 1.397 | 1.401 | 1.424 |
| HT $S_0$-min | 1.345 | 1.475 | 1.352 | 1.475 | 1.345 |
| TSC | 1.440 | 1.377 | 1.459 | 1.377 | 1.440 |
| CHD-Me2-1 $S_0$-min | 1.504 | 1.351 | 1.482 | 1.351 | 1.504 |
| $S_1$-min | 1.443 | 1.422 | 1.416 | 1.422 | 1.443 |
| $S_2/S_1$ MECI | 1.414 | 1.427 | 1.412 | 1.427 | 1.414 |
| $S_1/S_0$ MECI | 1.409 | 1.432 | 1.404 | 1.407 | 1.420 |
| HT-Me2-1 $S_0$-min | 1.343 | 1.483 | 1.357 | 1.483 | 1.343 |
| TSC | 1.438 | 1.373 | 1.485 | 1.373 | 1.438 |
| CHD-Me2-2 $S_0$-min | 1.509 | 1.350 | 1.463 | 1.350 | 1.509 |
| $S_1$-min | 1.454 | 1.423 | 1.405 | 1.423 | 1.454 |
| $S_2/S_1$ MECI | 1.419 | 1.431 | 1.400 | 1.431 | 1.419 |
| $S_1/S_0$ MECI | 1.410 | 1.441 | 1.395 | 1.403 | 1.425 |
| HT-Me2-2 $S_0$-min | 1.346 | 1.481 | 1.351 | 1.481 | 1.346 |
| TSC | 1.444 | 1.377 | 1.460 | 1.377 | 1.444 |
| CHD-Me4 $S_0$-min | 1.509 | 1.356 | 1.489 | 1.356 | 1.509 |
| $S_1$-min | 1.455 | 1.430 | 1.423 | 1.430 | 1.455 |
| $S_2/S_1$ MECI | 1.419 | 1.439 | 1.413 | 1.439 | 1.419 |
| $S_1/S_0$ MECI | 1.410 | 1.444 | 1.409 | 1.415 | 1.422 |
| HT-Me4 $S_0$-min | 1.343 | 1.495 | 1.352 | 1.494 | 1.344 |
| TSC | 1.442 | 1.383 | 1.482 | 1.383 | 1.442 |

large distance of 4.307 Å for HT-Me4.

This is mainly because the steric effect of methyl groups repels each other, making the $C_1$-$C_6$ bond a smaller one for the CHD-Me4 system, whereas in HT-Me4, to minimize the steric repulsion, methyl groups adjust themselves in such a way that the distance between $C_1$ and $C_6$ atoms becomes larger, which in turn makes the $\angle C_1C_2C_3C_4$ and $\angle C_3C_4C_5C_6$ (**Table 3.2**) the largest of the optimized product geometries. For $S_1/S_0$ MECI structures, the $C_1$-$C_6$ bond lengths have smaller values (about 0.050 Å for CHD and CHD-Me2-1 and about 0.100 Å for CHD-Me4) than those obtained by Polyak *et al.*[36]. However, our results closely resemble the one obtained by Mori *et al.*[38], except for the CHD-Me4 system. Further, the minimum of the initially excited state, $S_1$, possesses $C_1$-$C_6$ bond lengths smaller than $S_2/S_1$ MECI geometries in all the systems, which was also observed by Mori *et al.*[38] for CHD, where they used the MS-CASPT2 approach. Therefore, in the event of bond-breaking, there remains a chance for

**Table 3.2.** Dihedral angle parameters of optimized $S_0$ geometries at the SA-3-XMS-CASPT2(6,6)/6-31G(d) level of theory.

| | $\angle C_1C_2C_3C_4$ (°) | $\angle C_3C_4C_5C_6$(°) | $\angle C_2C_3C_4C_5$(°) |
|---|---|---|---|
| CHD | 2.27 | 2.27 | 15.28 |
| HT | 48.62 | 48.55 | 4.91 |
| CHD-Me2-1 | 1.08 | 1.08 | 17.64 |
| HT-Me2-1 | 58.06 | 58.05 | 7.78 |
| CHD-Me2-2 | 2.52 | 2.51 | 14.67 |
| HT-Me2-2 | 57.27 | 57.26 | 2.83 |
| CHD-Me4 | -1.87 | -1.87 | 22.73 |
| HT-Me4 | 90.65 | 91.01 | 0.52 |

the wavepacket to approach the first $CI^n$, even after it has undergone relaxation to the minimum of the initially excited state, $S_1$.

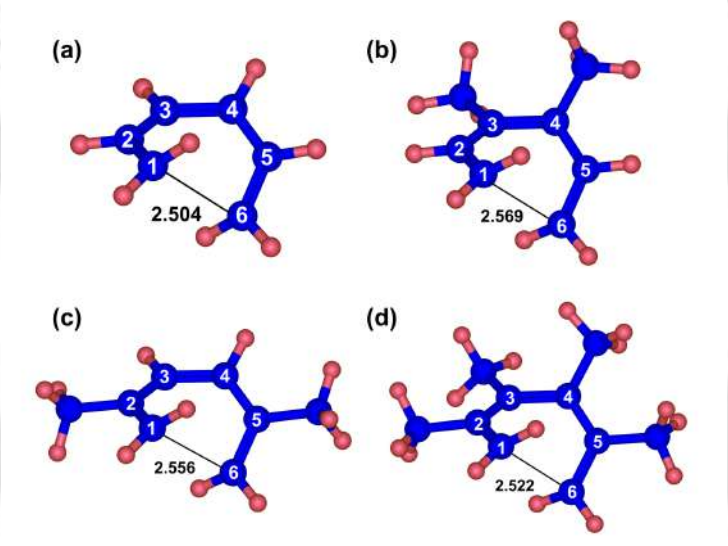


**Figure 3.6.** CASSCF(6,6)/6-31G(d) optimized $S_0$ first-order saddle points involved in (a) CHD, (b) CHD-Me2-1, (c) CHD-Me2-2, and (d) CHD-Me4 photochemical ring-opening reactions. Distances are in Å.

Transition state structures for the photochemical conrotatory (TSC) electrocyclic ring-opening of the considered systems are located using the CASSCF(6,6)/6-31G(d) level of theory. The optimized geometries are depicted in **Figure 3.6**. All the structures are found to have symmetric shapes with $C_2$ point group. Further, we obtained the $C_1$-$C_6$ bond length to be less than the corresponding product geometries and larger than the corresponding $S_1/S_0$ MECI geometries for all the systems. The optimized transition state structures are further chosen for investigating the IRC pathways connecting the closed reactant and open product geometries. **Figure A.4** (Appendix A) shows the IRC pathways calculated at the CASSCF(6,6)/6-31G(d) level of theory for all the systems.

**Table 3.3.** SA-3-XMS-CASPT2(6,6)/6-31G(d) calculated energies (in eV) of the lowest three singlet states. For TSC, corrected energies were used with the SA-3-XMS-CASPT2(6,6)/6-31G(d) approach. Energies are relative to the corresponding CHD derivatives.

| Optimized geometry | $S_0$ | $S_1$ | $S_2$ |
|---|---|---|---|
| CHD $S_0$-min | 0.00 | 5.38 | 6.44 |
| $S_1$-min | 1.50 | 4.49 | 5.19 |
| $S_2/S_1$ MECI | 2.62 | 4.57 | 4.57 |
| $S_1/S_0$ MECI | 3.96 | 3.96 | 6.62 |
| HT $S_0$-min | 1.08 | 7.53 | 7.94 |
| TSC | 3.07 | 4.52 | 5.24 |
| CHD-Me2-1 $S_0$-min | 0.00 | 5.35 | 6.44 |
| $S_1$-min | 1.46 | 4.44 | 5.15 |
| $S_2/S_1$ MECI | 2.69 | 4.55 | 4.55 |
| $S_1/S_0$ MECI | 3.97 | 3.97 | 6.55 |
| HT-Me2-1 $S_0$-min | 1.18 | 7.93 | 8.23 |
| TSC | 3.05 | 4.73 | 6.02 |
| CHD-Me2-2 $S_0$-min | 0.00 | 5.17 | 6.41 |
| $S_1$-min | 1.37 | 4.40 | 5.12 |
| $S_2/S_1$ MECI | 2.74 | 4.55 | 4.55 |
| $S_1/S_0$ MECI | 3.99 | 3.99 | 6.51 |
| HT-Me2-2 $S_0$-min | 1.16 | 7.94 | 8.03 |
| TSC | 3.19 | 4.67 | 5.53 |
| CHD-Me4 $S_0$-min | 0.00 | 5.23 | 6.42 |
| $S_1$-min | 1.47 | 4.29 | 4.87 |
| $S_2/S_1$ MECI | 2.70 | 4.44 | 4.44 |
| $S_1/S_0$ MECI | 3.88 | 3.88 | 6.35 |
| HT-Me4 $S_0$-min | 1.00 | 9.73 | 9.87 |
| TSC | 3.16 | 4.66 | 5.63 |

Vertical excitation energies to the corresponding Frank-Condon region for optimized stable and metastable chemical species are presented in **Table 3.3** (and **Figure A.5** of the Appendix A). For CHD, excitation to $S_1$ and $S_2$ states lies 0.44 eV and 0.23 eV higher in energies than the experimental values.[53] However, our results coincide with a maximum value of 0.10 eV for $S_1$ and 0.05 eV for $S_2$ with the results obtained by Mori *et al.*[38] for all the systems. For HT, the vertical excitation energy to $S_1$ and $S_2$ states are 6.45 eV and 6.86 eV, respectively. If we compare the $S_1$ state excitation energy calculated by Salazar and Faraji[218] using SF-BHHLYP/cc-pVDZ, this value is 0.22 eV lower than our value. Further, we obtained the highest values of $S_1$ and $S_2$ excitation energies of 8.73 eV and 8.87 eV, respectively, for the HT-Me4 system with no experimental or computational data, to the best of our knowledge, to compare.

Lack of dynamical correlation in the CASSCF approach can lead to imprecise estimation of energetic parameters. Therefore, we corrected the energy of transition state structures of all

systems using the SA-3-CASPT2(6,6) approach. It is seen from **Table 3.3** that the $S_0$ energies of TSC structures are lower than the $S_1/S_0$ MECI energies. The $CI^n$ is formed between the $S_1$ electronic state and $S_0$ electronic state. In contrast, the TSC is the saddle point on the $S_0$ electronic state that exists in the minimum energy pathway from the reactant (e.g., CHD) to the product (e.g., HT) molecule. Further, they have similar structures indicating their existence near each other. Therefore, from $S_1/S_0$ $CI^n$, the wavepacket can smoothly drop down to the conrotatory ring-opening pathway in the ground state and ultimately reach the stationary points. Further, we guesstimate that whenever the energy of the $S_1/S_0$ conical intersection seam is near the ground state reaction pathway, it becomes easier to communicate between them, which in turn affects the internal conversion process.

### 3.3.2 From Geodesic Interpolation to On-the-fly Molecular Dynamics

Accuracy of energies, gradients, and non-adiabatic couplings play a pivotal role in on-the-fly non-adiabatic molecular dynamics simulations, significantly influencing the outcomes. Depending on our computational resources, we opted to conduct molecular dynamics (MD) simulations using the SA-CASSCF level of theory. In previous work, Polyak *et al.*[36] performed MD simulations for CHD molecule employing the XMS-CASPT2 method with the reference wavefunction from the SA-3-CASSCF(6,6) level of theory. Additionally, Kim *et al.*[60] explored the dynamics of the CHD molecule's photochemistry using the ab initio multiple spawning (AIMS)[238–240] approach with the SA-3-CASSCF(6,4) level of theory. Consequently, we have compared the results of the high level of theory SA-3-XMS-CASPT2(6,6) and the relatively lower SA-3-CASSCF(6,4) level of theory. For this comparison, we employed geodesic interpolation[234] to trace the path from the ground state-optimized CHD molecule to both $S_2/S_1$ MECI and $S_1/S_0$ MECI. We assessed the electronic state energies along this interpolation pathway using two different methods: SA-3-CASSCF(6,4) and SA-3-XMS-CASPT2(6,6) based on SA-3-CASSCF(6,6) reference wavefunction, all in conjunction with a 6-31G(d) basis set, as illustrated in **Figure 3.7**. The behaviour of electronic state energies was found to have similar pattern showing similar convergence of the electronic state energies at the corresponding crossing points. Therefore, we believe SA-3-CASSCF(6,4) level of theory can be a good choice for non-adiabatic dynamics as it can provide sufficiently accurate results with low computational cost, and so, we proceeded with the same.

We explored the effect of substitution on the internal conversion process of wavepacket

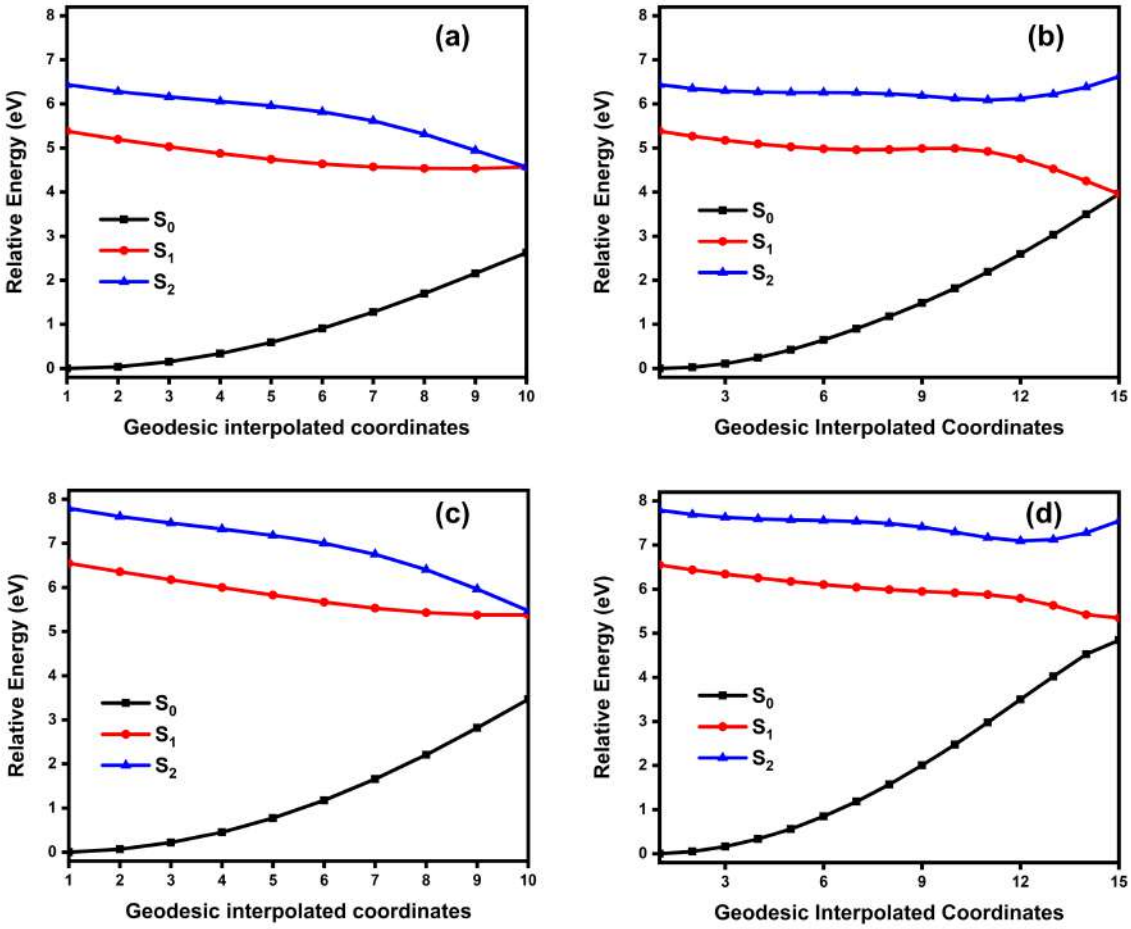


**Figure 3.7.** Geodesic interpolation calculated from reactant to (a) $S_2/S_1$ MECI at the SA-3-XMS-CASPT2(6,6)/6-31G(d), (b) $S_1/S_0$ MECI at the SA-3-XMS-CASPT2(6,6)/6-31G(d), (c) $S_2/S_1$ MECI at the SA-3-CASSCF(6,4)/6-31G(d), and (d) $S_1/S_0$ MECI at the SA-3-CASSCF(6,4)/6-31G(d) level of theory.

on passing through the conical intersections by employing on-the-fly surface hopping non-adiabatic molecular dynamics simulations. 100 trajectories for each system were run for 300 fs, and the photochemical phenomena were observed closely. The root-mean-square deviation (RMSD) plots associated with the geometries in the simulations are shown in **Figure A.6** of the Appendix A.

The time evolution of $C_1$-$C_6$ bond length and corresponding hopping types is shown in **Figure 3.8**(a)-(d). Most of the $S_1 \leftrightarrow S_2$ and $S_0 \leftrightarrow S_1$ hoppings occurred within the initial $\sim$ 150 fs of starting the dynamics simulations. For CHD and CHD-Me2-1, a thick hopping cluster was observed within $\sim$ 50 fs of the dynamics, whereas for the other two systems (CHD-Me2-2 and CHD-Me4), the hopping time was found to be distributed mostly over $\sim$0 - 150 fs. Further,

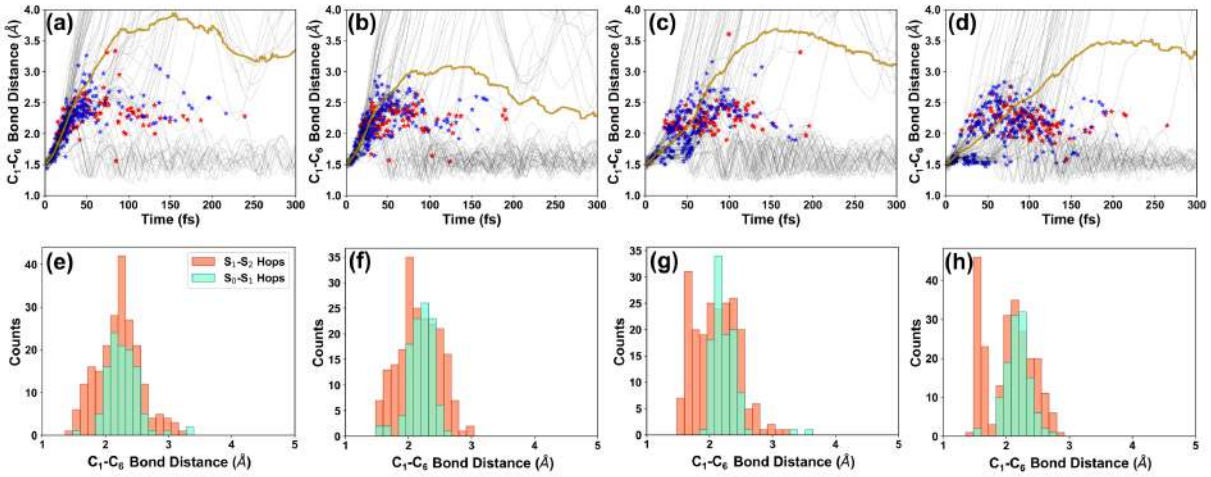


**Figure 3.8.** $C_1$-$C_6$ bond length variations for all the trajectories of (a) CHD, (b) CHD-Me2-1, (c) CHD-Me2-2, and (d) CHD-Me4 along with the hopping types (★:$S_1 \leftrightarrow S_2$, ★:$S_0 \leftrightarrow S_1$) at corresponding time and bond length; $C_1$-$C_6$ bond length distributions throughout the dynamics for (e) CHD, (f) CHD-Me2-1, (g) CHD-Me2-2, and (h) CHD-Me4.

among all systems, the average rate of increase in the $C_1$-$C_6$ bond length was less for CHD-Me4, depicting the decisive effect in the ring-opening dynamics because of the methylation on the CHD system. Histogram plots for the geometrical counts with $S_1 \leftrightarrow S_2$ and $S_0 \leftrightarrow S_1$ hoppings are shown in **Figure 3.8**(e)-(h), which defines the $C_1$-$C_6$ bond length distributions for the respective hopping to occur. For $S_1 \leftrightarrow S_2$ hopping, the $C_1$-$C_6$ bond length of the structures in dynamics was found to lie mostly within the range 1.5 - 3.2 Å, whereas for $S_0 \leftrightarrow S_1$ hopping, it was mainly found to be located within 2 - 3 Å. **Figure 3.8**(e)-(h) also shows that CHD-Me2-2 and CHD-Me4 display maximum counts of $S_1 \leftrightarrow S_2$ hopping near the equilibrium geometries of the ground state optimized minimum energy structures.

As the dihedral angle fluctuation can also influence the overall ring-opening process, we have investigated the fluctuation of inner dihedral angles $\angle C_3C_4C_5C_6$, $\angle C_2C_3C_4C_5$, and $\angle C_1C_2C_3C_4$ for all the systems, as shown in **Figure 3.9**. For all the trajectories, the $\angle C_2C_3C_4C_5$ dihedral angle fluctuates near its initial value, whereas a few trajectories of the other two inner dihedral angles show an increase in magnitude. The effect of substitutions is found to be more prominent in the CHD-Me4 system, where the fluctuation of all considered inner dihedral angles is less as compared to the other three systems. Moreover, the fluctuation in the angle $\angle C_2C_3C_4C_5$ can be discovered to rely primarily on the substituents at positions $C_3$ and $C_4$. In CHD-Me2-1 and CHD-Me4 systems, the variability of the angle $\angle C_2C_3C_4C_5$ is comparatively lower than in the other two systems (CHD and CHD-Me2-2). This can be attributed to the increased rigidity brought about by the substituents at the $C_3$ and $C_4$ positions.

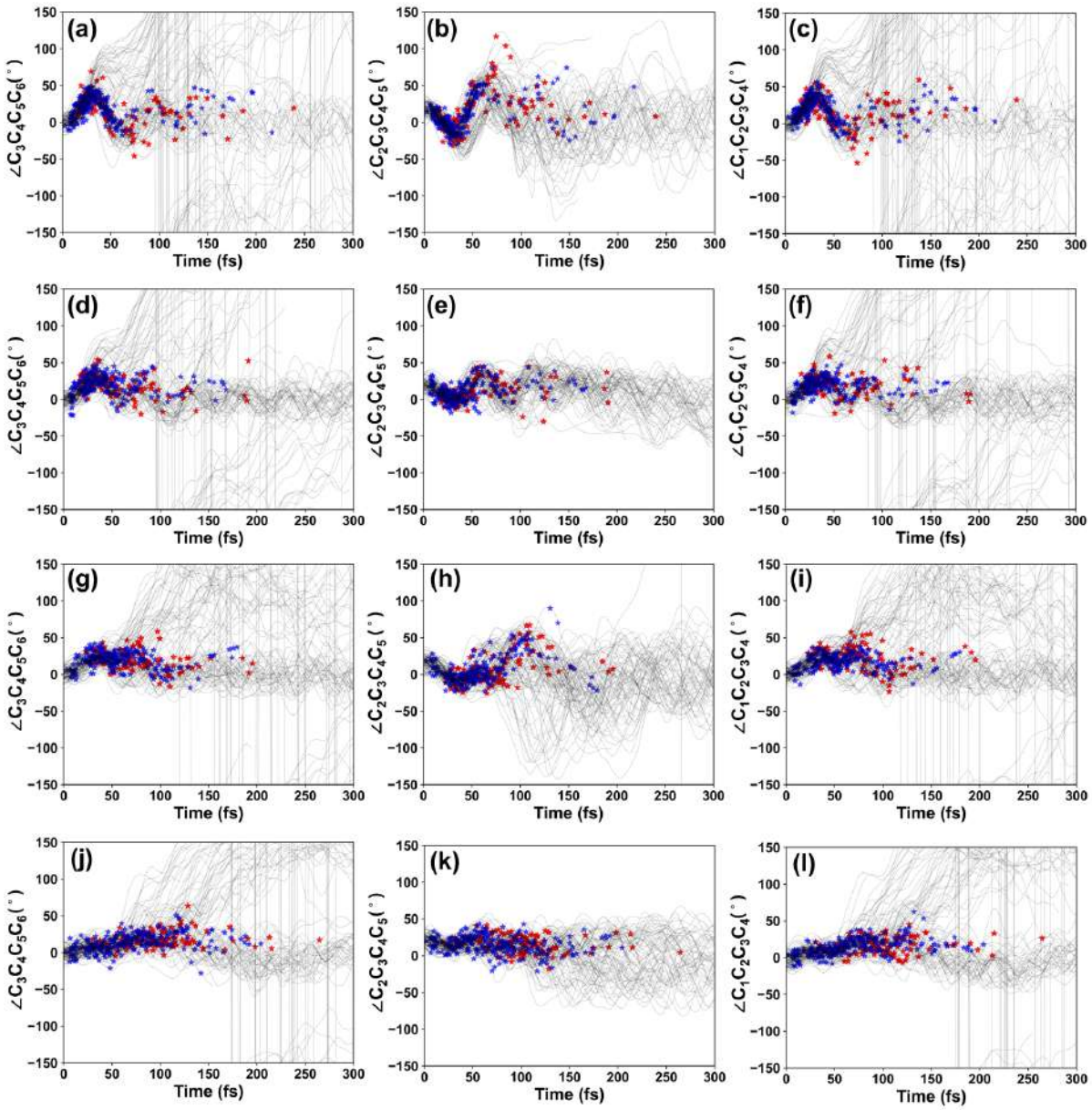


**Figure 3.9.** Dihedral angle variation for CHD: (a) $\angle C_3C_4C_5C_6$, (b) $\angle C_2C_3C_4C_5$, and (c) $\angle C_1C_2C_3C_4$; CHD-Me2-1: (d) $\angle C_3C_4C_5C_6$, (e) $\angle C_2C_3C_4C_5$, and (f) $\angle C_1C_2C_3C_4$; CHD-Me2-2: (g) $\angle C_3C_4C_5C_6$, (h) $\angle C_2C_3C_4C_5$, and (i) $\angle C_1C_2C_3C_4$; and CHD-Me4: (j) $\angle C_3C_4C_5C_6$, (k) $\angle C_2C_3C_4C_5$, and (l) $\angle C_1C_2C_3C_4$ along with the hopping types (★:$S_1 \leftrightarrow S_2$, ★:$S_0 \leftrightarrow S_1$) at corresponding time and angle.

After completion of 300 fs dynamics simulations, almost complete population transfer from the $S_1$ to the $S_0$ electronic state was acquired for all the systems. As shown in **Figure 3.10**, for systems CHD and CHD-Me2-1, there is a sharp decrease in the population within the initial ∼50 fs of the simulation, whereas the other two systems showed a steady shrink in the $S_1$ population throughout the dynamics. Further, for all the systems, the growth in the $S_2$ population followed by a fall was observed within ∼ 150 fs of the initial dynamics, indicating the passage

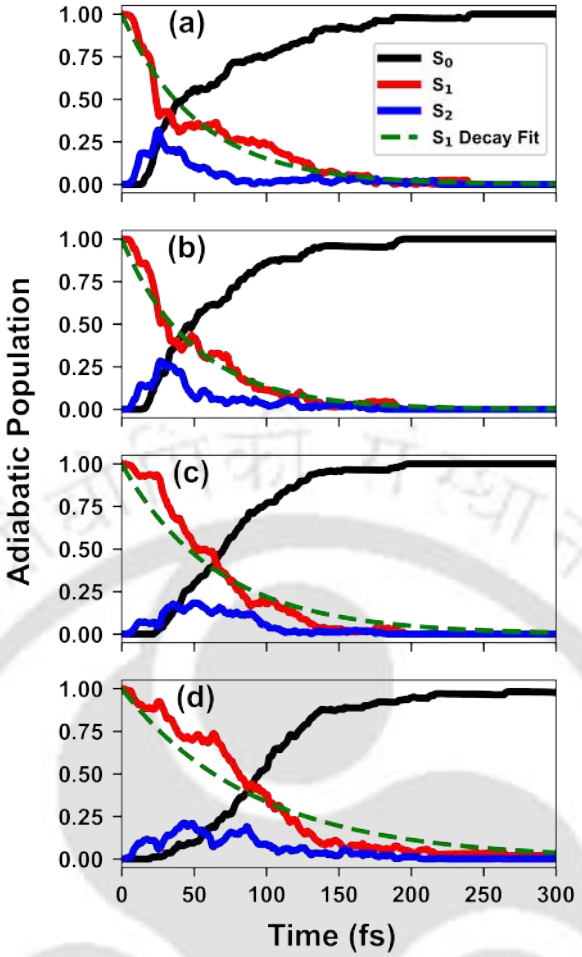


**Figure 3.10.** Ensemble-averaged adiabatic population of the system (a) CHD, (b) CHD-Me2-1, (c) CHD-Me2-2, and (d) CHD-Me4, along with fitted curve for $S_1$ population decay.

of the wavepacket through the $S_2/S_1$ crossings. A careful inspection of the $S_2$ population within these systems reveals that the maximum growth observed for the CHD-Me2-2 and CHD-Me4 systems reached $\sim 0.2$, notably lower than the values observed in the CHD and CHD-Me2-1 systems, $\sim 0.35$. Interestingly, the $S_2$ population growth in the CHD and CHD-Me2-1 systems occurred almost instantaneously, within a mere 25 fs, reaching the maximum value of approximately $\sim 0.35$. A mono-exponential fitting was performed to $S_1$ population decay using $N^{S_1} = \exp(-t/t_d)$, where $t_d$ represents the decay time. For CHD, the decay time was found to be 52 fs, which is equal to the one obtained by Schalk *et al.*[39] and close to the decay time of 47 fs reported by Ohta *et al.*[61] Here for comparison of decay time, $t_d$, among the systems, we have considered the instant decay of $S_1$ population after initial excitation. We observe that for CHD-Me2-1, the decay time, $t_d$, was found to be similar to the CHD system with 49 fs, whereas, for CHD-Me2-2 and CHD-Me4, it was found to be quite different from the CHD and CHD-Me2-1 with large values of 66 fs and 91 fs, respectively.

**Table 3.4.** Analysis of time to reach bond dissociation limit.

| | Total time (fs) | Number of trajectories | $t_{diss}$(fs) |
|---|---|---|---|
| CHD | 3145.5 | 75 | 42 |
| CHD-Me2-1 | 2756.0 | 64 | 43 |
| CHD-Me2-2 | 4405.5 | 67 | 66 |
| CHD-Me4 | 5935.0 | 74 | 80 |

We have calculated the average time of the trajectories required to reach the $C_1$-$C_6$ bond dissociation limit, which can be correlated to the decay time of the excited state and can support our mono-exponential fitting. For that purpose, we considered the dissociation of $C_1$-$C_6$ bond length to be $\sim$ 2.5 Å for all systems, which is nearly equal to the bond length at the transition state geometries of the respective systems, i.e., 2.504 Å for CHD, 2.569 Å for CHD-Me2-1, 2.556 Å for CHD-Me2-2 and 2.522 Å for CHD-Me4. For CHD, it is explained in the **Figure A.7** of the Appendix A. The average time of reaching the dissociation limit is calculated as -

$$t_{diss} = \frac{\text{Total time (fs)}}{\text{Number of trajectories}} \tag{3.1}$$

The average time of reaching the bond dissociation limit for all the systems is presented in **Table 3.4**. When analysing the decay times calculated using fitting process and bond dissociation limit process, we found that the excited state decay time is highly affected for the CHD-Me2-2 and CHD-Me4 systems compared to the other two systems CHD and CHD-Me2-1. Hence, the methylation effect is quite prominent for $S_1$ population decay, and therefore, we conclude that substitution can play a crucial role in the photodynamics of a molecular system.

We have plotted the ensemble-averaged electronic state energies and current electronic state energy evolution shown in **Figure 3.11**. The time evolutions of $S_1$ and $S_2$ state energies were found much nearer throughout the dynamics, whereas the $S_0$ and $S_1$ electronic states remain far apart. To understand this phenomenon, histogram plots for energy gap distributions among the considered electronic states are constructed and shown in **Figure A.8** of the Appendix A. The energy gap between $S_1$ and $S_2$ is much smaller than the corresponding $S_1$ - $S_0$ and $S_2$ - $S_0$ pairs. Furthermore, from **Figure 3.11**, we did not observe the involvement of the second excited electronic state, $S_2$, in the overall transition from the excited electronic state, $S_1$, to the ground state, $S_0$, for all the systems. In addition to that, for the system CHD and CHD-Me2-1,

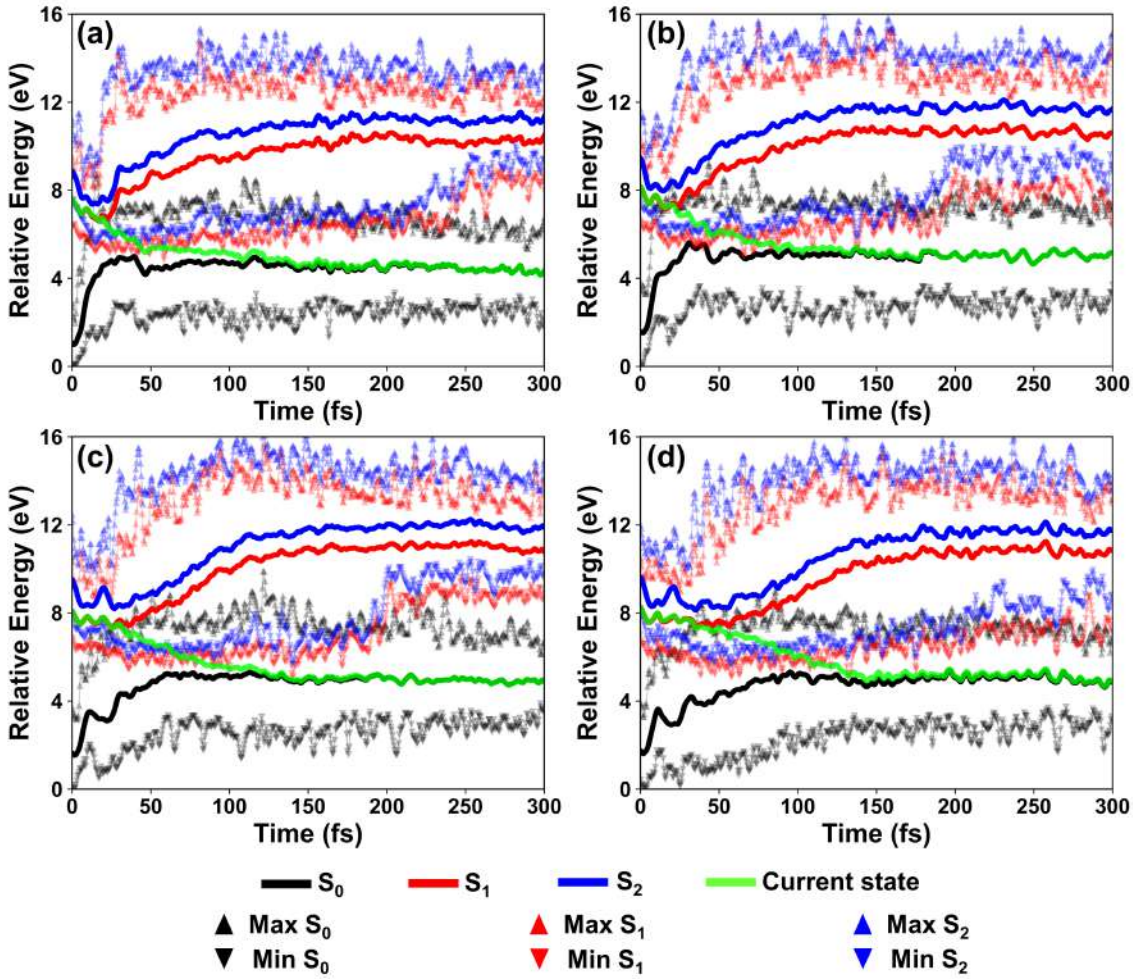


**Figure 3.11.** Ensemble-averaged adiabatic potential energy evolution of (a) CHD, (b) CHD-Me2-1, (c) CHD-Me2-2, and (d) CHD-Me4 systems.

we obtained a time of ∼25 fs at which the current electronic state of the molecule ultimately leaves its $S_1$ electronic state, whereas, for CHD-Me2-2 and CHD-Me4, this time was found to be ∼35 fs and ∼50 fs, respectively. This phenomenon can be correlated to the fast decay of the $S_1$ population in the CHD and CHD-Me2-1 systems compared to that of CHD-Me2-2 and CHD-Me4.

We have conducted the topography analysis around the $CI^n$ involved between the first excited state, $S_1$, and the ground electronic state, $S_0$, at the SA-3-CASSCF(6,4)/6-31G(d) level of theory for all the systems. This topography analysis is performed as described by Yarkony[241,242] and as implemented in the COLUMBUS[235] software package by Barbatti *et al.*[243] The topography analysis details and topographical parameters (**Table A.2**) are presented in the Appendix A. Using all the parameters, we have shown the constructed topographies calculated for all the systems at the conical intersection, $S_1/S_0$, in the **Figure 3.12**. The $CI^n$ topography of the CHD-

Me4 system was found to be more tilted or sloped and unsymmetrical among all the systems, which defines the inefficiency in the $S_1$ to $S_0$ transition. This ultimately affects the excited state decay, which was also observed in **Figure 3.11**, where we have seen a considerable delay in the transition time of the current state from $S_1$ to $S_0$ for the CHD-Me4 system.

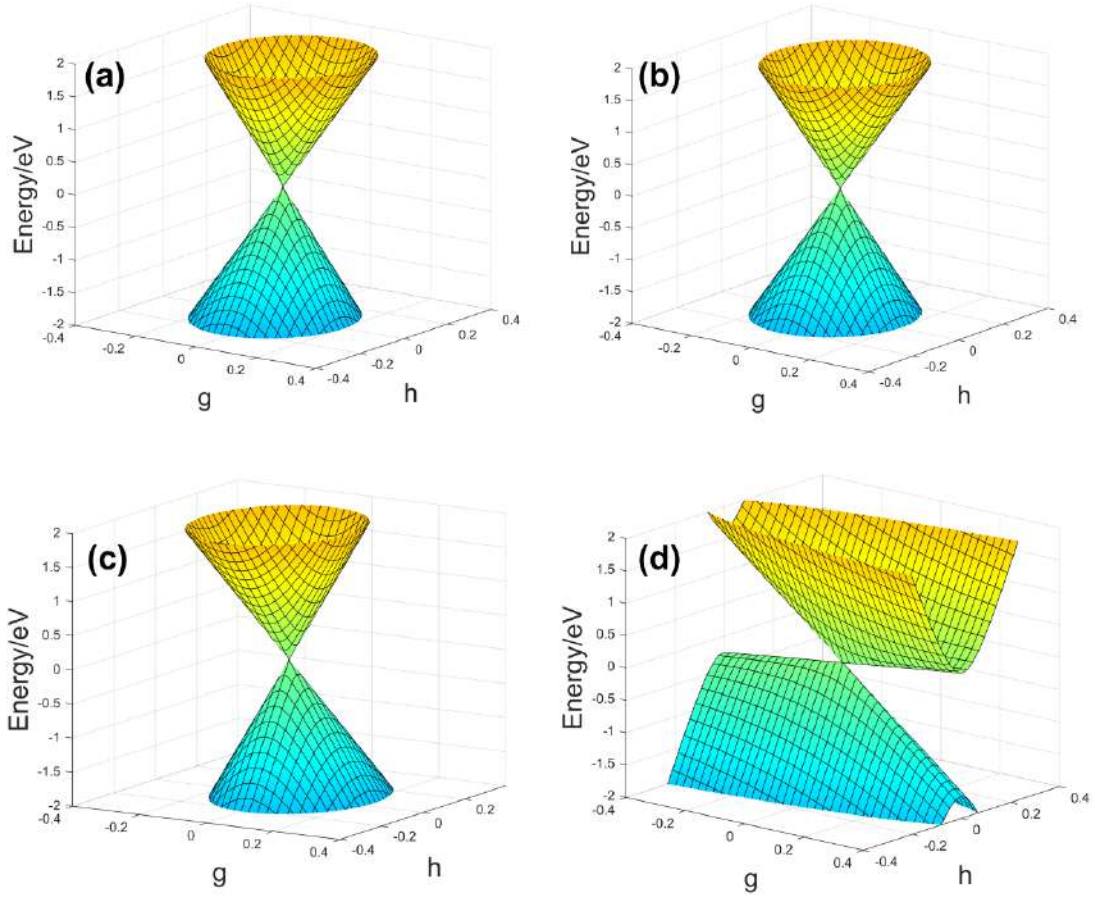


**Figure 3.12.** $S_1/S_0$ $CI^n$ topography calculated at the SA-3-CASSCF(6,4)/6-31G(d) level of theory for (a) CHD, (b) CHD-Me2-1, (c) CHD-Me2-2, and (d) CHD-Me4 systems.

From 100 trajectories run for each system, we obtained a number of 96, 97, 98, and 96 trajectories involving hopping from the excited electronic state, $S_1$, to the ground electronic state, $S_0$, for CHD, CHD-Me2-1, CHD-Me2-2, and CHD-Me4 systems, respectively. Among them, 7, 3, 3, and 10 trajectories involve the re-hopping from $S_0$ to $S_1$ for respective systems. However, they eventually found to end at the ground electronic state, $S_0$, after successive $S_1$ to $S_0$ hopping, except for one trajectory in case of the CHD-Me2-2 system. The typical trajectories for each system are shown in **Figure A.9** of the Appendix A. We obtained a number of 56, 45, 53, and 46 trajectories for CHD, CHD-Me2-1, CHD-Me2-2, and CHD-Me4, respectively, leading to photoproduct HT-derivatives' formation. The product formation condition was set

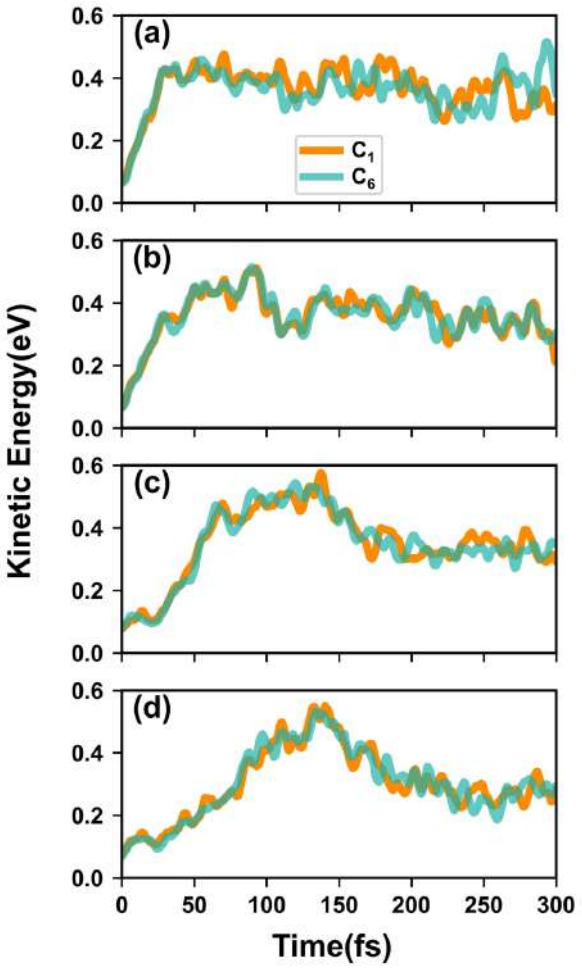


**Figure 3.13.** Ensemble-averaged kinetic energy variations for $C_1$ and $C_6$ atoms of (a) CHD, (b) CHD-Me2-1, (c) CHD-Me2-2, and (d) CHD-Me4 systmes.

in accordance with the $C_1$-$C_6$ bond length parameters of the optimized product geometries as shown in **Figure 3.5**, i.e., if a trajectory reaches the $C_1$-$C_6$ bond length parameters as in the optimized product geometries during the dynamics propagation, we considered the trajectory as successful one for product formation. Accordingly, we obtained 56% (56 out of 100 trajectories) of quantum yield for photochemical ring-opening of CHD to give HT molecule, which is closer to the one reported elsewhere.[36,61,62] Similarly, we got 45%, 53%, and 46% of quantum yield for the remaining three systems: CHD-Me2-1, CHD-Me2-2, and CHD-Me4, respectively.

For a deeper insight into how substitutions affect the dynamics of $C_1$-$C_6$ bond cleavage, we calculated the kinetic energies of the $C_1$ and $C_6$ atoms during the simulations and plotted them as ensemble-averaged data in **Figure 3.13**. For an individual molecular system, the kinetic energies of $C_1$ and $C_6$ follow a similar trend throughout the dynamics. However, if we compare the systems, there is a slow increase in the kinetic energy of both $C_1$ and $C_6$ atoms

for CHD-Me2-2 and CHD-Me4 systems, whereas, for CHD and CHD-Me2-1, we obtained a sharp increase in the kinetic energies within the initial ∼30 - 40 fs of the time and found to remain steady throughout the dynamics. This can be attributed to the rigidity brought about by the methyl groups in the systems, which was also visible in the **Figure 3.9**. However, this rigidity was more prominent in CHD-Me2-2 and CHD-Me4 systems. This is mainly because of a substituent near the carbon-carbon bond (for CHD-Me2-2 and CHD-Me4) responsible for bond-breaking in CHD derivatives. Due to this, it can affect the kinetic energies and momentum to a greater extent by adding extra mass during the ring-opening process of CHD systems to generate HT derivatives.

## 3.4 Conclusions

Throughout the work, we have investigated the effects of a substitution in reaction dynamics of photochemical ring-opening of 1,3-cyclohexadiene. We employed static electronic structure theory calculations and non-adiabatic surface hopping molecular dynamics simulations to carry out the investigation. We considered four systems: CHD, CHD-Me2-1, CHD-Me2-2, and CHD-Me4. For all the systems, the reactants, $S_1$ states, $CI^n$s, and products involved in the ring-opening reactions are optimized using the SA-3-XMS-CASPT2(6,6) approach, and the structural and energetic parameters are compared. Even though there is a structural similarity among the species of interest, the $C_1$-$C_6$ bond length was relatively smaller for the reactant, $S_1$-min species, and the two $CI^n$s for CHD-Me4. However, considerable $C_1$-$C_6$ bond lengths and large $\angle C_1C_2C_3C_4$ and $\angle C_3C_4C_5C_6$ dihedral angles were observed for HT-Me4. Further, all the conrotatory transition state structures showed a greater $C_1$-$C_6$ bond length than the corresponding $S_1/S_0$ $CI^n$s for all the systems. The SA-3-XMS-CASPT2(6,6) corrected energies for conrotatory transition states were also less than that of corresponding $S_1/S_0$ $CI^n$s.

An extensive exploration of the photochemical dynamics within the studied molecular entities (CHD, CHD-Me2-1, CHDMe2-2, and CHD-Me4) was conducted using non-adiabatic molecular dynamics simulations. During the molecular dynamics simulations, the investigation involved a comprehensive ensemble averaging analysis encompassing structural, energetic, and electronic state population aspects. Notably, a consistent trend in the electronic state energies was observed across all systems, wherein $S_1$ and $S_2$ exhibited congruent behaviour while maintaining a distinct separation from the $S_0$ electronic state. Comparative analysis of electronic

state hopping times and the dynamic behaviour of the $C_1$-$C_6$ bond length during surface hopping events aligned with previously documented outcomes for the CHD system. It is noteworthy, however, that the mean rate of $C_1$-$C_6$ bond rupture demonstrated a discernible reduction in the CHD-Me4 system. Intriguingly, non-adiabatic dynamics up to 300 fs show complete population redistribution from $S_1$ to $S_0$ manifested for all the systems. Even though no significant deviations in quantum yields were detected, conspicuous elongation in the decay time was identified for CHD-Me2-2 and CHD-Me4 systems. This substantiates the appreciable influence of substitution on excited state relaxation dynamics. Characteristic kinetic energy profiles of the $C_1$ and $C_6$ atoms divulged distinctive characteristics driven by the substitution phenomena, leading to subdued atomic displacements in CHD-Me2-2 and CHD-Me4 systems, attributable to proximate carbon atom substitution to the $C_1$-$C_6$ bond. Therefore, in light of these findings, our investigation is positioned to advance forthcoming theoretical and empirical analyses of photochemical reactions. The insights garnered from this study hold promise in guiding the design of novel, efficient molecular architectures associated with the CHD framework in prospective applications.

# Chapter 4

# Effect of Polar and Non-Polar Media on Photoinduced Ring-Opening of Cyclohexadiene: A QM/MM-based Surface Hopping Approach

*This work is under consideration*

## 4.1 Introduction

Photoinduced transformations, such as ring-opening/closing,[36,79,244–247] cis-trans isomerization,[92,120,180,248–253] etc., are key photochemical processes in which photon energy is utilized to induce mechanical motion at the molecular level. These processes are the core of many biological activities like vitamin D synthesis in the skin,[31] enabling vision by initiating the phototransduction cascade in the retinal,[254] etc. Beyond their biological relevance, these transformations are also crucial in the development of advanced synthetic materials, such as smart polymers capable of light-responsive conformational changes, and in the engineering of photo-responsive devices for applications in flexible electronics.[255–258]

In this regard, the photochemical transformation between 1,3-cyclohexadiene (CHD) and hexatriene (HT) moiety[259,260] is recognized as one of the fundamental light-induced phenomena, which serves as an exemplary model for evaluating the intricate dynamics of larger and more complex unsaturated molecules. **Section 1.3** of **Chapter 1** provided an overview of the photophysical events involved in the CHD to HT conversion.[36–41] By exploring the photochemistry of CHD, researchers gain critical insights into the essential mechanisms of energy transfor-

mation and molecular reconfiguration related to CHD derivatives. Analyzing such photochemical phenomena, our comprehension of analogous processes occurring in more sophisticated molecular systems can be enriched, which can facilitate the development and optimization of new materials with targeted characteristics and functionalities. The foundational understanding of how molecules behave under light is significantly advanced by several earlier studies,[259–270] which also lay the groundwork for practical applications in diverse fields such as materials science,[271,272] nanotechnology,[273,274] and biochemistry.[275–279]

Solvent properties like polarity, viscosity, and specific interactions with the solute molecule significantly influence photochemical processes by altering excited-state reaction pathways.[88–90] Furthermore, after photoexcitation, the instantaneous changes in the electronic and vibrational configurations of a molecular system can be stabilized over time by the dynamic nature of the solvent.[95] This highlights the important role of solvent molecules. Understanding these effects is vital for applications in photoredox catalysis,[96] biological imaging,[97,98] and the design of photoactive materials.[99,100]

Therefore, it is our purpose in this work to investigated the CHD photochemical ring-opening dynamics in solvent media, water, and n-hexane, which differ significantly in polarity. By performing classical molecular dynamics (MD) simulations of the CHD molecule in both solvent media, we have extracted a few random coordinates from the thermalized trajectory for further surface hopping MD simulations at the QM/MM level. The non-adiabatic surface hopping MD simulation is performed using Tully's trajectory-based algorithm.[165] Ensemble-averaged energies, electronic state populations, bond length evolutions, etc., are analyzed in detail to gain an overall perspective of the ring-opening behavior of the CHD molecule in a solvent medium. Representative trajectories are also examined, and the solute and solvent media interactions are explored.

## 4.2 Computational Details

### 4.2.1 Initial Molecular Geometry Optimizations

The geometry optimizations of CHD, HT, and solvent molecules (water and n-hexane) were performed using density functional theory (DFT) with the B3LYP functional and the cc-pVTZ basis set. Vibrational frequency analyses were performed to verify that the optimized structures are true minima, and the absence of imaginary frequencies confirms that they correspond to min-

imum energy configurations. Further, the excitation energy calculations were performed using the multireference state-averaged complete active space self-consistent field (SA-CASSCF) and extended multistate complete active space second-order perturbation theory (XMS-CASPT2) approach in conjunction with the cc-pVDZ basis set. For the multireference calculations, a state-averaged approach over three electronic states was employed with two different active spaces consisting of six electrons in four orbitals (6,4) and six electrons in six orbitals (6,6). The active molecular orbitals are illustrated in the **Figure B.1** of Appendix B. The conrotatory transition state (TSC) was also optimized at the CASSCF(6,4)/cc-pVDZ level of theory. Additionally, an intrinsic reaction coordinate (IRC) pathway analysis was performed to confirm that the TSC connects CHD and HT structures along the minimum energy pathway. Gaussian[233] software package was utilized for finding minimum energy geometries, while BAGEL[152,153] was used for calculations of excitation energies at SA-CASSCF and XMS-CASPT2 level of theory.

### 4.2.2 Classical Molecular Dynamics Simulations

The CHD molecule is packed with both the solvent molecule n-hexane and water using the PACKMOL[280] program. We have 200 n-hexane molecules within 35.06×35.06×35.06 Å$^3$ periodic cubic box, while for water, 24.6×24.6×24.6 Å$^3$ periodic cubic box with 500 water molecules. With these configurations, we have maintained the densities of 0.66 g/cm$^3$ for n-hexane and 0.99 g/cm$^3$ for water. For classical MD simulations, water molecules were modeled using the TIP3P[281] model. For n-hexane and the CHD molecule, intramolecular interactions, van der Waals interactions, and effective charges were taken from the OPLS-AA[282] force field. The OPLS-AA parameters were obtained from the LigParGen[283–285] webserver.

Classical MD simulations were performed using the TINKER[286] software package. We started our simulations by minimization of energy of both the packed systems by setting the RMS gradient per atom to 0.1 kcal/mol/Ang. After minimization, we carried out the thermalization of the systems for 100 ps at 300 K using an NVT ensemble. A modified Beeman integration method[287] updates the trajectory with a time step of 0.5 fs, and MD frames are recorded every 0.05 ps. During the minimization and thermalization procedure, the CHD molecule is restrained using a soft harmonic force. The restrained procedure ensures the CHD molecule remains in the middle of the periodic box along with the flexibility to fluctuate under the influence of the solvent environment.

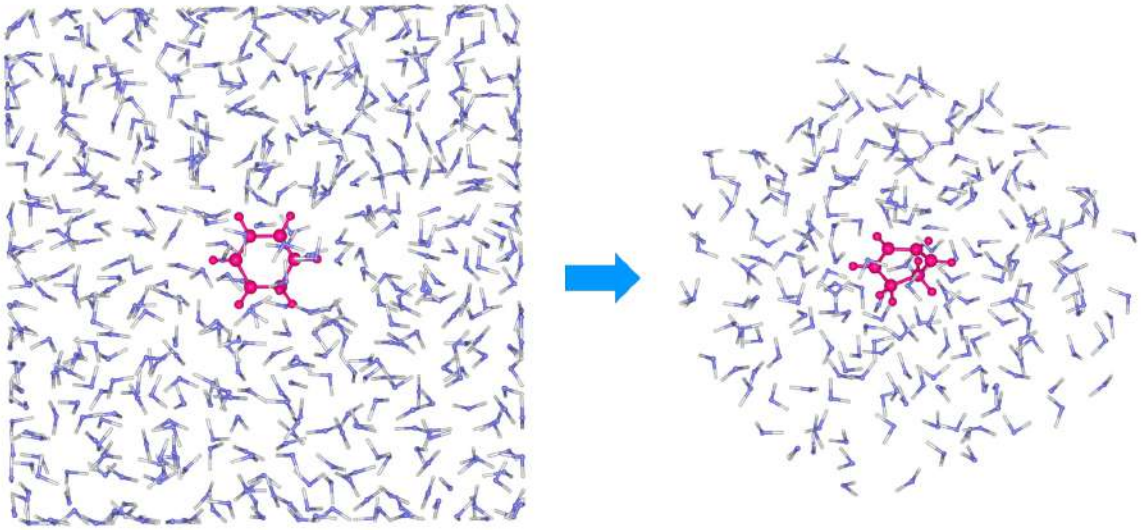


**Figure 4.1.** Cropping of cubic box to spherical shape for water solvated system around CHD (magenta). For n-hexane medium, the figure is shown in the **Figure B.2** of the Appendix B.

After completing the thermalization process, we collected 10 random PDB frames from the trajectories of both systems from the last 25 ps. These frames were labeled as p1, p2, p3, ..., p10. To prepare them for QM/MM surface hopping simulations, they are further cut into spherical shapes around the solute (CHD) molecule, as shown in **Figure 4.1**. Solvent shells of 10 Å and 15 Å around the solute molecule were considered for the water- and n-hexane-solvated systems, respectively. Truncating the randomly selected PDB structures into a spherical shape enables us to use spherical boundary conditions in the QM/MM surface hopping procedure, as implemented in the Newton-X[177–179] software package.

### 4.2.3 Non-adiabatic Surface Hopping Molecular Dynamics Simulations using QM/MM approach

To observe the effect of solvation on the photochemical ring opening of CHD molecules, we employed QM/MM surface hopping MD simulations. For the QM region, we have employed multireference SA-3-CASSCF(6,4)/cc-pVDZ level of theory. The active molecular orbitals are shown in **Figure B.1** of the Appendix B. The MM region was treated with an OPLS-AA force field. For water molecules, the TIP3P model was employed. The Newton-X package, utilized for QM/MM non-adiabatic surface hopping molecular dynamic simulation, uses the Columbus[235] package for QM calculations of energies, gradients, and non-adiabatic couplings, while

MM calculations are performed in the TINKER software package. For each of the 10 PDB frames collected per system from the thermalized classical MD trajectory, thirty random velocities were generated using the method as reported by Sellner *et al.*,[288] where the average kinetic energy at 300 K is distributed along 3N (N=Number of atoms) degrees of freedom. The procedure for generating initial conditions used in this study is consistent with that of Guo *et al.*, who achieved reliable results for 9-methylhypoxanthine photochemistry in aqueous media.[289] Accordingly, a total of 300 initial conditions for each of the solvated medium are generated. All the trajectories are initiated at the excited electronic state $S_1$. A default value of $\alpha = 0.1\ E_h$ was used for decoherence correction. The trajectories were run for 300 fs with a classical time step of 0.5 fs, and the dynamic behavior was analyzed.

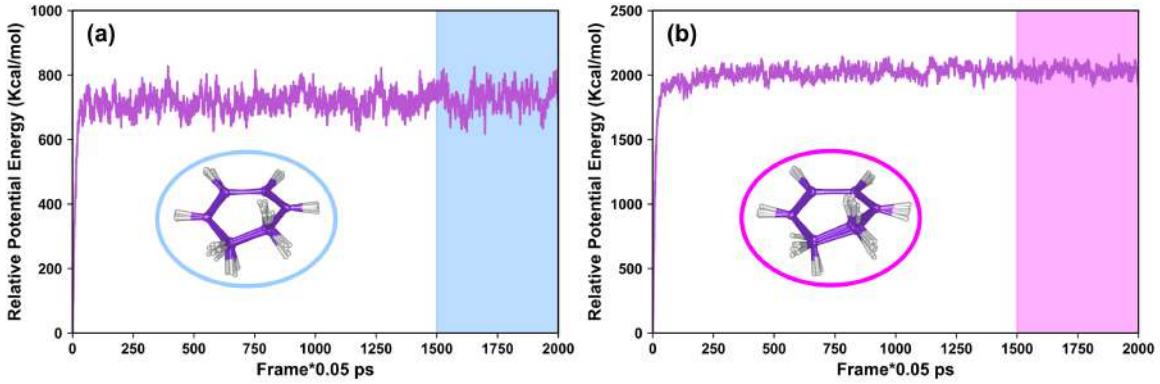


**Figure 4.2.** Relative potential energy of the thermalized trajectory of (a) n-hexane and (b) water-solvated medium along with the shaded region for collection of random PDB geometries are shown.

## 4.3 Results and Discussion

### 4.3.1 Excitation Energy of Classically Sampled Initial CHD Geometries

The potential energy profiles during the thermalization process in solvated n-hexane and water media are shown in **Figure 4.2**. The shaded regions in the plots indicate the time intervals from which PDB frames were selected for subsequent QM/MM surface hopping simulations. From the sampled PDB frames, the CHD geometries are superimposed on the B3LYP/cc-pVTZ optimized geometry of CHD and are presented in the corresponding plots to highlight how markedly they differ. The RMSD plots for the collected CHD geometries (10 each for n-hexane and water-solvated systems) are shown in **Figure B.3** of the Appendix B.

**Table 4.1.** Excitation energies (in eV) calculated for the collected CHD geometries at the SA-3-CASSCF(6,4)/cc-pVDZ level of theory. Values in parentheses correspond to those calculated at the SA-3-XMS-CAS(6,6)PT2/cc-pVDZ level of theory.

| CHD collected in water | | |
|---|---|---|
| PDB frame label | $S_1$ | $S_2$ |
| p1 | 6.28 (5.00) | 7.36 (6.07) |
| p2 | 6.42 (5.18) | 7.77 (6.48) |
| p3 | 6.32 (5.14) | 7.83 (6.55) |
| p4 | 6.55 (5.28) | 7.75 (6.43) |
| p5 | 6.34 (5.13) | 7.72 (6.46) |
| p6 | 6.51 (5.18) | 7.75 (6.32) |
| p7 | 6.24 (5.04) | 7.64 (6.41) |
| p8 | 6.19 (4.99) | 7.39 (6.13) |
| p9 | 6.27 (5.05) | 7.61 (6.28) |
| p10 | 5.96 (4.73) | 6.91 (5.73) |
| CHD collected in n-hexane | | |
| p1 | 6.02 (4.88) | 7.57 (6.37) |
| p2 | 6.19 (4.96) | 7.35 (6.06) |
| p3 | 6.04 (4.81) | 7.29 (6.02) |
| p4 | 6.58 (5.35) | 8.05 (6.64) |
| p5 | 6.34 (5.12) | 7.63 (6.31) |
| p6 | 6.32 (5.08) | 7.52 (6.24) |
| p7 | 6.29 (5.11) | 7.69 (6.43) |
| p8 | 5.99 (4.83) | 7.28 (6.03) |
| p9 | 6.52 (5.26) | 7.89 (6.53) |
| p10 | 6.03 (4.81) | 7.26 (6.02) |
| CHD[a] | 6.52 (5.28) | 7.92 (6.57) |

[a] Optimized at DFT-B3LYP/cc-pVTZ level of theory.

To initiate excited-state dynamics simulations of molecular systems, it is essential to ensure that the selected geometries exhibit reasonable excitation energies to the relevant excited state associated with the photophysical or photochemical process under investigation. Accordingly, we calculated excitation energy using the SA-3-CASSCF(6,4) and SA-3-XMS-CAS(6,6)PT2 methods, employing the cc-pVDZ basis set. The excitation energies are summarized in Table 4.1. At the SA-3-CASSCF(6,4) level, the excitation energies to the bright $S_1$ state range from 5.96 eV to a maximum of 6.58 eV. For the SA-3-XMS-CAS(6,6)PT2 method, the corresponding excitation energies lie between 4.73 eV and 5.35 eV. Thus, the excitation energy to the $S_1$ state varies within a narrow window of 0.62 eV for both approaches. Importantly, the excitation energies obtained using the SA-3-XMS-CAS(6,6)PT2 method remain in close proximity to the experimental value of 4.94 eV reported by Merchán *et al.*[53] This consistency supports

the reliability of the initial geometries, which were randomly sampled from a thermalized MD trajectory. Hence, these geometries were selected to initiate the QM/MM surface hopping simulations.

### 4.3.2 QM/MM Non-adiabatic Surface Hopping Simulations

**Figure 4.3** shows the adiabatic excited state populations averaged over 300 trajectories for both systems. The simulations were initiated from the bright excited state, $S_1$, for CHD. During the initial $\sim$ 20 fs, the population behavior of all electronic states in both solvent media was found to be similar, with a transition of the initial $S_1$ population to the $S_2$ state observed. Subsequently, a sharp increase in the $S_0$ population was noted for the water system compared to the n-hexane system. Similar to our previously reported gas-phase results,[244] where the $S_2$ population increased to $\sim$0.35 within $\sim$25 fs, a rise in the $S_2$ population is observed in both solvent media within $\sim$25-30 fs. However, the population dynamics of the $S_2$ state differed between

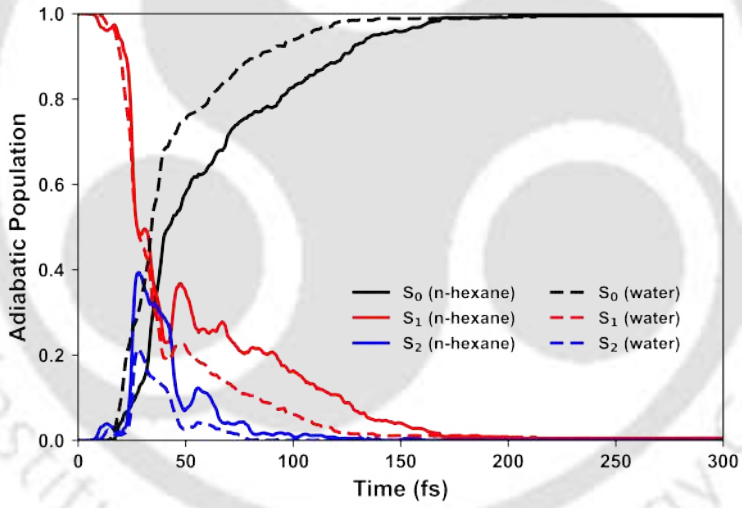


**Figure 4.3.** Ensemble averaged adiabatic population of electronic states during the surface hopping simulations.

the two solvents. In n-hexane, a significant rise in the $S_2$ population was observed, reaching $\sim$0.4, whereas in water, it was $\sim$0.2. Interestingly, within $\sim$20-35 fs, CHD in n-hexane exhibited greater population accumulation in the $S_2$ state than in $S_0$. Between $\sim$35–50 fs, a re-accumulation of the population in $S_1$ was observed for both systems. After this period, the $S_1$ population began to decrease similarly in both solvents. Furthermore, within $\sim$50–70 fs, a prominent increase in the $S_2$ population was observed for the n-hexane-solvated system.

To gain more insight into the significant $S_1 \leftrightarrow S_2$ population fluctuations for the n-hexane-

solvated system, we analyzed the hopping events that occur during the simulations. From the distributions of both hopping types, $S_1 \leftrightarrow S_0$ and $S_1 \leftrightarrow S_2$ (**Figure 4.4**), it is observed that till ∼25 fs, the number of $S_1 \leftrightarrow S_2$ hoppings is higher in the n-hexane medium compared to the water-solvated medium. The distributions of hoppings over the $C_1$–$C_6$ bond length also show that $S_1 \leftrightarrow S_0$ hoppings are more common in both solvents within the range of ∼2 Å to ∼2.5 Å, with a clear peak at ∼2.2 Å in the n-hexane medium. For $S_1 \leftrightarrow S_2$ hoppings, the n-hexane medium shows two peaks, around ∼2.0 Å and ∼2.5 Å, while the water-solvated system shows only one noticeable peak at ∼2.0 Å. Most importantly, in the water-solvated system, $S_1 \leftrightarrow S_0$ hoppings are more dominant than $S_1 \leftrightarrow S_2$ hoppings. This can be attributed to the ballistic and inertial motion of n-hexane, which is likely to help reach the geometry near regions of the potential energy surface (PES) favorable for $S_1 \leftrightarrow S_2$ hopping. Further, water, being a polar and more rigid solvent, has the potential to engage in specific interactions through its O–H bond with electron-rich regions, such as the $\pi$-electron cloud present in the CHD or HT moiety, which tends to dissipate the energy quickly, lowering the barrier for excited state decay, resulting in faster population transfer to the $S_0$ state.

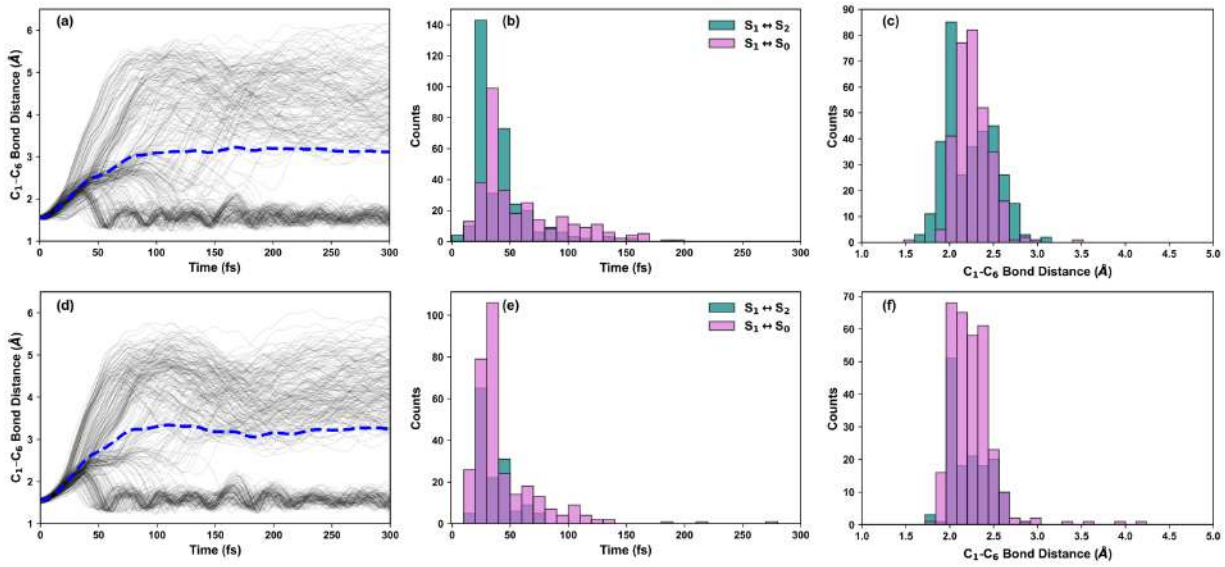


**Figure 4.4.** In the n-hexane-solvated medium: (a) time evolution of the $C_1$–$C_6$ bond length, (b) hopping distribution over time of simulation, and (c) hopping distribution over $C_1$–$C_6$ bond length. In the water-solvated medium: (d) time evolution of the $C_1$–$C_6$ bond length, (e) hopping distribution time of simulation, and (f) hopping distribution over $C_1$–$C_6$ bond length. The blue colored dotted line represents the ensemble averaged $C_1$–$C_6$ bond length.

For comparison, we have plotted the ensemble-averaged $C_1$–$C_6$ bond length evolution and bond alternation coordinate (BAC) for both solvents as shown in **Figure B.4** of the Appendix

B. The BAC is calculated using the formula: $r(C_1–C_6) + r(C_2–C_3) + r(C_4–C_5) – r(C_1–C_2) – r(C_5–C_6) – r(C_3–C_4)$, as used by Polyak *et al.*[36] If we compare the $C_1–C_6$ bond length as well as BAC in both solvent media, they increase more rapidly for the CHD in water. This rapid rise in $C_1–C_6$ bond length occurred within the initial ∼80 fs of the dynamics. Specifically, the bond length increased from ∼1.5 Å to 3.4 Å in water and to 3.1 Å in the n-hexane system. After reaching their peak values, the $C_1–C_6$ bond lengths fluctuated around 3.0 Å in both solvents over the 300 fs simulation period. A similar trend was observed in the BAC curves, where the BAC increased from ∼-0.25 Å to ∼2.0 Å for CHD in water, and up to ∼1.6 Å in n-hexane. These observations of the $C_1–C_6$ bond length and BAC evolution for CHD in both solvents indicate that solvent environment influences the ring-opening rate. In this case, the ring-opening dynamics is found to be notably higher in the water medium.

We have also plotted the potential energy evolution of the electronic states involved in the photochemical conversion of the CHD to HT system, as shown in **Figure 4.5**. At the start of the simulation, the $S_0$ electronic state remains well separated from the $S_1$ and $S_2$ states, while $S_1$ and $S_2$ stay close to each other throughout the simulation. This observation holds for both solvent media. Compared with the simulation in the gas phase,[244] the electronic states show similar behavior. The behavior of the current state in both solvent media is also noteworthy. After the simulation begins, the current state departs from the $S_1$ state at a relatively earlier time of around 20 fs in the water-solvated medium, compared to about 25 fs in the n-hexane-solvated system. As the simulation progresses, the current state eventually reaches the $S_0$ state in both solvents. In water, this occurs at approximately 90 fs, while in n-hexane, it takes slightly longer, around 120 fs.

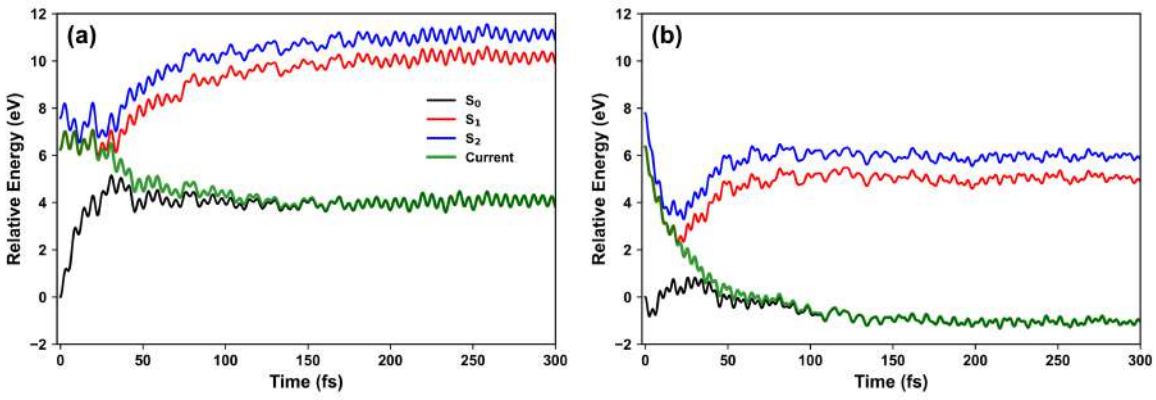


**Figure 4.5.** Ensemble averaged electronic state energy behavior in (a) n-hexane and (b) water-solvated medium. Energies are relative to the ensemble averaged value at time, t = 0 fs.

Furthermore, the energy range over which the electronic states of CHD evolve in the two different solvents was interesting to observe. To compare the potential energy evolutions, the ensemble averaged energies of the electronic states are plotted relative to the ensemble averaged energy of the $S_0$ state at time t = 0 fs, for each respective solvated medium. As time progresses, the behavior of the two solvents starts to deviate. In n-hexane, the $S_1$ and $S_2$ electronic states fluctuate within the ∼6–8 eV energy range until around 40 fs. After that, they gradually increase to ∼100 fs and remain within the ∼9–12 eV energy range. In contrast, in the water-solvated system, the $S_1$ and $S_2$ states show initial stabilization within the ∼2–4 eV energy range during the first ∼25 fs of the simulation. After this period, the energies of both states gradually increase until around 80 fs, after which they fluctuate within a ∼4–6 eV range. A similar stabilization of the $S_0$ state energy is also seen in the water-solvated medium. For the $S_0$ state in n-hexane, the energy increases from 0 eV to ∼5 eV within the first ∼35 fs, then decreases to ∼4 eV by ∼50 fs, and continues to fluctuate around that range for the rest of the simulation. In contrast, in the water-solvated medium, the $S_0$ energy stabilizes within the first ∼10 fs, followed by an increase to a maximum of ∼1 eV by ∼35 fs. Interestingly, after ∼35 fs, the $S_0$ energy starts to decrease and, from around 100 fs, fluctuates about 1 eV below the energy at the start of the simulation. This suggests that the nature of the solvent has a significant impact on the reaction dynamics of the CHD ring-opening process. Energy stabilization is more prominent in the water-solvated system, while in n-hexane, the behavior of the electronic states is less significant compared to their evolution in the gas phase.[244] A possible reason for this could be the interaction of solvent molecules with the $\pi$-cloud of the CHD system, which perturbs the electron density on the double bonds and, as a result, influences the electronic state energies to a greater extent. This solvent-induced energy stabilization can lead to a decrease in the energy barriers in the PES, and as a result, the ring-opening rate is also found to be higher in the case of water solvent.

We have also analyzed the quantum yield (QY) for the formation of the photoproduct HT during the MD simulation. The optimized CHD, HT, TSC geometry, and intrinsic reaction coordinate pathway (IRC) are shown in the **Figure B.5** of the Appendix B. The QY was calculated based on the $C_1$–$C_6$ bond length in the optimized geometry of HT at the B3LYP/cc-pVTZ level of theory, which is 3.51 Å. A trajectory was considered to yield the photoproduct if it crossed this bond length, and we also ensured that the trajectory was on the $S_0$ electronic state at the end of the simulation. Out of 300 trajectories run for each system, we observed that 161 trajectories led to HT formation in the n-hexane medium and 185 trajectories in the water-solvated medium.

This corresponds to a QY of 53 % for n-hexane and 61% for water, respectively.

Further, we have also analyzed the average time of bond breaking ($t_b$) and product formation ($t_f$) during the simulation. The formulas used for calculating $t_b$ and $t_f$ are given below:

$$t_b = \frac{\text{Total time to reach bond breaking limit}}{\text{Number of trajectories}} \tag{4.1}$$

$$t_f = \frac{\text{Total time to reach the photoproduct}}{\text{Number of trajectories}} \tag{4.2}$$

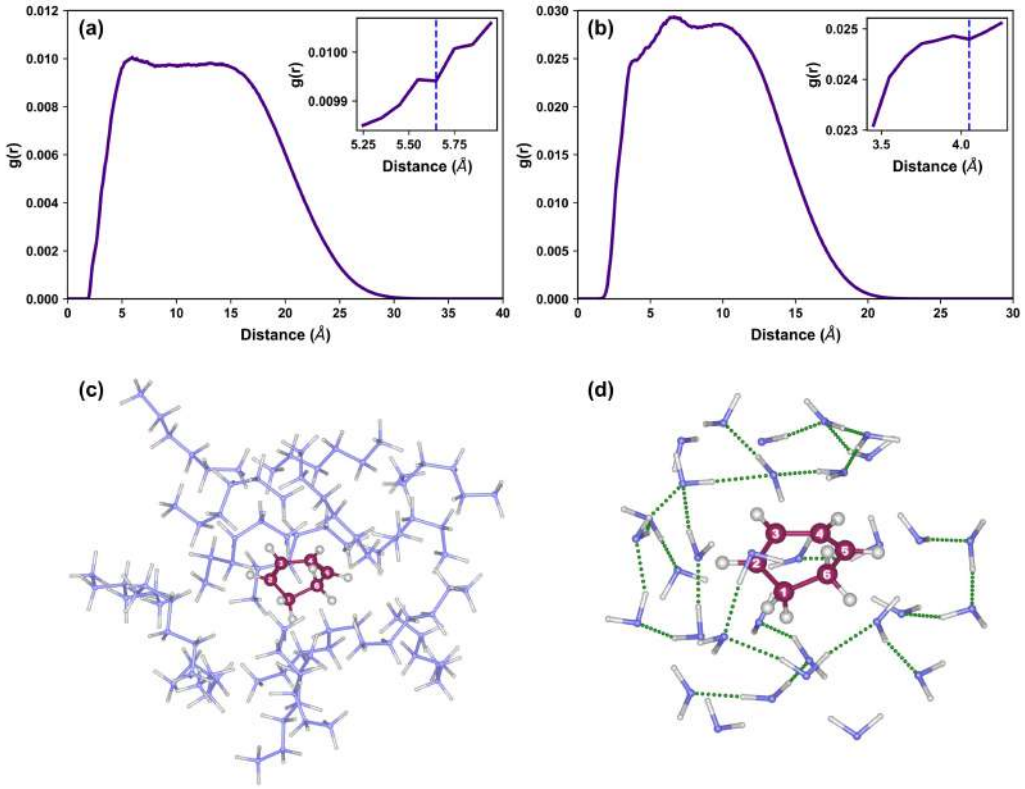


**Figure 4.6.** Radial pair distribution function, g(r), curve for (a) n-hexane, and (b) water-solvated medium; and the first solvation sphere (FSS) in (c) n-hexane, and (d) water medium. The green colored dotted lines represent the intermolecular hydrogen bonding in the FSS of water.

We obtained a $t_b$ value of 66 fs for n-hexane and 54 fs for water medium. For this calculation, the bond breaking limit was set based on the $C_1$–$C_6$ bond length of 2.85 Å, which corresponds to the conrotatory transition state geometry optimized at the CASSCF(6,4)/cc-pVDZ level of theory (Appendix B **Figure B.5**). It is assumed that once the $C_1$–$C_6$ bond length crosses this value from the reactant side, the system can enter the potential well on the product side. Similarly, while calculating the average product formation time, $t_f$, we used the $C_1$–$C_6$ bond length of 3.51 Å, which is the same as for calculating the QY of product formation. We obtained a $t_f$

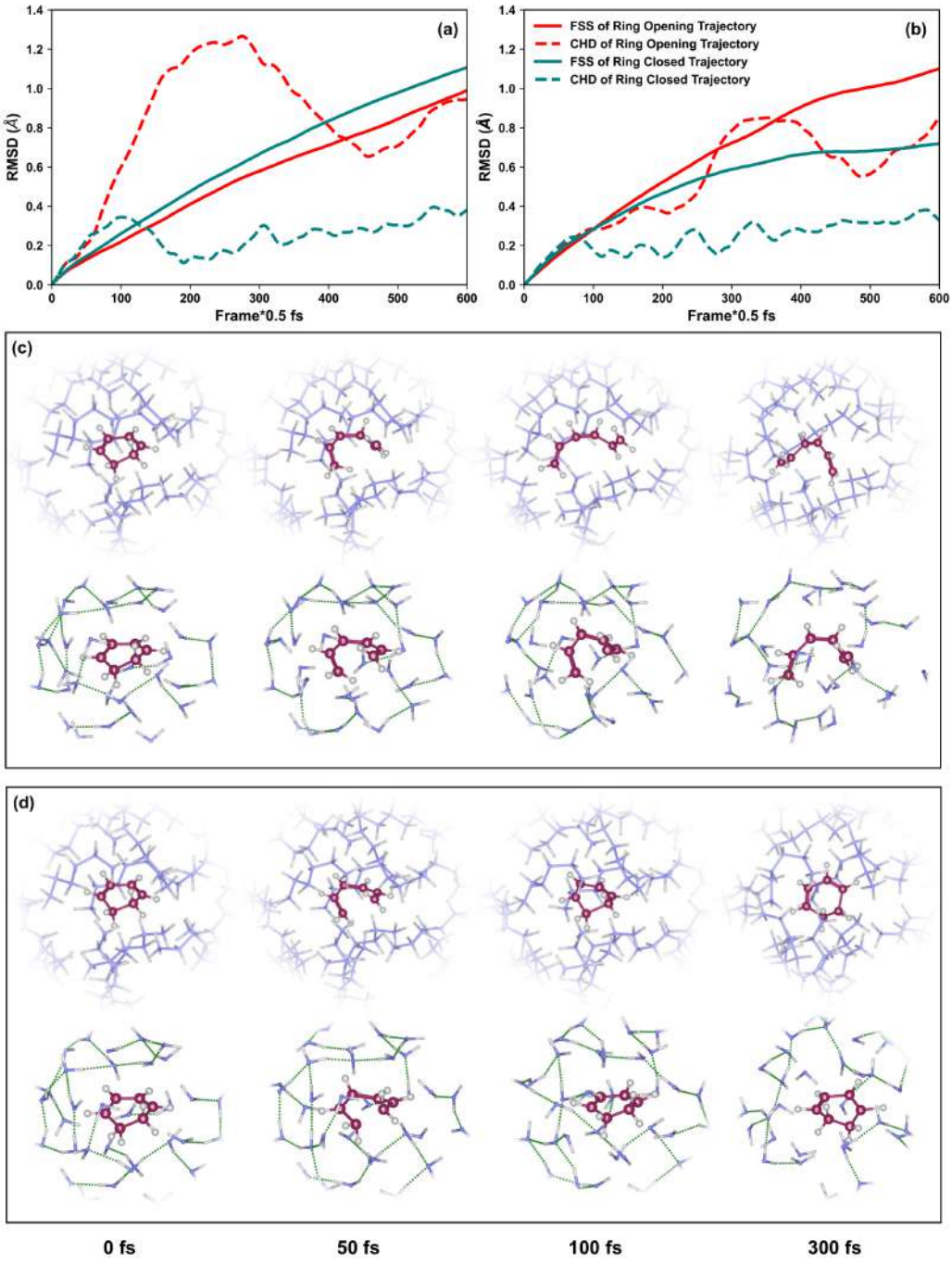


**Figure 4.7.** RMSD curves of CHD and first solvation sphere (FSS) for ring opening and ring-closed typical trajectories for (a) n-hexane and (b) water-solvated media. (c) Ring-opening (upper row: n-hexane, lower row: water) and (d) ring-closed (upper row: n-hexane, lower row: water) typical trajectory snapshots at 0 fs, 50 fs, 100 fs, and 300 fs. The green colored dotted lines represent the intermolecular hydrogen bonding in the FSS of water.

value of 85 fs for n-hexane and 70 fs for water medium. While analyzing the $t_b$ and $t_f$ values, we observed an interesting behavior in the dynamics. In the n-hexane medium, 13 trajectories showed bond breaking but did not lead to product formation. In contrast, in the water medium, this number was only 2. The delayed bond-breaking, slower product formation, and reduced

QY observed in the n-hexane-solvated system can be largely attributed to its inability to stabilize the potential energy surfaces that favor the ring-opening reaction as effectively as in the water-solvated system. Moreover, the higher frictional environment in water suppresses non-productive nuclear motions more efficiently than hexane, promoting the ring-opening process.

To observe the behavior of solvent molecules around the solute CHD molecule, we performed a first solvation sphere (FSS) movement analysis in both solvent systems. The FSS was determined using the radial pair distribution function, g(r), curve. The g(r) curves for both solvents were constructed from the MD thermalized trajectories and are presented in **Figure 4.6**. According to the position of the first minimum in the g(r) curve, the FSS was defined within a radius of 4.05 Å for water and 5.65 Å for n-hexane. All molecules within or partially within the specified distance were included in the analysis. To study this phenomenon, we selected one representative typical trajectory, each that leads to ring opening and one that does not for CHD solvated in both solvents. **Figure 4.6**c and **Figure 4.6**d (PDB with FSS), shows the PDB structures of the systems with selected FSS clusters. These structures correspond to the initial geometry “p1" used in surface hopping simulations. For “p1" initial geometry of both the solvated systems, the ensemble-averaged evolutions of the RMSD distribution, $C_1$–$C_6$ bond length, dihedral angle, and adiabatic populations of surface hopping simulations are shown in Appendix B **Figure B.6** and **Figure B.7**.

**Figure 4.7** shows the RMSD plots for the FSS and the CHD molecule in the solvated media: n-hexane (**Figure 4.7**a) and water (**Figure 4.7**b). Additionally, the snapshots of the ring-opening and ring-closed trajectories are shown in **Figure 4.7**c-d. From **Figure 4.7**a-b, it is evident that in the case of the water-solvated medium, for the trajectory that does not undergo ring-opening, the RMSD of the FSS is lower compared to the RMSD values of the other three trajectories. However, in the n-hexane medium, the RMSD values follow a similar increasing trend throughout the dynamics, regardless of whether the trajectory leads to ring-opening. For the ring-opening process in water, the RMSD values for both the CHD molecule and the FSS cluster increase over time, indicating a strong influence of the ring-opening process on the solvent environment or vice versa. The FSS cluster in water is more rigid due to intermolecular hydrogen bonds, which helps it remain more stable. This stability allows stronger interactions with the $\pi$-cloud of CHD/HT molecule as the dynamics progress and ring-opening occurs. As a result, this interaction can help stabilize the energies of electronic states crucial for photochemical ring-opening reactions and enhance the decay of the excited state.

## 4.4 Conclusions

In this work, we have explored the effect of polar (water) and non-polar (n-hexane) solvents on the photochemical ring-opening dynamics of the CHD molecule. We have employed a combination of electronic structure theory, classical MD simulations, and QM/MM non-adiabatic surface hopping simulations to reach a conclusive understanding of the photochemical processes. By performing classical MD simulations, we gathered a few initial geometries for excited-state dynamics. The initial velocities were generated by applying an average kinetic energy to the systems at room temperature. The fairness of the classically collected geometries was validated by performing excitation energy calculations at the SA-3-CASSCF(6,4) and SA-3-XMS-CAS(6,6)PT2 levels of theory with the cc-pVDZ basis set.

Our non-adiabatic surface hopping MD simulations at the QM/MM level reveal a strong dependence of the nature of the solvent on the photochemical ring-opening dynamics of CHD to give HT molecule. We obtained faster and more efficient ring-opening dynamics in the polar (water), supported by the excited-state population, bond length evolution, and potential energy profiles. This observation is backed by the fact that we found a higher QY (61 % in water vs. 53 % in n-hexane), faster bond breaking, and quicker product formation. Furthermore, due to significant solvent to solute $\pi$-cloud interactions, the electronic states in the water get more stabilized, which in turn lowers the energy barriers and can suppress non-productive nuclear motions. The analysis of solvation shell dynamics was also performed to gain more information on how the solvent affects the ring-opening process or vice versa. We found that, for a ring-opening trajectory in water, the first solvation sphere fluctuates more than in a trajectory where ring-opening does not occur, while in n-hexane, the solvent appears to be unaffected by the ring-opening process. These findings suggest that solvent polarity and the frictional environment significantly influence the photochemical reaction pathway of CHD. Therefore, our study highlights how the solvent environment plays a critical role in directing the excited-state dynamics and can be rationally used to control photochemical reactivity in solution. By exploring the detailed insights into solvent-induced effects on photochemical reaction pathways in CHD molecule, our findings can significantly influence future developments in areas such as molecular electronics, photopharmacology, and solar energy conversion, thereby contributing to broader advances in photochemical and materials science research.

# Chapter 5

# Photochemistry and Functionality in a Fulgide Molecule with Hexatriene Core

This work was published as an article in

The Journal of Chemical Physics

J. Chem. Phys. **160**, 154308 (2024)

## 5.1 Introduction

Photochromism, a fascinating phenomenon, encompasses a reversible transformation between two isomers.[101,290,291] This intriguing process occurs under the influence of photoirradiation at distinct wavelengths.[292] Among the pantheon of organic photochromic systems, fulgides[101,293] emerge as versatile photochromic compounds ideally suited for applications in optical data storage media[294,295] and as molecular functional units, notably in optical switches.[296,297] Fulgides are prominent compounds, showcasing its photochromic prowess in solutions and solid-state environments.[298,299] As depicted in **Figure 5.1**, photochromism involves the conversion of the E isomer into the closed C isomer, alongside the transformation to the Z form through specific UV irradiation processes.[300]

The core photochromic features of these molecules are based on pericyclic ring-closure and ring-opening reactions of the hexatriene/cyclohexadiene motif (**Figure 5.1**).[50,200] This interconversion between the closed and open forms is mainly governed by one photon excitation to

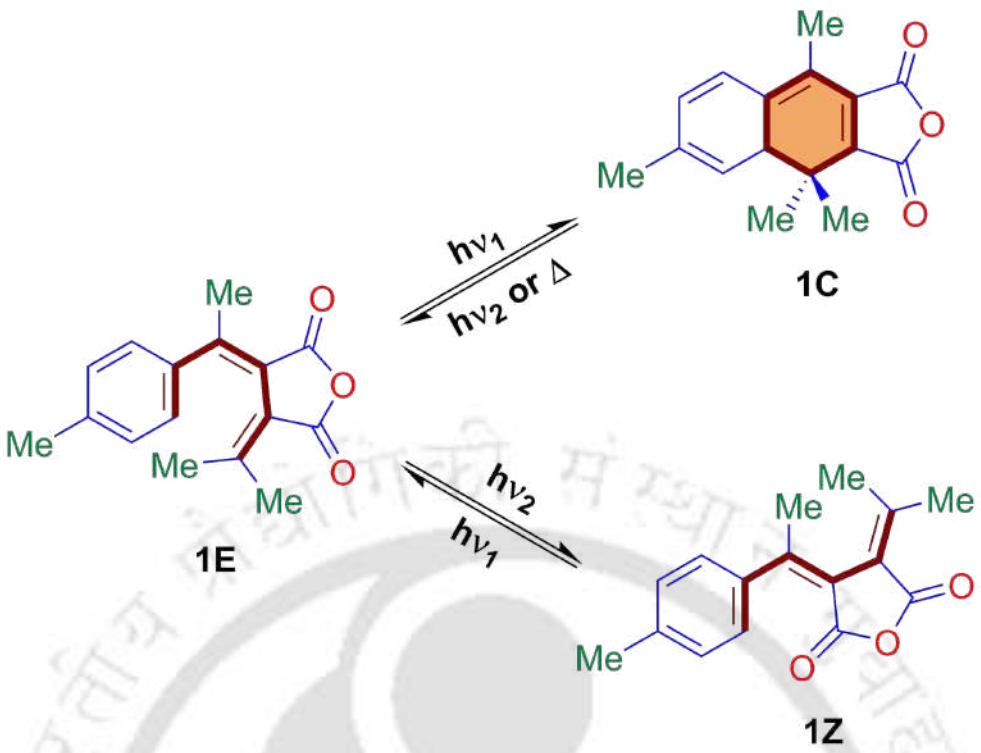


**Figure 5.1.** Photochromism of (E)-*p*-methylacetophenylisopropylidenesuccinic anhydride (1E) studied in this work.[300]

the bright first excited electronic state.[199,203] Nonetheless, there exists a distinction in the character of the first excited reactive state, $S_1$, between cyclohexadiene and molecules associated with fulgide. The former manifests covalent character, while the latter exhibits an ionic nature.[301] Furthermore, the position of the conical intersection between the first excited state and the ground state in the reaction profile wields significant influence over the decay process and/or fluorescence phenomena.[301,302] Recently, there has been a significant evolution in the investigation of the photochemistry of organoboron compounds.[303–306] Researchers have extensively explored these reactions using both density functional theory (DFT) and wavefunction-based approaches, such as the complete active space self-consistent field (CASSCF)[80,224] and its second-order perturbation (CASPT2)[149,220] method. This development not only advances the insight into excited-state dynamics in various organoboron systems but also broadens our understanding of the pivotal role played by conical intersections in photochemical processes. Numerous experimental and theoretical reports are there where the dynamics of ring-closure and ring-opening processes are studied to unveil the intricate photochemical behavior in fulgide related molecular systems and the ring-closure time scale and quantum yields were reported.[307–312] However, the photochromism phenomena have not yet been completely explored, which is cru-

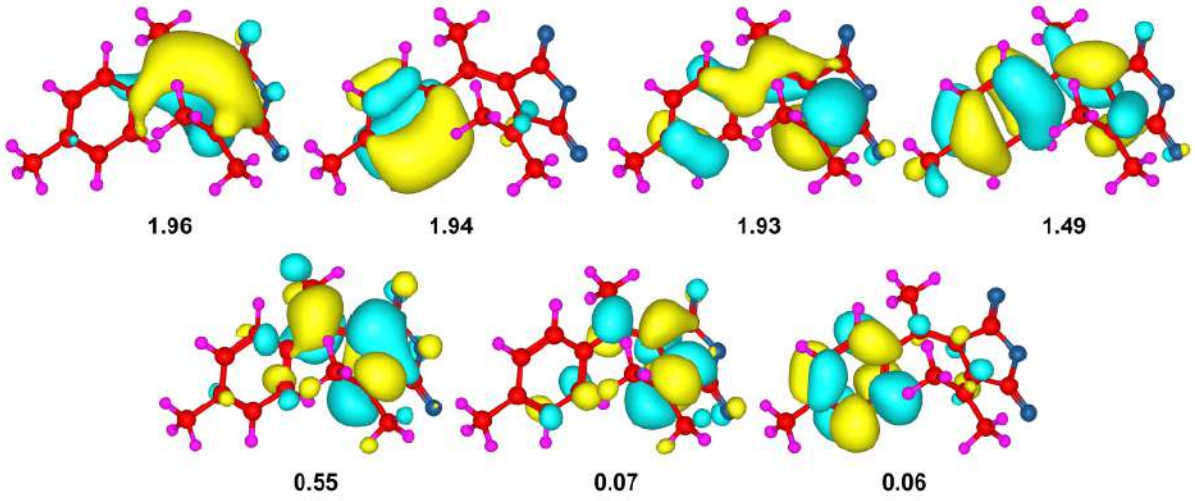


**Figure 5.2.** Active molecular orbitals of 1E molecule taken within the active space of SA-2-CASSCF(8,7)/cc-pVDZ calculations along with the electron occupation number.

cial for designing new efficient novel fulgide-based molecules for optoelectronic materials.

While UV/visible experiments provide valuable insights, they fall short of elucidating intricate molecular reaction mechanisms. To bridge this gap, time-resolved spectroscopy in the mid-IR domain, a complementary tool for examining structural and vibrational dynamics hold promise. Notably, Braun and colleagues pioneered time-resolved IR-probe experiments on indolylfulgimides within ground states, promising a deeper understanding of these molecular reactions.[313–315] Moreover, when examining the structural arrangement of fulgide, one might anticipate a reaction mechanism akin to that of indolylfulgimides. Nevertheless, the inclusion of diverse heteroaromatic rings can exert a notable impact on factors such as reactivity, quantum yields, and, consequently, the behavior of photochromism.

Photoinduced conformational changes of the photochromic molecules lead to orbital swapping between HOMO and LUMO, resulting in significant conduction switching when placed between metallic electrodes[316]. Fulgides, a class of organic molecular switches, hold significant prominence within the realm of thermally irreversible photochromic optical switches. These switches exhibit remarkable photostability and immense potential in diverse applications such as optical memory devices, fluorescence modulation and electron/energy transfer, enzyme activity, etc[101,111,317]. Hence, it is essential to understand the behavior of photoinduced single molecular isomers when it is connected to a metal surface to introduce and develop a molecular optical switch[318].

Therefore, in this work, we have considered a newly synthesized fulgide molecule, (E)-*p*-

methylacetophenylis-opropylidenesuccinic anhydride (1E),[300] to explore the ring closure photochemical dynamics using computational tools. Employing density functional theory (DFT) we have optimized ground state geometries and validated against experimental crystal data. Employing multireference methods, we probed the dynamics of the excited state, scrutinizing the conical intersection between the first excited state and the ground electronic state, especially along the ring-closing pathway. Our investigation further encompassed calculations for vertical excitation energies (VEE), charge transfer dynamics, and geodesic interpolation. Non-adiabatic dynamics[165] is employed to unveil the intricate photochemical processes and transitions between electronic states. The electrocyclic ring closure or opening of the fulgide derivatives stimulated via irradiation with UV/visible light can act as an on/off switching entities. Therefore, to address the nature of conduction shifting between the two isomers, we have investigated the current-voltage (I-V) characterization plot using non-equilibrium Green's functions formalism combined with DFT (NEGF-DFT)[319,320].

## 5.2 Computational Details

Ground state molecular geometries of 1E and 1C are initially optimized using DFT by utilization of the functional $\omega$B97xD[321] with the cc-pVDZ basis set. To confirm about the minima, we have performed frequency analysis at the same level of theory. We did not observe any imaginary frequency for the optimized geometries, which confirms the geometries to be at a true minimum. VEE calculations were performed using time-dependent density functional theory (TDDFT) with various DFT functionals: B3LYP[322,323], CAM-B3LYP[324], M06-2X[325], PBE0[326] and $\omega$B97xD[321] in conjunction with the cc-pVDZ basis set. We have also carried out the VEE calculations using domain-based local pair natural orbital similarity transformation based equation of motion coupled cluster singles and doubles (DLPNO-STEOM-CCSD)[327] approach with the def2-TZVP basis set.

To study non-adiabatic effects in the photochromism process, a multireference approach was employed. The investigation utilized the CASSCF approach using a state-average (SA-CASSCF)[225,226] procedure of the lowest two electronic states with an active space of 8 electrons in 7 orbitals, i.e. SA-2-CASSCF(8,7). The active molecular orbitals considered within the active space (8,7) is shown in **Figure 5.2**. The minimum of the first excited state ($S_1$) and the minimum energy conical intersection (MECI) was then optimized at the SA-2-CASSCF(8,7)

level of theory. Transition state structure in the conrotatory ring closing pathway (TSC: transition state conrotatory) is optimized and intrinsic reaction coordinate (IRC) pathway calculation is carried out using the CASSCF(8,7) level of theory. For a comprehensive characterization of electronic transitions, natural transition orbitals (NTOs) analyses were performed using B3LYP/cc-pVDZ and SA-2-CASSCF(8,7) levels of theory, visually capturing the nature of excitations. Charge transfer properties during electronic transitions were elucidated through Mulliken charge analysis at extended multistate complete active space second-order perturbation (XMS-CASPT2)[84] theory, SA-2-XMS-CAS(8,7)PT2, based on SA-2-CASSCF(8,7) calculated reference wavefunction. Geodesic interpolations[234] were investigated by connecting the reactant to the MECI molecule employed both SA-2-CASSCF(8,7) and SA-2-XMS-CAS(8,7)PT2 approaches. Additionally, interpolation between the reactant and the product was established using the SA-2-CASSCF approach with two different active spaces: (8,7) and (4,3). The XMS-CASPT2 calculations were carried out using a level shift parameter of 0.2 $E_h$. The exploration of electronic state structure involved topography analysis at the SA-2-CASSCF(8,7) level of theory, providing a thorough understanding of the electronic states landscape and its influence on photochemical processes. For performing all the multireference calculations cc-pVDZ basis set is employed. We conducted all DFT calculations and optimized the TSC using the GAUSSIAN[233] software package. The DLPNO-STEOM-CCSD calculation was performed using the ORCA[328] software, while the multireference calculations utilized the BAGEL[152,153] and OpenMolcas[150] software.

Geometry optimization and single-point energy calculations at the geodesic interpolated points are carried out using the BAGEL software[152,153] package. As already mentioned, the multireference calculations were executed using the cc-pVDZ basis set. Consequently, when utilizing the BAGEL software[152,153] for electronic structure and non-adiabatic dynamics calculations, we employed the corresponding density-fitting (DF) basis set: cc-pVDZ-JKFit. We utilized the OpenMolcas[150] software to conduct Wavefunction analysis and Mulliken Charge analysis at the XMS-CASPT2 level of theory. Additionally, this software facilitated the extraction of oscillator strength for vertical excitations and Natural Transition Orbitals (NTOs) analysis through its RASSI module.

Non-adiabatic surface hopping molecular dynamics simulations were performed to gain deeper insights into the dynamic behavior of the considered system. We followed the surface hopping approach developed by Tully[165] and utilized the Newton-X[177,329] software interfaced

with the BAGEL [152,153] software package. A total of 50 initial coordinates were prepared based on the normal modes calculated at the SA-2-CASSCF(8,7)/cc-pVDZ level of theory. These initial conditions were generated by employing the Wigner distribution model related to the harmonic oscillator using the default initial temperature of 0 K, which corresponds to the zero-point energy (ZPE). [236,330] Conducting non-adiabatic dynamics simulations using the Andersen thermostat [331], we investigated the evolution of both ground ($S_0$) and excited electronic ($S_1$) states for all 50 trajectories. Decoherence correction was handled using a default $\alpha$ value of 0.1 $E_h$. [167,237] We initiated all the trajectories from the first excited state, $S_1$, using a classical time step of 0.2 fs and a quantum step of 0.01 fs. The trajectories were initially simulated for 200 fs, following which an extension to 300 fs was implemented to facilitate a thorough observation of dynamic behavior. For the calculation of energies, gradients, and non-adiabatic coupling vectors involved in the two electronic states, an on-the-fly approach was employed using the SA-2-CASSCF(4,3)/cc-pVDZ level of theory.

The electron transport calculations were performed using the TranSiesta software package [332] within the framework of NEGF-DFT. [320] The nonlocal norm-conserving Troullier-Martins pseudopotentials [333] and single-$\zeta$ polarized (SZP) basis set were used to treat the core and valence electrons, respectively. The energy convergence standard for self-consistent calculations is $10^{-4}$, while the cutoff energy is 300 Ry with the general gradient approximation (GGA)-Perdew-Burke-Ernzerhof (PBE) [334]exchange-correlation functional. The Brillouin zone was sampled with $1 \times 1 \times 100$ Monkhorst-Pack k-point [335]. The current flow through the device by applying a specific external voltage (V) is determined by Landauer-Buttiker formulism, using equation 5.1 [336].

$$I(V_b) = \frac{2e^2}{h} \int_{\mu_L}^{\mu_R} T(E,V_b)[f(E-\mu_L) - f(E-\mu_R)]dE \tag{5.1}$$

Here, $\frac{2e^2}{h}$ is quantum conductance and $\mu_L/\mu_R$ is the electrochemical potential of the left/right electrode. The transmission coefficient at bias voltage V is denoted as T(E,V). The term refers to the overall probability of electrons with energy E flowing between the electrodes across the device. This can be defined as

$$T(E,V) = T_r[\Gamma_L(E)G^R(E)\Gamma_R(E)G^A(E)] \tag{5.2}$$

The functions $G^R(E)$ and $G^A(E)$ denote retarded and advanced Green's function of the scatter-

ing region. $\Gamma_{L/R}$(E) represents the coupling between the scattering region and the left (right) electrode[337]. Furthermore, Inelastic code[338] has been used to perform calculations of molecular projected self-consistent Hamiltonian (MPSH) eigenstates.

## 5.3 Results and Discussion

### 5.3.1 Optimization of the Molecular Structures: Ground State, Excited State, MECI, and TSC

At first, the ground state minimum energy geometries of 1E and 1C were investigated using DFT based $\omega$B97xD functional with the cc-pVDZ basis set. **Figure 5.3**a illustrates the notation used for bond length and dihedral angle parameters, while **Figure 5.3**(b,c) displays the ground state minimum energy geometries with the $r_{EC}$ bond length parameters. We have also compared the optimized geometry 1E with the experimentally reported crystal data[300] by superimposing them as shown in **Figure 5.3**d. The root-mean-square deviation (RMSD) value is reasonably small, indicating a satisfactory optimization procedure. Further, the important dihedral angle parameters are reported in **Table 5.1**.

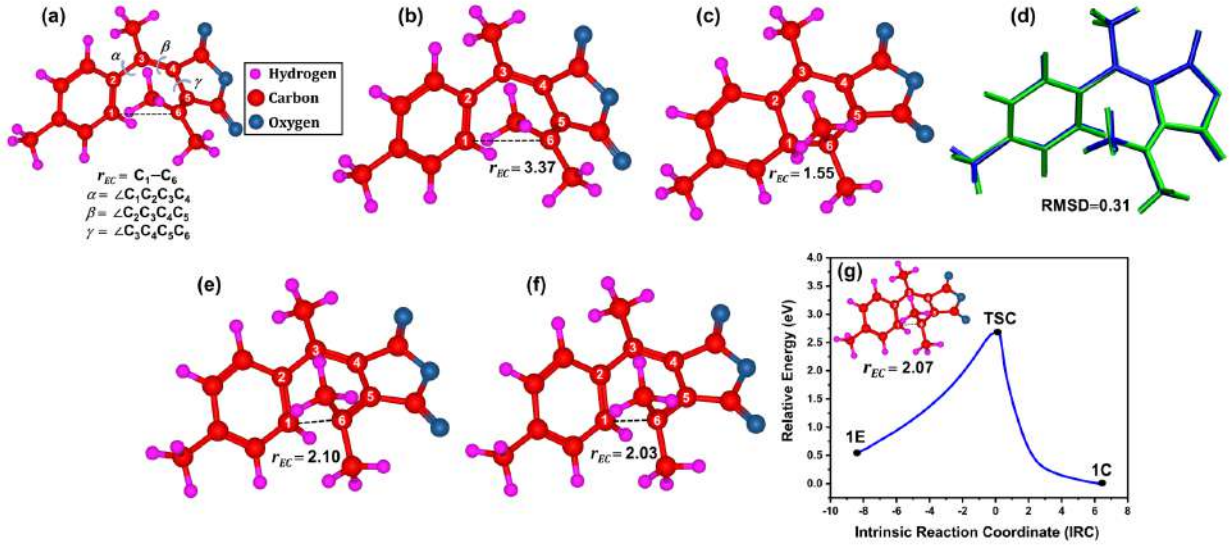


**Figure 5.3.** (a) Bond length and dihedral angle notation used throughout the work, (b) optimized 1E-$S_0$ at the $\omega$B97xD, (c) optimized 1C-$S_0$ at the $\omega$B97xD, (d) superimposed structures of DFT optimized (Green) and crystal structure[300] (Blue) (e) optimized $S_1$-min at the SA-2-CASSCF(8,7), (f) optimized $S_1/S_0$ MECI at SA-2-CASSCF(8,7), (g) optimized TSC at the CASSCF(8,7) along with the IRC pathway. Calculations are performed with the cc-pVDZ basis set.

**Table 5.1.** Dihedral angle parameters of optimized geometries.

| | Level of Theory[a] | $\alpha$ (°) | $\beta$ (°) | $\gamma$ (°) |
|---|---|---|---|---|
| 1E-$S_0$ | $\omega$B97xD | -49.69 | -5.14 | -43.58 |
| $S_1$-min | SA-2-CASSCF(8,7) | -32.08 | -4.57 | -11.42 |
| $S_1$/$S_0$ MECI | SA-2-CASSCF(8,7) | -38.85 | 0.98 | -15.01 |
| TSC | CASSCF(8,7) | -35.45 | -2.11 | -10.04 |
| 1C-$S_0$ | $\omega$B97xD | -8.17 | -11.95 | -1.09 |

[a]Using cc-pVDZ basis set.

**Table 5.2.** Vertical excitation energy (VEE) to the $S_1$ state of 1E with oscillator strength.

| Method | VEE (eV) | Oscillator strength |
|---|---|---|
| B3LYP/cc-pVDZ | 3.84 | 0.21 |
| CAM-B3LYP/cc-pVDZ | 4.24 | 0.26 |
| M06-2X/cc-pVDZ | 4.23 | 0.24 |
| PBE0/cc-pVDZ | 3.94 | 0.22 |
| $\omega$B97xD/cc-pVDZ | 4.23 | 0.26 |
| SA-2-CASSCF(8,7)/cc-pVDZ | 5.70 | 0.33 |
| SA-2-XMS-CAS(8,7)PT2/cc-pVDZ | 4.60 | 0.23 |
| DLPNO-STEOM-CCSD/def2-TZVP | 4.08 | 0.27 |
| Experimental[300] | 3.39 | – |

**Figure 5.3**(e,f) shows the optimized minimum energy structure in the excited state, $S_1$, of the molecule 1E and MECI geometry along with the $r_{EC}$ bond length parameters both optimized at SA-2-CASSCF(8,7)/cc-pVDZ level of theory. The $r_{EC}$ bond length of the $S_1$-minima is found to be less than that of the ground state optimized geometry of the reactant (1E) and larger than the MECI geometry. This indicates the presence of the $S_1$-minimum before the conical intersection as we go from the reactant side in the direction of the ring closing pathway. We have also located the conrotatory transition state, TSC, connecting the open reactant (1E) and closed reactant (1C) in the ground electronic state ($S_0$) using the CASSCF(8,7)/cc-pVDZ level of theory and is shown in **Figure 5.3**g. Further, this transition state geometry is employed to investigate the intrinsic reaction coordinate (IRC) pathway involved in the ground state reaction. The calculated IRC pathway is shown in **Figure 5.3**g.

### 5.3.2 Vertical Excitation to the First Excited State

**Table. 5.2** shows the calculated VEE to the first excited state, $S_1$. Upon comparison of the DFT and wavefunction level calculated gas phase VEE, they were found to be considerably higher than the solid-state experimental value.[300] The surrounding environment, whether gas, liquid, or solid, of a molecular system, can alter the intramolecular charge transfer (ICT) process and

absorption properties. Particularly in solid-state, the intermolecular interactions that occur during the packing of molecules significantly influence the ICT.[339] Therefore, we considered the calculations of the VEE to the $S_1$ state using a sufficiently higher level of theory DLPNO-STEOM-CCSD/def2-TZVP to perform a meaningful comparison. Given that CASSCF is recognized for its tendency to overestimate VEE, our results showed a slightly elevated VEE for the $S_1$ state if compared to the DLPNO-STEOM-CCSD/def2-TZVP level of theory, even with the application of the CASPT2 approach. Further, we have performed the hole-particle analysis of the excitation to the $S_1$ state by employing NTOs calculations at the B3LYP/cc-pVDZ and SA-2-CASSCF(8,7)/cc-pVDZ levels of theory. In **Figure 5.4**a, we have shown the NTOs

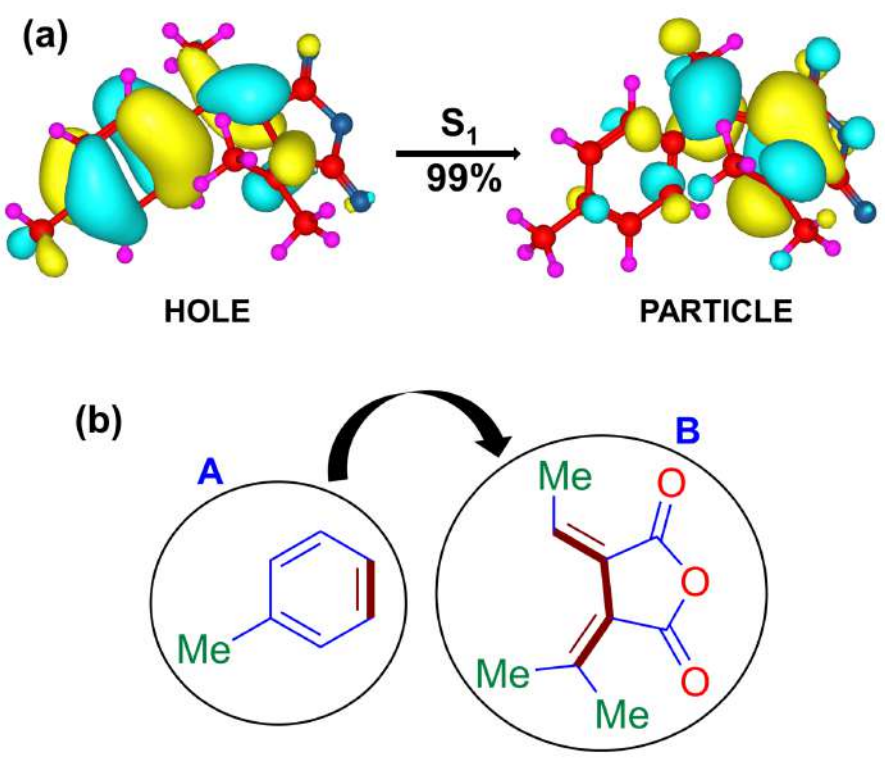


**Figure 5.4.** (a) NTOs calculated at the SA-2- CASSCF(8,7)/cc-pVDZ level of theory and (b) fragmentation representation of our considered molecular system for charge transfer analysis.

calculated at the SA-2-CASSCF(8,7)/cc-pVDZ level of theory, the B3LYP/cc-pVDZ approach calculated NTOs are presented in the Appendix C **Figure C.1**. In both cases, the localization of hole and particle is mostly found on toluene and anhydride parts, respectively.

We have also analysed the charge transfer from the toluene part (part A) to the anhydride part (part B) due to photoexcitation to the first excited state $S_1$ (**Figure 5.4**b). For that purpose, we have performed a Mulliken charge analysis of the molecule at the SA-2-XMS-CAS(8,7)PT2/cc-pVDZ level of theory during the excitation process. **Table 5.3** shows the charge analysis, dipole

**Table 5.3.** Wavefunction analysis and Mulliken charge investigation during the excitation to $S_1$ at the SA-2-XMS-CAS(8,7)PT2/cc-pVDZ level of theory. u and d represent up spin and down spin, respectively.

| Species | Electronic States | Wavefunction configuration | Dipole moment | A (**Figure 5.4**b) | B (**Figure 5.4**b) |
|---|---|---|---|---|---|
| 1E | $S_0$ | 2222000 (0.898) | 6.31 | -0.078 | 0.078 |
| | $S_1$ | 222ud00 (0.900) | 15.43 | 0.506 | -0.506 |
| 1C | $S_0$ | 2220200 (0.815) | 5.33 | 0.039 | -0.039 |
| | $S_1$ | 222ud00 (0.826) | 12.51 | 0.259 | -0.259 |

moment, and wavefunction analysis during excitation. We observed a significant difference in charge and dipole moment associated with the excitation to the $S_1$ state of the optimized reactant (1E) and product (1C) geometry which was also observed in similar compound, as reported earlier.[301,302]

### 5.3.3 Conical Intersection Topography and Reaction Energy Profile Diagram

The topography around the conical intersection involved in the photochromism of the 1E molecule is constructed to get a qualitative idea about photochemical behavior. Two types of topographies are associated with a conical intersection: sloped or peaked. These configurations of a conical intersection are very helpful in describing the behavior of electronic states around the conical intersection and efficiency of photochemical product formation. As described by Yarkony[242] and Atchity *et al.*[340], the sloped topography can lead to a slow rate of internal conversion and peaked topography defines the conical intersection to be a funnel that can result in a high rate of internal conversion process. In our case, we performed topography analysis as implemented in the Columbus software package.[235,241–243] We have observed that the conical intersection is a characteristic of a significantly sloped shape (**Figure 5.5**a). Therefore, we conclude that the internal conversion through the conical intersection would be slow. The topographical parameters are reported in the **Table C.1** of the Appendix C.

All the optimized geometries at DFT, CASSCF, and SA-2-CASSCF levels of theory are subjected to the single point energy correction to at the SA-2-XMS-CAS(8,7)PT2/cc-pVDZ level of theory. This single point energy correction is performed to include the dynamical electron correlation effect in their energies. The corrected energies are reported in the **Table C.2** of the Appendix C. Even though the XMS-CASPT2 level of theory predicts the $S_1$ VEE energy to be higher, to get a qualitative reaction pathway, we can consider this method,

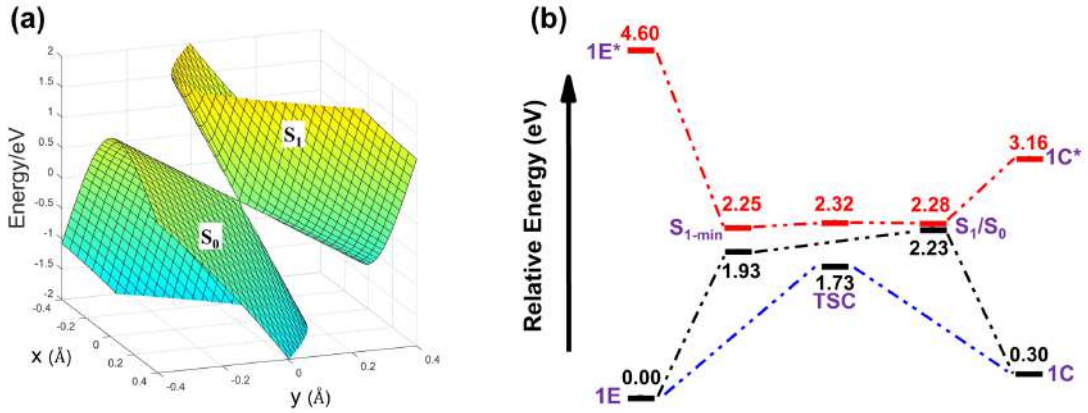


**Figure 5.5.** (a) $S_1/S_0$ MECI topography calculated at the SA-2-CASSCF(8,7)/cc-pVDZ level of theory and (b) energy profile diagram calculated at the SA-2-XMS-CAS(8,7)PT2/cc-pVDZ level of theory.

as the CASPT2 approach is well-known to produce the excited states with the correct order. **Figure 5.5**b shows the calculated energy profile diagram for considered molecular system. The reactive chemical species are placed in the decreasing order of the $r_{EC}$ bond length parameter as we are considering the ring-closing process. As we go from the open form (1E) to the ring closing side, $S_1$-minima exists before the $S_1/S_0$ MECI. Further, the position of the metastable species in a reaction pathway can decide the reactivity, product formation, etc.[301,302] Therefore, there is a possibility of the wavepacket to return to the ground state of the reactant by deactivating through the radiative phenomena: fluorescence. However, if we consider the case of the reverse reaction, i.e., from closed form (1C) to the open form (1E), it will be much easier for the wavepacket to get transferred from the excited electronic state to the ground electronic state through the conical intersection, and as a result, we may get a higher quantum yield of formation of the open form (1E).

### 5.3.4 Geodesic Interpolation

We have calculated the geodesic interpolation connecting the ground state minimum energy configuration of 1E to the $S_1/S_0$ MECI. We have performed these calculations using SA-2-CASSCF(8,7) and SA-2-XMS-CAS(8,7)PT2 levels of theory, and are shown in **Figure 5.6**a. The behavior of electronic state energies is found to be similar, even though the SA-2-CASSCF(8,7) highly overestimates the energies of the two electronic states. Further, the SA-2-CASSCF(8,7) and SA-2-XMS-CAS(8,7)PT2 levels of theory calculated interpolation shows the crossing at the optimized $S_1/S_0$ MECI structure.

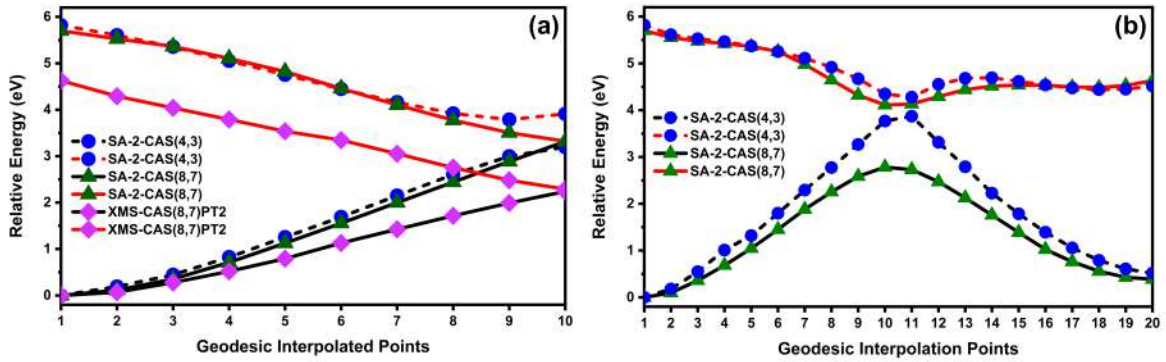


**Figure 5.6.** Geodesic interpolation calculated between (a) 1E-$S_0$ and $S_1/S_0$ MECI [at SA-2-CASSCF(4,3), SA-2-CASSCF(8,7), and XMS-CAS(8,7)PT2 approach] and (b) 1E-$S_0$ and 1C-$S_0$ [at SA-2-CASSCF(4,3) and SA-2-CASSCF(8,7) approach]. Calculations are performed using the cc-pVDZ basis set.

Additionally, **Figure 5.6**a also reports the interpolation calculation from 1E to the $S_1/S_0$ MECI using a smaller active space at the SA-2-CASSCF(4,3) level of theory. Choosing a more compact active space was driven by our intent to conduct non-adiabatic molecular dynamics simulations at a relatively less expensive computational method, taking into consideration the availability of computational resources. Upon comparing the interpolation pathways, the evolution patterns of both the electronic states ($S_0$ and $S_1$) were found to be similar across all considered levels of theories. Moreover, to assess the complete pathway from reactant (1E) to product (1C), interpolation calculations were performed using both SA-2-CASSCF(8,7) and SA-2-CASSCF(4,3) levels of theory as depicted in **Figure 5.6**b. Notably, the results indicate that SA-2-CASSCF(4,3) effectively represents the entire reaction pathway with an initial convergence starting from the reactant to the geometry having $r_{EC}$ bond length 2.12 Å with the smallest energy difference between the electronic states of 0.4 eV. We recently reported non-adiabatic dynamics simulations of 1,3-cyclohexadiene derivatives to observe substituent effects on excited state dynamics, where we compared the interpolation pathways between reactant and conical intersection geometries at different approaches and concluded about the electronic structure method for non-adiabatic dynamics.[244] Therefore, considering all the facts, we infer that the SA-2-CASSCF approach with the compact active space of (4,3) can effectively describe the electronic state behavior. Consequently, we proceeded with the SA-2-CASSCF(4,3)/cc-pVDZ level of theory for calculating energies, gradients, and non-adiabatic couplings during on-the-fly surface hopping molecular dynamics simulations.

### 5.3.5 Surface Hopping Molecular Dynamics Simulation

We have performed a surface hopping non-adiabatic molecular dynamics simulation of the open form (1E) to observe the photochemical ring closing dynamics. In **Figure C.2** of the Appendix C, the RMSD plots that characterize the geometrical variations during the simulations are provided. We have performed the ensemble-averaged analysis of the molecular dynamics simulation data to study the electronic state transformation, excited state relaxation,

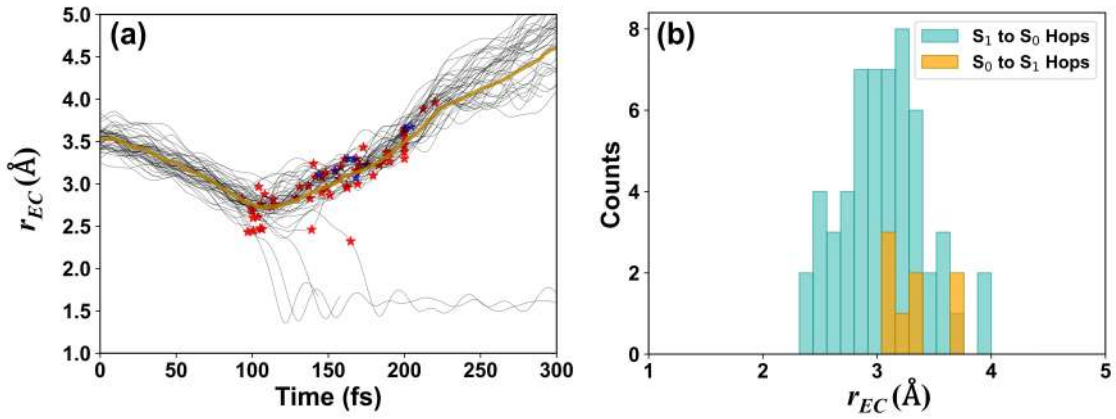


**Figure 5.7.** (a) Time evolution of $r_{EC}$ bond length of all trajectories (★:$S_1 \rightarrow S_0$,★:$S_0 \rightarrow S_1$, Golden line represents the average $r_{EC}$ value) and (b) $r_{EC}$ bond length distribution during the dynamics.

photoproduct formation, etc. In **Figure 5.7**a, the time evolution of $r_{EC}$ bond length is shown for all the trajectories considered for our dynamics simulation, along with hopping types. The dihedral angle fluctuation is presented in **Figure C.3** of the Appendix C. We have seen that most of the hoppings were taking place within the range of ∼90 fs to ∼220 fs. Further, **Figure 5.7**b shows the $r_{EC}$ bond length distribution at the $S_1 \leftrightarrow S_0$ hopping. During $S_1 \rightarrow S_0$ transition, the $r_{EC}$ bond length is mainly concentrated within ∼2.5 Å to 4 Å. While there is a considerable number of $S_1 \rightarrow S_0$ hoppings were observed, a smaller number of $S_0 \rightarrow S_1$ hoppings were obtained and during this $S_0$ to $S_1$ transition the $r_{EC}$ bond length parameters were found to fall within ∼3 Å to 4 Å.

**Figure 5.8** shows a trajectory that involves the formation of photoproduct 1C during the dynamics simulation. Throughout the simulation, we plotted the $r_{EC}$ bond length variation along with the electronic state transformation (**Figure 5.8**a). As the simulation is initiated, the electronic state energies start to get converge to where the hopping takes place. Further, the $r_{EC}$ bond length parameter decreases from ∼3.5 Å to ∼1.5 Å within ∼ 125 fs and then oscillates

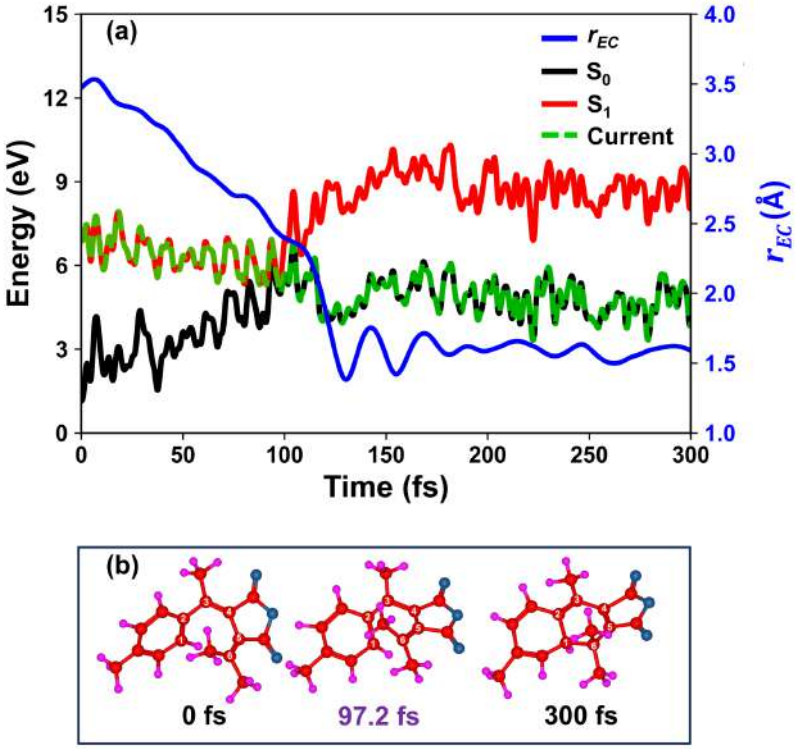


**Figure 5.8.** One trajectory showing the formation of 1C with (a) potential energy and $r_{EC}$ bond length evolution and (b) initial (0 fs), hopping (97.2 fs), and last (300 fs) snapshots of the molecule.

near 1.5 Å. We also showed the $\beta$ dihedral angle (**Figure C.4**a of the Appendix C) for the same trajectory. At the start of the simulation, the dihedral angle was ∼-5°, then it reached a dihedral angle of ∼-50°; after that, it again come to ∼-5°. Further, we have shown one trajectory that does not give the closed photoproduct 1C, rather it goes to the open form 1Z, in **Figure 5.9**. To observe the phenomena of 1Z formation, we can take the help of $\beta$ dihedral angle variation (**Figure 5.9**a). We can see that at the initial time of simulation, the dihedral angle parameter was near ∼-5°; however, with time, it starts to opens up and at the end of the simulation it reaches a value of ∼ -150°. As the simulation is initiated, the $r_{EC}$ bond starts (**Figure C.4**b of the Appendix C) to decrease to ∼ 2.5 Å within ∼ 85 fs, and then it starts to increase to a maximum value of ∼ 5 Å at the end the simulation.

Once we plotted the ensemble-averaged time evolution of electronic state energies along with the current electronic state energy (**Figure 5.10**a), we observed that the current state of the molecule remains significantly on the electronic excited state, $S_1$, for a considerable amount of time ∼100 fs and reaches the ground electronic state, $S_0$, at ∼160 fs. We have also analysed the ensemble-averaged adiabatic population transfer during the simulation, as shown in

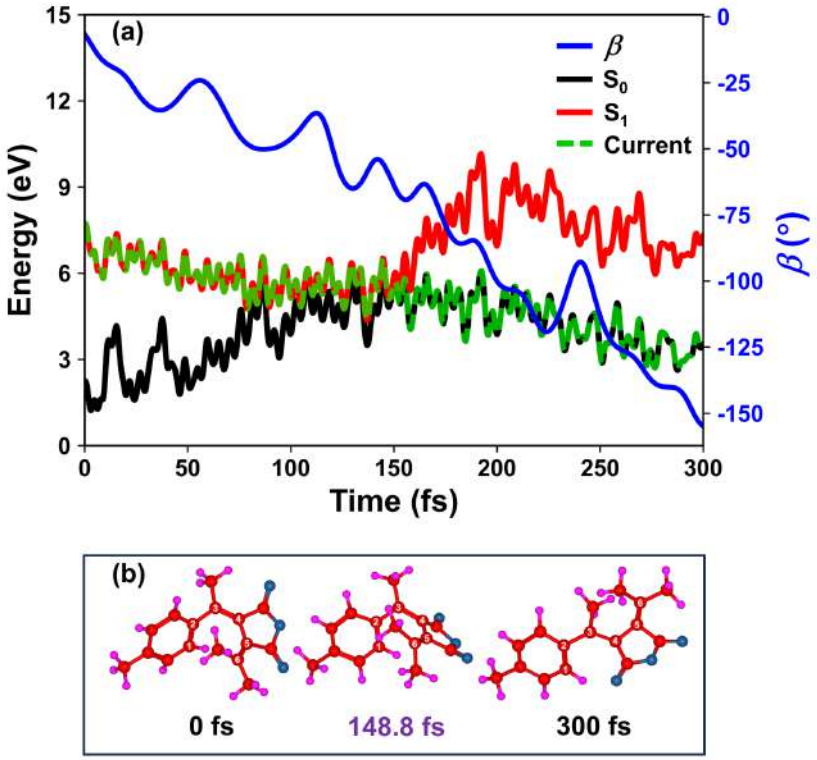


**Figure 5.9.** One trajectory showing the formation of 1Z with (a) potential energy and $\beta$ dihedral angle evolution and (b) initial (0 fs), hopping (148.8 fs), and last (300 fs) snapshots of the molecule.

**Figure 5.10**b. This population transformation for $S_1$ to $S_0$ is mostly occurs within a window of ∼130 fs, starting from ∼90 fs to the complete transfer at ∼220 fs. We have calculated the average time of reaching the bond formation limit, which can be correlated to the decay time of the excited state. As visible from the IRC pathway calculated at the CASSCF(8,7)/cc-pVDZ level of theory, once the highest energy limit is overcome from the open form (1E) side, the bond formation can take place in the ground electronic state. Therefore, considering the $r_{EC}$ bond length at the TSC structure as the bond formation limit, we have calculated the average time of reaching the bond formation limit ($t_{for}$) as shown below-

$$t_{for} = \frac{\text{Total time (fs)}}{\text{Number of trajectories}} \tag{5.3}$$

In our case, we found only 4 no. of trajectories that give us the photoproduct 1C and the total time required by the trajectories is 535.2 fs. Therefore, we observed a decay time of around ∼ 134 fs for excited state $S_1$. Further, the quantum yield of the formation of closed structure for our considered reaction is 8% (4 out of 50), aligning closely with the ∼10% quantum yield observed for the indolylfulgide molecule in acetonitrile medium reported elsewhere.[311] This

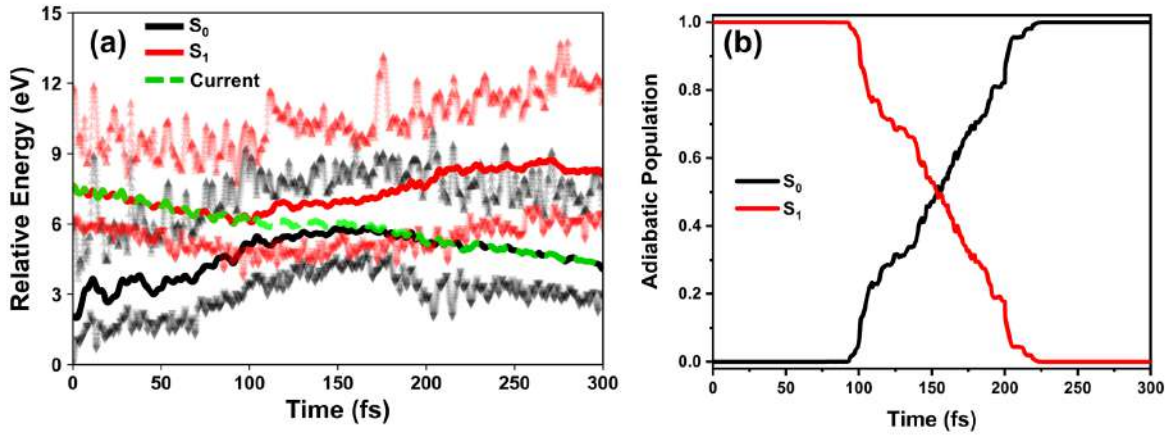


**Figure 5.10.** Ensemble-averaged, (a) potential energy evolution (upward triangle: maximum value, downward triangle: minimum value) and (b) adiabatic population during the dynamics.

smaller quantum yield of formation of closed isomers can be correlated to the existence of the $S_1$-min just after the Franck-Condon region and before the $S_1/S_0$ conical intersection and the sloped topography around the $S_1/S_0$ conical intersection.

### 5.3.6 Electron Transport Calculations

As the light-driven organic molecules are promising candidates for molecular electronics, we have built a device model wherein the molecules (both 1E and 1C isomers) are positioned between two parallel Au (111) electrodes, as shown in **Figure 5.11**[341,342]. Typically, electrodes made of noble metals, such as gold or platinum, are suitable as they have excellent ohmic contact properties[343]. Since the hydrogen atoms are unable to bind with metallic surfaces, sulfur

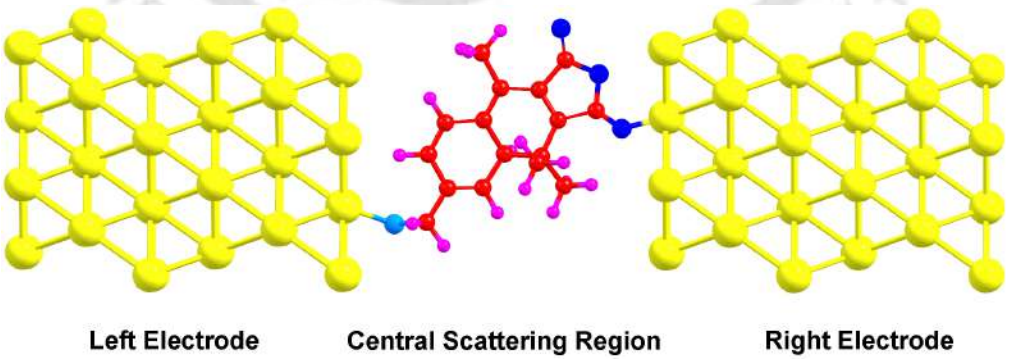


**Figure 5.11.** Schematic representation of the molecular device, where the 1C-isomer of the fulgide derivative is sandwich between Au (111) electrode. Yellow, blue, red, pink, and light blue balls denote gold, oxygen, carbon, hydrogen, and sulfur, atoms respectively.

atoms were used in their substitute[320], and the bridging distance was fixed at 1.95/2.05 Å between the metallic surface and O/S. The current-voltage (I-V) curves of the molecular device

with different isomers (1E and 1C) have been displayed in **Figure 5.12**a. With a 0.2 V step size, the current was measured across a range of bias voltages from 0 V to +2 V. The linear growth of current in both isomers with voltage suggests that the conduction mechanism is driven by ohmic behavior[344].**Figure 5.12**a clearly illustrates the switching behavior of the fulgide molecular system between its two forms (1E and 1C). The 1C-isomer exhibits greater current than the 1E-isomer across the whole bias range. Therefore, when the molecule in the device undergoes a transition from the 1E to 1C isomer due to photoexcitation, it is expected that the device will go from a state of low conductance (OFF) to high conductance (ON) and vice versa. The **Figure 5.12**a also shows the on-off ratio ($R = I_{1C}/I_{1E}$) as a function of bias. The highest switching yield was achieved at a bias of 0.2 V, with a maximum current ratio of approximately 17.6.

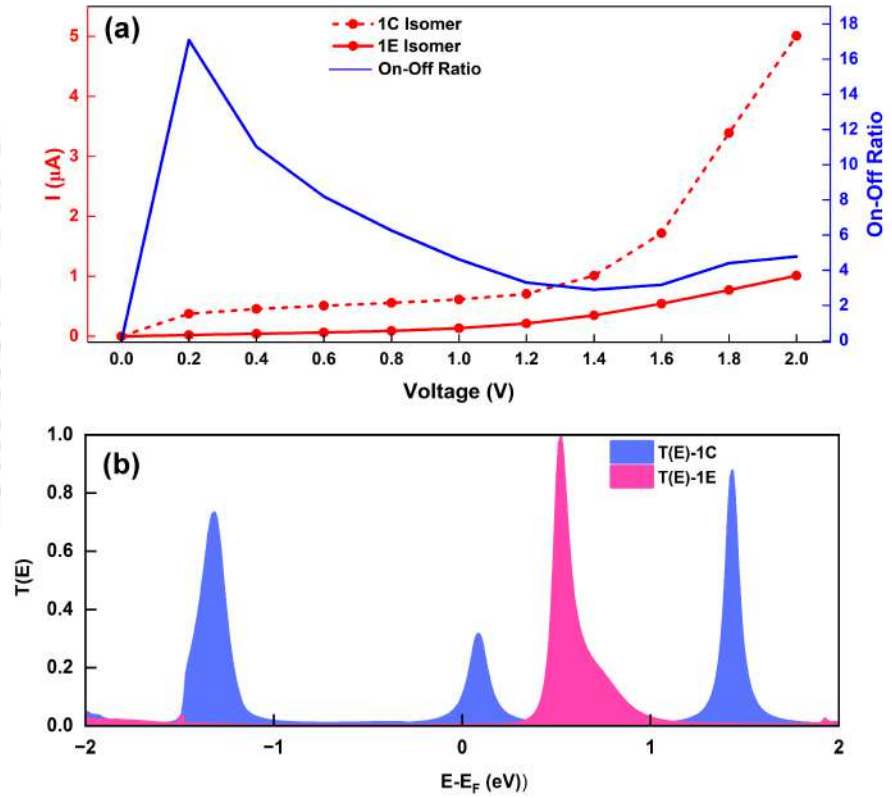


**Figure 5.12.** (a) The I–V characteristic of the molecular switch with two isomers (1E and 1C) along with the current on-off ratio. (b) Zero bias transmission spectra T(E) plot of 1E and 1C isomers.

The significant disparity in conductivity seen between these two isomers can be attributed to assessing the possibility of electron transmission[345]. **Figure 5.12**b illustrates stark differences in the transmission probability [T(E)] of both the 1E and 1C isomers. The T(E) spectra of the 1C-isomer show higher transmission around the Fermi level, which increases the conductance of the system[346]. To identify the contribution of the molecular orbitals (MOs) to the transmis-

sion, we have further calculated the molecular projected self-consistent Hamiltonian (MPSH) eigenstates by diagonalizing the scattering region Hamiltonian[347,348]. Only MPSH states of HOMO-LUMO orbitals maps are shown in **Figure C.5** of the Appendix C, along with the MO of the single molecule for comparison. The small delocalization of the 1E LUMO-MPSH states as compared to 1C-isomer leads to low transmission coefficients as depicted in **Figure 5.12**b[345]. In addition, the lower electron transmission probability of the 1E isomer can also be explained from their larger HOMO-LUMO gap of 3.24 eV (in the case of 1C-isomer, the HOMO-LUMO gap was found to be 1.73 eV)[349].

## 5.4 Conclusions

In conclusion, our computational study unravelled intricate details of the photochromic fulgide molecule (1E). We successfully optimized ground state geometries at the DFT level of theory, validated against experimental crystal data, and explored the $S_1$ minimum energy structure and MECI at the SA-2-CASSCF(8,7)/cc-pVDZ level of theory. The distinct $r_{EC}$ bond length parameters between the $S_1$-minima and the MECI geometry indicated the presence of the $S_1$-minima before the conical intersection, particularly along the ring-closing pathway. The calculated VEE showed a significant difference from the experimental one attributable to the solid-state environment of the experimental condition. Therefore, we compared our gas phase calculated data with a relatively higher DLPNO-STEOM-CCSD/def2-TZVP level of theory. Charge transfer dynamics during photoexcitation, analyzed through Mulliken charge and dipole moment assessments, revealed significant changes. Topography analysis at the conical intersection showcased a sloped configuration, impacting the internal conversion dynamics.

Geodesic interpolation and surface hopping molecular dynamics simulation provided a detailed view of the photochemical ring-closing dynamics. Trajectory analysis during surface hopping molecular dynamics simulation depicted the formation of closed isomer 1C and open isomer 1Z. Exploration of bond lengths, dihedral angles, and electronic state transformations across trajectories provided a comprehensive understanding of photochemical ring-closing dynamics. Notably, our results indicated a bond formation time or decay time of approximately 134 fs for the excited state $S_1$ and a quantum yield of around $\sim$8% for the formation of the closed structure (1C). The observed quantum yield aligns with similar systems reported in the literature. Further, the low transmission coefficient, localized HOMO and LUMOs, along with

the significantly large HOMO-LUMO gap, inferred that the 1E isomer exhibits lower conductivity compared to 1C-isomer. Overall, our study advances the comprehension of fulgide photochromism, shedding light on challenges and opportunities in the computational modelling of complex photochemical processes. Experimental validations inspired by our findings may pave the way for designing tailored photochromic molecules for applications in molecular switches and optoelectronic devices.

# Chapter 6

# Application and Comparison of Machine Learning Potentials in Studying Photochemistry of Cyclohexadiene

*This work will be communicated soon*

## 6.1 Introduction

Photochemistry plays a vital role in numerous scientific and technological applications, including energy generation,[350,351] functioning of molecular motors,[352,353] and the development of advanced materials such as organic LEDs and solar cells.[354–356] Understanding the behavior of molecules upon exposure to light, especially their dynamics in the excited state, is important for designing efficient photoreactive systems. Under a computational chemistry framework, these processes are studied using traditional quantum mechanical (QM) methods like time-dependent density functional theory (TD-DFT),[39,357,358] multireference approaches, such as complete active space self-consistent field (CASSCF),[79,244,247] and coupled-cluster approaches.[359] These theoretical approaches have proven to be the main tool for dissecting the detailed mechanistic insights into electronic states involved in a photochemical process.

However, these theoretical techniques often have a higher computational cost, limiting their applications to small systems or short timescales and restricting their usage in large-scale or long-duration simulations. The limitations of conventional QM techniques create a high demand for faster, yet reliable, alternatives. Machine learning (ML) models have emerged as a promising option, which can predict the molecular properties with near-QM accuracy at a fraction of the computational cost.[113,191,360] It has been successfully used in chemistry to predict properties

such as reaction pathways, excited-state energies, and atomic forces.[361–364]

When it comes to exploring photochemical and photophysical processes, the trajectory surface hopping (TSH) approach is a vital computational technique for simulating non-adiabatic molecular dynamics.[165,169–172,177] It helps the researchers to investigate how the molecules evolve after absorption of light by propagating several trajectories under mixed-quantum classical approximations, where the nuclei are treated classically and the electronic states' properties, such as energies, non-adiabatic couplings, gradients, spin-orbit couplings, etc., are obtained based on the QM approach. However, the traditional QM-based TSH remains limited by its high computational expense and complexity. Therefore, to overcome these limitations, several efforts have been made to utilize ML models for performing TSH simulation with lower computational cost, which have been found to give sufficiently accurate results.[27,113–120]

One of the most popular techniques is the single-state ANI (SS-ANI) models, which can predict energies and/or gradients for individual electronic states, and have been used to accelerate simulations of methylenimmonium cation,[365] 6-aminopyrimidine,[116] nonlinear time-resolved electronic spectra of pyrazine,[366] etc. Recently, machine learning potentials are rapidly advancing, and the Dral group reported multi-state ANI (MS-ANI)[120] models, which are capable of learning all relevant electronic states for photochemical transformation within a molecular system in one instance. It has the potential for more accurate and efficient exploration of complex photochemical processes, addressing previous limitations by providing scalable, transferable, and high-accuracy predictions across diverse chemical spaces. However, in comparison to SS-ANI models, how well they can predict and quantify the important properties, like key geometrical features (i.e., bond length and dihedral angles), electronic state energies, excited state decay times and lifetimes, etc., has not been explored in enough detail. Therefore, a thorough and systematic evaluation of these aspects is essential to establish the robustness and broaden the applicability of such models in excited-state dynamics.

Photoinduced ring-opening of 1,3-Cyclohexadiene (CHD)[36,61,244] reaction can be considered as the prototype that helps scientists to understand the insights into the reaction mechanism of complex photochemical processes and enables benchmarking newly developed methods[36,41] or software implementations[176] to simulate the excited state dynamics. As described in **Section 1.3** of **Chapter 1**, the photochemistry of CHD molecule mainly involves three diabatic electronic states, $1^1A$, $1^1B$, and $2^1A$, under $C_2$ point group symmetry. Moreover, the CHD ring opening reaction proceeds via two conical intersections, formed between the first and second

singlet excited state, CI-$S_1/S_2$, and the first excited state and the ground state, CI-$S_1/S_0$, before leading to the photoproduct all-cis-hexatriene (HT) molecule.[36–39,41,218] Therefore, in this work, we aim to explore the photochemical dynamics of the CHD molecule using two different neural networks (NN)-based machine learning potential (MLP) models: SS-ANI and MS-ANI. To get a comprehensive idea of the SS-ANI and MS-ANI model performance, we trained the models with three different sets of data and the predicted energy gap, interpolation pathways, and ensemble-averaged surface hopping results are scrutinized.

## 6.2 Preparation of Dataset for Training the MLP Models

For training and testing of the MLP models, we have sampled three types of datasets varying in size. For sampling data, we have employed the surface hopping simulations based on the Landau-Zener-Belyaev-Lebedev (LZBL)[172] surface hopping algorithm explained in **Section 2.6** of **Chapter 2**. As already mentioned, to study the photochemistry of CHD molecule, it is required to consider three singlet electronic states $S_0$, $S_1$, and $S_2$, where the first excited electronic state, $S_1$, is the "bright" state. This photoinduced ring-opening reaction is widely

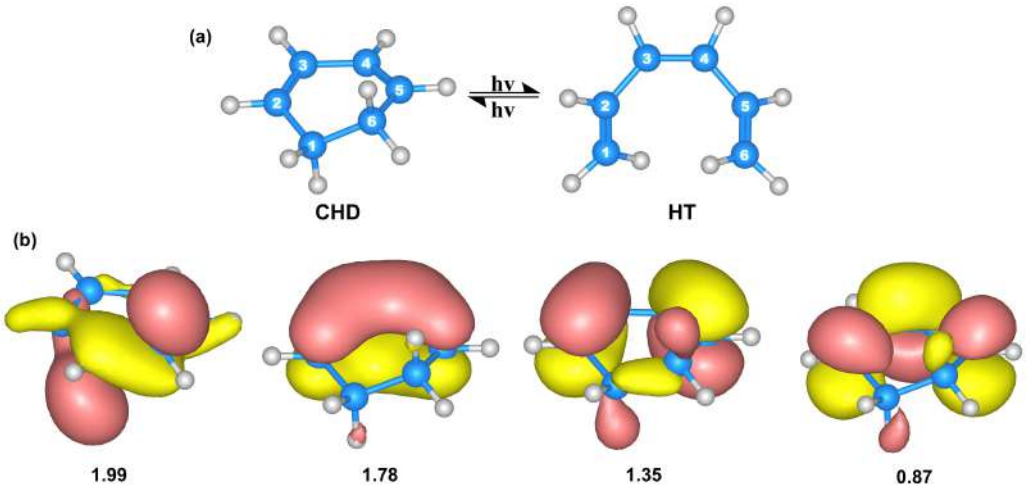


**Figure 6.1.** (a) Photochemical conversion of CHD to HT with the atom numbering used throughout the work, (b) active molecular orbitals used for the CASSCF approach along with the occupation number.

studied mostly using the multireference state-averaged complete active space self-consistent field (SA-CASSCF)[225,226] approach and complete active space second-order perturbation theory (CASPT2)[219,220] using different active space, e.g., SA-3-CASSCF(6,4),[60,244] SA-3-CASSCF(6,6),[38] SA-3-CASSCF(14,8),[39] XMS-CASPT2(6,6),[36,367] etc. Among which the SA-3-CASSCF(6,4) can be considered as one of the approaches which is computation-

ally less expensive and can describe the relevant electronic excited states in the correct order. Therefore, during our surface hopping simulations, we have considered that method along with cc-pVDZ basis set to calculate the energies and gradients on-the-fly. The photoinduced ring-opening reaction of CHD and active orbitals considered for our simulations are shown in **Figure 6.1**.

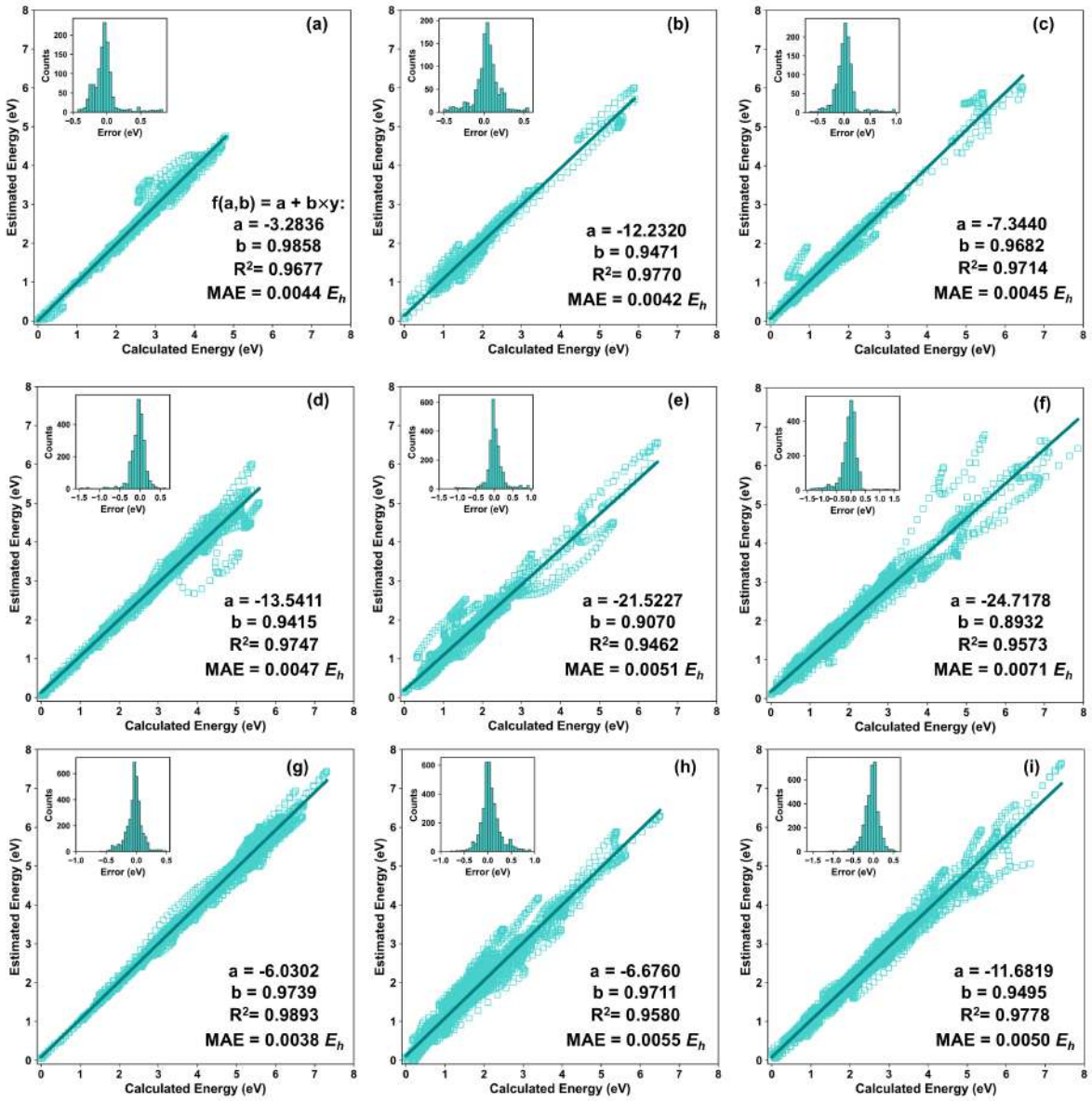


**Figure 6.2.** Testing results of SS-ANI MLP models using TYPE-1 dataset for the state (a) $S_0$, (b) $S_1$, and (c) $S_2$; using TYPE-2 dataset for the state (d) $S_0$, (e) $S_1$, and (f) $S_2$; using TYPE-3 dataset for the state (g) $S_0$, (h) $S_1$, and (i) $S_2$.

The first set of data, TYPE 1, is generated by propagating 10 trajectories from both the CHD and HT sides of the reaction. We used a classical time step of 0.2 fs, and the trajectories were run for 60 fs. All the trajectories were initiated in the first excited state, $S_1$. Data sampling from

both sides, i.e., from CHD and HT sides, gives a proper description of all the electronically excited state PESs followed by the wavepacket during photochemical ring-opening reactions to yield the HT photoproduct. The second (TYPE 2) and third (TYPE 3) datasets are generated in the same manner as used for TYPE 1, but running a total of 20 and 30 trajectories, respectively, from both the CHD and HT sides. We generated 6020, 12040, and 18060 labeled data in TYPE 1, TYPE 2, and TYPE 3 sets, respectively. From this, 80% of the labeled data is used for training both the SS-ANI and MS-ANI PES models, and 20% is used for testing of the same. Further, for QM-based surface hopping, the initial conditions are generated using the Wigner distribution for a harmonic oscillator model.[236] This QM-based surface hopping calculations are performed in mlatom package,[180] interfacing the BAGEL software.[152,153] Further, the training of PES models and ML-based surface hopping simulations are performed in the mlatom package.

## 6.3 Results and Discussion

### 6.3.1 Training and Testing of PES Models

The interconversion between CHD and HT involves complex electronic state transformations that occur via multiple conical intersections between the electronic states. Therefore, the preparation of a dataset for training the PES models is a crucial step. The use of Wigner distribution[236] at the optimized CHD or HT geometry, which is common for generating datasets for training PES models, may not lead to the production of a representative labeled dataset for the whole reaction pathway. Therefore, in this case, surface hopping simulations are essential and were carried out from both sides of the reaction (**Figure 6.1**), i.e., from the CHD and HT sides. In this way, the models are introduced to both sides of the reaction pathway and also to the PESs' behavior near the local minima. **Figure 6.2** and **Figure 6.3** show the results of testing the ANI models for energy predictions using all the different datasets, TYPE-1, TYPE-2, and TYPE-3. We have also reported the error counts, $R^2$ value, mean absolute error (MAE), and linear regression parameters, a and b. It is observed that for all the PES models with all types of datasets, the error counts are mostly peaked at 0.0 eV. For the TYPE-2-$S_2$ state, both the SS-ANI and MS-ANI models show high MAE values among all the PES models. Moreover, the TYPE-3 PES model for $S_0$ state is found to show the lowest MAE values for both the models, SS-ANI and MS-ANI, where the error counts are also within $\sim$ -0.5 eV to 0.5 eV energy range. As presented in **Figure 6.4**, the RMSE values for all trained PES models for energy predictions fall within a range of 0.12 eV to 0.31 eV. The models with errors closer to 0.12 eV represent an

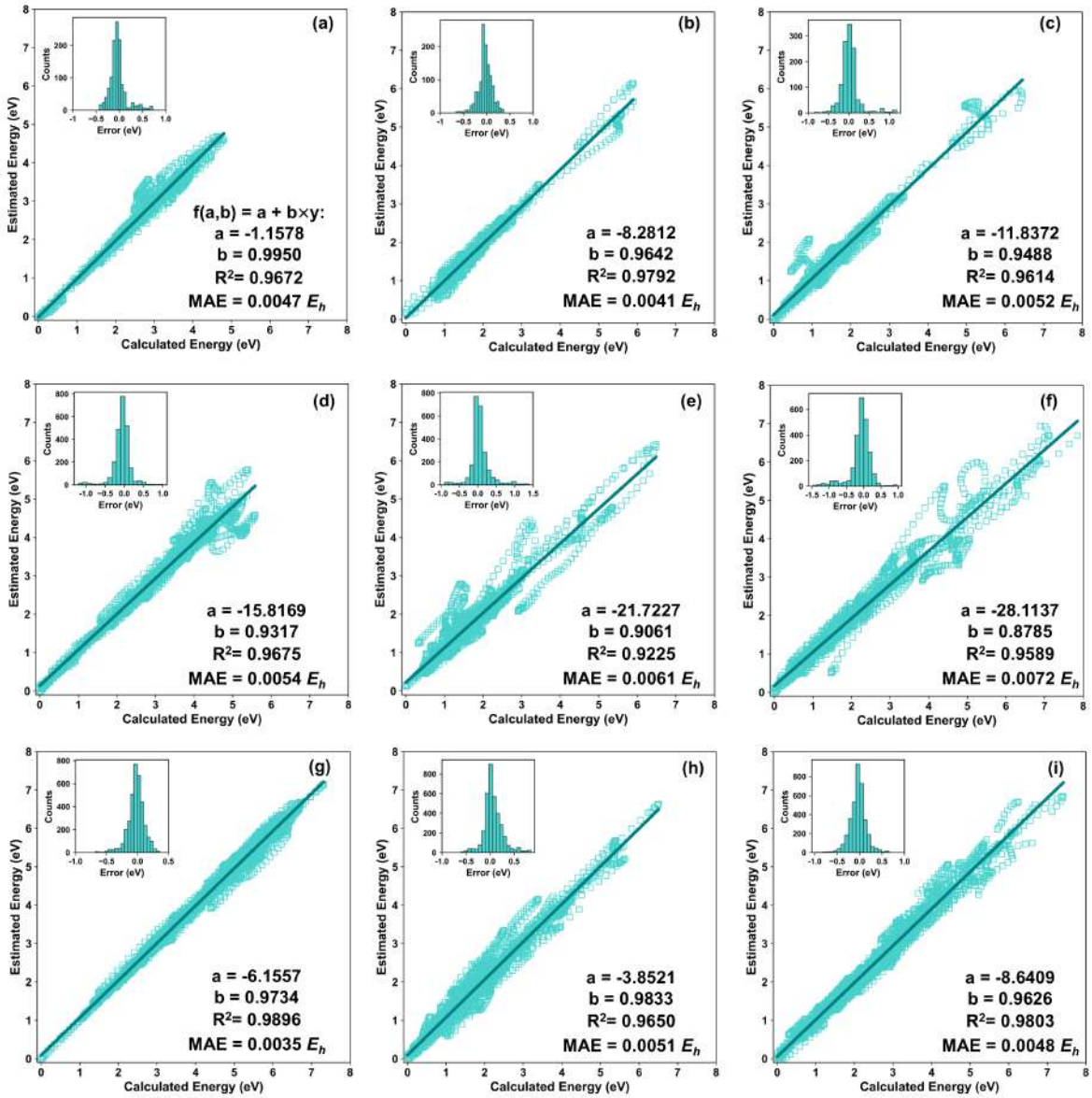


**Figure 6.3.** Testing results of MS-ANI MLP models using TYPE-1 dataset for the state (a) $S_0$, (b) $S_1$, and (c) $S_2$; using TYPE-2 dataset for the state (d) $S_0$, (e) $S_1$, and (f) $S_2$; using TYPE-3 dataset for the state (g) $S_0$, (h) $S_1$, and (i) $S_2$.

excellent fit, while even the highest errors of 0.31 eV can be considered respectable for these types of calculations involving multiple electronic states. This demonstrates that all models are sufficiently reliable for reproductions of the expensive reference QM calculations, and they are therefore a valid basis to carry out further analyses.

The advantage of using the MS-ANI model is that one can concurrently train the required PES models for every electronic state relevant to the photochemical process, by maintaining the correlations among all the electronic states. In contrast, the SS-ANI models are required to train separately for each electronic state. To assess the computational cost associated with

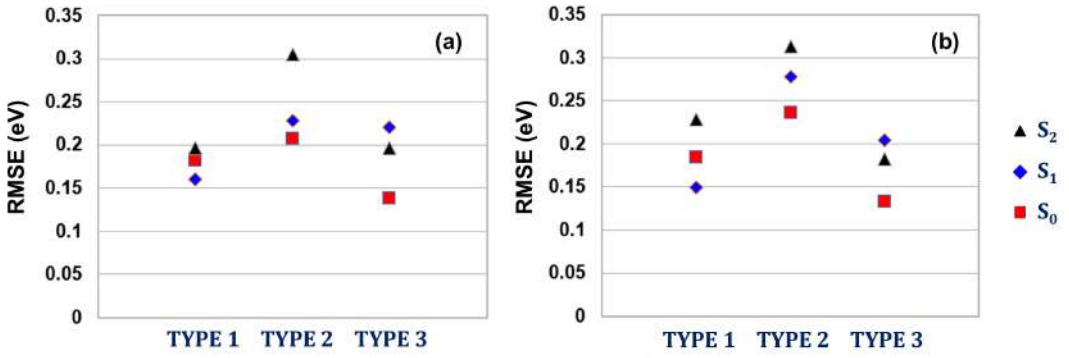


**Figure 6.4.** Root Mean Square Error (RMSE) related to energy predictions of the models (a) SS-ANI and (b) MS-ANI.

different machine learning potentials, we have also reported the number of epochs and the time required for training the models, as shown in the **Table 6.1**. All models were trained using four CPU cores. The training time for SS-ANI models increased with dataset complexity, taking approximately 8.77, 17.23, and 26.33 hours for TYPE 1, TYPE 2, and TYPE 3, respectively. Even though the number of epochs for training was almost comparable, as the dataset became larger, the models needed more a longer time for each epoch to finish learning properly. In contrast, the MS-ANI models are found to be more efficient while training across all dataset types. The total training times for all the MS-ANI models remained significantly lower: 8.19 hours (TYPE 1), 5.44 hours (TYPE 2), and 6.96 hours (TYPE 3). These results suggest that MS-ANI models are not only scalable but also computationally more efficient. Overall, the MS-ANI approach appears favorable in terms of both training time and adaptability across diverse datasets.

**Table 6.1.** Number of epochs and the time taken for training the models.

| Data Type | Models | No. of epochs | Approximate time (sec) per epoch | Total time (hr) |
|---|---|---|---|---|
| TYPE 1 | SS_ANI $S_0$ | 974 | 10 | 8.77 |
| | SS_ANI $S_1$ | 1103 | 10 | |
| | SS_ANI $S_2$ | 1080 | 10 | |
| TYPE 2 | SS_ANI $S_0$ | 865 | 20 | 17.23 |
| | SS_ANI $S_1$ | 952 | 23 | |
| | SS_ANI $S_2$ | 1038 | 22 | |
| TYPE 3 | SS_ANI $S_0$ | 1113 | 34 | 26.33 |
| | SS_ANI $S_1$ | 1106 | 34 | |
| | SS_ANI $S_2$ | 586 | 33 | |
| TYPE 1 | M5_ANI | 1965 | 15 | 8.19 |
| TYPE 2 | M5_ANI | 456 | 43 | 5.44 |
| TYPE 3 | M5_ANI | 457 | 55 | 6.96 |

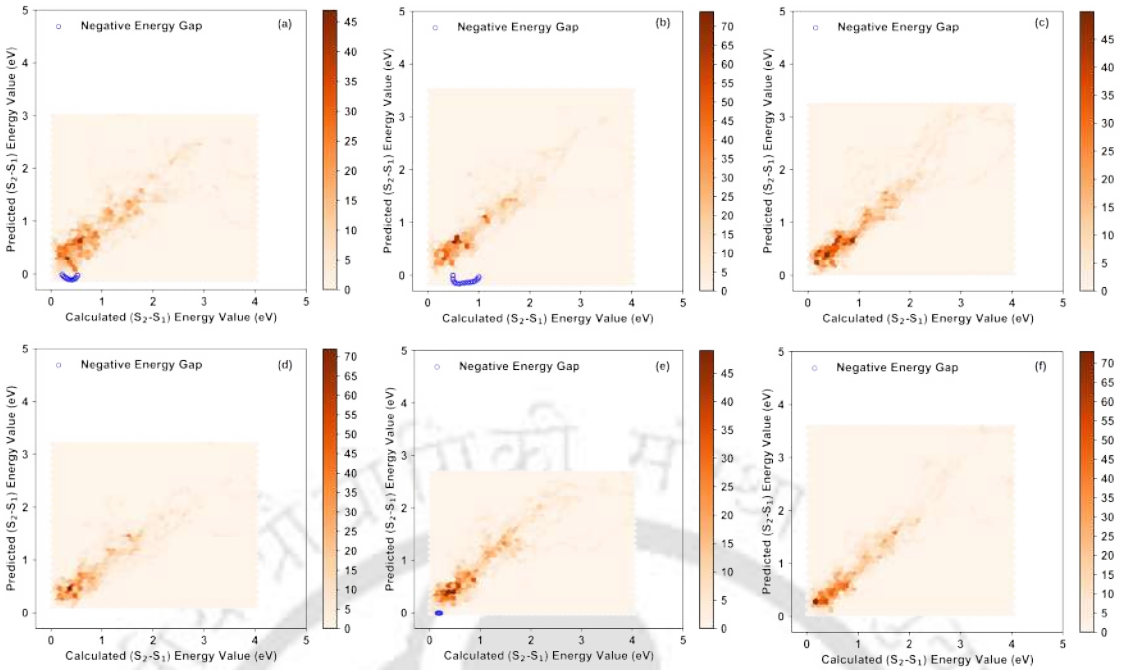


**Figure 6.5.** The energy gap predictions between $S_1$ and $S_2$, by the SS-ANI (a) TYPE-1, (b) TYPE-2, and (c) TYPE-3 models; and by the MS-ANI (d) TYPE-1, (e) TYPE-2, and (f) TYPE-3 models.

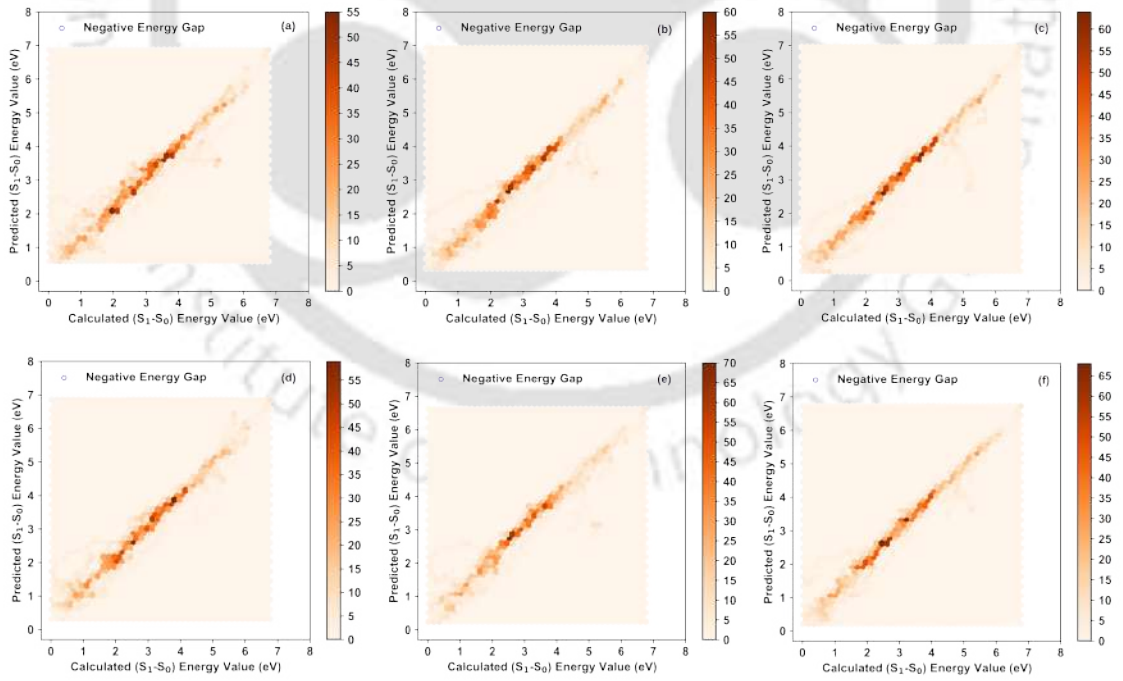


**Figure 6.6.** The energy gap predictions between $S_1$ and $S_0$, by the SS-ANI (a) TYPE-1, (b) TYPE-2, and (c) TYPE-3 models; and by the MS-ANI (d) TYPE-1, (e) TYPE-2, and (f) TYPE-3 models.

### 6.3.2 Energy Gap Analysis

The energy gap between the electronic states is an important parameter for non-adiabatic surface hopping molecular dynamics simulations. Particularly, in the case of the LZBL surface hopping algorithm, the hopping probability is mainly reliant on the energy gap parameters between the electronic states and does not require the explicit calculations of non-adiabatic couplings. Further, in the trajectory surface hopping algorithm we followed, the total time-dependent elec-

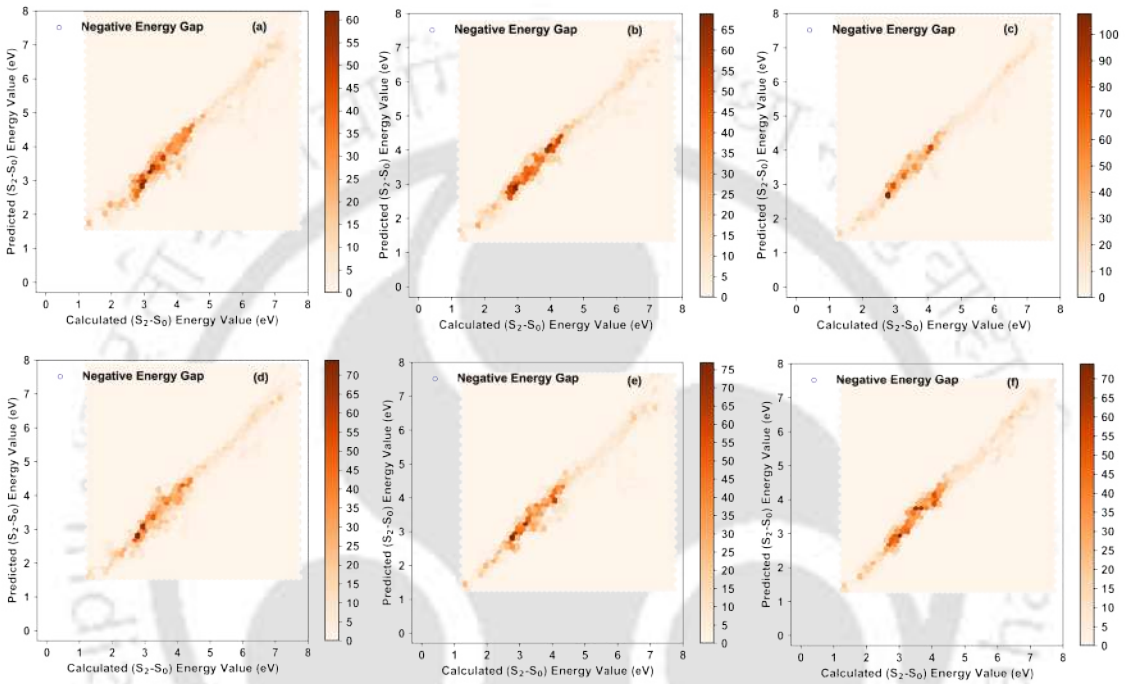


**Figure 6.7.** The energy gap predictions between $S_2$ and $S_0$, by the SS-ANI (a) TYPE-1, (b) TYPE-2, and (c) TYPE-3 models; and by the MS-ANI (d) TYPE-1, (e) TYPE-2, and (f) TYPE-3 models.

tronic wave function of the system is expanded in terms of adiabatic electronic basis functions and therefore the energy gap between two electronic states, i.e., "$S_i$-$S_j$" with i > j, cannot give a negative value. In the case of CHD systems, as reported by earlier studies,[41,244] the evolution of all the electronic states during the simulations has a specific pattern. The $S_1$ and $S_2$ states mostly remain far from the $S_0$ state except for hopping times. However, the $S_1$ and $S_2$ states mostly remain closer to each other during simulations. Therefore, during the simulation, it is highly likely that the ML models may produce a negative ($S_2$-$S_1$) value. Hence, for analyzing the energy gaps between the electronic states, we have generated another set of data by running 10 surface hopping dynamics trajectories from the HT side with 0.2 fs for 60 fs, which leads to the generation of 3010 labeled data points. This new set of labeled data was generated to do the

energy gap analysis on the same set of data using all the SS-ANI and MS-ANI PES models.

Further, for dealing with the energy gaps of electronic states, Dral group developed the MS-ANI model by implementing a special loss term, $L_{\text{gap}}$, which takes care of the errors associated with the predictions of the energy gap between two adjacent adiabatic electronic states, the total loss term ($L$),

$$L = w_e L_e + w_f L_f + w_{\text{gap}} L_{\text{gap}} \tag{6.1}$$

Here, $L_e$ and $L_f$ are the loss terms associated with the energy and force, respectively, and $w$ is the weight.[120]

**Figure 6.5** shows the energy gaps predicted by all the PES models between the $S_1$ and $S_2$ states. We have plotted the "$S_2$-$S_1$" value for reference and predicted calculations. Further, the energy gap analysis between $S_1$ and $S_0$, and $S_2$ and $S_0$ states are reported in the **Figure 6.6** and **Figure 6.7**, respectively. From, **Figure 6.5**, it is observed that the TYPE-1 and TYPE-2 SS-ANI models produces negative energy gaps, however, all the MS-ANI models produce correct "$S_2$-$S_1$" value except for the TYPE-2 MS-ANI models with four negative values. Therefore, regarding predicting the energy gaps, these MS-ANI PES models can be more accurate than the SS-ANI models, which are crucial for non-adiabatic surface hopping MD simulations.

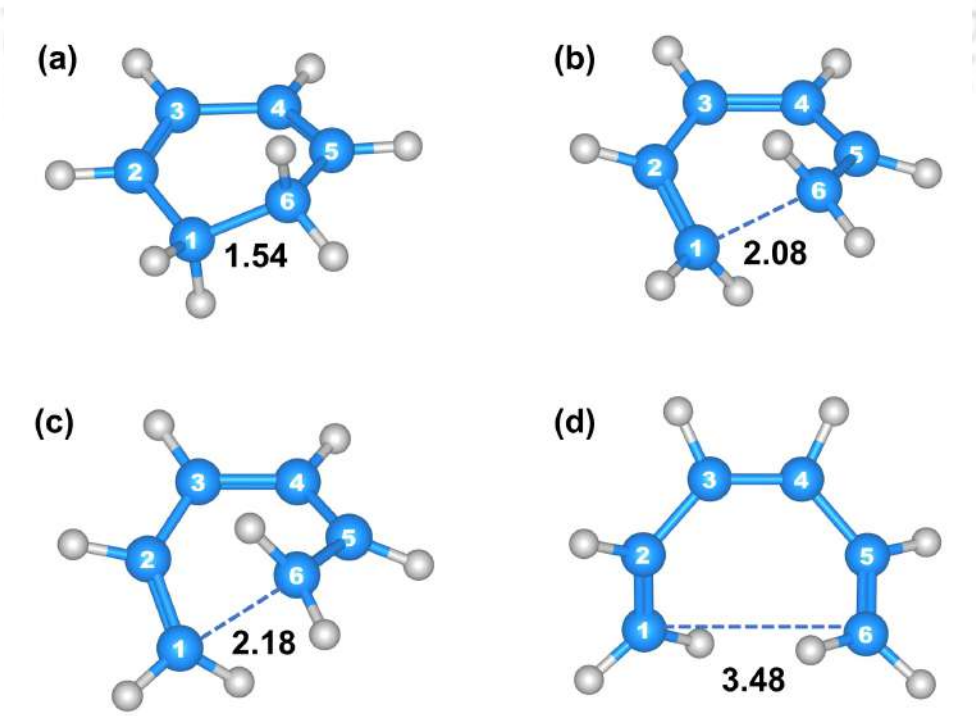


**Figure 6.8.** Optimized (a) $S_0$-CHD at B3LYP/cc-pVDZ, (b) CI-$S_1$/$S_2$ at SA-3-CASSCF(6,4)/cc-pVDZ, (c) CI-$S_0$/$S_1$ at SA-3-CASSCF(6,4)/cc-pVDZ, and (d) $S_0$-HT at B3LYP/cc-pVDZ level of theory, along with the $C_1$-$C_6$ bond length (Å) parameter.

### 6.3.3 Geodesic Interpolations of Electronic States Energies

We also calculated the geodesic interpolation[234] pathways using both the QM reference methods and the MLP models. In the photochemistry of CHD, after excitation to the bright $S_1$ state,

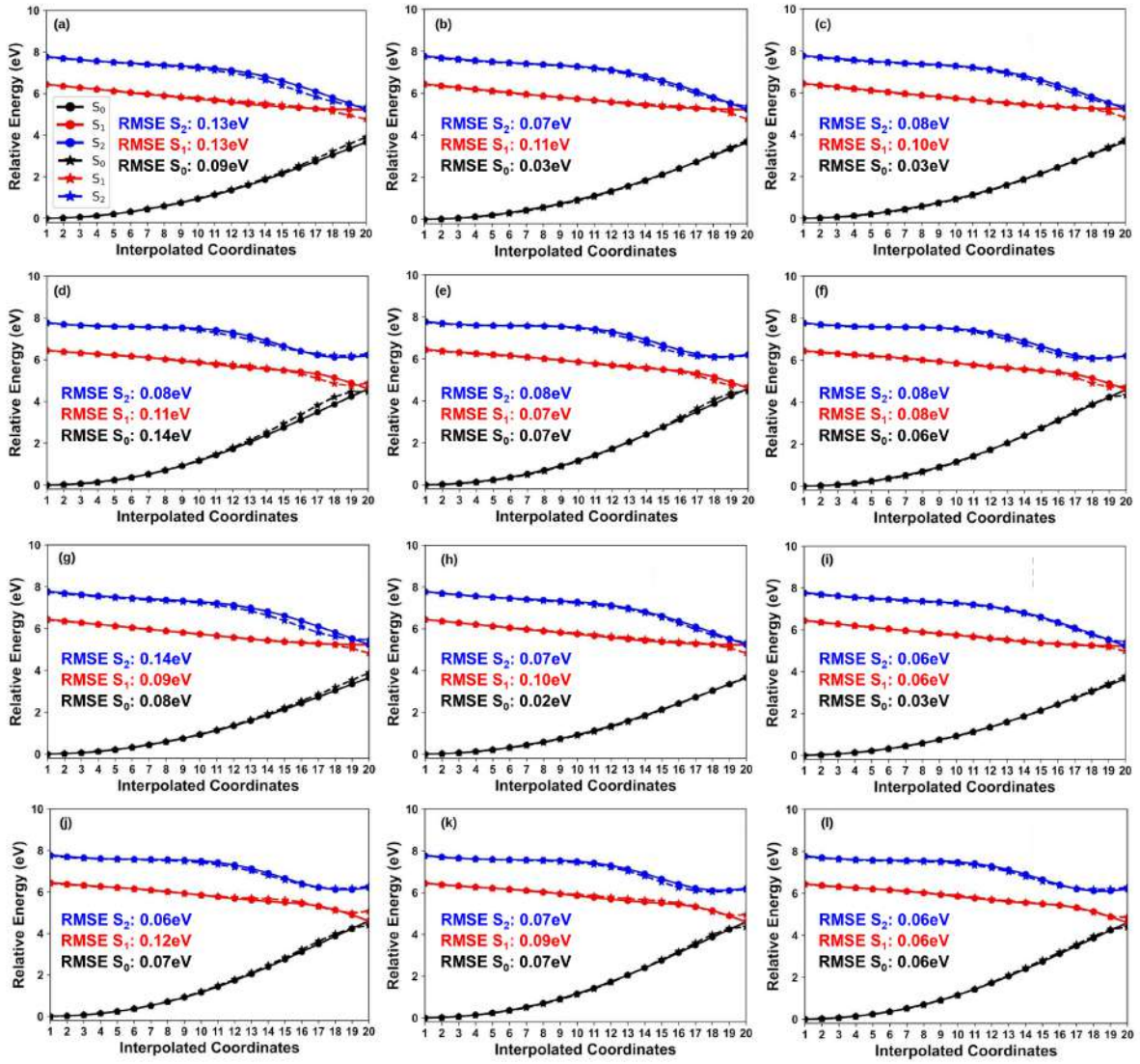


**Figure 6.9.** Geodesic interpoaltion pathways, calculated from $S_0$-CHD to CI-$S_1/S_2$ by SS-ANI (a) TYPE-1, (b) TYPE-2, and (c) TYPE-3 model; from $S_0$-CHD to CI-$S_1/S_0$ by SS-ANI (d) TYPE-1, (e) TYPE-2, and (f) TYPE-3 model; from $S_0$-CHD to CI-$S_1/S_2$ by MS-ANI (g) TYPE-1, (h) TYPE-2, and (i) TYPE-3 model; and from $S_0$-CHD to CI-$S_1/S_0$ by MS-ANI (j) TYPE-1, (k) TYPE-2, and (l) TYPE-3 model (—○— QM, —⋆— MLP).

the wavepacket moves toward the first conical intersection (CI) formed between the $S_1$ and $S_2$ states, CI-$S_1/S_2$. It then proceeds to the second conical intersection, CI-$S_1/S_0$, formed between the $S_1$ and $S_0$ states. Therefore, we optimized $S_0$-CHD, $S_0$-HT, CI-$S_1/S_2$, and CI-$S_1/S_0$ and are provided in **Figure 6.8**. Then, we calculated the interpolation pathways from the ground-state optimized geometry of CHD to each of these CI geometries, and the results are shown in

**Figure 6.9**. We also reported the RMSE values for the predicted electronic state energies. These RMSE values range between 0.02 and 0.14 eV. Among all the models trained with both SS-ANI and MS-ANI datasets, the TYPE-3 MS-ANI model performed the best, producing accurate interpolation pathways with RMSE values between 0.02 to 0.06 eV across all electronic states. These results also confirm that the PES models are highly effective in reproducing the electronic state energies of interpolated pathways based on the reference method, which offers a powerful and efficient tool for subsequent analyses of surface hopping simulations.

### 6.3.4 Surface Hopping Simulations

Finally, we carried out non-adiabatic surface hopping MD simulations to study the photochemical ring-opening process of the CHD molecule. A total of 500 trajectories were run for 200 fs each, with a time step of 0.2 fs, using all the MLP models, resulting in six sets of MD simulations. During the simulations, we monitored key parameters such as the $C_1$-$C_6$ bond length, electronic state energies, and adiabatic populations.

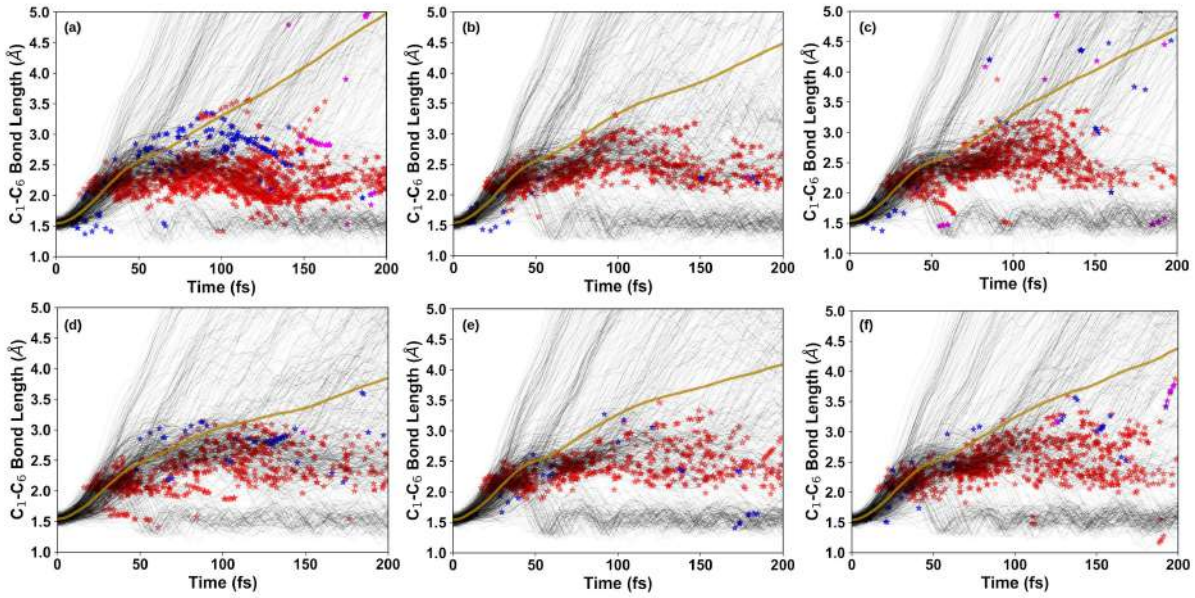


**Figure 6.10.** $C_1$-$C_6$ bond length evolutions along with hopping types (★:$S_1 \leftrightarrow S_2$, ★:$S_0 \leftrightarrow S_1$, ★:$S_0 \leftrightarrow S_2$) during surface hopping simulations performed using, SS-ANI (a) TYPE-1, (b) TYPE-2, and (c) TYPE-3 PES models; MS-ANI (d) TYPE-1, (e) TYPE-2, and (f) TYPE-3 PES models. The golden solid line represents the ensemble-averaged $C_1$-$C_6$ bond length.

### $C_1$-$C_6$ Bond Length Evolution

**Figure 6.10** shows the evolution of the $C_1$-$C_6$ bond length across all 500 trajectories, as well as the ensemble-averaged trend over time. Compared to previous reports,[36,244] the bond length evolutions from our simulations did not show any unusual behavior, and the ring-opening dynamics appeared normal. However, differences were observed between the models. The SS-ANI model trained with the TYPE-1 dataset showed relatively faster ring-opening, with the average $C_1$-$C_6$ bond length reaching up to ∼5.0 Å within 200 fs. In contrast, the MS-ANI model with the same TYPE-1 dataset displayed slower ring-opening dynamics, reaching a maximum average bond length of about ∼3.7 Å over the same period.

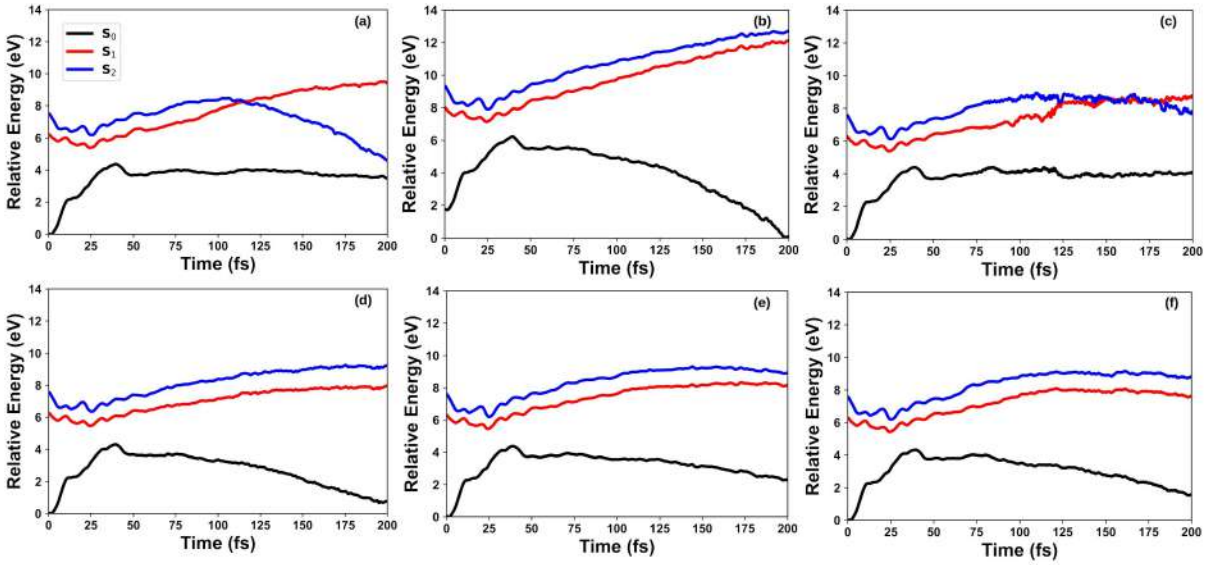


**Figure 6.11.** Ensemble-averaged electronic state energy evolutions during surface hopping simulations performed using SS-ANI (a) TYPE-1, (b) TYPE-2, and (c) TYPE-3 PES models; MS-ANI (d) TYPE-1, (e) TYPE-2, and (f) TYPE-3 PES models.

### Electronic State Energy Evolution

The ensemble-averaged potential energy evolutions over 500 trajectories for each set of surface hopping simulations are shown in **Figure 6.11**. All the SS-ANI models performed poorly in predicting the potential energies during the simulations. The TYPE-1 SS-ANI model showed reasonable energy predictions up to around 90 fs, but after that, the $S_2$ energy dropped from ∼8 eV to ∼4 eV crossing the $S_1$ energy evolution at around 115 fs, which is not expected in typical surface hopping simulations. In the case of TYPE-2 SS-ANI model, even though we did not observe any crossing as that of the TYPE-1 model, the energy evolution of $S_0$

and both $S_1$ and $S_2$ together splits apart resulting in reaching an energy evolution window of $\sim$ 13 eV. Further, in the case of the TYPE-3 SS-ANI model, after about 100 fs, the $S_1$ and $S_2$ energies started to come closer and eventually crossed, which is also unusual. On the other hand, with the MS-ANI models, the $S_1$ and $S_2$ energies stayed close to each other throughout the simulation and the $S_0$ state remained separated from both excited states. Most importantly, the energy profiles remained stable and did not show unexpected changes, which is what we would normally expect in surface hopping simulations as seen in an earlier study.[244]

### Adiabatic Population Analysis

The ensemble-averaged population is also analyzed and presented in **Figure 6.12**. As the excited state dynamics is initiated in the first excited state, $S_1$, the population transfer occurs from the $S_1$ state to the other two electronic states. For the SS-ANI model trained with TYPE-1 and

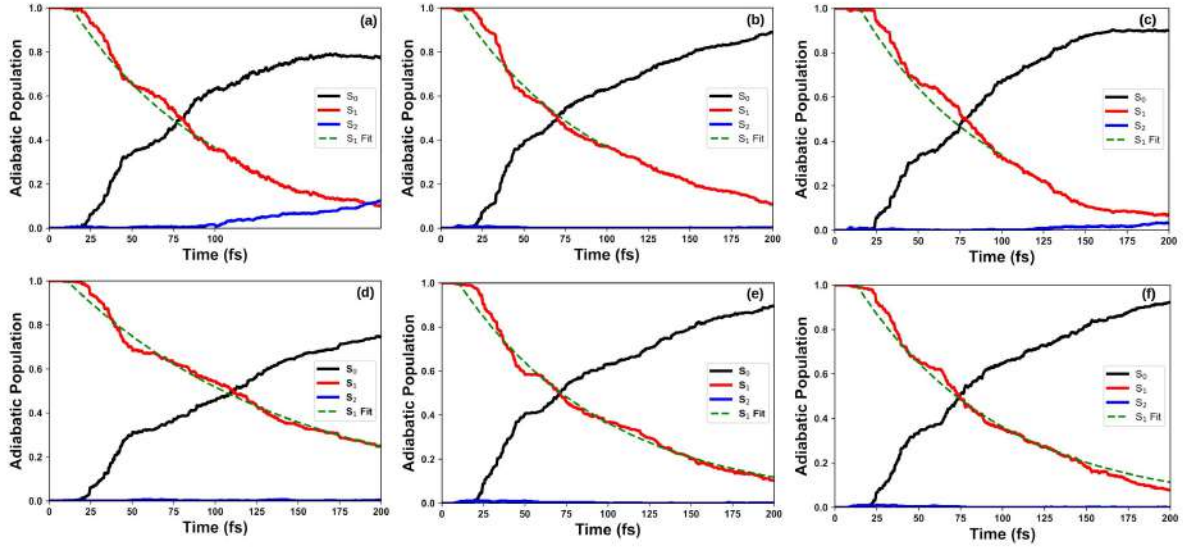


**Figure 6.12.** Ensemble-averaged adiabatic population evolutions during surface hopping simulations performed using, SS-ANI (a) TYPE-1, (b) TYPE-2, and (c) TYPE-3 PES models; MS-ANI (d) TYPE-1, (e) TYPE-2, and (f) TYPE-3 PES models.

TYPE-3 data set, the behavior of the ensemble-averaged population was found to be normal till $\sim$ 95 fs. However, after that, increase in the population of $S_2$ was observed, which is against the conventional population behavior of the CHD ring-opening photochemistry, where only in the initial period of time the $S_2$ population growth is significant. Along with that, during the later part of the simulation, the populations are mostly dominated by the increase in the $S_0$ and decrease in the $S_1$ state.[36,41,176,244] Even though the behavior of the population in the simulations performed using the MLP models was found to be normal, it exhibited a different population

decay pattern of the $S_1$ state. To quantify the decay process, we fitted the population decay of the $S_1$ state with a monoexponential function, $N^{S_1} = \exp(-(t+t_1)/t_d)$, where $t_l$ represents the latency time and $t_d$ represents the decay time, and together, i.e., $(t_l + t_d)$, represents the lifetime of the $S_1$ state.

**Table 6.2.** Time measurements for different types of MLP models.

| Models | TYPE 1 | | | TYPE 2 | | | TYPE 3 | | |
|---|---|---|---|---|---|---|---|---|---|
| | $t_l$ (fs) | $t_d$ (fs) | lifetime (fs) | $t_l$ (fs) | $t_d$ (fs) | lifetime (fs) | $t_l$ (fs) | $t_d$ (fs) | lifetime (fs) |
| SS-ANI | 13 | 86 | 99 | 11 | 88 | 99 | 14 | 78 | 92 |
| MS-ANI | 10 | 135 | 145 | 10 | 88 | 98 | 13 | 85 | 98 |

**Table 6.2** shows the time constants related to the entire set of simulations. Interestingly, except for the MS-ANI model trained with the TYPE-1 dataset, all other sets of simulations represent similar time constants, and if compared with one of the previously reported studies performed by Zhang *et al.*,[41] where they utilized the LZSH-SF-BHHLYP/cc-pVDZ level of theory, the constants coincide with the $t_l$ = 12 fs and $t_d$ = 84 fs. Although the SS-ANI models successfully predicted the time constants, they showed severe inconsistencies in other critical aspects of surface hopping simulations, such as electronic state energy evolution and $S_2$ state population.

## 6.4 Conclusions

We have performed a comprehensive comparison of MLP models, specifically SS-ANI and MS-ANI, to study the photochemistry of the CHD molecule. The ring-opening dynamics of the CHD system, which involves two low-lying singlet electronic excited states along with the ground state, are observed by performing LZBL-based surface hopping dynamics using MLP models, and important geometrical and energetic parameters are analyzed. To train the MLP models, we generated datasets using surface hopping simulations based on QM calculations with the SA-3-CASSCF method and cc-pVDZ basis set. Three dataset types, TYPE-1, TYPE-2, and TYPE-3, varying in size, were used to train and evaluate the models. Our investigation shows a clear advantage of MS-ANI models over SS-ANI models, particularly in modeling multiple electronic states simultaneously with higher accuracy and stability. The MS-ANI approach effectively captures the correlations among states, resulting in reliable energy predictions, stable energy gap behaviors, and more accurate population dynamics during photochemical processes.

This robustness makes MS-ANI models well-suited for non-adiabatic molecular dynamics simulations, providing consistent energy profiles and correct state crossing behaviors.

In contrast, SS-ANI models exhibited significant limitations. They produced inaccurate energy gaps, sometimes predicting negative values, and showed less reliable energy and population evolution patterns, which can greatly impact simulation fidelity. Moreover, SS-ANI models required longer training times as dataset complexity increased. The dataset type also substantially influences model performance. Larger, more diverse datasets like TYPE-3 improved the accuracy and stability of both models; however, MS-ANI models benefited most from such comprehensive training, which shows the importance of dataset quality and representativeness. Therefore, the MS-ANI models are promising for accurate, scalable, and multi-state photochemical simulations, provided they are trained with well-curated, extensive datasets. Properly designed training data is essential for maximizing their predictive capabilities. Finally, while MS-ANI models offer notable advantages, their success depends on careful dataset selection. Thus, MS-ANI models offer a powerful alternative to SS-ANI for machine learning-driven excited-state simulations, opening new avenues for exploring complex photochemical phenomena.

# Chapter 7

# Summary and Conclusions

Photochemistry helps sustain life on Earth by playing a key role in living systems and modern technologies. For instance, the light-driven ring-opening reaction of the CHD molecule to yield HT is essential for producing Vitamin $D_3$ in our bodies, which helps maintain healthy bones and immune function by aiding calcium absorption. Understanding such light-induced chemical reactions, which often follow complex non-adiabatic pathways, is important for scientists to uncover how these processes work and to design new materials that can improve our daily lives through technological innovations. Therefore, this thesis mainly focuses on studying the photochemical ring-opening/closure reactions related to CHD/HT derivatives. By employing various theoretical and computational approaches, the investigations were carried out. Specifically, electronic structure methods such as DFT, CASSCF, and XMS-CASPT2, which provided accurate descriptions of potential energy surfaces and excited states, were used. Further, our exploration also includes the use of QM/MM approach and machine learning-based potentials for mixed quantum-classical dynamics simulations. In this thesis, the investigations carried out are framed into four working chapters.

In the first working chapter, i.e., Chapter 3, we investigated how chemical substituents, mainly -$CH_3$, affect the photochemical ring-opening of CHD. Using a multireference approach and surface hopping simulations, we analyzed the reaction dynamics of CHD and its three substituted derivatives. Results show that the systems with a substituent near the carbon-carbon single bond responsible for the ring-opening process hinder bond cleavage and reduce ring-opening efficiency. Substituted systems also exhibit longer excited-state lifetimes and restricted atomic motions. These insights highlight the significant role of substitution in modulating non-adiabatic dynamics, contributing to better design strategies for light-responsive molecules in future applications.

Next working chapter, Chapter 4, is dedicated exploring the crucial role of the environment around the CHD molecule in directing excited state dynamics. This study explains how polar solvents like water can facilitate faster decay of the excited state, decrease the energy barriers, affect the quantum yields, and emphasize the importance of solute-solvent interactions in controlling photochemical reactivity. These insights are highly relevant to designing novel photochemical systems in solution, particularly molecular switches, solar energy harvesting, and light-activated therapeutics.

The third working, i.e., Chapter 5, explores the photochemistry of a synthesized fulgide molecule with an HT core to observe its ring-closure dynamics using DFT, wavefunction-based methods, and surface hopping simulations. A sloped $S_1/S_0$ conical intersection was found to exist in the reaction pathway, which suggests a low quantum yield ($\sim 8\%$) for closed isomer formation and favors reformation of the open isomer. Electron transport analysis was carried out to examine its potential for molecular electronic applications, and closed form was found to be promising one. These findings extend the understanding of photoinduced ring-closure mechanisms and open avenues for designing efficient molecular switches based on similar frameworks.

In the last working chapter, Chapter 6, the machine learning potentials (MLP), specifically SS-ANI and MS-ANI, were used to simulate the excited-state dynamics of CHD, and the results were compared. Three differently sized datasets, generated from SA-3-CASSCF-based surface hopping simulations, were used to train the MLP models. For SS-ANI models, we observed that the training time increased with the size of the dataset, while MS-ANI models required similar training time regardless of size. Furthermore, MS-ANI outperformed SS-ANI by more accurately modeling multiple electronic states, maintaining stable energy gaps, and providing reliable population dynamics. Therefore, this finding highlights MS-ANI's strength for non-adiabatic dynamics, especially when trained on large, diverse, and well-curated datasets.

We believe these contributions can significantly advance the field of computational photochemistry and set the stage for future innovations. Researchers can design new photoswitchable molecules by altering their structure or environment to control their photochemical behavior. Further improvements in machine learning potential models using hybrid machine learning techniques could enable their application to larger systems, allowing the exploration of complex photochemical processes over extended timescales.

# Appendix A

## A.1 Active molecular orbitals of CHD derivatives

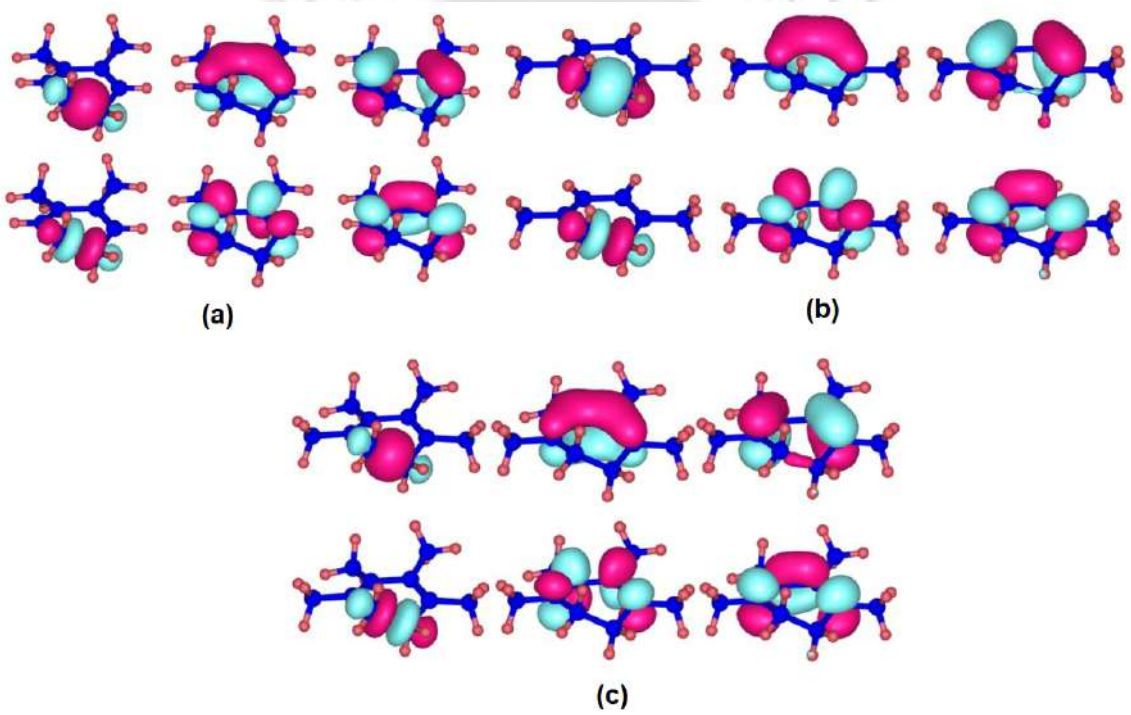


**Figure A.1.** Active molecular orbitals of (a) CHD-Me2-1, (b) CHD-Me2-2, and (c) CHD-Me4 obtained within the active space of SA-3-CASSCF(6,6) calculations.

## A.2 Active orbitals used in molecular dynamics simulations

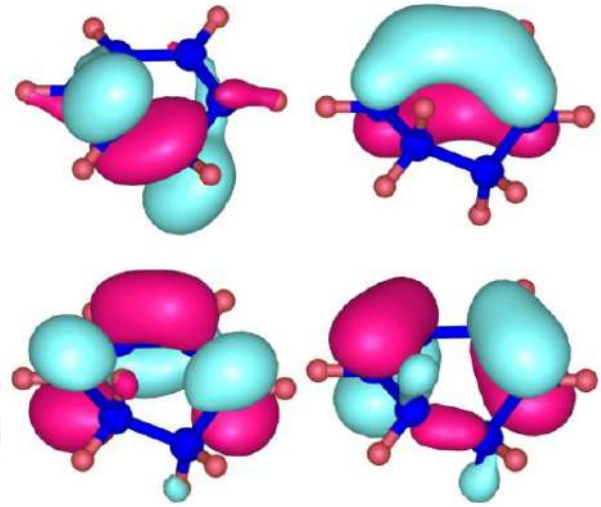

**Figure A.2.** Active orbitals of the CHD molecule used in molecular dynamics simulations at the SA-3-CASSCF(6,4)/6-31G(d) level of theory.

## A.3 Optimized $S_1$ minimum energy geometries at XMS-CASPT2/6-31G(d) level of theory

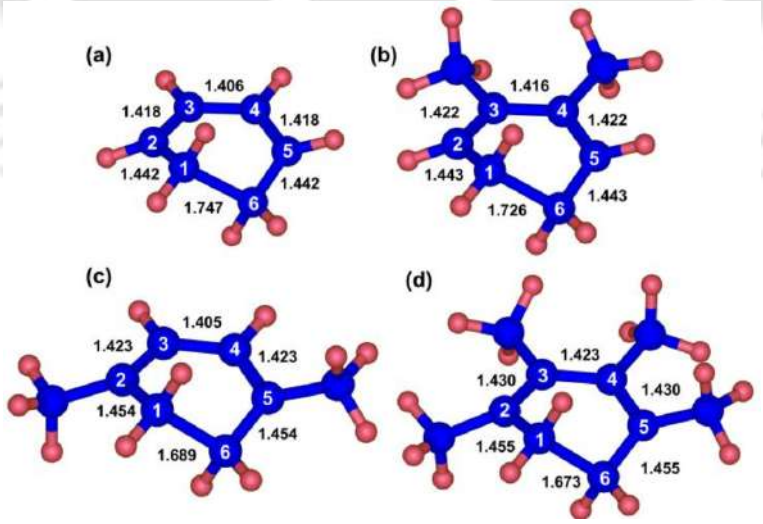


**Figure A.3.** Active orbitals of the CHD molecule used in molecular dynamics simulations at the SA-3-CASSCF(6,4)/6-31G(d) level of theory.

## A.4 Statistical comparison of three sets of dynamics simulations

**Table A.1.** Statistical comparison of three sets of trajectories (100, 150, 200 Traj).

| No. of Trajectories | % Trajectories Showing Hopping $S_1$ to $S_2$ | % Trajectories Showing Hopping $S_2$ to $S_1$ | % Trajectories Showing Hopping $S_1$ to $S_0$ | HT Formation within 100 fs (%) |
|---|---|---|---|---|
| 100 Traj | 57 (57%) | 57 (57%) | 81 (81%) | 31/100 = 31% |
| 150 Traj | 88 (58%) | 88 (58%) | 119 (79%) | 51/150 = 34% |
| 200 Traj | 119 (59%) | 119 (59%) | 159 (79%) | 70/200 = 35% |

## A.5 Topography analysis and topographical parameters.

This topography analysis is performed as described by Yarkony[241,368] and as implemented in the Columbus software package by Barbatti et al.[243] The conical intersection topographies are constructed using the following equation,

$$E_{1,2} = s_x x + s_y y \pm d_{gh}\left[\left(\frac{x^2+y^2}{2}\right) + \Delta_{gh}\left(\frac{x^2-y^2}{2}\right)\right]^{1/2} \tag{1}$$

where, $s_x$ and $s_y$ are the projection of the summed gradient, $s$, on the branching or g-h plane, $d_{gh}$ defines the pitch, and $\Delta_{gh}$ defines the shift from cylindrical symmetry.

$$s_x = s \cdot x, \quad x = \frac{\mathbf{g}}{|\mathbf{g}|} \tag{2}$$

$$s_y = s \cdot y, \quad y = \frac{\mathbf{h}}{|\mathbf{h}|} \tag{3}$$

where **g** and **h** are the gradient difference vector and non-adiabatic coupling vector, respectively.

$$\Delta_{gh} = \frac{|\mathbf{g}|^2 - |\mathbf{h}|^2}{|\mathbf{g}|^2 + |\mathbf{h}|^2} \tag{4}$$

$$d_{gh} = \sqrt{|\mathbf{g}|^2 + |\mathbf{h}|^2} \tag{5}$$

For our systems, the topographical parameters are shown below in Table S7: for the $S_1/S_0$ conical intersection at the SA-3-CASSCF(6,4)/6-31G(d) level of theory.

**Table A.2.** Topographical parameters for $S_1/S_0$ conical intersection at SA-3-CASSCF(6,4)/6-31G(d) level of theory.

| System | $s_x$ | $s_y$ | $\Delta_{gh}$ | $d_{gh}$ |
|---|---|---|---|---|
| CHD | -0.89 | -0.22 | 0.09 | 12.09 |
| CHD-Me2-1 | -0.96 | 0.36 | 0.08 | 12.11 |
| CHD-Me2-2 | 0.50 | 1.06 | 0.20 | 11.97 |
| CHD-Me4 | -1.77 | -0.68 | -0.92 | 11.96 |

## A.6 Intrinsic reaction coordinate (IRC) pathways for conrotatory transition state of all considered photochemical reactions

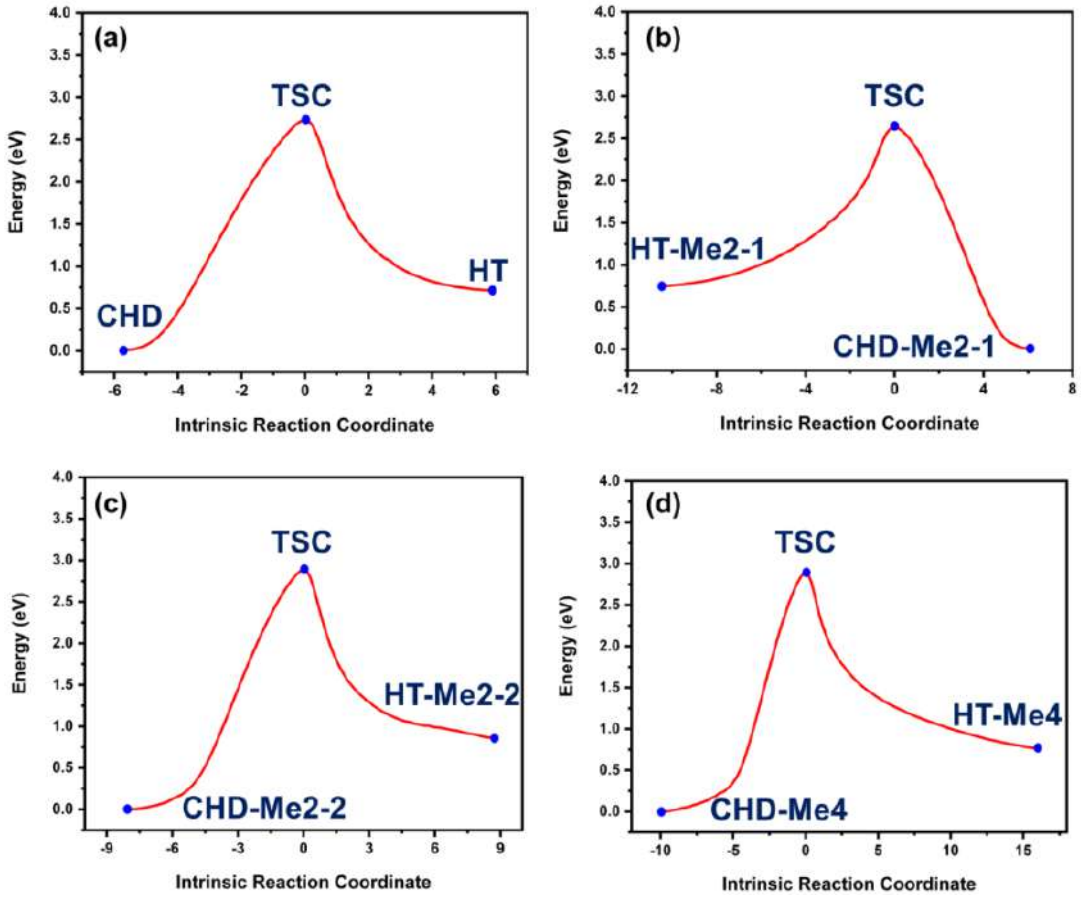


**Figure A.4.** CASSCF(6,6)/6-31G(d) calculated intrinsic reaction coordinate (IRC) pathways for (a) CHD, (b) CHD-Me2-1, (c) CHD-Me2-2, and (d) CHD-Me4. Energies are relative to the corresponding CHD derivatives.

# A.7 XMS-CASPT2/6-31G(d) level of theory generated energy profile diagram for all the systems

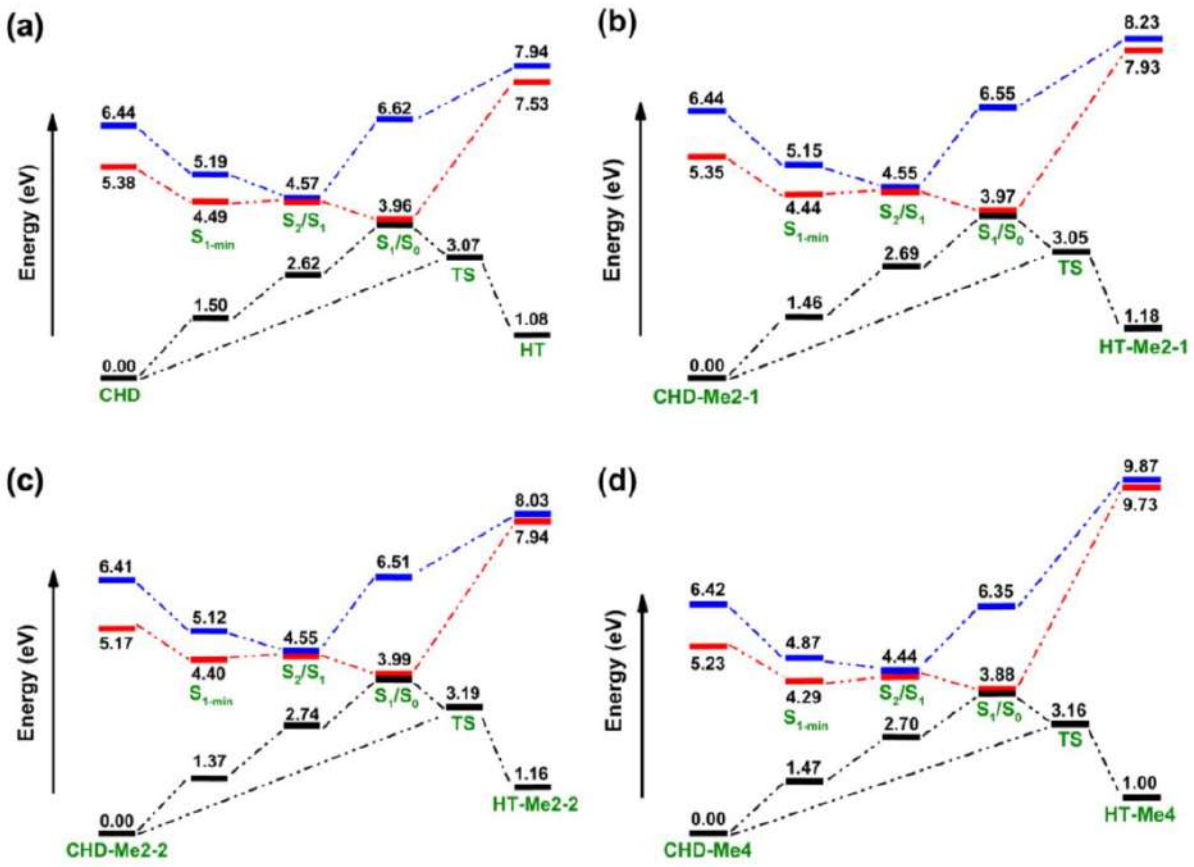


**Figure A.5.** SA-3-XMS-CASPT2 level generated energy profile diagram of (a) CHD, (b) CHD-Me2-1, (c) CHD-Me2-2, and (d) CHD-Me4. Energies are relative to the corresponding CHD derivatives.

## A.8 The root-mean-square deviation (RMSD) plots of the geometries associated with on-thefly molecular dynamics simulation.

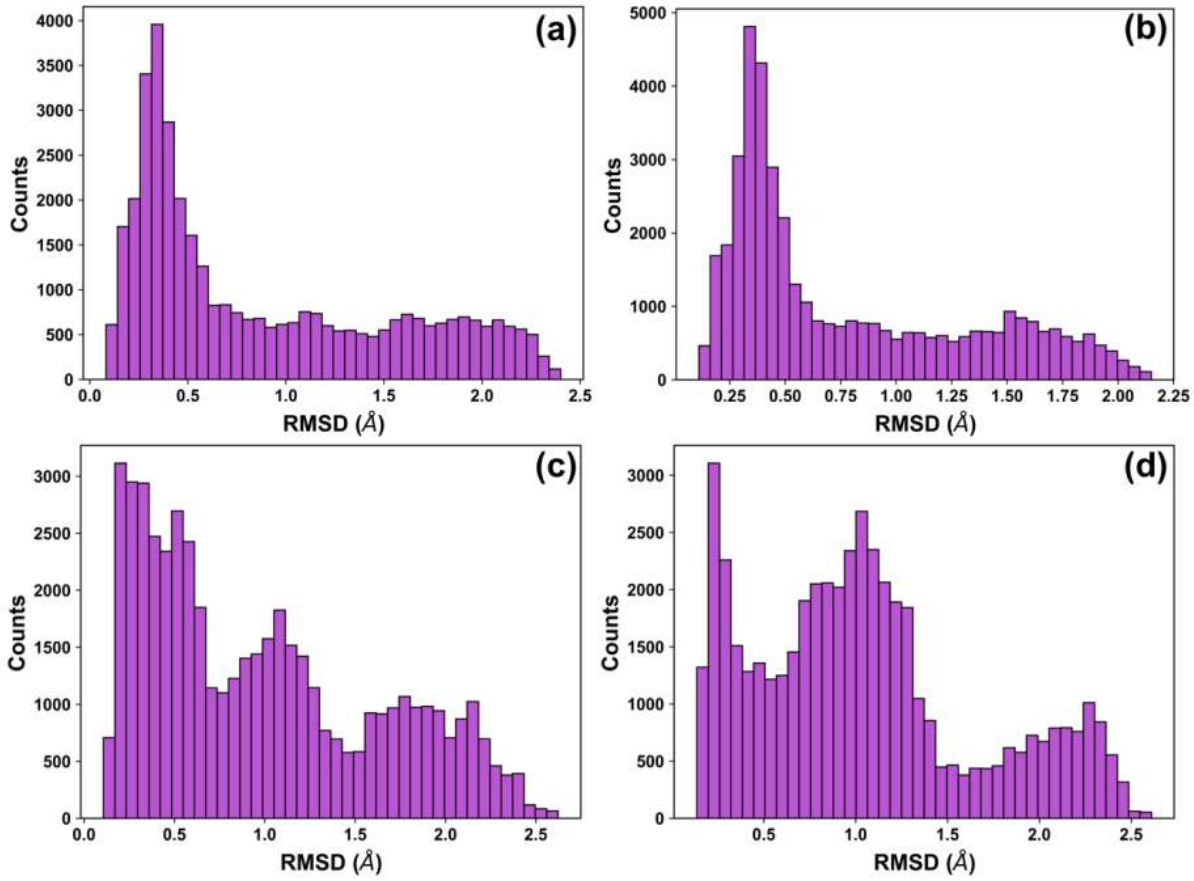


**Figure A.6.** The root-mean-square deviation (RMSD) plots for (a) CHD, (b) CHD-Me2-1, (c) CHD-Me2-2, and (d) CHD-Me4.

# A.9 Bond dissociation limit explanation for CHD molecule.

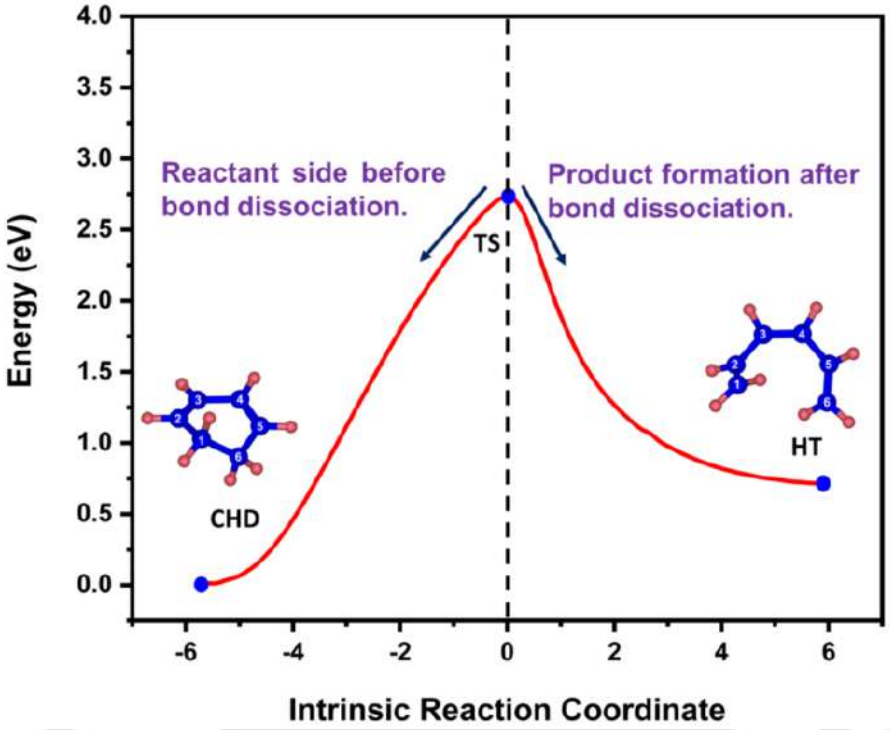


**Figure A.7.** Bond dissociation in CHD molecule.

## A.10 Histogram plots for energy gap distributions among the considered electronic states during molecular dynamics simulation of each system.

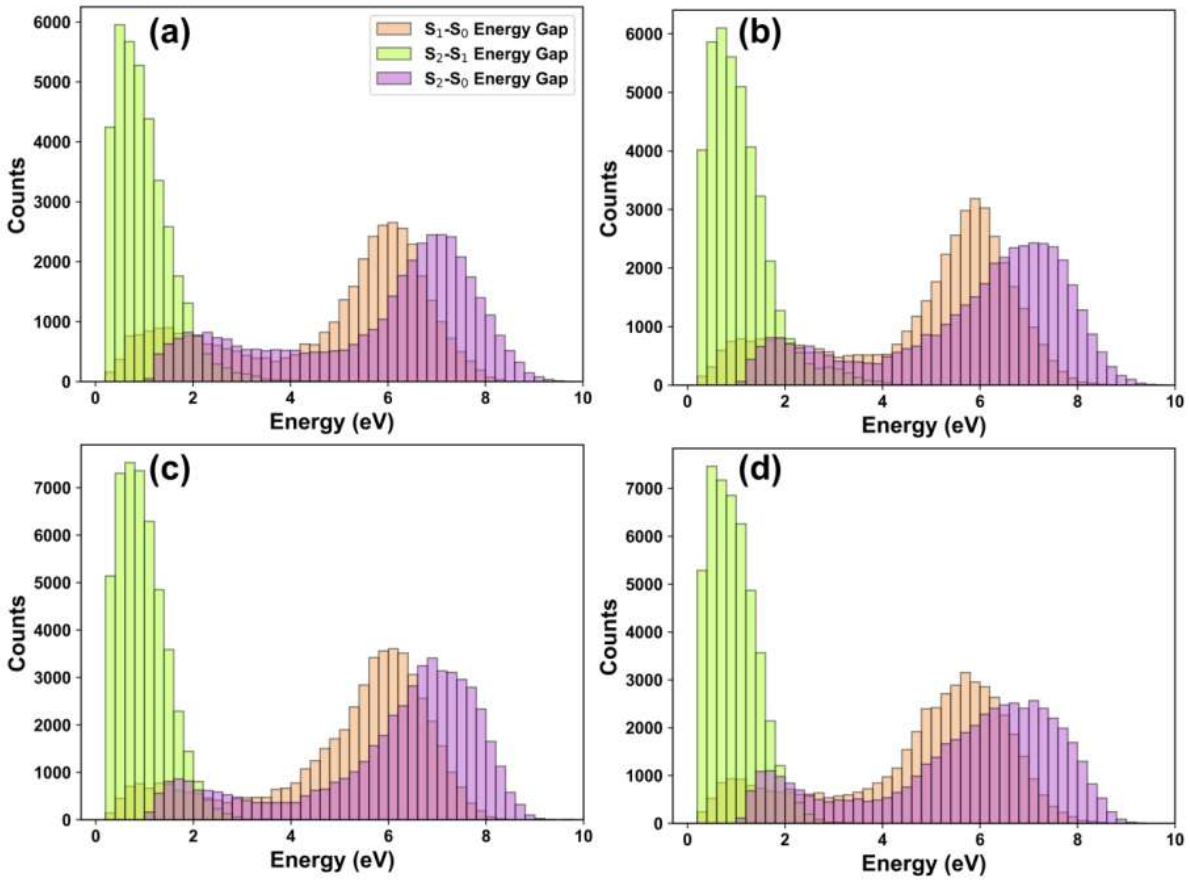


**Figure A.8.** Energy gap distributions throughout the dynamics for (a) CHD, (b) CHD-Me2-1, (c) CHD-Me2-2, and (d) CHD-Me4.

## A.11 Typical trajectories for each system during non-adiabatic molecular dynamics simulation.

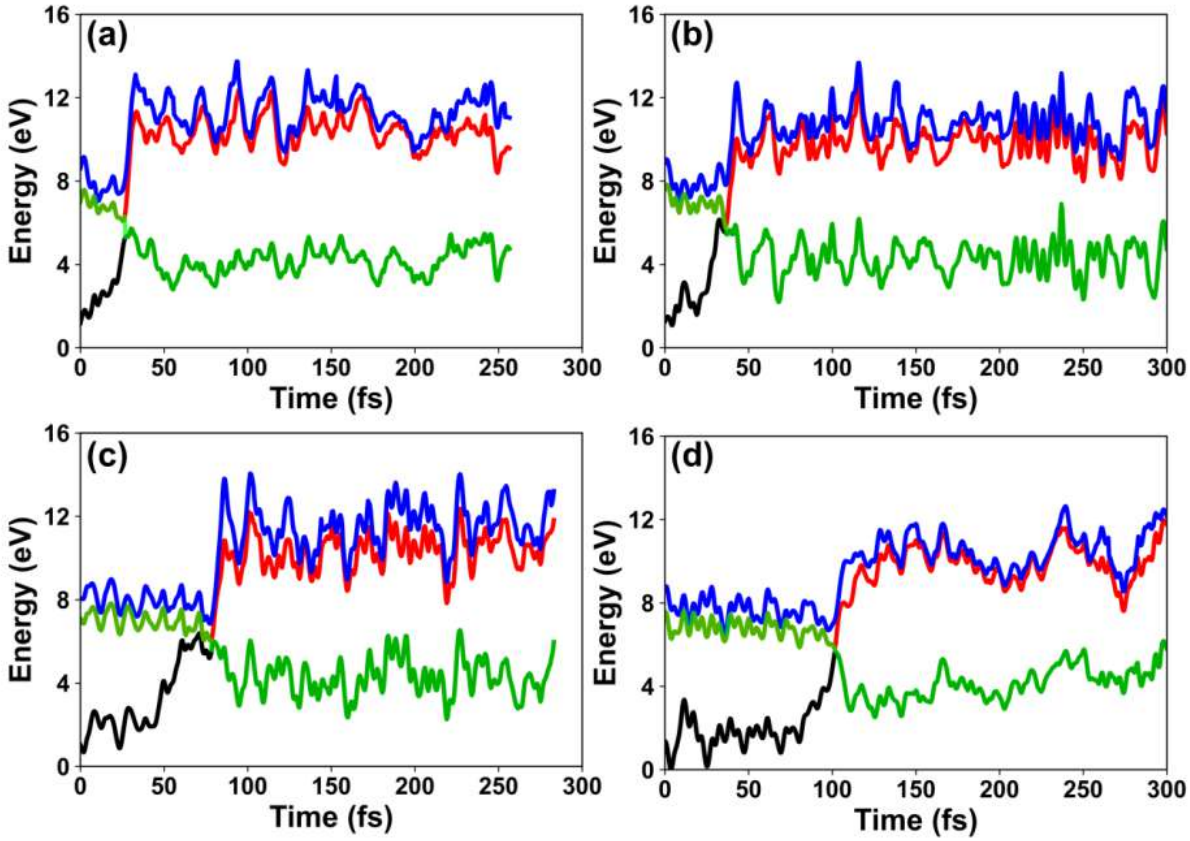


**Figure A.9.** SA-3-XMS-CASPT2 level generated energy profile diagram of (a) CHD, (b) CHD-Me2-1, (c) CHD-Me2-2, and (d) CHD-Me4. Energies are relative to the corresponding CHD derivatives.

## A.12 Ensemble-averaged non-adiabatic coupling vector (h) norms.

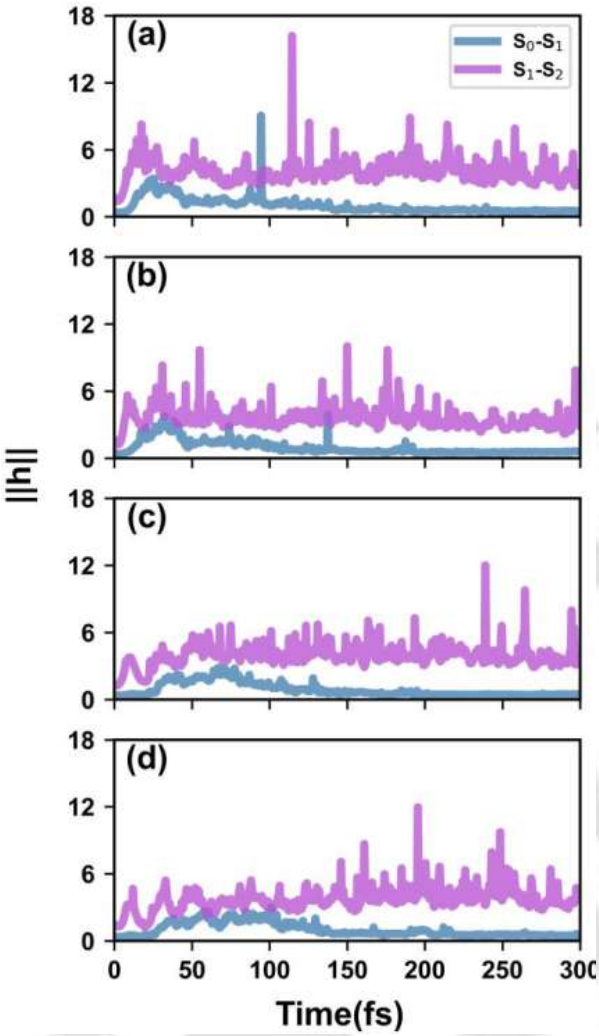


**Figure A.10.** SA-3-XMS-CASPT2 level generated energy profile diagram of (a) CHD, (b) CHD-Me2-1, (c) CHD-Me2-2, and (d) CHD-Me4. Energies are relative to the corresponding CHD derivatives.

# Appendix B

## B.1 Active molecular orbitals used for the multireference approach

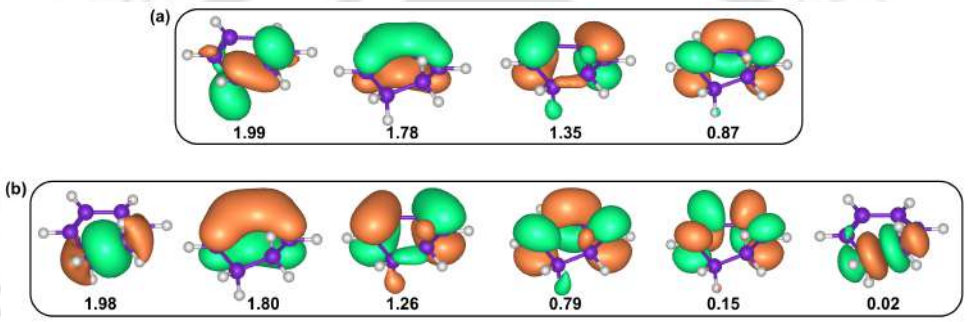


**Figure B.1.** Molecular orbitals considered within the active space of (a) six electrons in four orbitals, (6,4), (b) six electrons in six orbitals, (6,6).

## B.2 Truncation from cubic to spherical shape for n-hexane solvated system

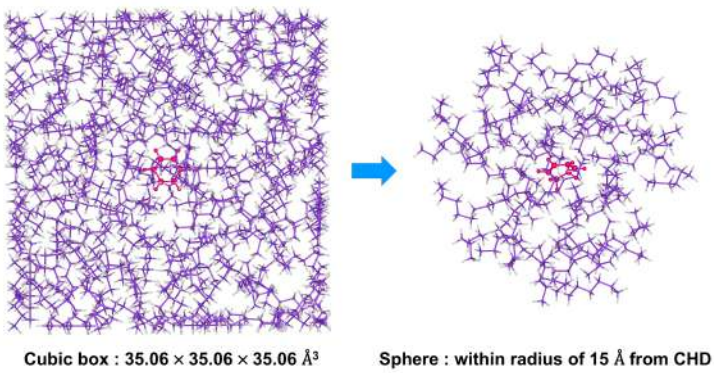


**Figure B.2.** Cropping the cubic box to a spherical shape for n-hexane-solvated system.

## B.3 RMSD plots for the collected geometries for n-hexane and water-solvated systems

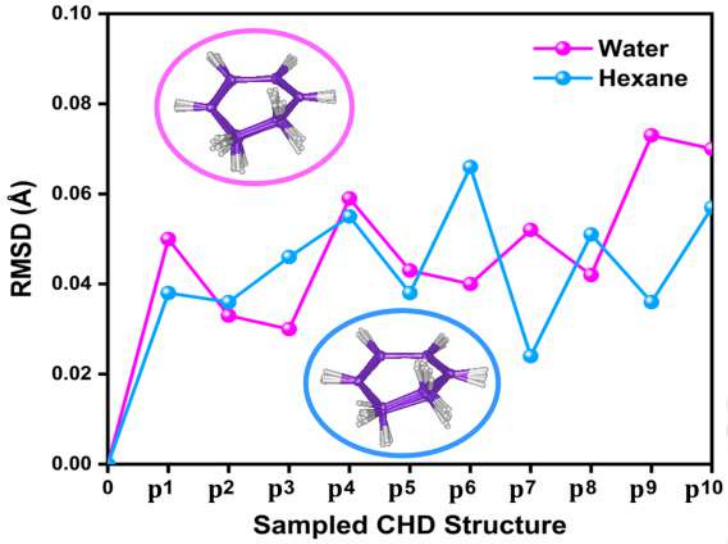


**Figure B.3.** RMSD plots for the collected CHD geometries of p1, p2, ..., p10 PDB frames in both (n-hexane and water) medium. The first geometry corresponds to the optimized CHD geometry.

## B.4 Ensemble averaged $C_1$–$C_6$ bond length and bond alteration coordinate (BAC) variation

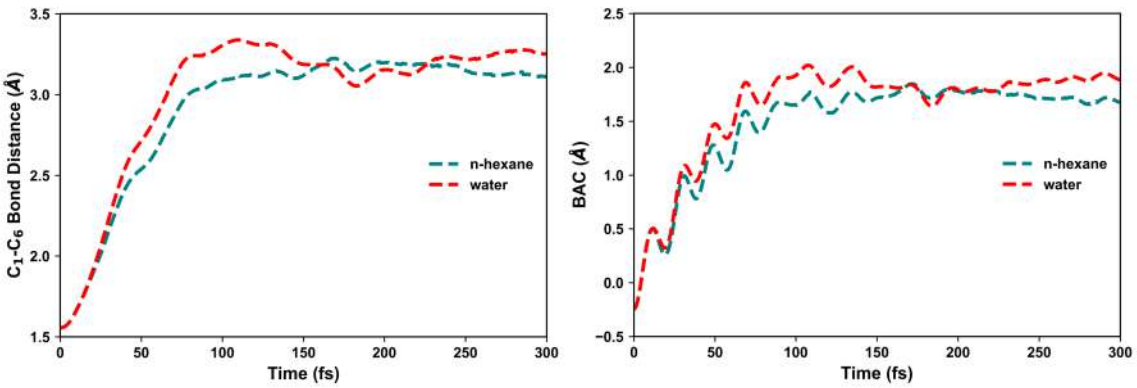


**Figure B.4.** Ensemble averaged (a) $C_1$-$C_6$ bond length and (b) bond alteration coordinate (BAC) evolution during the surface hopping simulations.

# B.5 Optimized cyclohexadiene, hexatriene, conrotatory transition state geometry, and IRC pathway

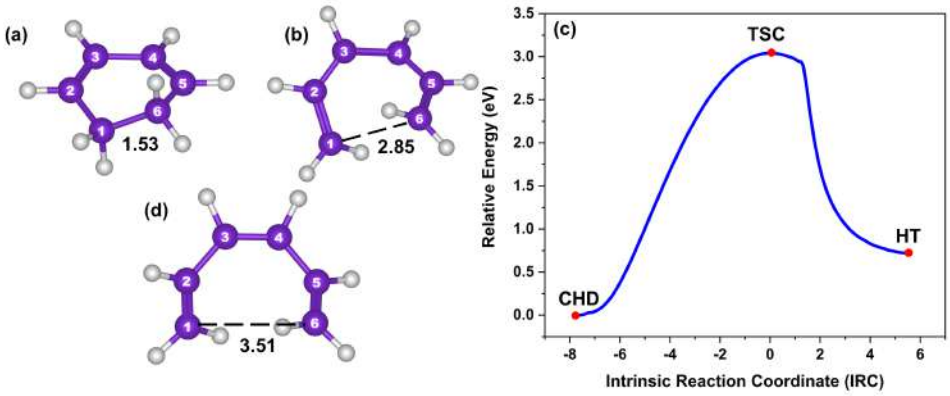


**Figure B.5.** (a) Optimized CHD at B3LYP/cc-pVTZ, (b) optimized conrotatory transition state geometry at CASSCF(6,4)/cc-pVDZ, (c) intrinsic reaction coordinate (IRC) pathway at CASSCF(6,4)/cc-pVDZ, and (d) optimized HT geometry at B3LYP/cc-pVTZ level of theory.

# B.6 Surface hopping MD simulation results for n-hexane solvated system

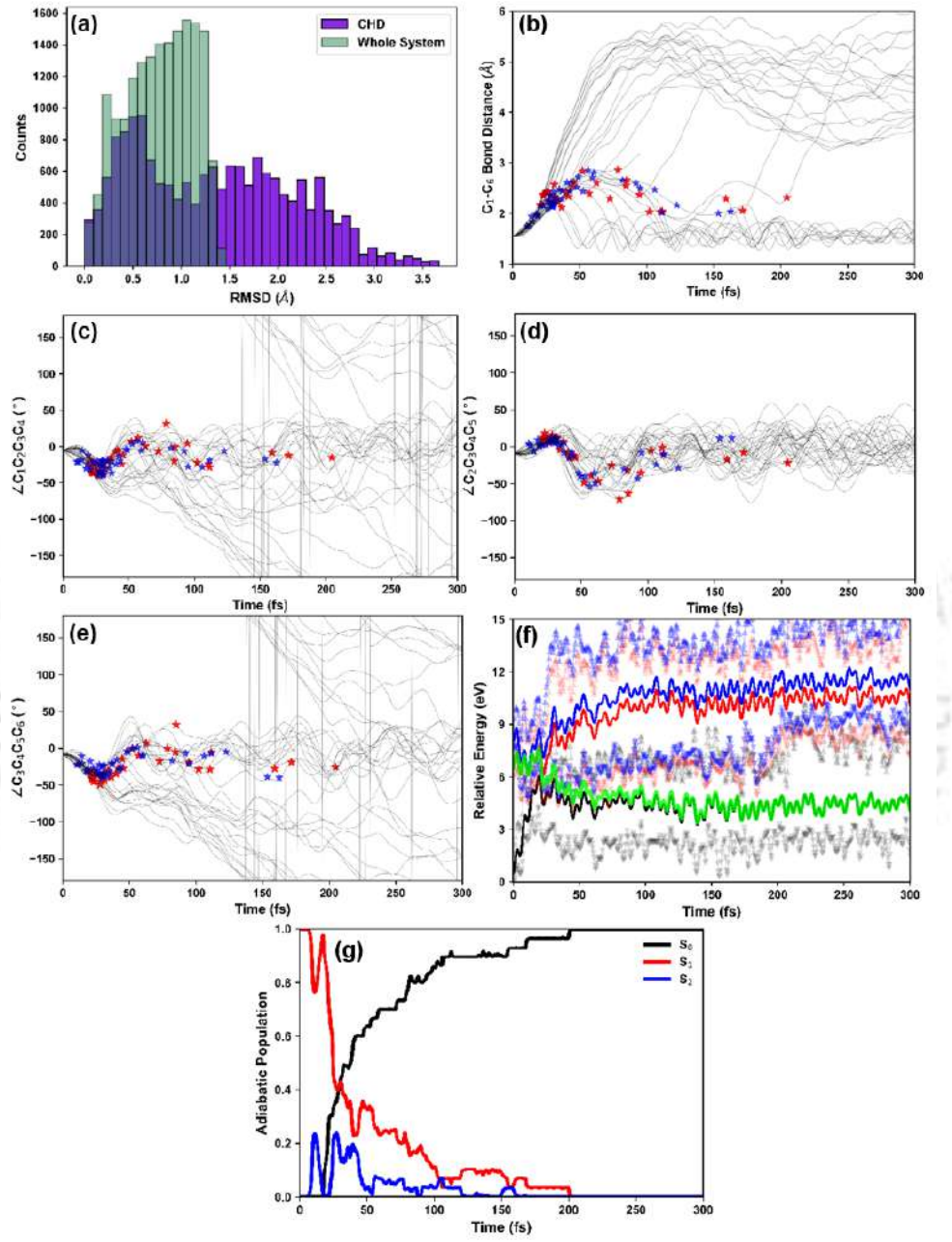


**Figure B.6.** (a) RMSD distribution, (b) $C_1$-$C_6$ bond length, (c) dihedral angle evolution, (d) electronic state energies, and (e) population evolution during surface hopping simulations of 30 trajectories for the initial geometry 'p1' in n-hexane medium.

# B.7 Surface hopping MD simulation results for water solvated system

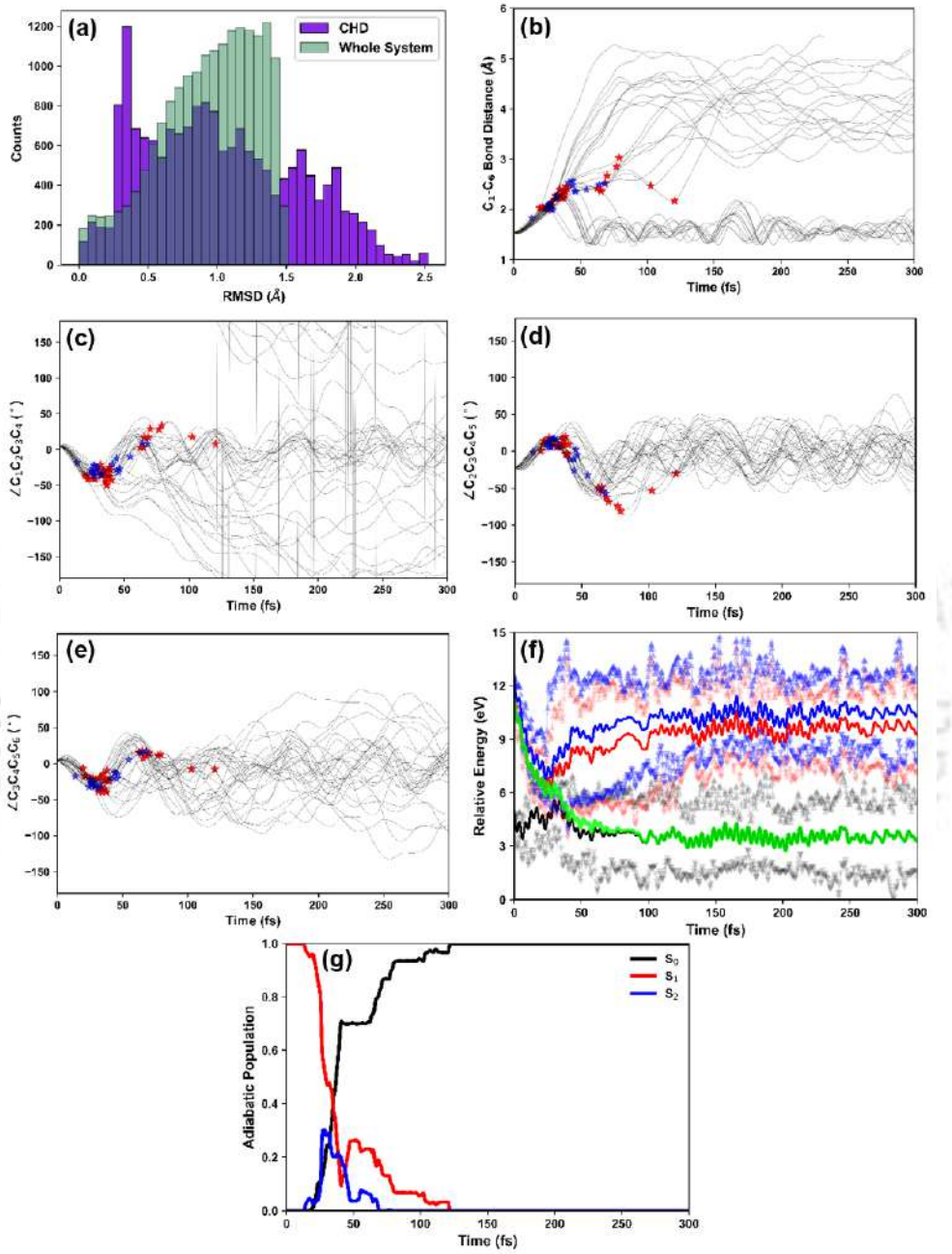


**Figure B.7.** (a) RMSD distribution, (b) $C_1$-$C_6$ bond length, (c) dihedral angle evolution, (d) electronic state energies, and (e) population evolution during surface hopping simulations of 30 trajectories for the initial geometry 'p1' in water medium.

# Appendix C

## C.1 Topography analysis and topographical parameters.

We performed this topography analysis as implemented in the Columbus software package.[235,241–243]

The conical intersection topographies are constructed using the following equation,

$$E_{1,2} = s_x x + s_y y \pm d_{gh}\left[\left(\frac{x^2+y^2}{2}\right) + \Delta_{gh}\left(\frac{x^2-y^2}{2}\right)\right]^{1/2} \tag{6}$$

where $s_x$ and $s_y$ are the projection of the summed gradient, $s$, on the branching or g-h plane, $d_{gh}$ defines the pitch, and $\Delta_{gh}$ defines the shift from cylindrical symmetry.

For our system, the topographical parameters are shown below:

**Table C.1.** Topographical parameters for $S_1/S_0$ conical intersection calculated at the SA-2 CASSCF(8,7)/6-31G(d) level of theory.

| System | $s_x$ | $s_y$ | $\Delta_{gh}$ | $d_{gh}$ |
|---|---|---|---|---|
| $S_1/S_0$ MECI | 1.91 | -7.08 | 0.50 | 7.86 |

## C.2 Single point corrected energies (in Hartree) of optimized geometries using SA-2-XMS-CAS(8,7)PT2 level of theory.

**Table C.2.** Single point corrected molecular energies at the SA-2-XMS-CAS(8,7)PT2/cc-pVDZ level of theory.

| **Species** | $S_0$ | $S_1$ |
|---|---|---|
| 1E | -842.53832992 | -842.36911481 |
| $S_1$-Min | -842.46729252 | -842.45560264 |
| TSC | -842.47477452 | -842.45290107 |
| $S_1/S_0$ MECI | -842.45649654 | -842.45441543 |
| 1C | -842.52720660 | -842.42204140 |

## C.3 Natural Transition Orbitals (NTOs) related to the excitation to $S_1$ calculated at the B3LYP/cc-pVDZ level of theory.

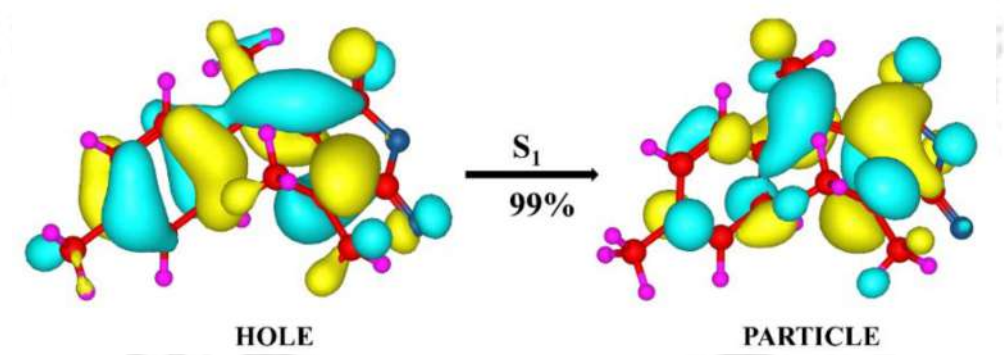


**Figure C.1.** NTOs calculated at B3LYP/cc-pVDZ level of theory.

## C.4 Root-Mean-Square Deviation (RMSD) plots associated with the molecular geometries during surface hopping simulations.

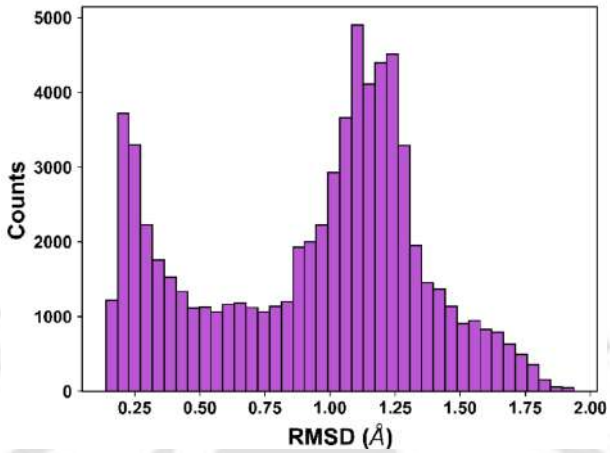


**Figure C.2.** Root-mean-square deviation (RMSD) plots during the surface hopping simulations.

## C.5 Dihedral angle variation during the trajectory surface hopping simulation.

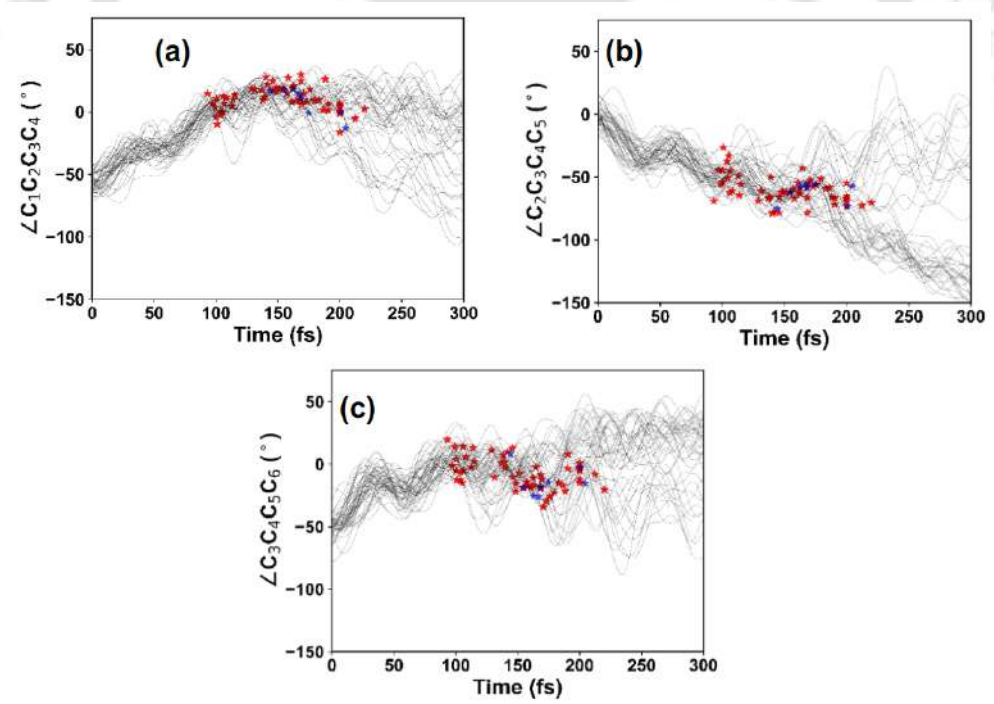


**Figure C.3.** Time evolution of dihedral angles, (a) $\angle C_1C_2C_3C_4$, (b) $\angle C_2C_3C_4C_5$, and (c) $\angle C_3C_4C_5C_6$ during surface hopping simulations of all trajectories.

## C.6 Dihedral angle and $C_1 - C_6$ bond length variation of two different single trajectories.

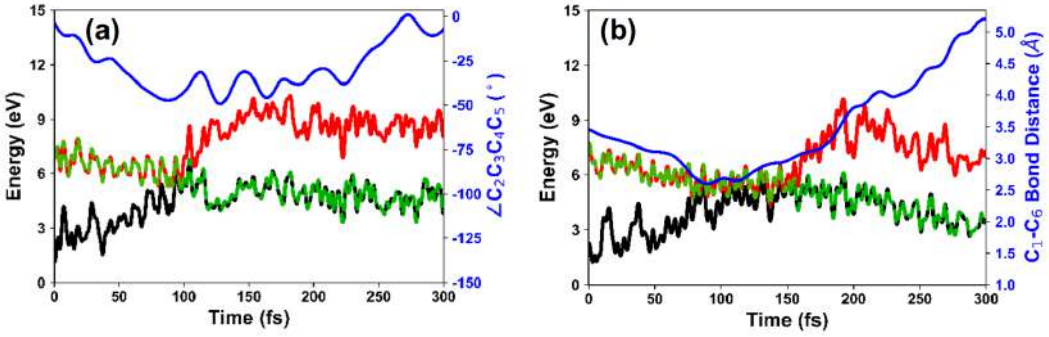


**Figure C.4.** Time evolution of (a) $\angle C_2C_3C_4C_5$ dihedral angle in the trajectory resulting in 1C, and (b) $C_1 - C_6$ bond length in the trajectory resulting in 1Z, during surface hopping simulations.

## C.7 Molecular projected self-consistent Hamiltonian (MPSH).

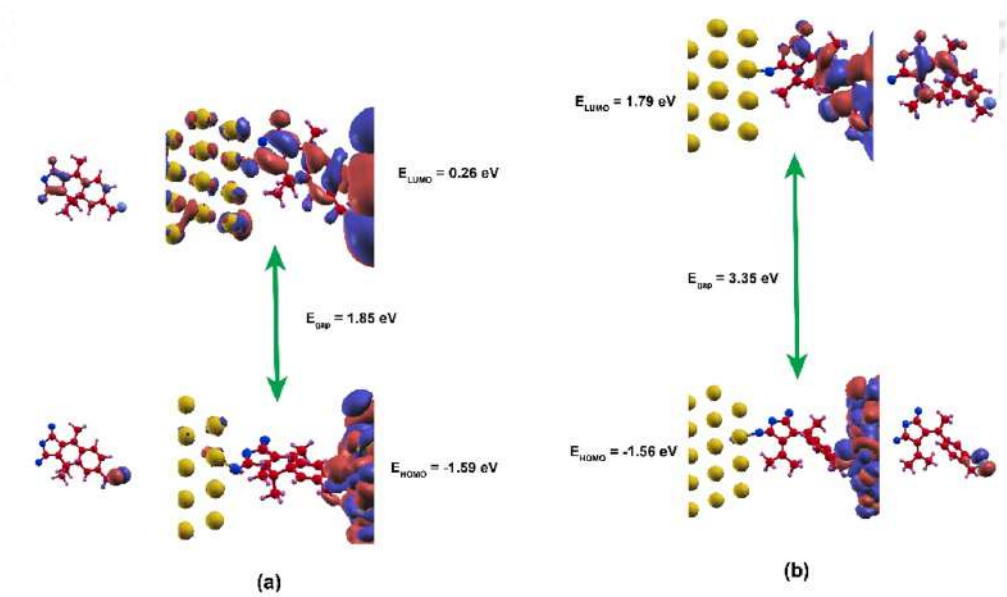


**Figure C.5.** At zero bias, molecular projected self-consistent Hamiltonian (MPSH) orbitals of Fulgide molecule [1C (a) and 1E (b) isomer] and electrode interactions along with the HOMO-LUMO of the isolated molecules.

# Bibliography


[1] G. Ciamician, Science **36**, 385 (1912).

[2] G. K. Rollefson and M. Burton, *Photochemistry and the mechanism of chemical reactions*, Prentice-Hall chemistry series (Prentice-Hall, 1939).

[3] R. Norrish and C. Bamford, Nature **140**, 195 (1937).

[4] G. N. Lewis and M. Kasha, J. Am. Chem. Soc. **66**, 2100 (1944).

[5] G. N. Lewis and M. Calvin, J. Am. Chem. Soc. **67**, 1232 (1945).

[6] G.-N. Porter, Proc. R. Soc. Lond. A Math. Phys. Sci. **200**, 284 (1950).

[7] R. G. W. Norrish and G. Porter, Proc. R. Soc. Lond. A Math. Phys. Sci. **210**, 439 (1952).

[8] G. Porter and F. J. Wright, Trans. Faraday Soc. **51**, 1469 (1955).

[9] L. Salem, J. Am. Chem. Soc. **90**, 543 (1968).

[10] R. G. Pearson, J. Am. Chem. Soc. **85**, 3533 (1963).

[11] R. B. Woodward and R. Hoffmann, J. Am. Chem. Soc. **87**, 395 (1965).

[12] R. B. Woodward and R. Hoffmann, Angew. Chem. Int. Ed. **8**, 781 (1969).

[13] T. Förster, Radiat. Res. Suppl. **2**, 326 (1960).

[14] J. Murrell and K. J. Laidler, Trans. Faraday Soc. **64**, 371 (1968).

[15] J. Jortner, M. Ottolenghi, and G. Stein, J. Phys. Chem. **68**, 247 (1964).

[16] N. J. Turro, *Modern molecular photochemistry* (University Science Books, 1991).

[17] A. J. Bard, J. Photochem. **10**, 59 (1979).

[18] M. A. Fox, Chem. Rev. **79**, 253 (1979).

[19] J. G. Black, P. Kolodner, M. Shultz, E. Yablonovitch, and N. Bloembergen, Phys. Rev. A **19**, 704 (1979).

[20] H. D. Roth, Pure Appl. Chem. **73**, 395 (2001).

[21] M. Grätzel, Comments Inorg. Chem. **12**, 93 (1991).

[22] M. R. Hoffmann, S. T. Martin, W. Choi, and D. W. Bahnemann, Chem. Rev. **95**, 69 (1995).

[23] S. E. Braslavsky, Pure Appl. Chem. **79**, 293 (2007).

[24] Z. J. Garlets, J. D. Nguyen, and C. R. Stephenson, Isr. J. Chem. **54**, 351 (2014).

[25] B. E. Hetzler, P. Donthamsetti, Z. Peitsinis, C. Stanley, D. Trauner, and E. Y. Isacoff, J. Am. Chem. Soc. **145**, 18778 (2023).

[26] M. H. Berry, A. Holt, J. Broichhagen, P. Donthamsetti, J. G. Flannery, and E. Y. Isacoff, Curr. Opin. Pharmacol. **65**, 102259 (2022).

[27] P. O. Dral and M. Barbatti, Nat. Rev. Chem. **5**, 388 (2021).

[28] J. Westermayr and P. Marquetand, Chem. Rev. **121**, 9873 (2020).

[29] G. Wald, Science **162**, 230 (1968).

[30] H. Dartnall, Vis. Res. **8**, 339 (1968).

[31] E. Havinga, Experientia **29**, 1181 (1973).

[32] S. Mai and L. González, Angew. Chem., Int. Ed. **59**, 16832 (2020).

[33] L. Cederbaum, W. Domcke, H. Köppel, and W. Von Niessen, Chem. Phys. **26**, 169 (1977).

[34] M. F. Holick, J. MacLaughlin, M. Clark, S. Holick, J. Potts Jr, R. Anderson, I. Blank, J. Parrish, and P. Elias, Science **210**, 203 (1980).

[35] M. Holick, J. Frommer, S. McNeill, N. Richtand, J. Henley, and J. Potts Jr, Biochem. Biophys. Res. Commun. **76**, 107 (1977).

[36] I. Polyak, L. Hutton, R. Crespo-Otero, M. Barbatti, and P. J. Knowles, J. Chem. Theory Comput. **15**, 3929 (2019).

[37] H. Tamura, S. Nanbu, H. Nakamura, and T. Ishida, Chem. Phys. Lett. **401**, 487 (2005).

[38] T. Mori and S. Kato, Chem. Phys. Lett. **476**, 97 (2009).

[39] O. Schalk, T. Geng, T. Thompson, N. Baluyot, R. D. Thomas, E. Tapavicza, and T. Hansson, J. Phys. Chem. A **120**, 2320 (2016).

[40] E. Salazar and S. Faraji, Mol. Phys. **118**, e1764120 (2020).

[41] L. Zhang, Y. Shu, S. Bhaumik, X. Chen, S. Sun, Y. Huang, and D. G. Truhlar, J. Chem. Theory Comput. **18**, 7073 (2022).

[42] S. Trushin, W. Fuß, T. Schikarski, W. Schmid, and K. Kompa, J. Chem. Phys. **106**, 9386 (1997).

[43] W. Fuß, W. Schmid, and S. Trushin, J. Chem. Phys. **112**, 8347 (2000).

[44] M. Garavelli, C. Page, P. Celani, M. Olivucci, W. Schmid, S. Trushin, and W. Fuss, J. Phys. Chem. A **105**, 4458 (2001).

[45] N. Kuthirummal, F. M. Rudakov, C. L. Evans, and P. M. Weber, J. Chem. Phys. **125**, 133307 (2006).

[46] K. Kosma, S. Trushin, W. Fuß, and W. Schmid, Phys. Chem. Chem. Phys. **11**, 172 (2009).

[47] C. C. Pemberton, Y. Zhang, K. Saita, A. Kirrander, and P. M. Weber, J. Phys. Chem. A **119**, 8832 (2015).

[48] S. Adachi, M. Sato, and T. Suzuki, J. Phys. Chem. Lett. **6**, 343 (2015).

[49] P. Celani, S. Ottani, M. Olivucci, F. Bernardi, and M. A. Robb, J. Am. Chem. Soc. **116**, 10141 (1994).

[50] P. Celani, F. Bernardi, M. A. Robb, and M. Olivucci, J. Am. Chem. Soc. **100**, 19364 (1996).

[51] M. Garavelli, P. Celani, M. Fato, M. J. Bearpark, B. R. Smith, M. Olivucci, and M. A. Robb, J. Phys. Chem. A **101**, 2023 (1997).

[52] M. Robb *et al.*, Faraday Discuss. **110**, 51 (1998).

[53] M. Merchán, L. Serrano-Andrés, L. S. Slater, B. O. Roos, R. McDiarmid, and X. Xing, J. Phys. Chem. A **103**, 5468 (1999).

[54] A. Nenov, P. Kolle, M. A. Robb, and R. de Vivie-Riedle, J. Org. Chem. **75**, 123 (2010).

[55] A. Hofmann and R. de Vivie-Riedle, J. Chem. Phys. **112**, 5054 (2000).

[56] A. Hofmann and R. de Vivie-Riedle, Chem. Phys. Lett. **346**, 299 (2001).

[57] J. Schonborn, J. Sielk, and B. Hartke, J. Phys. Chem. A **114**, 4036 (2010).

[58] A. Li, S. Yuan, Y. Dou, Y. Wang, and Z. Wen, Chem. Phys. Lett. **478**, 28 (2009).

[59] E. Tapavicza, A. M. Meyer, and F. Furche, Phys. Chem. Chem. Phys. **13**, 20986 (2011).

[60] J. Kim, H. Tao, T. J. Martinez, and P. Bucksbaum, J. Phys. B: At., Mol. Opt. Phys. **48**, 164003 (2015).

[61] A. Ohta, O. Kobayashi, S. O. Danielache, and S. Nanbu, Chem. Phys. **459**, 45 (2015).

[62] Y. Lei, H. Wu, X. Zheng, G. Zhai, and C. Zhu, J. Photochem. Photobiol. A: Chem. **317**, 39 (2016).

[63] M. Filatov, S. K. Min, and K. S. Kim, Mol. Phys. **117**, 1128 (2019).

[64] M. P. Minitti, J. M. Budarz, A. Kirrander, J. Robinson, T. J. Lane, D. Ratner, K. Saita, T. Northey, B. Stankus, V. Cofer-Shabica, *et al.*, Faraday Discuss. **171**, 81 (2014).

[65] M. Minitti, J. Budarz, A. Kirrander, J. Robinson, D. Ratner, T. Lane, D. Zhu, J. Glownia, M. Kozina, H. Lemke, *et al.*, Phys. Rev. Lett. **114**, 255501 (2015).

[66] T. J. Wolf, D. M. Sanchez, J. Yang, R. Parrish, J. Nunes, M. Centurion, R. Coffee, J. Cryan, M. Gühr, K. Hegazy, *et al.*, Nat. Chem. **11**, 504 (2019).

[67] M. Olivucci, F. Bernardi, S. Ottani, and M. A. Robb, J. Am. Chem. Soc. **116**, 2034 (1994).

[68] O. Schalk, A. E. Boguslavskiy, and A. Stolow, J. Phys. Chem. A **114**, 4058 (2010).

[69] S. P. Neville, Y. Wang, A. E. Boguslavskiy, A. Stolow, and M. S. Schuurman, J. Chem. Phys. **144** (2016).

[70] G. Wu, A. E. Boguslavskiy, O. Schalk, M. S. Schuurman, and A. Stolow, J. Chem. Phys. **135**, 164309 (2011).

[71] R. J. MacDonell and M. S. Schuurman, Chem. Phys. **515**, 360 (2018).

[72] K. R. Herperger, A. Röder, R. J. MacDonell, A. E. Boguslavskiy, A. B. Skov, A. Stolow, and M. S. Schuurman, J. Chem. Phys. **153**, 244307 (2020).

[73] R. J. MacDonell, M. E. Corrales, A. E. Boguslavskiy, L. Bañares, A. Stolow, and M. S. Schuurman, J. Chem. Phys. **152**, 084308 (2020).

[74] R. J. MacDonell, O. Schalk, T. Geng, R. D. Thomas, R. Feifel, T. Hansson, and M. S. Schuurman, J. Chem. Phys. **145** (2016).

[75] R. J. MacDonell and M. S. Schuurman, J. Phys. Chem. A **123**, 4693 (2019).

[76] A. Lee, J. Coe, S. Ullrich, M.-L. Ho, S.-J. Lee, B.-M. Cheng, M. Zgierski, I. Chen, T. Martinez, and A. Stolow, J. Phys. Chem. A **111**, 11948 (2007).

[77] M. S. Schuurman and A. Stolow, Annu. Rev. Phys. Chem. **69**, 427 (2018).

[78] P. Chakraborty, R. C. Couto, and N. H. List, J. Phys. Chem. A **127**, 5360 (2023).

[79] P. Kalita, B. Medhi, H. K. Singh, H. P. Bhattacharyya, N. Gupt, and M. Sarma, ChemPhysChem **24**, e202200727 (2023).

[80] B. O. Roos, P. R. Taylor, and P. E. Sigbahn, Chem. Phys. **48**, 157 (1980).

[81] B. O. Roos, P. Linse, P. E. Siegbahn, and M. R. Blomberg, Chem. Phys. **66**, 197 (1982).

[82] A. D. Becke, J. Chem. Phys. **98**, 5648 (1993).

[83] S. Grimme, J. Antony, S. Ehrlich, and H. Krieg, J. Chem. Phys. **132** (2010), 154104.

[84] T. Shiozaki, W. Győrffy, P. Celani, and H.-J. Werner, J. Chem. Phys. **135**, 081106 (2011).

[85] M. P. Grubb, P. M. Coulter, H. J. Marroux, B. Hornung, R. S. McMullen, A. J. Orr-Ewing, and M. N. Ashfold, Nat. Chem. **8**, 1042 (2016).

[86] C. G. Elles and F. F. Crim, Annu. Rev. Phys. Chem. **57**, 273 (2006).

[87] A. Rosspeintner, B. Lang, and E. Vauthey, Annu. Rev. Phys. Chem. **64**, 247 (2013).

[88] C. Reichardt and T. Welton, *Solvents and solvent effects in organic chemistry* (John Wiley & Sons, 2010).

[89] W. Liptay, Angew. Chem. Int. Ed. Engl. **8**, 177 (1969).

[90] V. Ravi Kumar, C. Verma, and S. Umapathy, J. Chem. Phys. **144**, 064302 (2016).

[91] B. F. Curchod and T. J. Martínez, Chem. Rev. **118**, 3305 (2018).

[92] D. Polli, P. Altoè, O. Weingart, K. M. Spillane, C. Manzoni, D. Brida, G. Tomasello, G. Orlandi, P. Kukura, R. A. Mathies, *et al.*, Nature **467**, 440 (2010).

[93] M. Maroncelli, J. MacInnis, and G. R. Fleming, Science **243**, 1674 (1989).

[94] B. Bagchi and B. Jana, Chem. Soc. Rev. **39**, 1936 (2010).

[95] J. N. Israelachvili, *Intermolecular and surface forces* (Academic press, 2011).

[96] N. A. Romero and D. A. Nicewicz, Chem. Rev. **116**, 10075 (2016).

[97] M. Havenith, Angew. Chem., Int. Ed. **55**, 1218 (2016).

[98] B. Bagchi, *Water in biological and chemical processes: from structure and dynamics to function* (Cambridge University Press, 2013).

[99] H. Qian, S. Pramanik, and I. Aprahamian, J. Am. Chem. Soc. **139**, 9140 (2017).

[100] S. H. M. Jafri, T. Blom, K. Leifer, M. Strömme, H. Löfås, A. Grigoriev, R. Ahuja, and K. Welch, nanotech **21**, 435204 (2010).

[101] Y. Yokoyama, Chem. Rev. **100**, 1717 (2000).

[102] Y. Yokoyama, New J. Chem. **33**, 1314 (2009).

[103] S. Kawata and Y. Kawata, Chem. Rev. **100**, 1777 (2000).

[104] M. Müri, K. C. Schuermann, L. De Cola, and M. Mayor, "Shape-switchable azo-macrocycles," (2009).

[105] K. G. Yager and C. J. Barrett, J. Photochem. Photobiol. A: Chem. **182**, 250 (2006).

[106] R. Siewertsen, J. B. Schönborn, B. Hartke, F. Renth, and F. Temps, Phys. Chem. Chem. Phys. **13**, 1054 (2010).

[107] M.-M. Russew and S. Hecht, Adv. Mater. **22**, 3348 (2010).

[108] A. A. Beharry, L. Wong, V. Tropepe, and G. A. Woolley, Angew. Chem., Int. Ed. **50**, 1325 (2011).

[109] M. Irie, Chem. Rev. **100**, 1685 (2000).

[110] K. Matsuda and M. Irie, J. Photochem. Photobiol. C **5**, 169 (2004).

[111] F. Renth, R. Siewertsen, and F. Temps, Int. Rev. Phys. Chem. **32**, 1 (2013).

[112] S. Matsika, Chem. Rev. **121**, 9407 (2021).

[113] J. Zhang, D. Chen, Y. Xia, Y.-P. Huang, X. Lin, X. Han, N. Ni, Z. Wang, F. Yu, L. Yang, *et al.*, J. Chem. Theory Comput. **19**, 4338 (2023).

[114] K. T. Butler, D. W. Davies, H. Cartwright, O. Isayev, and A. Walsh, Nature **559**, 547 (2018).

[115] J. Behler, K. Reuter, and M. Scheffler, Phys. Rev. B **77**, 115421 (2008).

[116] D. Hu, Y. Xie, X. Li, L. Li, and Z. Lan, J. Phys. Chem. Lett. **9**, 2725 (2018).

[117] F. Kossoski and M. Barbatti, Chem. Sci. **11**, 9827 (2020).

[118] W. Chu, W. A. Saidi, and O. V. Prezhdo, ACS nano **14**, 10608 (2020).

[119] J. Li and S. A. Lopez, Chem. Phys. Rev. **4**, 031309 (2023).

[120] M. Martyka, L. Zhang, F. Ge, Y.-F. Hou, J. Jankowska, M. Barbatti, and P. O. Dral, npj Comput Mater. **11**, 132 (2025).

[121] J. Li, R. Stein, D. M. Adrion, and S. A. Lopez, J. Am. Chem. Soc. **143**, 20166 (2021).

[122] J. Li, P. Reiser, B. R. Boswell, A. Eberhard, N. Z. Burns, P. Friederich, and S. A. Lopez, Chem. Sci. **12**, 5302 (2021).

[123] J. Li and S. A. Lopez, Chem. Eur. J. **28**, e202200651 (2022).

[124] L. Wang, C. Salguero, S. A. Lopez, and J. Li, Chem **10**, 2295 (2024).

[125] J. L. Mancuso, A. M. Mroz, K. N. Le, and C. H. Hendon, Chem. Rev. **120**, 8641 (2020).

[126] J. Zupan and J. Gasteiger, Anal. Chim. Acta **248**, 1 (1991).

[127] J. S. Smith, O. Isayev, and A. E. Roitberg, Chem. Sci. **8**, 3192 (2017).

[128] T. Lenzen and U. Manthe, J. Chem. Phys. **147**, 084105 (2017).

[129] C. Xie, X. Zhu, D. R. Yarkony, and H. Guo, J. Chem. Phys. **149**, 144107 (2018).

[130] J. S. Smith, B. T. Nebgen, R. Zubatyuk, N. Lubbers, C. Devereux, K. Barros, S. Tretiak, O. Isayev, and A. E. Roitberg, Nat. Commun. **10**, 2903 (2019).

[131] S. Käser, L. I. Vazquez-Salazar, M. Meuwly, and K. Töpfer, DD **2**, 28 (2023).

[132] T. T. Duignan, ACS Phys. Chem. Au. **4**, 232 (2024).

[133] A. P. Bartók, M. C. Payne, R. Kondor, and G. Csányi, Phys. Rev. Lett. **104**, 136403 (2010).

[134] A. P. Bartók, R. Kondor, and G. Csányi, Phys. Rev. B **87**, 184115 (2013).

[135] S. Chmiela, H. E. Sauceda, K.-R. Müller, and A. Tkatchenko, Nat. Commun **9**, 3887 (2018).

[136] S. Chmiela, H. E. Sauceda, I. Poltavsky, K.-R. Müller, and A. Tkatchenko, Comput. Phys. Commun. **240**, 38 (2019).

[137] A. S. Christensen, L. A. Bratholm, F. A. Faber, and O. Anatole von Lilienfeld, J. Chem. Phys. **152**, 044107 (2020).

[138] B. Huang and O. A. von Lilienfeld, Nat. Chem. **12**, 945 (2020).

[139] A. Szabo and N. S. Ostlund, *Modern quantum chemistry: introduction to advanced electronic structure theory* (Courier Corporation, 1996).

[140] L. S. Cederbaum, "Born-oppenheimer approximation and beyond," in *Conical Intersections*, pp. 3–40.

[141] G. A. Worth and L. S. Cederbaum, Annu. Rev. Phys. Chem. **55**, 127 (2004).

[142] C. D. Sherrill and H. F. Schaefer III, in *Advances in quantum chemistry*, Vol. 34 (Elsevier, 1999) pp. 143–269.

[143] D. R. Hartree, in *Mathematical Proceedings of the Cambridge Philosophical Society*, Vol. 24 (Cambridge University Press, 1928) pp. 89–110.

[144] V. Fock, J. Phys. **61**, 126 (1930).

[145] W. Pauli, C. P. Enz, and K. Von Meyenn, *Writings on physics and philosophy*, Vol. 133 (Springer, 1994).

[146] J. W. Park, R. Al-Saadon, M. K. MacLeod, T. Shiozaki, and B. Vlaisavljevich, Chem. Rev. **120**, 5878 (2020).

[147] K. Hirao, *Recent Advances in Multireference Methods* (WORLD SCIENTIFIC, 1999).

[148] P. E. Siegbahn, J. Almlöf, A. Heiberg, and B. O. Roos, J. Chem. Phys. **74**, 2384 (1981).

[149] J. Finley, P.-Å. Malmqvist, B. O. Roos, and L. Serrano-Andrés, Chem. Phys. Lett. **288**, 299 (1998).

[150] I. Fdez. Galvan, M. Vacher, A. Alavi, C. Angeli, F. Aquilante, J. Autschbach, J. J. Bao, S. I. Bokarev, N. A. Bogdanov, R. K. Carlson, *et al.*, J. Chem. Theory Comput. **15**, 5925 (2019).

[151] H.-J. Werner, P. J. Knowles, G. Knizia, F. R. Manby, and M. Schütz, WIREs Comput. Mol. Sci. **2**, 242 (2012).

[152] T. Shiozaki, WIREs Comput. Mol. Sci. **8**, e1331 (2018).

[153] T. Shiozaki, BAGEL Brilliantly Advanced General Electronic-structure Library http://www.nubakery.org under the GNU General Public License.

[154] S. A. Hollingsworth and R. O. Dror, Neuron **99**, 1129 (2018).

[155] L. Verlet, Phys. Rev. **159**, 98 (1967).

[156] M. A. Cuendet and W. F. van Gunsteren, J. Chem. Phys. **127** (2007).

[157] D. Frenkel and B. Smit, *Understanding molecular simulation: from algorithms to applications* (Elsevier, 2023).

[158] M. A. González, École thématique de la Société Française de la Neutronique **12**, 169 (2011).

[159] W. L. Jorgensen, D. S. Maxwell, and J. Tirado-Rives, J. Am. Chem. Soc. **118**, 11225 (1996).

[160] Y. Duan, C. Wu, S. Chowdhury, M. C. Lee, G. Xiong, W. Zhang, R. Yang, P. Cieplak, R. Luo, T. Lee, *et al.*, J. Comput. Chem. **24**, 1999 (2003).

[161] J. Huang and A. D. MacKerell Jr, J. Comput. Chem. **34**, 2135 (2013).

[162] N. Schmid, A. P. Eichenberger, A. Choutko, S. Riniker, M. Winger, A. E. Mark, and W. F. Van Gunsteren, Eur. Biophys. J. **40**, 843 (2011).

[163] S. J. Marrink, H. J. Risselada, S. Yefimov, D. P. Tieleman, and A. H. De Vries, J. Phys. Chem. B **111**, 7812 (2007).

[164] F. James, Rep. Prog. Phys. **43**, 1145 (1980).

[165] J. C. Tully, J. Chem. Phys. **93**, 1061 (1990).

[166] R. Crespo-Otero and M. Barbatti, Chem. Rev. **118**, 7026 (2018).

[167] G. Granucci and M. Persico, J. Chem. Phys. **126**, 134114 (2007).

[168] A. Jain and A. Sindhu, ACS omega **7**, 45810 (2022).

[169] B. J. Schwartz, E. R. Bittner, O. V. Prezhdo, and P. J. Rossky, J. Chem. Phys. **104**, 5942 (1996).

[170] J. E. Subotnik, A. Jain, B. Landry, A. Petit, W. Ouyang, and N. Bellonzi, Annu. Rev. Phys. Chem. **67**, 387 (2016).

[171] C. Wittig, J. Phys. Chem. B **109**, 8428 (2005).

[172] A. K. Belyaev and O. V. Lebedev, Phys. Rev. A. **84**, 014701 (2011).

[173] A. Belyaev and O. Lebedev, *Journal of Physics: Conference Series*, Vol. 388 (2012) p. 092007.

[174] A. K. Belyaev, C. Lasser, and G. Trigila, J. Chem. Phys. **140**, 224108 (2014).

[175] M. Barbatti, J. Chem. Theory Comput. **17**, 3010 (2021).

[176] E. X. Salazar, M. F. Menger, and S. Faraji, J. Chem. Theory Comput. **20**, 5796 (2024).

[177] M. Barbatti, M. Ruckenbauer, F. Plasser, J. Pittner, G. Granucci, M. Persico, and H. Lischka, WIREs Comput. Mol. Sci. **4**, 26 (2014).

[178] M. Ruckenbauer, M. Barbatti, B. Sellner, T. Muller, and H. Lischka, J. Phys. Chem. A **114**, 12585 (2010).

[179] M. Ruckenbauer, M. Barbatti, T. M"uller, and H. Lischka, J. Phys. Chem. A **114**, 6757 (2010).

[180] L. Zhang, S. V. Pios, M. Martyka, F. Ge, Y.-F. Hou, Y. Chen, L. Chen, J. Jankowska, M. Barbatti, and P. O. Dral, J. Chem. Theory Comput. **20**, 5043 (2024).

[181] E. Posenitskiy, F. Spiegelman, and D. Lemoine, Mach. Learn.: Sci. Technol. **2**, 035039 (2021).

[182] J. Suchan, J. Janos, and P. Slavicek, J. Chem. Theory Comput. **16**, 5809 (2020).

[183] M. Xu, T. Zhu, and J. Z. Zhang, J. Phys. Chem. A **123**, 6587 (2019).

[184] M. Xu, T. Zhu, and J. Z. Zhang, Front. Chem. **9**, 692200 (2021).

[185] J. Zeng, L. Cao, M. Xu, T. Zhu, and J. Z. Zhang, Nat. Commun. **11**, 5713 (2020).

[186] J. Zeng, L. Zhang, H. Wang, and T. Zhu, Energy Fuels **35**, 762 (2020).

[187] B. Freeman, S. Löwel, and W. Singer, J. Neurosci. Methods **20**, 115 (1987).

[188] A. Krogh, Nat. Biotechnol. **26**, 195 (2008).

[189] I. Goodfellow, Y. Bengio, A. Courville, and Y. Bengio, *Deep learning*, Vol. 1 (MIT Press Cambridge, 2016).

[190] T. Hastie, R. Tibshirani, J. H. Friedman, and J. H. Friedman, *The elements of statistical learning: data mining, inference, and prediction*, Vol. 2 (Springer, 2009).

[191] P. O. Dral, J. Phys. Chem. Lett. **11**, 2336 (2020).

[192] A. Karthikeyan and U. D. Priyakumar, J. Chem. Sci. **134**, 2 (2022).

[193] Y. Zhang, C. Hu, and B. Jiang, J. Phys. Chem. Lett. **10**, 4962 (2019).

[194] R. Srinivasan, J. Am. Chem. Soc. **90**, 4498 (1968).

[195] M. T. Reetz, Angew. Chem. Int. Ed. **11**, 129 (1972).

[196] H. E. Zimmerman, Acc. Chem. Res. **4**, 272 (1971).

[197] M. Dewar, Tetrahedron **22**, 75 (1966).

[198] E. Mawer, G. Lumb, and S. Stanbury, Nature **222**, 482 (1969).

[199] S. Sakai and S.-y. Takane, J. Phys. Chem. A **103**, 2878 (1999).

[200] C. Gaasbeek, H. Hogeveen, and H. Volger, Recl. Trav. Chim. Pays-Bas **91**, 821 (1972).

[201] S. Karashima, A. Humeniuk, R. Uenishi, T. Horio, M. Kanno, T. Ohta, J. Nishitani, R. Mitric, and T. Suzuki, J. Am. Chem. Soc. **143**, 8034 (2021).

[202] V. A. Guner, K. Houk, and I. W. Davies, J. Org. Chem. **69**, 8024 (2004).

[203] S. Deb and P. M. Weber, Annu. Rev. Phys. Chem. **62**, 19 (2011).

[204] E. Salazar, S. Reinink, and S. Faraji, Phys. Chem. Chem. Phys. **24**, 11592 (2022).

[205] M. Morimoto, S. Kobatake, and M. Irie, Photochem. Photobiol. Sci. **2**, 1088 (2003).

[206] R. Hoffmann and R. Woodward, J. Am. Chem. Soc. **87**, 2046 (1965).

[207] H. Longuet-Higgins and E. Abrahamson, J. Am. Chem. Soc. **87**, 2045 (1965).

[208] M. H. Farag, T. L. Jansen, and J. Knoester, J. Phys. Chem. Lett. **7**, 3328 (2016).

[209] M. Born and J. R. Oppenheimer, Ann. Phys. **84**, 457 (1927).

[210] H. C. Longuet-Higgins, U. Öpik, M. H. L. Pryce, and R. Sack, Proc. R. Soc. Lond. Ser. Math. Phys. Sci. **244**, 1 (1958).

[211] Q. Li, D. Mendive-Tapia, M. J. Paterson, A. Migani, M. J. Bearpark, M. A. Robb, and L. Blancafort, Chem. Phys. **377**, 60 (2010).

[212] K. C. Moore, Photomed. Laser Surg. **31**, 563 (2013).

[213] H. Lui and R. R. Anderson, Dermatol. Clin. **11**, 1 (1993).

[214] J. K. Gimzewski and C. Joachim, Science **283**, 1683 (1999).

[215] R. J. Coulston, H. Onagi, S. F. Lincoln, and C. J. Easton, J. Am. Chem. Soc. **128**, 14750 (2006).

[216] L. Andreoni, M. Baroncini, J. Groppi, S. Silvi, C. Taticchi, and A. Credi, Energy Fuels **35**, 18900 (2021).

[217] V. Balzani, A. Credi, and M. Venturi, Chem. - Eur. J. **8**, 5524 (2002).

[218] E. Salazar and S. Faraji, Mol. Phys. **118**, e1764120 (2020).

[219] K. Andersson, P. A. Malmqvist, B. O. Roos, A. J. Sadlej, and K. Wolinski, J. Phys. Chem. **94**, 5483 (1990).

[220] K. Andersson, P.-Å. Malmqvist, and B. O. Roos, J. Chem. Phys. **96**, 1218 (1992).

[221] T. Mori and S. Kato, Chem. Phys. Lett. **476**, 97 (2009).

[222] R. Iikubo, T. Sekikawa, Y. Harabuchi, and T. Taketsugu, Faraday Discuss. **194**, 147 (2016).

[223] K. Kaneshima, Y. Ninota, and T. Sekikawa, Opt. Express **26**, 31039 (2018).

[224] J. Olsen, Int. J. Quantum Chem. **111**, 3267 (2011).

[225] H.-J. Werner and W. Meyer, J. Chem. Phys. **74**, 5794 (1981).

[226] R. N. Diffenderfer and D. R. Yarkony, J. Phys. Chem. **86**, 5098 (1982).

[227] S. Nanbu, T. Ishida, and H. Nakamura, Chem. Sci. **1**, 663 (2010).

[228] C. Zhu, K. Nobusada, and H. Nakamura, J. Chem. Phys. **115**, 3031 (2001).

[229] C. Zhu, H. Kamisaka, and H. Nakamura, J. Chem. Phys. **115**, 11036 (2001).

[230] C. Zhu, H. Kamisaka, and H. Nakamura, J. Chem. Phys. **116**, 3234 (2002).

[231] P. Oloyede, G. Mil'nikov, and H. Nakamura, J. Chem. Phys. **124**, 144110 (2006).

[232] H. Nakamura, J. Phys. Chem. A **110**, 10929 (2006).

[233] M. J. Frisch, G. W. Trucks, H. B. Schlegel, G. E. Scuseria, M. A. Robb, J. R. Cheeseman, G. Scalmani, V. Barone, G. A. Petersson, H. Nakatsuji, X. Li, M. Caricato, A. V. Marenich, J. Bloino, B. G. Janesko, R. Gomperts, B. Mennucci, H. P. Hratchian, J. V. Ortiz, A. F. Izmaylov, J. L. Sonnenberg, D. Williams-Young, F. Ding, F. Lipparini, F. Egidi, J. Goings, B. Peng, A. Petrone, T. Henderson, D. Ranasinghe, V. G. Zakrzewski, J. Gao, N. Rega, G. Zheng, W. Liang, M. Hada, M. Ehara, K. Toyota, R. Fukuda, J. Hasegawa, M. Ishida, T. Nakajima, Y. Honda, O. Kitao, H. Nakai, T. Vreven, K. Throssell, J. A. Montgomery, Jr., J. E. Peralta, F. Ogliaro, M. J. Bearpark, J. J. Heyd, E. N. Brothers, K. N. Kudin, V. N. Staroverov, T. A. Keith, R. Kobayashi, J. Normand, K. Raghavachari, A. P. Rendell, J. C. Burant, S. S. Iyengar, J. Tomasi, M. Cossi, J. M. Millam, M. Klene, C. Adamo, R. Cammi, J. W. Ochterski, R. L. Martin, K. Morokuma, O. Farkas, J. B. Foresman, and D. J. Fox, "Gaussian 16 Revision C.01," (2019), Gaussian Inc. Wallingford CT.

[234] X. Zhu, K. C. Thompson, and T. J. Martínez, J. Chem. Phys. **150**, 164103 (2019).

[235] H. Lischka, T. Müller, P. G. Szalay, I. Shavitt, R. M. Pitzer, and R. Shepard, WIREs Comput. Mol. Sci. **1**, 191 (2011).

[236] R. Davies and K. Davies, Ann. Phys. **89**, 261 (1975).

[237] G. Granucci, M. Persico, and A. Zoccante, J. Chem. Phys. **133**, 134111 (2010).

[238] M. Ben-Nun and T. J. Martínez, Adv. Chem. Phys. **121**, 439 (2002).

[239] M. Ben-Nun and T. J. Martınez, J. Chem. Phys. **108**, 7244 (1998).

[240] M. Ben-Nun, J. Quenneville, and T. J. Martínez, J. Phys. Chem. A **104**, 5161 (2000).

[241] D. R. Yarkony, J. Chem. Phys. **114**, 2601 (2001).

[242] D. R. Yarkony, J. Phys. Chem. A **105**, 6277 (2001).

[243] M. Barbatti, A. J. Aquino, and H. Lischka, J. Phys. Chem. A **109**, 5168 (2005).

[244] B. Medhi and M. Sarma, J. Phys. Chem. A **128**, 2025 (2024).

[245] O. Travnikova, T. Pitesa, A. Ponzi, M. Sapunar, R. J. Squibb, R. Richter, P. Finetti, M. Di Fraia, A. De Fanis, N. Mahne, *et al.*, J. Am. Chem. Soc. **144**, 21878 (2022).

[246] L. Huang, L. Bertram, L. Ma, N. Goff, S. W. Crane, A. Odate, T. Northey, A. M. Carrascosa, M. Simmermacher, S. B. Muvva, *et al.*, J. Phys. Chem. A **128**, 4992 (2024).

[247] B. Medhi, U. Nath, and M. Sarma, J. Chem. Phys. **160**, 154308 (2024).

[248] C. Dugave and L. Demange, Chem. Rev. **103**, 2475 (2003).

[249] J. E. Kim, M. J. Tauber, and R. A. Mathies, Biochemistry **40**, 13774 (2001).

[250] A. Cembran, F. Bernardi, M. Garavelli, L. Gagliardi, and G. Orlandi, J. Am. Chem. Soc. **126**, 3234 (2004).

[251] J. W. Crump, J. Org. Chem. **28**, 953 (1963).

[252] S. Kovalenko, A. Dobryakov, I. Ioffe, and N. Ernsting, Chem. Phys. Lett. **493**, 255 (2010).

[253] Y. Dou, B. R. Torralva, and R. E. Allen, J. Phys. Chem. A **107**, 8817 (2003).

[254] H. Stecher, M. H. Gelb, J. C. Saari, and K. Palczewski, J. Biol. Chem. **274**, 8577 (1999).

[255] J. Conyard, A. Cnossen, W. R. Browne, B. L. Feringa, and S. R. Meech, J. Am. Chem. Soc. **136**, 9692 (2014).

[256] A. Raiol, A. R. da Cunha, V. Manzoni, T. Andrade-Filho, and R. Gester, J. Mol. Liq. **340**, 116887 (2021).

[257] J. Zhang and J. Liu, Nanoscale **12**, 2914 (2020).

[258] W. Y. Kim, Y. C. Choi, S. K. Min, Y. Cho, and K. S. Kim, Chem. Soc. Rev. **38**, 2319 (2009).

[259] M. Olivucci, F. Bernardi, P. Celani, I. Ragazos, and M. A. Robb, J. Am. Chem. Soc. **116**, 1077 (1994).

[260] C. C. Hayden and D. W. Chandler, J. Phys. Chem. **99**, 7897 (1995).

[261] M. Ben-Nun and T. J. Martınez, Chem. Phys. Lett. **298**, 57 (1998).

[262] C. F. Bender, T. H. Dunning Jr, H. F. Schaefer III, W. A. Goddard III, and W. J. Hunt, Chem. Phys. Lett. **15**, 171 (1972).

[263] B. R. Brooks and H. F. Schaefer III, J. Am. Chem. Soc. **101**, 307 (1979).

[264] R. J. Buenker, V. Bonačić-Koutecký, and L. Pogliani, J. Chem. Phys. **73**, 1836 (1980).

[265] E. Evleth and A. Sevin, J. Am. Chem. Soc. **103**, 7414 (1981).

[266] C. Petrongolo, R. J. Buenker, and S. D. Peyerimhoff, J. Chem. Phys. **76**, 3655 (1982).

[267] G. J. Dormans, G. C. Groenenboom, and H. M. Buck, J. Chem. Phys. **86**, 4895 (1987).

[268] G. J. Dormans, G. C. Groenenboom, W. C. Van Dorst, and H. M. Buck, J. Am. Chem. Soc. **110**, 1406 (1988).

[269] D. H. Waldeck, Chem. Rev. **91**, 415 (1991).

[270] R. J. Sension, S. T. Repinec, A. Z. Szarka, and R. M. Hochstrasser, J. Chem. Phys. **98**, 6291 (1993).

[271] T. W. Ebbesen, Acc. Chem. Res. **49**, 2403 (2016).

[272] E. Titov and A. Beqiraj, Adv. Theory Simul. **6**, 2200907 (2023).

[273] J. Zhang, X. Lu, D. Tang, S. Wu, X. Hou, J. Liu, and P. Wu, ACS Applied Materials & Interfaces **10**, 40808 (2018).

[274] H. Wang, S. Jiang, S. Chen, D. Li, X. Zhang, W. Shao, X. Sun, J. Xie, Z. Zhao, Q. Zhang, *et al.*, Adv. Mater. **28**, 6940 (2016).

[275] C. W. Whitehead and C. A. Whitesitt, J. Med. Chem. **17**, 1298 (1974).

[276] F. Reyes, R. Fernandez, A. Rodríguez, A. Francesch, S. Taboada, C. Avila, and C. Cuevas, Tetrahedron **64**, 5119 (2008).

[277] M. A. Jordan and L. Wilson, Nat. Rev. Cancer **4**, 253 (2004).

[278] T. Fukaminato, S. Ishida, and R. Métivier, NPG Asia Mater. **10**, 859 (2018).

[279] A. J. Josiah, K. K. Govender, P. P. Govender, and S. Sinha Ray, Adv. Theory Simul. **7**, 2400377 (2024).

[280] L. Martínez, R. Andrade, E. G. Birgin, and J. M. Martínez, J. Comput. Chem. **30**, 2157 (2009).

[281] W. L. Jorgensen, J. Am. Chem. Soc. **103**, 335 (1981).

[282] W. L. Jorgensen and N. A. McDonald, J. Mol. Struct.: THEOCHEM **424**, 145 (1998).

[283] W. L. Jorgensen and J. Tirado-Rives, Proc. Natl. Acad. Sci. U.S.A. **102**, 6665 (2005).

[284] L. S. Dodda, J. Z. Vilseck, J. Tirado-Rives, and W. L. Jorgensen, J. Phys. Chem. B **121**, 3864 (2017).

[285] L. S. Dodda, I. Cabeza de Vaca, J. Tirado-Rives, and W. L. Jorgensen, Nucleic Acids Res. **45**, W331 (2017).

[286] J. W. Ponder, Washington University School of Medicine, St. Louis (2004).

[287] D. Beeman, J. Comput. Phys. **20**, 130 (1976).

[288] B. Sellner, M. Barbatti, and H. Lischka, J. Chem. Phys. **131**, 024312 (2009).

[289] X. Guo, H. Yuan, B. An, Q. Zhu, and J. Zhang, J. Chem. Phys. **144**, 154306 (2016).

[290] G. H. Brown, Tech. Chem **3**, 853 (1971).

[291] S. Kobatake, S. Takami, H. Muto, T. Ishikawa, and M. Irie, Nature **446**, 778 (2007).

[292] M. Irie, T. Fukaminato, K. Matsuda, and S. Kobatake, Chem. Rev. **114**, 12174 (2014).

[293] Y. Du, C.-R. Huang, Z.-K. Xu, W. Hu, P.-F. Li, R.-G. Xiong, and Z.-X. Wang, JACS Au **3**, 185 (2023).

[294] Z. Gao, K. Wang, Y. Yan, J. Yao, and Y. S. Zhao, Natl. Sci. Rev. **8**, nwaa162 (2021).

[295] H. Dong, H. Zhu, Q. Meng, X. Gong, and W. Hu, Chem. Soc. Rev. **41**, 1754 (2012).

[296] D. Bléger and S. Hecht, Angew. Chem., Int. Ed. **54**, 11338 (2015).

[297] T. Tsujioka and M. Irie, J. Photochem. Photobiol. C **11**, 1 (2010).

[298] K. Ichimura and S. Watanabe, Bull. Chem. Soc. Jpn. **49**, 2220 (1976).

[299] M. Morimoto, S. Kobatake, and M. Irie, J. Am. Chem. Soc. **125**, 11080 (2003).

[300] R. K. Weerasekara, H. Uekusa, and C. V. Hettiarachchi, Cryst. Growth Des. **17**, 3040 (2017).

[301] G. Tomasello, M. J. Bearpark, M. A. Robb, G. Orlandi, and M. Garavelli, Angew. Chem., Int. Ed. **49**, 2913 (2010).

[302] A. Nenov, W. J. Schreier, F. O. Koller, M. Braun, R. de Vivie-Riedle, W. Zinth, and I. Pugliesi, J. Phys. Chem. A **116**, 10518 (2012).

[303] H.-Y. Zhu and Q.-S. Li, ChemPhysChem **24**, e202300435 (2023).

[304] H.-Y. Zhu and Q.-S. Li, Chem. Eur. J. **28**, e202201360 (2022).

[305] X.-Y. Du and Q.-S. Li, Chem. Eur. J. **26**, 12891 (2020).

[306] F.-P. Li, H.-Y. Zhu, Q.-S. Li, and Z.-S. Li, Phys. Chem. Chem. Phys. **21**, 8376 (2019).

[307] I. Ramsteiner, A. Hartschuh, and H. Port, Chem. Phys. Lett. **343**, 83 (2001).

[308] M. Handschuh, M. Seibold, H. Port, and H. C. Wolf, J. Phys. Chem. A **101**, 502 (1997).

[309] S. Kurita, A. Kashiwagi, Y. Kurita, H. Miyasaka, and N. Mataga, Chem. Phys. Lett. **171**, 553 (1990).

[310] R. Siewertsen, F. Strübe, J. Mattay, F. Renth, and F. Temps, Phys. Chem. Chem. Phys. **13**, 3800 (2011).

[311] T. Cordes, T. T. Herzog, S. Malkmus, S. Draxler, T. Brust, J. A. DiGirolamo, W. J. Lees, and M. Braun, Photochem. Photobiol. Sci. **8**, 528 (2009).

[312] S. Draxler, T. Brust, S. Malkmus, F. O. Koller, B. Heinz, S. Laimgruber, C. Schulz, S. Dietrich, K. Rück-Braun, W. Zinth, *et al.*, J. Mol. Liq. **141**, 130 (2008).

[313] F. O. Koller, W. J. Schreier, T. E. Schrader, A. Sieg, S. Malkmus, C. Schulz, S. Dietrich, K. Rück-Braun, W. Zinth, and M. Braun, J. Phys. Chem. A **110**, 12769 (2006).

[314] S. Malkmus, F. O. Koller, S. Draxler, T. E. Schrader, W. J. Schreier, T. Brust, J. A. DiGirolamo, W. J. Lees, W. Zinth, and M. Braun, Adv. Funct. Mater. **17**, 3657 (2007).

[315] F. O. Koller, W. J. Schreier, T. E. Schrader, S. Malkmus, C. Schulz, S. Dietrich, K. Rück-Braun, and M. Braun, J. Phys. Chem. A **112**, 210 (2008).

[316] J. Li, G. Speyer, and O. F. Sankey, Phys. Rev. Lett. **93**, 248302 (1 (2004).

[317] A. Perrier, F. Maurel, and D. Jacquemin, Acc. Chem. Research **45**, 1173 (2012).

[318] V. Darugar, M. Vakili, S. A. Brandán, and S. Adli, J Mol. Graph. Model. **120**, 108420 (2023).

[319] H. Basch, R. Cohen, and M. A. Ratner, Nano Lett. **5**, 1668 (2005).

[320] A. Sarmah, A. Wasfi, P. Hobza, and N. Tit, Chem. Mater. **33**, 8786 (2021).

[321] J.-D. Chai and M. Head-Gordon, Phys. Chem. Chem. Phys. **10**, 6615 (2008).

[322] A. D. Becke, J. Chem. Phys. **96**, 2155 (1992).

[323] C. Lee, W. Yang, and R. G. Parr, Phys. Rev. B **37**, 785 (1988).

[324] T. Yanai, D. P. Tew, and N. C. Handy, Chem. Phys. Lett. **393**, 51 (2004).

[325] Y. Zhao and D. G. Truhlar, Theor. Chem. Acc. **120**, 215 (2008).

[326] C. Adamo and V. Barone, J. Chem. Phys. **110**, 6158 (1999).

[327] R. Berraud-Pache, F. Neese, G. Bistoni, and R. Izsák, J. Chem. Theory Comput. **16**, 564 (2019).

[328] F. Neese, WIREs Comput Mol Sci. **12**, e1606 (2022).

[329] J. W. Park and T. Shiozaki, J. Chem. Theory Comput. **13**, 3676 (2017).

[330] M. Barbatti, M. Bondanza, R. Crespo-Otero, B. Demoulin, P. O. Dral, G. Granucci, F. Kossoski, H. Lischka, B. Mennucci, S. Mukherjee, *et al.*, J. Chem. Theory Comput. **18**, 6851 (2022).

[331] H. C. Andersen, J. Chem. Phys. **72**, 2384 (1980).

[332] N. Papior, N. Lorente, T. Frederiksen, A. García, and M. Brandbyge, Comput. Phys. Commun. **212**, 8 (2017).

[333] N. Troullier and J. L. Martins, Phys. Rev. B **43**, 1993 (1991).

[334] J. P. Perdew, K. Burke, and M. Ernzerhof, Phys. Rev. Lett. **77**, 3865 (1996).

[335] H. J. Monkhorst and J. D. Pack, Phys. Rev. B **13**, 5188 (1976).

[336] M. Büttiker, Y. Imry, R. Landauer, and S. Pinhas, Phys. Rev. B **31**, 6207 (1985).

[337] J. Song, Y. Yang, H. Liu, L. Guo, and Z. Zhang, J. Semicond. **31**, 114003 (2010).

[338] T. Frederiksen, M. Paulsson, M. Brandbyge, and A.-P. Jauho, Phys. Rev. B **75**, 205413 (2007).

[339] A. Castillo, P. Ceballos, P. Santos, M. Cerón, P. Venkatesan, E. Pérez-Gutiérrez, M. Sosa-Rivadeneyra, S. Thamotharan, M. A. Siegler, and M. J. Percino, Molecules **26**, 1500 (2021).

[340] G. J. Atchity, S. S. Xantheas, and K. Ruedenberg, J. Chem. Phys. **95**, 1862 (1991).

[341] A. Nitzan and M. A. Ratner, Science **300**, 1384 (2003).

[342] G. Dhivya, V. Nagarajan, and R. Chandiramouli, Chem. Phys. Lett. **660**, 27 (2016).

[343] V. Nagarajan and R. Chandiramouli, arXiv preprint arXiv:1812.08532 (2018).

[344] E. Zhao, D. Liu, L. Liu, X. Yang, W. Kan, and Y. Sun, J. Mater. Sci. Mater. **28**, 11749 (2017).

[345] A. Kanaani, M. Vakili, and D. Ajloo, Optik **219**, 165295 (2020).

[346] X. Yin, Y. Zang, L. Zhu, J. Z. Low, Z.-F. Liu, J. Cui, J. B. Neaton, L. Venkataraman, and L. M. Campos, Sci. Adv. **3**, eaao2615 (2017).

[347] K. R. Das and S. Dutta, arXiv preprint arXiv:2308.05468 (2023).

[348] B. Bian, Y. Zheng, P. Yuan, B. Liao, W. Chen, X. An, X. Mo, and Y. Ding, Phys. Lett. A **381**, 2748 (2017).

[349] Z. Sayyar, M. Vakili, A. Kanaani, and H. Eshghi, J. Comput. Electron. **19**, 917 (2020).

[350] A. Ghosh, B. Ball, S. Pal, and P. Sarkar, J. Phys. Chem. Lett. **13**, 7898 (2022).

[351] G. Di Liberto, L. A. Cipriano, S. Tosoni, and G. Pacchioni, Chem. Eur. J. **27**, 13306 (2021).

[352] N. Koumura, R. W. Zijlstra, R. A. van Delden, N. Harada, and B. L. Feringa, Nature **401**, 152 (1999).

[353] G. S. Kottas, L. I. Clarke, D. Horinek, and J. Michl, Chem. Rev. **105**, 1281 (2005).

[354] D. Thakur, M. Ram Nagar, S. Kumar, Shahnawaz, A. Tomar, A. Karmakar, S. Banik, J.-H. Jou, and S. Ghosh, Chem. Eur. J. **29**, e202203282 (2023).

[355] Y.-N. Chen, T.-F. He, Y.-X. Cheng, H.-M. Zhan, A.-M. Ren, T.-S. Wu, B.-H. Zhang, Y.-L. Zhang, H.-X. Zhang, and L.-Y. Zou, Org. Electron. **97**, 106185 (2021).

[356] X. Rodríguez-Martínez, E. Pascual-San-José, and M. Campoy-Quiles, Energy Environ. Sci. **14**, 3301 (2021).

[357] E. Runge and E. K. Gross, Phys. Rev. Lett. **52**, 997 (1984).

[358] M. E. Casida, in *Recent Advances In Density Functional Methods: (Part I)* (World Scientific, 1995) pp. 155–192.

[359] Y. Damour, A. Scemama, D. Jacquemin, F. Kossoski, and P.-F. Loos, J. Chem. Theory Comput. **20**, 4129 (2024).

[360] L. Zhang, J. Han, H. Wang, R. Car, and W. E, Phys. Rev. Lett. **120**, 143001 (2018).

[361] B. Jiang, J. Li, and H. Guo, Int. Rev. Phys. Chem. **35**, 479 (2016).

[362] F. Häse, S. Valleau, E. Pyzer-Knapp, and A. Aspuru-Guzik, Chem. Sci. **7**, 5139 (2016).

[363] F. A. Faber, A. Lindmaa, O. A. Von Lilienfeld, and R. Armiento, Phys. Rev. Lett. **117**, 135502 (2016).

[364] S. Ghosh and S. Hammes-Schiffer, J. Phys. Chem. Lett. **6**, 1 (2015).

[365] J. Westermayr, M. Gastegger, M. F. Menger, S. Mai, L. González, and P. Marquetand, Chem. Sci. **10**, 8100 (2019).

[366] S. V. Pios, M. F. Gelin, A. Ullah, P. O. Dral, and L. Chen, J. Phys. Chem. Lett. **15**, 2325 (2024).

[367] H. Jiang, J. Zhang, T. Wang, J. Peng, C. Jin, X. Zou, P. Zhu, T. Jiang, Z. Lan, H. Yong, *et al.*, Nat. Commun. **16**, 6703 (2025).

[368] D. R. Yarkony, J. Chem. Phys. **112**, 2111 (2000).